Spectroscopic investigation of the three-dimensional topological insulators $(MnBi_2Te_4)(Bi_2Te_3)_n$ and HgTe: band structure, orbital symmetries, and influence of the cation *d*-states

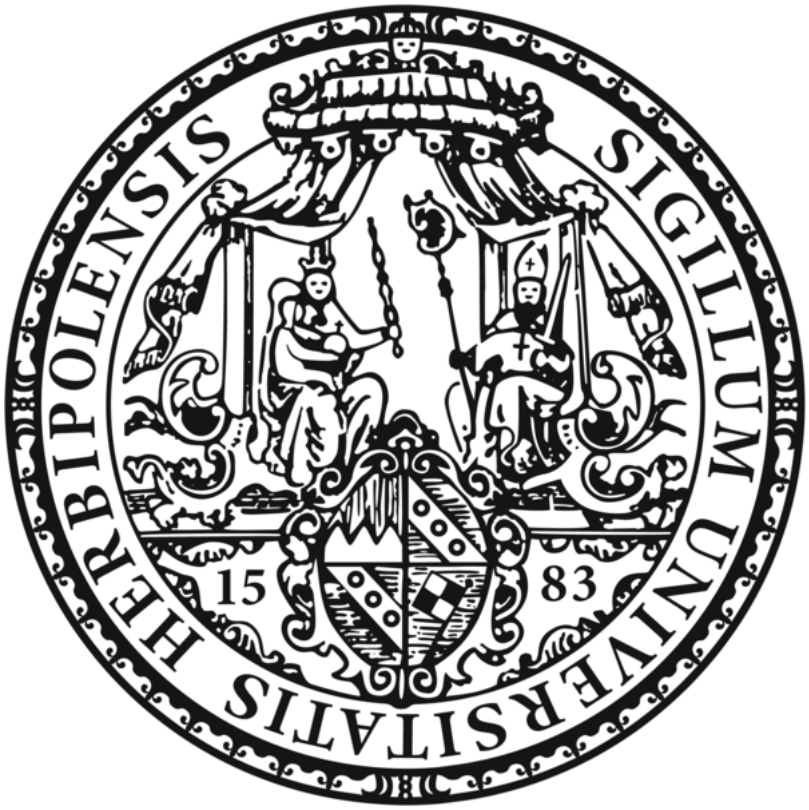

Dissertation zur Erlangung des
naturwissenschaftlichen Doktorgrades
der Julius-Maximilians-Universität Würzburg

vorgelegt von

Can Raphael Crespo Vidal
aus Frankfurt am Main

Würzburg 2021

Eingereicht am: 06.12.2021
bei der Fakultät für Physik und Astronomie

1. Gutachter: Prof. Dr. Friedrich Reinert
2. Gutachter: Prof. Dr. Ralph Claessen
3. Gutachter: Prof. Dr. Mark Golden
der Dissertation

Vorsitzende(r): Prof. Dr. Haye Hinrichsen

1. Prüfer: Prof. Dr. Friedrich Reinert
2. Prüfer: Prof. Dr. Ralph Claessen
3. Prüfer: Prof. Dr. Giorgio Sangiovanni
im Promotionskolloquium

Tag des Promotionskolloquiums: 10.03.2023
Doktorurkunde ausgehändigt am: _____

All we have to decide is what to do with the time that is given us.

– J. R. R. Tolkien, The Fellowship of the Ring

Zusammenfassung

Die Untersuchung von Materialien mit nicht-trivialer Bandtopologie nimmt in der aktuellen Erforschung kondensierter Materie eine zentrale Rolle ein. Stetig werden neuartige und exotische Quantenphasen in sowohl neuen als auch in bereits existierenden Materialien vorhergesagt und nachgewiesen. Jedoch befindet sich dieses Forschungsfeld in mancher Hinsicht noch immer in seinen Kinderschuhen und ein umfassendes Verständnis der elektronischen Bandstruktur, welche die topologischen Eigenschaften bedingt, ist eines der Hauptanliegen. In dieser Doktorarbeit werden die elektronischen Eigenschaften zweier Materialien untersucht, welche die Realisierung und Beobachtung neuartiger topologischer Phänomene versprechen. Hierbei bildet die winkelaufgelöste Photoemission die experimentelle Grundlage zur Untersuchung der elektronischen Eigenschaften. Des Weiteren wird die magnetische Ordnung mittels Röntgendichroismus untersucht.

Zum einen wird die elektronische Struktur der Volumenzustände sowie des Oberflächenzustandes von epitaktisch gewachsenem HgTe in der Phase eines dreidimensionalen topologischen Isolators untersucht. Dafür wird eine Präparationsmethode vorgestellt, die oberflächensensitive Messungen an *ex situ* Proben durch das Aufbringen und durch das anschließende mechanische Ablösen einer schützenden Deckschicht auf der Dünnschichtprobe ermöglicht. Die Leistungsfähigkeit dieser Präparationsmethode wird in der anschließenden experimentellen Studie demonstriert, in der mittels Synchrotronstrahlung die dreidimensionale Bandstruktur und die Orbitalzusammensetzung der Volumenzustände mithilfe von photonenenergieabhängigen beziehungsweise polarisationsabhängigen Photoemissionsmessungen untersucht wird. Darüber hinaus wird der topologische Oberflächenzustand an *in situ* gewachsenen Proben mittels einer Laborstrahlungsquelle untersucht. Die sich daraus ergebenden experimentellen Daten erlauben es, die durch die Bandinversion hervorgerufene impulsabhängige Änderung des Orbitalcharakters der Volumenzustände nachzuweisen. Die Analyse wird von theoretischen Berechnungen basierend auf der Dichtefunktionaltheorie ergänzt. Diese bestätigen zum einen den experimentell beobachteten Wechsel des Orbitalcharakters der Valenzbandzustände, zum anderen belegen sie einen dispersiven Charakter der Hg $5d$ Orbitale und zeigen deren Wichtigkeit für ein quantitatives Verständnis der elektronischen Struktur von HgTe.

Des Weiteren wird eine neuartige Serie von Van-der-Waals-Verbindungen, $(MnBi_2Te_4)(Bi_2Te_3)_n$, untersucht. Diese Materialklasse birgt die Möglichkeit, topologisch nicht-triviales Verhalten mit langreichweitiger magnetischer Ordnung zu kombinieren, wobei letztere die Zeitumkehrsymmetrie des Systems brechen soll. Zunächst werden die

magnetischen Eigenschaften der ersten beiden Vertreter der Reihe, $MnBi_2Te_4$ und $MnBi_4Te_7$, untersucht. Während $MnBi_2Te_4$ eine antiferromagnetische Ordnung senkrecht zur Oberfläche aufweist, zeigt $MnBi_4Te_7$ eindeutige Hinweise auf eine endliche remanente Magnetisierung. Auf die magnetische Charakterisierung folgt die Vorstellung eines experimentellen Verfahrens zur Identifikation der verschiedenen Oberflächenterminierungen, deren Anzahl durch die n interkalierten Bi_2Te_3 Lagen gegeben ist. Die Identifizierung geschieht durch die spektrale Signatur der Mn-Atome, deren Detektion durch Synchrotron-Photoemissionsmessungen mit einem Strahldurchmesser von einigen 10 µm ermöglicht wird. Unter Anwendung dieser Methode wird der topologische Oberflächenzustand der beiden Terminierungen von $MnBi_4Te_7$ mittels zirkulardichroitischer, photonenenergieabhängiger und spinaufgelöster Photoemission analysiert. Diese Analyse ergibt, dass der topologische Zustand auf der ($MnBi_2Te_4$)-Terminierung in Form eines freistehenden Dirac-Kegels auftritt, dessen Dirac-Punkt in der Volumenbandlücke liegt. Dahingegen hybridisiert der Oberflächenzustand einer (Bi_2Te_3)-Terminierung mit den Valenzbandzuständen, wodurch eine spektrale Lücke in seiner Dispersion entsteht. Überdies weist er einen Dirac-Punkt auf, der im Bereich des Kontinuums der Volumenzustände liegt und somit von diesem überlagert wird. Auch hier werden die experimentellen Ergebnisse teilweise von Dichtefunktionaltheorie-Rechnungen untermauert. Abschließend wird der in der Literatur vorhandene Mangel an eindeutigen Beweisen einer temperaturabhängigen Öffnung der Energielücke am Dirac-Punkt anhand von $MnBi_2Te_4$ diskutiert.

Abstract

The study of materials with non-trivial band topology has taken a pivotal role in contemporary condensed matter research. New and exotic quantum phases are continually being predicted and detected in both novel and existing materials. In some ways, however, the research field is still in its infancy and a comprehensive understanding of electronic band structures that host these topological properties is one of the key objectives. This thesis examines the electronic properties of two materials that promise the realization and observation of novel exotic quantum phenomena. For this purpose, angle-resolved photoemission forms the experimental basis for the investigation of the electronic properties. Furthermore, the magnetic order is investigated utilizing X-ray dichroism measurements.

First, the bulk and surface electronic structure of epitaxially grown HgTe in its three-dimensional topological insulator phase is investigated. A preparation method is introduced that allows for surface-sensitive measurements on *ex situ* samples by deposition and subsequent exfoliation of a protective capping layer on the thin film. The capability of this preparation method is demonstrated in the ensuing experimental study, in which synchrotron radiation is used to address the three-dimensional band structure and orbital composition of the bulk states by employing photon-energy-dependent and polarization-dependent measurements, respectively. In addition, the topological surface state is examined on *in situ* grown samples using a laboratory photon source. The resulting data provide a means to experimentally localize the bulk band inversion in momentum space and to evidence the momentum-dependent change in the orbital character of the inverted bulk states. Throughout this analysis, the experimental data are supplemented by theoretical calculations based on density functional theory. On the one hand, these calculations reproduce the experimentally observed change in the orbital character of the valence band states. On the other hand, they show an itinerant character of the Hg $5d$ electrons and demonstrate their importance for a quantitative understanding of the electronic structure of HgTe.

Furthermore, a rather new series of van der Waals compounds, $(MnBi_2Te_4)(Bi_2Te_3)_n$, is investigated. This material platform promises to merge topological non-trivial behavior with long-range magnetic ordering, the latter of which is intended to break the time-reversal symmetry in the system. First, the magnetic properties of the first two members of the series, $MnBi_2Te_4$ and $MnBi_4Te_7$, are studied via X-ray absorption-based techniques. While the former exhibits an out-of-plane antiferromagnetic ordering, the latter shows clear indications of a finite magnetic moment in remanence. The magnetic characterization is followed by the introduction of an experimental procedure to identify the surface terminations at hand,

the number of which is determined by the n intercalated (Bi_2Te_3)-layers. The identification is based on a spectral feature of the Mn species and is enabled by synchrotron measurements with a beam diameter of several tens of μm. Applying this method, the topological surface state on the two terminations of $MnBi_4Te_7$ is analyzed using circular dichroic, photon-energy-dependent, and spin-resolved photoemission. The analysis concludes that the topological state on the ($MnBi_2Te_4$)-layer termination shows a free-standing Dirac cone with its Dirac point located in the bulk band gap. In contrast, on the (Bi_2Te_3)-layer termination the surface state hybridizes with the bulk valences states, forming a spectral weight gap, and exhibits a Dirac point that is buried within the bulk continuum. Again, the experimental spectra are accompanied by density functional calculations, which strengthen the interpretation of the data. Lastly, the lack of unambiguous evidence in the literature showing a temperature-dependent mass gap opening in these magnetic topological insulators is discussed through $MnBi_2Te_4$.

Table of contents

1 Introduction **1**

2 Topological phases in condensed matter physics **5**

2.1 Electronic states in solids 5

2.2 $\mathbb{Z}_2$ topological insulators 6

2.2.1 The band inversion mechanism in HgTe 9

2.3 Non-trivial topology and time-reversal symmetry breaking 11

3 Methodology **15**

3.1 Photoelectron spectroscopy 15

3.1.1 Angle-resolved photoelectron spectroscopy 16

3.1.2 The transition matrix element and symmetry considerations 17

3.1.3 Spin-resolved photoelectron spectroscopy 20

3.1.4 Resonant photoelectron spectroscopy 21

3.2 X-ray absorption spectroscopy 22

3.2.1 X-ray magnetic circular dichroism 24

3.2.2 X-ray magnetic linear dichroism 25

3.3 Density functional theory 26

3.4 Experimental setups and geometry 28

3.4.1 Photoemission setups 28

3.4.2 X-ray absorption setup 34

3.5 Sample synthesis and preparation 35

4 Bulk and surface electronic structure of HgTe(001)/CdTe **41**

4.1 Material properties and preceding characterization 42

4.2 Bulk band structure 45

4.3 Influence of $p-d$ hybridization on the valence states 49

4.4 Orbital composition of the bulk electronic structure of HgTe(001) 55

4.5 Temperature dependence of the chemical potential 60

5 Magnetic and electronic structure of $(MnBi_2Te_4)(Bi_2Te_3)_n$ **63**

5.1 Crystal structure and general properties of $(MnBi_2Te_4)(Bi_2Te_3)_n$ 64

5.2 Magnetic and electronic properties of the Mn species in $(MnBi_2Te_4)(Bi_2Te_3)_n$ 66

5.3 Surface electronic structure of $(MnBi_2Te_4)(Bi_2Te_3)_n$ 78

5.3.1 Termination dependence of the electronic structure 78

5.3.2 Orbital complexity in the surface electronic structure of $MnBi_4Te_7$. 85
5.3.3 Temperature dependence and magnetic gap opening in $MnBi_2Te_4$. 100

6 Concluding discussion & outlook **107**

Appendix **115**

Bibliography **120**

List of own publications **149**

Danksagung **153**

1 Introduction

The advent of topology in condensed matter physics forms a landmark in modern physics and has been shaping the research landscape for the past 15 years. Topological insulators do not fall into the conventional paradigm of phases which are classified by the spontaneous breaking of symmetries. Instead, they exhibit a global quantity that is a property of the occupied states, the valence band ensemble, and that is conserved as long as a finite energy gap between the valence and conduction band states is maintained [1]. The underlying premise of these materials can be formulated as the statement that not all insulating phases are equivalent in a way that they can be continuously transformed to an atomic insulator without bridging the energy gap.

While possible applications of topological insulators are in the field of metrology [2], probably their most promising potential lies in their implementation in spintronics and quantum computing applications. The long spin coherence favors the use of these materials in spin-based applications due to the possibility of fault-tolerant information storage. Additionally, the interplay between topological insulators and conventional phases such as superconductivity or magnetism enriches the possibilities and creates novel quantum phenomena [3]. The former, for instance, allows inducing the long-sought Majorana fermions, whose zero-mode could serve as a building block for qubits [4]. On the other hand, introducing magnetism into a topological system can lead to spin-polarized dissipationless transport in the form of the quantum anomalous Hall effect [5–7]. Within this context, both materials studied in this work are at the center of contemporary research. Mercury telluride constitutes a topological system that allows controlled transport experiments in a variety of non-trivial phases, including topological superconductivity [8], whereas $MnBi_2Te_4$ and its derivatives are predicted to be the first instances of intrinsic (anti-)ferromagnetic topological insulators [9, 10].

The hallmark characteristic of a topological insulator is the occurrence of metallic states on its boundaries when interfaced with trivial materials or the vacuum. These topological edge or surface states are protected by time-reversal symmetry in the sense that they cannot be localized or gapped by non-magnetic defects, as they are a consequence of the topological properties of the bulk [11]. Surface-sensitive measurement techniques, such as angle-resolved photoelectron spectroscopy, are thus ideally suited to explore, in particular, the two-dimensional surface states of three-dimensional topological insulators.

The first experimentally accessible topological insulator was predicted by B. A. Bernevig *et al.* and experimentally realized shortly thereafter by a Würzburg group under L. W. Molenkamp in the form of HgTe quantum wells [12, 13]. This two-dimensional system is also referred to as a quantum spin Hall insulator. The concept of topological insulators was soon after extended to the third dimension and the first material platforms hosting these physics emerged in the form of $Bi_{1-x}Sb_x$, Bi_2Te_3, and uniaxially strained bulk HgTe [14–16].

Since the discovery of its topological properties, HgTe has maintained a pivotal role in the research of topological materials. This is due to the fact that in addition to the two phases already mentioned, this material platform is able to host a variety of other non-trivial phases like Weyl physics, Kane Fermions, and traces of topological superconductivity [4, 8, 17, 18]. This becomes particularly relevant since, contrary to recent theoretical studies which predict an abundance of topological materials, the number of systems that are well enough controlled for detailed experimental investigations is nonetheless quite limited [19]. In particular, HgTe represents one of the few material systems that allows for controlled transport experiments.

Despite its persistent relevance in the field of topological materials, studies that quantitatively address the global electronic structure of HgTe are still lacking. Relativistic effects and a sizeable hybridization between the cation d-states and the p-derived valence states exert significant influence on the band positions and even the band ordering of the valence states, which is the root of the topological properties of this system. As a result, theoretical descriptions of the electronic structure of HgTe are often limited to small regions in momentum space or qualitative assertions. Furthermore, experimental studies are challenged by the volatile nature of the Hg species, creating significant obstacles to the synthesis of thin films as well as their preparation for surface-sensitive measurements which require pristine surface quality.

Overcoming these obstacles motivates the investigation of this versatile material platform. The goal is to establish a surface preparation routine that allows for high-resolution photoemission experiments on *ex situ* samples. The resulting data not only form the basis of the experimental investigation of the electronic structure but also serve as a necessary reference for a quantitative theoretical modeling of the system. Combining experimental and theoretical approaches will allow us to unveil the intricacies in the bulk and surface electronic structure of HgTe.

Even though topological insulators, such as HgTe, are not defined by a spontaneous breaking of symmetries, the invariance to certain symmetries opens intriguing scientific venues to explore. In particular, the interplay of broken time-reversal symmetry and non-trivial band topology has the potential to generate remarkable quantum phases like the quantum

anomalous Hall effect, the axion insulator phase, or Majorana fermions [20–22]. Until recently, the approaches of realizing magnetic topological insulators relied on introducing the magnetic order extrinsically into a topological system via doping with magnetically active adatoms or by proximity effects [5, 23, 24]. Such systems pose significant challenges to their experimental investigation due to the delicate fine-tuning of material parameters required. Additionally, the increased disorder in doped and alloyed systems creates a constraint on acquiring high-resolution photoemission data. For these reasons, it is desirable to find a material platform that combines non-trivial band topology with intrinsic magnetic ordering in a stoichiometric compound, thus alleviating many of the aforementioned obstructions.

Within this context, the van der Waals compound $MnBi_2Te_4$ will be investigated in the second half of this work. This material introduces a manganese-containing sublattice into the quintuple layers of the three-dimensional topological insulator Bi_2Te_3, forming septuple layers. The system is expected to host a combination of long-range magnetic ordering, due to magnetic moments provided by the Mn atoms, and the inverted bulk band structure of Bi_2Te_3 [9, 10, 25]. In fact, $MnBi_2Te_4$ represents the progenitor of a heterostructural $(MnBi_2Te_4)(Bi_2Te_3)_n$ series of layered van der Waals compounds [26, 27]. The intercalation of non-magnetic (Bi_2Te_3)-layers separates the magnetically active layers, altering the magnetic properties of the system and creating more complex phase diagrams [28]. Consequently, this structural modification could open up a rich playground for the exploration of the interplay of non-trivial topology and magnetic order [29–32].

This work represents a further step in the exploration of topological materials by offering insights into the electronic structure of two outstanding material systems, those being HgTe and $(MnBi_2Te_4)(Bi_2Te_3)_n$. On the one hand, HgTe is investigated, which is the first topological material and which remains relevant in a rapidly changing scientific environment by allowing to induce several distinct topological phases through the tuning of external parameters. The samples investigated in this work are epitaxially grown thin films in the three-dimensional regime. On the other hand, $(MnBi_2Te_4)(Bi_2Te_3)_n$, which represents the first intrinsic magnetic topological insulator and offers a rather accessible and straightforward material system for the exploration of the impact of time-reversal breaking in topological materials, will be examined. The first three members $MnBi_2Te_4$, $MnBi_4Te_7$, and $MnBi_6Te_{10}$ are studied concerning different aspects, with the focus placed on the former two compounds.

Photoelectron spectroscopy and related sub-techniques are employed to access the properties of the initial state wave function, like orbital character or orbital angular momentum. In addition, the elemental selectivity of X-ray absorption-based methods is utilized to gain information on the magnetic and electronic properties of the Mn species in $(MnBi_2Te_4)(Bi_2Te_3)_n$ for $n = 0, 1$.

The following two chapters establish the scientific and methodological knowledge base for the further discussion of the data in the subsequent sections. Chapter 2 introduces the notion of electronic states in solids, non-trivial band ordering, and the effect of broken time-reversal symmetry on the topological order. In addition, the band inversion mechanism in HgTe is illustrated in more detail. Chapter 3 provides an overview of the underlying principles of the experimental methods. Besides the explanation of the applied photoemission and absorption-based techniques, this also includes a brief overview of the experimental setups, the growth and preparation procedures for both materials, as well as a concise illustration of calculations based on density functional theory. The latter were employed by collaborators to complement the experimental data and to allow for a more comprehensive discussion.

This is followed by a presentation and discussion of the experimental and theoretical findings. Chapter 4 is focused on the bulk and surface electronic structure of HgTe. The orbital composition of the bulk electronic structure is disentangled and the impact of $p-d$ hybridization on the low energy states is explored. Additionally, the strong temperature dependence of the chemical potential is addressed.

Chapter 5 focuses on the second material system, $(MnBi_2Te_4)(Bi_2Te_3)_n$, with section 5.1 providing information on its general properties. Section 5.2 explores the electronic and magnetic properties of the Mn species by element selective spectroscopic methods. In section 5.3, the surface electronic structure is examined. First, an experimental route is presented by which the surface spectra are assigned to their respective termination. Subsequently, the surface electronic structures of both $MnBi_4Te_7$ terminations are analyzed in detail. Finally, the dependence of the electronic structure on the magnetic phase and the possible formation of a gap in the topological surface state are discussed based on $MnBi_2Te_4$.

Lastly, chapter 6 provides a brief summary of the core results of this work as well as an outlook on further interesting scientific avenues to be explored.

Topological phases in condensed matter physics

2

2.1 Electronic states in solids

The full solution of the problem of an N electron system in a solid is a many-body state taking the interactions between all particles into account, that is, the full Hamiltonian $\mathcal{H}$ contains the interaction with the massive nuclei as well as all electron-electron interactions. This complex problem can be simplified by the independent one-electron approximation in which the interactions are described by an effective one-electron potential $V(\boldsymbol{r})$. In an ideal, infinitely periodic crystal, this assumption leads to one-electron Schrödinger equations:

$$\mathcal{H}\Psi = \left(\frac{\boldsymbol{p}^2}{2m_e} + V(\boldsymbol{r})\right)\Psi = \varepsilon\Psi, \tag{2.1}$$

where the first term describes the kinetic energy of the particle with momentum $\boldsymbol{p}$ and mass m_e, the second term represents an effective potential $V(\boldsymbol{r}) = V(\boldsymbol{r}+\boldsymbol{R})$, which respects the translational invariance of the lattice with translation vector $\boldsymbol{R}$, and Ψ and ε are the eigenstates and eigenvalues, respectively [33].

According to Bloch's theorem, the solution to this one-electron Hamiltonian can be expressed in the form of a plane wave modulated by a function $u_{\boldsymbol{k}}(\boldsymbol{r}) = u_{\boldsymbol{k}}(\boldsymbol{r}+\boldsymbol{R})$, which obeys the periodicity of the lattice [34, 35]:

$$\Psi_{\boldsymbol{k}}(\boldsymbol{r}) = e^{i\boldsymbol{k}\cdot\boldsymbol{r}}\, u_{\boldsymbol{k}}(\boldsymbol{r}). \tag{2.2}$$

The energy eigenvalues $\varepsilon(\boldsymbol{k})$ corresponding to these Bloch wavefunctions describe dispersing energy bands, which are periodic in momentum space.

Besides the translational symmetry of the crystal lattice, other symmetries may play a crucial role and can modify the properties of the electronic bands. **T**ime-**r**eversal **s**ymmetry (TRS) and spatial inversion symmetry, in particular, will be encountered in the course of this work and shall therefore be briefly explained.

The time-reversal operation transforms the time $t \to -t$ and can be expressed by the anti-unitary operator $\mathcal{T}$. The Bloch Hamiltonian of a time-reversal symmetric system satisfies

$$\mathcal{T}\mathcal{H}(\boldsymbol{k})\mathcal{T}^{-1} = \mathcal{H}(-\boldsymbol{k}). \tag{2.3}$$

As a result, an eigenvalue ε at $\boldsymbol{k}$ is also an eigenstate of $\mathcal{H}$ at $-\boldsymbol{k}$ with the same energy but reversed spin orientation:

$$\varepsilon(\boldsymbol{k},\uparrow) = \varepsilon(-\boldsymbol{k},\downarrow), \tag{2.4}$$

which is known as Kramers theorem [36]. The arrows $\uparrow$ and $\downarrow$ denote the orientation of the electron spin.

Some points of the Brillouin zone Λ are of particular interest because they appear invariant under time-reversal, i.e., $\Lambda = -\Lambda + \boldsymbol{K}$ applies, where $\boldsymbol{K}$ is a reciprocal lattice vector. At these points, which are termed **t**ime-**r**eversal **i**nvariant **m**omenta (TRIM), the two Kramers partners are necessarily degenerate. In a two-dimensional Brillouin zone there exist 4 TRIM, whereas in three dimensions there are 8.

In addition, if the crystal system is invariant under spatial inversion $\mathcal{P}$, which transforms the spacial coordinates $\boldsymbol{r} \to -\boldsymbol{r}$, there is a second constraint on the eigenvalues:

$$\varepsilon(\boldsymbol{k},\uparrow) = \varepsilon(-\boldsymbol{k},\uparrow), \tag{2.5}$$

which, combined with the constraint from TRS, leads to a global twofold degeneracy of the energy bands [1]:

$$\varepsilon(\boldsymbol{k},\uparrow) = \varepsilon(-\boldsymbol{k},\downarrow) = \varepsilon(\boldsymbol{k},\downarrow). \tag{2.6}$$

In other words, for a non-magnetic and inversion-symmetric system, there is no energy splitting depending on the electron spin and the bulk states exhibit no spin-orbit splitting, like it is the case for noble metals which crystallize in the face-centered cubic structure [37].

In contrast to the above assumed infinite lattice, real crystals have surfaces that terminate the crystal potential and break the translation and spatial inversion symmetry. The surface can be described through a step function that takes the constant value of the vacuum level V_0 outside the crystal. This allows for new solutions of the Schrödinger equation whose wave functions decay exponentially into the vacuum. Moreover, the wave vector component perpendicular to the surface $k_\perp$ can assume complex values, corresponding to wave functions that are damped within the crystal, with increasing distance from the surface [38]. These surface states are localized in the energy gap of the bulk states, which have exclusively real-valued wave vectors.

2.2 $\mathbb{Z}_2$ topological insulators

One of the greatest achievements of the last century in the field of condensed matter physics is the classification of many-body quantum states by the principle of spontaneous symme-

try breaking [1]. For instance, phases like the formation of crystalline solids or magnetic ordering can be attributed to the breaking of translational and time-reversal symmetry, respectively. In the last decades, a new class of phases emerged, which does not follow this principle of spontaneous symmetry breaking. Instead, these phases can be classified by a topological invariant, which is independent of the details of the system.

These phases are termed in analogy to the mathematical field of topology, which is concerned with the properties of geometric objects under continuous deformations. As an example, two-dimensional surfaces can be classified by their genus, that is, the number of holes, and all objects with the same genus belong to the same topological class, irrespective of the details of their geometry. As an often cited paradigm, a cup and a donut belong to the same topological class, since both exhibit one hole and can be continuously transformed into each other without closing or creating a hole [39]. Like in mathematics, topological phases in a physical system can be classified by an invariant or topological index.

As introduced in the previous section, electronic single-particle energy states in a periodic potential take the form of Bloch states. In an insulator, all states are either fully occupied or empty, that is, the system exhibits an energy gap separating the ground state from the excited state. Coming back to the example from mathematics, the genus of an object can be determined by an integral over the local curvature of the surface. While the integrand depends on the surface geometry, the integral is independent of such details and only reflects the global topology [40]. A similar statement applies to the physical system in which the calculation of the topological index may depend on the details of the electronic states. The topological index, however, is a property of the valence band ensemble and remains unchanged as long as the energy gap persists [1]. At an interface of two systems with different topological indices, the energy gap has to be closed in order to continuously interpolate from one valence band ensemble to the other. As a consequence, the surface of a **t**opological **i**nsulator (TI) is necessarily metallic, since it can be understood as the interface with the vacuum, which itself can be interpreted as a trivial insulator [39].

Albeit not defined by the spontaneous breaking of symmetries, topological phases may still depend on the presence or absence of certain symmetries. Arguably the most prominent example is the class of $\mathbb{Z}_2$ topological insulators, which occurs in time-reversal invariant systems subject to strong **s**pin-**o**rbit **c**oupling (SOC) [41]. In two dimensions, this phase is synonymously termed quantum spin Hall insulator and was first predicted and subsequently realized in HgTe quantum wells [12, 13]. As stated in the introduction, the subsequent extension of this principle to three-dimensional systems produced the first three-dimensional topological insulators which include uniaxially strained HgTe [14–16, 42, 43]. Shortly thereafter, the first topological van der Waals compounds were predicted and experimentally confirmed in the form of the chalcogenides Bi_2Se_3, Bi_2Te_3, and Sb_2Te_3 [44–47].

In the following, the $\mathbb{Z}_2$ topology in three dimensions is explained using Bi_2Te_3 as an example. First, because this system serves as an accessible model system and second, because it is the progenitor of the material $MnBi_2Te_4$ and the general mechanism of topological band inversion in these two systems is equivalent.

While a 2D $\mathbb{Z}_2$ insulator is classified by a single topological index $\nu = 0, 1$, in three dimensions there exist 4 invariants $(\nu_0;\nu_1,\nu_2,\nu_3)$. The first index classifies strong TI, whereas the latter three can be understood as indices classifying weak TI [39]. The invariant ν_0 can either be 0, which describes a topologically trivial system, or 1, in which case the system is a non-trivial insulator.

There are several formalisms by which the $\mathbb{Z}_2$ index can be calculated [15, 41, 48]. The full set of eigenstates is always trivial, but since there are two well-defined subsets of eigenstates in an insulator, namely the fully occupied valence band and the fully emptied conduction band, it is crucial to consider the topology of the valence states [1]. In a system with spatial inversion symmetry, as is the case for Bi_2Te_3, the calculation is simplified and the $\mathbb{Z}_2$ index can be calculated via the parity eigenvalues $\xi_{2m}(\Lambda_a) = \pm 1$ of the $2m$th occupied band at the eight TRIM Λ_a [42]:

$$(-1)^{\nu_0} = \prod_{a=1}^{8} \prod_{m=1}^{N} \xi_{2m}(\Lambda_a). \tag{2.7}$$

To obtain a topological index of $\nu_0 = 1$, there needs to be a parity inversion at an odd number of TRIM. In the case of Bi_2Te_3, this is realized by a band inversion of states with opposite parity at the Γ-point. The states near the Fermi level are derived from Bi and Te p-orbitals. The combination of chemical bonding and crystal field splitting leads to a situation, where the highest occupied and lowest unoccupied bands are derived from p_z-orbitals with opposite parity. If the spin-orbit coupling is additionally included, a level repulsion of the p_z-states from the remaining p-orbitals occurs and leads to an inversion of the two p_z-states with inversed parity [44]. This dependence on the strength of SOC makes it evident why Sb_2Se_3, the material that combines the two lightest elements of the $(Bi,Sb)_2(Te,Se)_3$ series, is a trivial insulator.

At the surface, a reinversion of the inverted bands occurs, inducing the aforementioned surface state which bridges the bulk energy gap. This **t**opological **s**urface **s**tate (TSS) forms the main hallmark of TI, which is accessible via angle-resolved photoemission. The TSS can be described by a Hamiltonian in the form of [49]:

$$\mathcal{H}_{\mathrm{TSS}} = v_{\mathrm{F}} \left(-k_y \sigma_x + k_x \sigma_y,\right), \tag{2.8}$$

where v_{F} is the Fermi velocity, $k_{x,y}$ are the in-plane components of the momentum, and

$\sigma_{x,y}$ are the Pauli matrices for spin. The resulting dispersion is schematically shown in Fig. 2.2 (a). It exhibits a linear dispersion obeying the Dirac equation of massless fermions and, due to its appearance, is termed a Dirac cone. The upper and lower parts of the Dirac cone merge at the Dirac point which is located at the TRIM. Moreover, the states are helical in nature since their spin orientation is determined by the direction of propagation and counterpropagating electrons exhibit opposite spin orientations, forming a helical spin structure in momentum space [50]. This spin-momentum locking is a manifestation of the constraint imposed by TRS on the TSS and is the root of the dissipationless transport enabled in TI since backscattering by non-magnetic defects is prohibited [51].

Away from the vicinity of the Dirac point, higher-order terms of $\boldsymbol{k}$ become relevant and may break the continuous rotational symmetry of the TSS. In particular, a cubic term in $\boldsymbol{k}$ emerges, which creates a threefold rotation symmetry around the z-axis due to the C_{3v} symmetry of the $R3\bar{m}$ space group, to which Bi_2Te_3 belongs [52]. Although the Hamiltonian is threefold symmetric, the resulting modification of the band structure exhibits a sixfold symmetry because of the presence of TRS. This effect leads to a hexagonal warping of the Fermi surface of the TSS away from the Dirac point. In addition to the warping, the cubic term induces a finite z-component to the spin polarisation of the TSS [53]. Two effects, which will later be encountered in the derivative $MnBi_4Te_7$.

Spin-orbit coupling is often referred to as the driving force behind the band inversion in topological materials. While this is partially true for the second material class in this work, HgTe, additional relativistic effects have to be taken into account in order to draw the full picture in this material system. The following section will be used to outline the cause of these effects as well as their impact on the band structure of HgTe.

2.2.1 The band inversion mechanism in HgTe

The band structure of HgTe around the high-symmetry Γ-point can be described by $\boldsymbol{k}\cdot\boldsymbol{p}$ perturbation method. Here, this type of description is chosen because it provides an illustrative representation of the additional contributions to the non-relativistic Hamiltonian. The $\boldsymbol{k}\cdot\boldsymbol{p}$ term originates from applying the Schrödinger equation for a single electron in a periodic potential $V(\boldsymbol{r})$ to the Bloch wave function. Using $\boldsymbol{p} = -i\hbar\vec{\nabla}$ and inserting equation (2.2) into equation (2.1) yields [54]:

$$\mathcal{H}_{\boldsymbol{k}\cdot\boldsymbol{p}}\, u_{\boldsymbol{k}}(\boldsymbol{r}) = \left(\frac{p^2}{2m_e} + V(\boldsymbol{r}) + \frac{\hbar}{m_0}\boldsymbol{k}\cdot\boldsymbol{p}\right) u_{\boldsymbol{k}}(\boldsymbol{r}) = \varepsilon(\boldsymbol{k}) u_{\boldsymbol{k}}(\boldsymbol{r}), \tag{2.9}$$

where $\varepsilon(\boldsymbol{k}) = \left(E(\boldsymbol{k}) - \frac{\hbar^2 k^2}{2m_e}\right)$. The third summand accounts for coupling between the bands and is treated as a perturbation in the $\boldsymbol{k}\cdot\boldsymbol{p}$ framework. Using a basis representation for the

outermost valence states of HgTe, omitting spin for the moment, leads to four eigenvalues and thus four energy bands: a triplet state derived from the Te p orbital with Γ_{15} symmetry and a Hg s-derived singlet state with Γ_1 symmetry [54]. The resulting band dispersion is schematically shown in Fig. 2.1 (a). The state with Hg s orbital character forms the conduction band, whereas the valence band comprises states with Te p character. Away from $\boldsymbol{k} = 0$, the valence band splits into light hole (lh) and heavy hole (hh) bands, due to the lack of inversion symmetry that is inherent to the zinc blende crystal structure.

Owing to the high atomic number of Hg ($Z = 80$) and Te ($Z = 52$), relativistic terms have to be taken into account. The effect of SOC, which arises due to the interaction of a particles spin with its motion inside an electric potential, may be expressed in the framework of non-relativistic quantum mechanics by an additional correction term to the Schrödinger equation [55]:

$$\mathcal{H}_{\mathrm{SO}} = \frac{\hbar}{4m_e^2c^2}\,(\nabla V \times \boldsymbol{p})\cdot\boldsymbol{\sigma}, \tag{2.10}$$

where the vector of Pauli matrices $\boldsymbol{\sigma} = (\sigma_x, \sigma_y, \sigma_z)$ is the spin operator and c is the speed of light. The potential gradient ∇V and thus the strength of the SO interaction scales with the atomic number Z. The inclusion of the SOC Hamiltonian $\mathcal{H}_{\mathrm{SO}}$ into the $\boldsymbol{k}\cdot\boldsymbol{p}$ formalism induces an additional modification of the valence band structure, which is schematically depicted in Fig. 2.1 (b). The SOC acts on the Te p states, separating the states with total momentum $J = 3/2$ from the split-off band with $J = 1/2$ by an energy scale Δ_{SO}. The inclusion of spin changes the applicable representation and the double group representations $S^{-1}\Gamma_1 \to \Gamma_6$ and $S^{-1}\Gamma_{15} \to \Gamma_7 + \Gamma_8$ have to be applied [54]. As can be seen from Fig. 2.1 (b), the energetic order of the s- and p-derived bands is unchanged by the spin-orbit interaction.

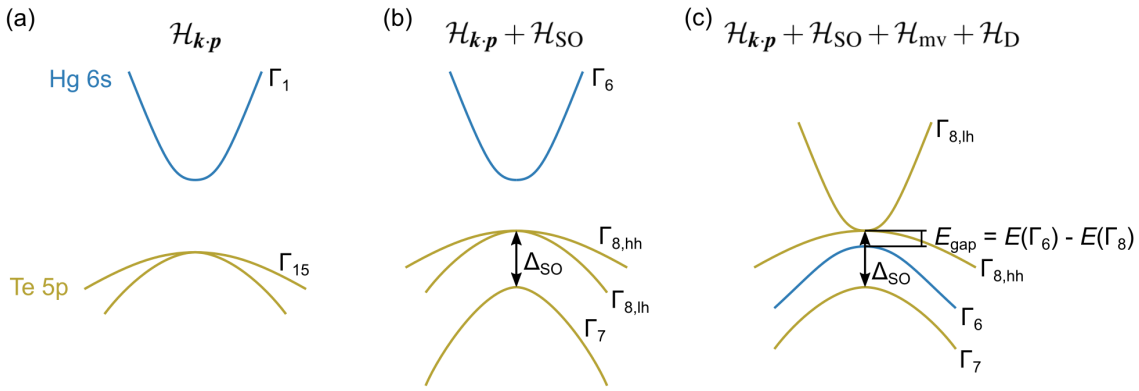

Figure 2.1: Schematic depiction of the band structure of HgTe in the vicinity of the Γ-point considering various relativistic effects. The representations correspond to an unperturbed Hamiltonian $\mathcal{H}$ with corrections for (a) $\boldsymbol{k}\cdot\boldsymbol{p}$ interaction, (b) $\boldsymbol{k}\cdot\boldsymbol{p}$ and SOC, and (c) the mass velocity and Darwin terms in addition to the previous ones.

In the case of HgTe, two additional relativistic correction terms must be factored in to describe the band inversion in this system. First, one must consider the mass-velocity correction which occurs if the velocity of a particle approaches the speed of light. The increment in mass results in a contraction of the orbital, shifting the electron closer to the nucleus and therefore lowering its energy. The effect is more pronounced for *s*-electrons because their probability density function is higher at the center of the atom compared to *p*- and *d*-electrons. The correction term may be described as [56]:

$$\mathcal{H}_{\mathrm{mv}} = -\frac{p^4}{8m_e^3c^2}. \tag{2.11}$$

The second is the Darwin term, which arises because the electron is constantly performing rapid quantum oscillations [57]. It can be understood as the interaction with virtual electron-positron pairs, or vacuum fluctuations, and acts as an effective smearing-out of the electrostatic potential [58]. The correction term can be expressed as [59]:

$$\mathcal{H}_{\mathrm{D}} = \frac{\hbar^2}{4m_0^2c^2}\Delta V. \tag{2.12}$$

The Darwin correction raises the energy of the *s*-states and thus partially compensates for the effect of the mass velocity correction. The cumulative effect of $\mathcal{H}_{\mathrm{mv}}$ and $\mathcal{H}_{\mathrm{D}}$ on the band structure is depicted in Fig. 2.1 (c). The Fermi energy lies at the point of contact of the $\Gamma_{8,\mathrm{lh}}$- and $\Gamma_{8,\mathrm{hh}}$-bands, classifying HgTe as a topological non-trivial semi-metal. The inverted bulk band gap is defined as the energetic spacing between Γ_6 and Γ_8.

All three additions to the Hamiltonian — Spin-orbit coupling, mass-velocity correction, and Darwin correction — lead to a modified band structure were the Hg *s*-derived Γ_6-band lies in between the spin-orbit split Γ_8- and Γ_7-bands, and thus their conjunct effects are necessary in order to describe the band inversion mechanism in HgTe. Similar to Bi_2Te_3, the bulk band inversion is localized at $\boldsymbol{k} = 0$ in momentum space and away from the immediate vicinity of the Γ-point, the character of the bands regain the trivial ordering Γ_6–Γ_8–Γ_7.

2.3 Non-trivial topology and time-reversal symmetry breaking

Over two decades before the prediction and subsequent discovery of $\mathbb{Z}_2$ topology, a class of non-trivial systems with explicitly broken TRS was discovered. This phase occurs when a two-dimensional electron gas is exposed to a magnetic field applied perpendicular to it and manifests itself in chiral, dissipationless edge states whose direction of propagation is

determined by the sign of the charge and of that of the magnetic field [60]. Due to its relation to the classical Hall effect, it was termed the quantum Hall effect. It was interpreted in the framework of topology and can be characterized by a TKNN or Chern number [61, 62]. Naturally, the question arose whether the effect can occur without the presence of an external magnetic field in the form of the **q**uantum **a**nomalous **H**all **e**ffect (QAHE), akin to the relation of the Hall effect and the anomalous Hall effect.

In 1988, Haldane proposed a model which, by broken TRS but without a net magnetic moment, should exhibit a non-zero Chern number [63]. The experimental realization of the QAHE only followed after the discovery of the $\mathbb{Z}_2$ topological insulator, when it was proposed that a Chern insulator can be realized by combining the band inversion due to the strong SOC of a $\mathbb{Z}_2$ TI with magnetic ordering induced by doping or proximity effects [20]. Consequently, the $\mathbb{Z}_2$ TI known at the time were chosen as the basis for the doping approach and, while the magnetic moments in Mn-doped HgTe do not align without an external magnetic field, the QAHE could be realized in Cr and V doped $(Bi_{1-x}Sb_x)_2Te_3$ [5, 23, 64].

Introducing a spontaneous out-of-plane magnetization into a 3D TI breaks the TRS and is therefore accompanied by crucial modifications to the surface electronic structure. The exchange coupling of the conduction electrons with the magnetic ordering leads to a mass gap m in the TSS in the form of:

$$\mathcal{H}_{\mathrm{TSS}} = v_{\mathrm{F}} \left(-k_y \sigma_x + k_x \sigma_y, \right) + m \sigma_z, \tag{2.13}$$

which leads to a deviation from the ideal linear dispersion of the Dirac fermions [49]. The effect on the dispersion of the TSS as well as its spin orientation is schematically depicted in Fig. 2.2 (b).

Anti**f**erromagnetic **t**opological **i**nsulators (AFTI) represent a special case of systems with broken TRS. This is similar to Haldane's model, where the particular ordering of magnetic moments leads to broken TRS $\mathcal{T}$ and parity symmetry $\mathcal{P}$, but the intact combination of both [65]. Here, the staggered arrangement of magnetic moments leads to a situation where $\mathcal{T}$ symmetry and a translational symmetry by a primitive lattice vector $\mathcal{L}$ are both violated, but the combined symmetry in the form of $\mathcal{S} = \mathcal{T}\mathcal{L}$ remains preserved. Since this new symmetry explicitly involves a lattice operation, it is sensitive to modification of the lattice, for instance by the presence of a surface.

Without loss of generality, in the following a system will be considered in which the magnetic ordering breaks the translational invariance along the z-axis. Within the Brillouin zone plane $k_z = 0$, the Hamiltonian of such a system holds:

$$\mathcal{S}\mathcal{H}\left(k_x, k_y, 0\right)\mathcal{S}^{-1} = \mathcal{H}\left(-k_x, -k_y, 0\right), \tag{2.14}$$

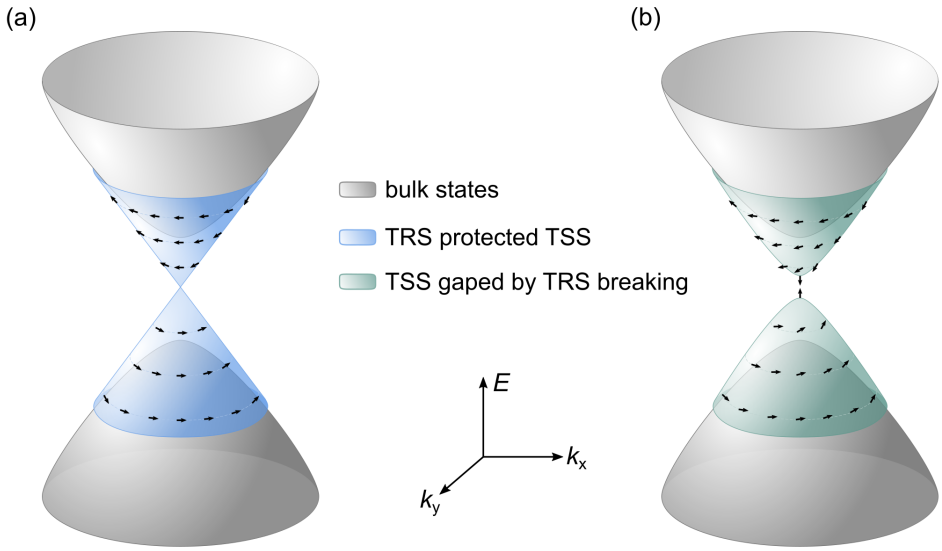

Figure 2.2: Schematic depiction of the effect of broken time-reversal symmetry on a topological surface state. (a) Unperturbed, linear dispersing surface state with helical spin orientation, imposed by spin-orbit coupling and the Kramers theorem. (b) A topological surface state under an out-of-plane magnetic exchange field. The state exhibits a gap and the spins undergo a canting, the angle of which increases towards the former Dirac point. The grey areas represent the bulk conduction and valence states. The spin orientation is indicated by black arrows.

with the antiunitary operator $\mathcal{S}$ satisfying $\mathcal{S}^2 = -1$, which enables a $\mathbb{Z}_2$ topological classification [65]. If the system is invariant under spatial inversion $\mathcal{P}$, the $\mathbb{Z}_2$ invariant can be determined by considering the four TRIM within the $(k_z = 0)$-plane, analogous to equation 2.7. In contrast, within the $(k_z = \pi)$-plane $\mathcal{S}^2 = +1$ and no invariant can be associated with this plane [65]. As in the case of the TRS invariant $\mathbb{Z}_2$ insulator, the bulk electronic structure must exhibit a gap to enable a topological classification.

For an AFTI there exist two types of surfaces, depending on the relative orientation of the respective surface plane and the magnetic ordering, those that break the $\mathcal{S}$ symmetry of the bulk and those that preserve it. A surface with a net magnetic moment will always break the bulk symmetry, while for a surface with **a**nti**f**erro**m**agnetic (AFM) ordering, a primitive lattice vector can be found within the surface plane, which enables the $\mathcal{S}$ invariance [65]. In the former case, there is no symmetry protection imposed on the TSS and the magnetic exchange field enables a gap opening.

Magnetic ordering has been predicted for the ternary **v**an **d**er **W**aals (vdW) layered compounds MBi_2Te_4 for M = (Ti, Vi, Mn, Ni, Eu) [10]. Of these possible candidates, only manganese is expected to exhibit a magnetic easy axis parallel to the vdW stacking direction, i.e., the [0001] direction, with ferromagnetic intralayer coupling [10]. Accordingly, this material system would allow the observation of a TRS-broken TSS on its (0001) surface, which is the natural cleavage plane of the system.

3 Methodology

3.1 Photoelectron spectroscopy

Photo**e**lectron **s**pectroscopy (PES) has been established to be one of the major experimental techniques for the investigation of the configuration of electronic states near the surface. It is based on the photoelectric effect which was discovered by H. Hertz and W. Hallwachs in 1887 [66, 67]. A. Einstein explained this effect in 1905 in his Nobel Prize-winning publication as the liberation of an electron from its bound state in a solid to a free electron state through the energy provided by a light quantum [68]. A paraphrased version of Einstein's formula describes the energetics of the photoexcitation as:

$$E_{\mathrm{kin}}^{\mathrm{S}} = h\nu - |E_{\mathrm{bin}}| - \Phi^{\mathrm{S}}, \tag{3.1}$$

where $E_{\mathrm{kin}}^{\mathrm{S}}$ is the kinetic energy of the photoemitted electron, $h\nu$ is the energy of the impinging photon, $|E_{\mathrm{bin}}|$ is the binding energy of the unperturbed electron relative to the Fermi energy, and Φ^{S} is the work function of the material under study [69, 70]. Therefore, the maximum kinetic energy of the photoelectron relates to the frequency ν of the incident light and not its intensity.

Normally, when performing a PES experiment, the sample and the analyzer are electrically grounded together and thus their electrochemical potentials are aligned. As a result, the kinetic energy and the work function may be related to the analyzer instead of the sample. In that case, $E_{\mathrm{kin}}^{\mathrm{A}}$ is the kinetic energy detected by the analyzer and Φ^{A} is the work function of the analyzer. When investigating a metallic system, Φ^{A} can be determined by measuring the kinetic energy at the Fermi level where $|E_{\mathrm{bin}}| = 0$.

The spatial depth from which information can still be resolved is limited by the inelastic mean free path of the photoelectron $\lambda_{\mathrm{IMFP}}^{\mathrm{el}}$. It represents the average travel length of an electron before it collides with another particle. Even though $\lambda_{\mathrm{IMFP}}^{\mathrm{el}}$ is a material-specific quantity, its dependence on the kinetic energy of the electron E_{kin} can be approximated as [71]:

$$\lambda_{\mathrm{IMFP}}^{\mathrm{el}}[\mathrm{nm}] = \frac{143}{E_{\mathrm{kin}}^2} + 0.054 \cdot \sqrt{E_{\mathrm{kin}}}, \tag{3.2}$$

where the kinetic energy E_{kin} is given in eV. This empirical representation is commonly known as the universal curve. For kinetic energies between 20 eV and 100 eV, which are

typical values for a PES experiment, $\lambda^{\mathrm{el}}_{\mathrm{IMFP}}$ undergoes a minimum of about 5 Å and even at elevated energies it does not exceed several nanometers. PES is, therefore, a surface-sensitive technique, ideally suited for exploring the surface electronic structure of solids.

3.1.1 Angle-resolved photoelectron spectroscopy

In **a**ngle-**r**esolved **p**hoto**e**lectron **s**pectroscopy (ARPES) the emission angle is resolved in addition to the kinetic energy of the electron. These quantities can be used to determine the crystal momentum $\hbar\boldsymbol{k}$ of the photoelectrons and thus the dispersion of the electronic states in the crystal $E(\boldsymbol{k})$.

A phenomenological model that is often used to describe the excitation of photoelectrons is the three-step model, in which the photoemission process is divided into three consecutive stages – optical excitation of the electron to a final state inside the crystal, propagation of the electron to the surface, and transition of the electron into the vacuum [69].

The first step describes an excitation inside the solid between two Bloch states, which are eigenstates of an infinite crystal [72]. Because of the periodicity of the crystal, the wave vector of the electron $\boldsymbol{k}$ is defined modulo a reciprocal lattice vector $\boldsymbol{K}$ [72]. Under the assumption of a negligible photon momentum, the momenta of the initial and final state $\boldsymbol{k}_{\mathrm{i}}$ and $\boldsymbol{k}_{\mathrm{f}}$, respectively, are related by $\boldsymbol{k}_{\mathrm{f}} - \boldsymbol{k}_{\mathrm{i}} = \boldsymbol{K}$. Alternatively, in the view of a reduced Brillouin zone, the allowed optical transitions are vertical and the momentum relation of initial and final state simplifies to $\boldsymbol{k}_{\mathrm{f}} - \boldsymbol{k}_{\mathrm{i}} = 0$ [73].

The assumption of a negligible photon momentum is justifiable in the domain of **u**ltra**v**iolet (UV) light where the wave vector of the photon is small in comparison to the size of the Brillouin zone. To provide an example, the wave vector of the commonly used He I_α-line (21.2 eV) is $\sim 0.01\,\mathrm{Å}^{-1}$, which is less than a percent of typical Brillouin zone scales.
In the second step, the electron propagates towards the surface. During its passage, the excited electron can interact with the remaining system through various mechanisms that lead to a change in its momentum and energy, and thus to a loss of information. Only primary electrons that have not suffered such a loss of information are of interest for the photoemission experiment. This step is thus directly related to the aforementioned mean free path of the electron.

The last step is to cross the surface and escape from the crystal. At the surface, the photoelectron gets refracted due to the breaking of translational invariance along the surface normal. The potential barrier that breaks this symmetry leads to a non-conservation of the perpendicular component of the electron wave vector $k_\perp \neq k_\perp^{\mathrm{vac}}$. In contrast, the translational

symmetry parallel to the surface remains preserved and therefore also the in-plane wave vector components $\boldsymbol{k}_{\parallel} = \boldsymbol{k}_{\parallel}^{\mathrm{vac}}$. The emission angle can be separated into a polar angle ϑ relative to the surface normal and an azimuthal angle ϕ defined within the surface plane. Under the assumption of a free electron outside the solid whose energy is dominated by its kinetic energy and using the geometrical relation $|\boldsymbol{k}_{\parallel}| = \sqrt{k_x^2 + k_y^2}$, one can retrieve the parallel components of the crystal momentum from the measured quantities as [74]:

$$k_x = \sqrt{\frac{2m_{\mathrm{e}}}{\hbar^2} E_{\mathrm{kin}}}\, \sin\vartheta \cos\phi, \tag{3.3}$$

and

$$k_y = \sqrt{\frac{2m_{\mathrm{e}}}{\hbar^2} E_{\mathrm{kin}}}\, \sin\vartheta \sin\phi, \tag{3.4}$$

where $\hbar$ is the reduced Planck's constant.

Even though the momentum component $k_{\perp}$ is not conserved, it can still be estimated from measurable quantities. By adopting a free-electron-like description for the final state inside the solid, one obtains:

$$k_{\perp} = \sqrt{\frac{2m_{\mathrm{e}}}{\hbar^2}\, (E_{\mathrm{kin}} \cos^2\vartheta + V_0)}. \tag{3.5}$$

The relation between $k_{\perp}$ and $k_{\perp}^{\mathrm{vac}}$ is now reduced to a function of the inner potential V_0, which corresponds to the energetic difference from the bottom of the valence band to the vacuum level [74]. The inner potential can either be determined by the aid of theoretical band structure calculations or by inferring it from the experimentally observed periodicity in the photoemission spectra. The latter is realized by collecting photoelectrons at varying photon energies and deducing the high-symmetry points along $k_{\perp}$ from the periodicity of the observed dispersion.

In contrast to the bulk states, two-dimensional electronic states like the topological surface state show no $k_{\perp}$-dispersion due to a lack of repetition units perpendicular to the surface.

3.1.2 The transition matrix element and symmetry considerations

So far only the energetics and kinematics of the photoemission process have been addressed. In the following, a more detailed treatment of the excitation process will be considered in the form of a perturbed system of independent electrons. By considering more intricate effects, this description allows for a deeper understanding of the physics of the initial state, aside from just the mere mapping of the electronic band structure.

The photocurrent $I(\boldsymbol{k}, E_{\mathrm{kin}})$ at a given momentum $\boldsymbol{k}$ and photoelectron kinetic energy E_{kin} is proportional to the transition probability $w_{\mathrm{i,f}}$ of an optical excitation from an initial state Ψ_{i} to a final state Ψ_{f} [69]. This transition probability can be described by Fermi's Golden rule as a result of first-order perturbation theory [70]:

$$w_{\mathrm{i,f}} \propto \frac{2\pi}{\hbar} \left|\langle \Psi_{\mathrm{f}} | \mathcal{H}_{\mathrm{int}} | \Psi_{\mathrm{i}} \rangle\right|^2 \delta\left(E_{\mathrm{f}} - E_{\mathrm{i}} - h\nu\right), \tag{3.6}$$

where the δ-function reflects the conservation of energy between the inital and final state energies E_{i} and E_{f}, and $\mathcal{H}_{\mathrm{int}}$ is the interaction Hamiltonian, which accounts for the perturbation of the initial system by the incident photon with energy $h\nu$.

In the process, the incident photon is absorbed by a spin-less, bound electron and transfers its energy and momentum to it. A quantum mechanical description is given by the substitution $\boldsymbol{p} \rightarrow \boldsymbol{p} - \frac{e}{c}\boldsymbol{A}$ of the momentum operator $\boldsymbol{p}$ in the unperturbed Hamiltonian $\mathcal{H}_0 = p^2/2m_{\mathrm{e}} + V(\boldsymbol{r})$, yielding [72]:

$$\mathcal{H} = \frac{\left[\boldsymbol{p} - \frac{e}{c}\boldsymbol{A}(\boldsymbol{r},t)\right]^2}{2m_{\mathrm{e}}} + e\phi(\boldsymbol{r},t) + V(\boldsymbol{r}). \tag{3.7}$$

Here, $V(\boldsymbol{r})$ is the potential energy due to the other particles of the system, and $\boldsymbol{A}$ and ϕ are the vector and scalar potential of the eletromagnetic field, respectively. The Hamiltonian can be rewritten as the sum of the unperturbed Hamiltonian $\mathcal{H}_0$ and $\mathcal{H}_{\mathrm{int}}$, which accounts for the interaction with the electromagnetic field, giving:

$$\mathcal{H}_{\mathrm{int}} = -\frac{e}{2m_e c}\left(\boldsymbol{A}\cdot\boldsymbol{p} + \boldsymbol{p}\cdot\boldsymbol{A}\right) + \frac{e^2}{2m_e c^2}|\boldsymbol{A}|^2 + e\phi. \tag{3.8}$$

The term quadratic in $\boldsymbol{A}$ can be neglected for conventional light sources [70]. Furthermore, because of the commutation relation $[\boldsymbol{p},\boldsymbol{A}] = -i\hbar\nabla\cdot\boldsymbol{A}$, the perturbation Hamiltonian $\mathcal{H}_{\mathrm{int}}$ can be written as:

$$\mathcal{H}_{\mathrm{int}} = -\frac{e}{2m_e c}\left(2\,\boldsymbol{A}\cdot\boldsymbol{p} - i\hbar\nabla\boldsymbol{A}\right) + e\phi. \tag{3.9}$$

The further treatment of these terms depends on the chosen gauge for the electromagnetic field, which leaves the observed electric and magnetic fields unchanged but alters the expressions for the vector or the scalar potential. In the following, a gauge is chosen in such way that the scalar potential is zero. In Addition, a constant vector field can be assumed, that is, $\nabla\boldsymbol{A} = 0$, which holds for wavelengths in the UV regime [72]:

$$\mathcal{H}_{\mathrm{int}} = -\frac{e}{m_e c}\,\boldsymbol{A}\cdot\boldsymbol{p}, \tag{3.10}$$

which can be inserted in the matrix element $M_{\mathrm{i,f}} = \langle \Psi_{\mathrm{f}} | \boldsymbol{A}\cdot\boldsymbol{p} | \Psi_{\mathrm{i}} \rangle$ in equation 3.6.

It should be noted, that for low photon energies an additional contribution to the photoemission process may occur due to the presence of the surface [75]. This surface photoelectric effect, which occurs due to a discontinuity of the dielectric function at the surface, is associated with the $\nabla \boldsymbol{A}$ term and may interfere with the direct photoexcitation, leading to asymmetric lineshapes [76, 77].

Since the photon transfers its energy and momentum to the electron, not only the energy conservation but also the conservation of momentum must be respected. As stated before, in the UV regime the momentum of the photon is negligible with respect to the momentum of the electron [72]. Therefore, the allowed transitions by the optical absorption are vertical in the first Brillouin zone and the initial and final states Ψ_i and Ψ_f are characterized by the same wave vector.

The transition probability given by the matrix element $M_{\mathrm{i,f}}$ depends on the product of the irreducible representations of the initial state, the final state, and the perturbation operator [72]. This is generally a complex problem that can be facilitated by imposing symmetry constraints on the experiment. If both the **p**lane **o**f **i**ncidence (POI) as well as the detection plane of the analyzer coincide with a mirror plane of the crystal system, the symmetry of the experiment is constrained to the symmetry of the plane containing the wave vector, and thus there are only two irreducible representations: even or odd with respect to the mirror plane.

The product that is the integrand of the matrix element $\langle \Psi_\mathrm{f} | \boldsymbol{A} \cdot \boldsymbol{p} | \Psi_\mathrm{i} \rangle$ has to be of even parity, in order to give a non-zero transition probability. Moreover, the final state has to be of even symmetry as well, since an odd final state exhibits a node in the analyzer plane and is thus not detectable [72]. This leaves the condition of equal parity for the initial state and the perturbation operator, i.e., Ψ_i and $\boldsymbol{A} \cdot \boldsymbol{p}$ are both of even or odd symmetry with respect to the mirror plane.

Using the commutation relation $[\mathcal{H}, \boldsymbol{r}] = i\hbar \boldsymbol{p}/m$, the matrix element can be written as $M_{\mathrm{i,f}} \propto \langle \Psi_\mathrm{f} | \boldsymbol{\varepsilon} \cdot \boldsymbol{r} | \Psi_\mathrm{i} \rangle$, where $\boldsymbol{\varepsilon}$ is the directional unit vector of the polarization of $\boldsymbol{A}$ and $\boldsymbol{r}$ is the spatial coordinate [74]. For a transversal electromagnetic wave, the direction of the vector potential $\boldsymbol{\varepsilon}$ is defined as perpendicular to the Poynting vector, and since the POI is defined by the surface normal and the propagation direction of the incoming photons, two orthogonal linear polarizations can be chosen, one lying within the POI and the other perpendicular to it, which are termed *p*- and *s*-polarization, respectively. While *p*-polarized light exhibits even symmetry with respect to the mirror plane, *s*-polarization is of odd parity. With the condition of an overall even parity, formulated above, it follows that states of even symmetry within the POI can be excited by *p*-polarization and odd states by *s*-polarized light.

For the case of a POI which lies perpendicular to the detection and mirror plane, *s*-polarization is of even parity and thus excites states with even symmetry. In this configuration, the directional unit vector of *p*-polarized light can be separated into two components, one lying within the mirror plane and one perpendicular to it. These two components are then again of even and odd parity, respectively, and their ratio depends on the angle of incidence.

3.1.3 Spin-resolved photoelectron spectroscopy

Spectroscopy of the electron spin is a crucial step towards the examination of the complete electronic state - energy, momentum, and spin. The separation of the spin-integrated signal is implemented by a spin-dependent scattering process which introduces a quantifiable spin separation to the photocurrent. The underlying scattering mechanism is either based on spin-orbit coupling or spin-exchange coupling. The former is used in Mott detectors or in spin-polarized low-energy electron diffraction, whereas the latter is applied in detectors based on **v**ery **l**ow-**e**nergy **e**lectron **d**iffraction (VLEED), which is the type of detectors utilized in this work [78–80].

If the energy of the scattered electrons is sufficiently low, the radius of the Ewald sphere becomes smaller than the smallest reciprocal lattice vector; higher-order diffraction ceases and only the specularly reflected electrons can be observed [80]. The intensity of the specular beam then depends on the **d**ensity **o**f **s**tates (DOS) of the target material. An impinging electron can only be absorbed if the scatterer offers empty states to the electron. If no such states exist, i.e., the scattering material has a band gap in the given energy region, the probability for reflection is greatly enhanced. Furthermore, if, for the respective energy, the target DOS exhibits an imbalance for different spin components, like in ferromagnetic materials for their majority and minority spin, the scattering process is spin-dependent. In the case of a dominating majority (minority) partial DOS, the reflection probability is diminished for electrons with spins coaligned to the majority (minority) spin direction.

The measured asymmetry

$$A(E_{\text{bin}},\boldsymbol{k}_{\parallel}) = \frac{I^{+}(E_{\text{bin}},\boldsymbol{k}_{\parallel}) - I^{-}(E_{\text{bin}},\boldsymbol{k}_{\parallel})}{I^{+}(E_{\text{bin}},\boldsymbol{k}_{\parallel}) + I^{-}(E_{\text{bin}},\boldsymbol{k}_{\parallel})} \tag{3.11}$$

is gained by sequential measurement of I^{+} and I^{-} under reversed target magnetization. The asymmetry A is related to the spin polarization P by:

$$A(E_{\text{bin}},\boldsymbol{k}_{\parallel}) = S_{\text{eff}} \cdot P(E_{\text{bin}},\boldsymbol{k}_{\parallel}), \tag{3.12}$$

where S_{eff} is the effective Sherman function which describes the measured asymmetry in the case of complete polarisation $P = 1$. It is a detector specific parameter which gauges the spin-resolving efficiency [81].
The spin-dependent spectra can be recovered from the polarization $P(E_{\text{bin}}, \boldsymbol{k}_{\parallel})$ and the spin-integrated spectrum $I_{\text{tot}}(E_{\text{bin}}, \boldsymbol{k}_{\parallel}) = I^{+}(E_{\text{bin}}, \boldsymbol{k}_{\parallel}) + I^{-}(E_{\text{bin}}, \boldsymbol{k}_{\parallel})$ via [82]:

$$I^{\uparrow}(E_{\text{bin}}, \boldsymbol{k}_{\parallel}) = I_{\text{tot}}(E_{\text{bin}}, \boldsymbol{k}_{\parallel}) \cdot (1 + P(E_{\text{bin}}, \boldsymbol{k}_{\parallel}))/2 \tag{3.13}$$

and

$$I^{\downarrow}(E_{\text{bin}}, \boldsymbol{k}_{\parallel}) = I_{\text{tot}}(E_{\text{bin}}, \boldsymbol{k}_{\parallel}) \cdot (1 - P(E_{\text{bin}}, \boldsymbol{k}_{\parallel}))/2. \tag{3.14}$$

Fe(001) thin films have been chosen as scattering material due to their high intrinsic exchange splitting [83]. A major concern, the fast degradation of the Fe(001) surface, is resolved by a p(1 × 1)O overlayer, significantly prolonging the intervals after which the target has to be freshly prepared [84]. This target material exhibits a maximal spin asymmetry in its DOS at an energy of $E = 6\,\text{eV}$.

3.1.4 Resonant photoelectron spectroscopy

Resonant **p**hoto**e**lectron **s**pectroscopy (ResPES) can be utilized to gain insight into the contribution of a specific atomic species to the valence band states. Similar to its use in the field of diluted magnetic semiconductors [85, 86], the technique is employed in this work to disentangle the contribution of the magnetic species to the valence states. The underlying effect occurs when the energy of the exciting photon coincides with an absorption threshold, i.e., the energy corresponding to the binding energy associated with a core electron of the species. In that case, the excitation channel of direct photoemission from the valence band competes with an additional emission process via the excitation of a core electron.

Tuning the photon energy to the absorption threshold enables excitation of a core electron which gets elevated into an unoccupied valence state [72]. In this work the contribution of the Mn species to the valence states will be investigated, we thus describe this process by the excitation of a Mn $2p$ electron into a free $3d$ valence state:

$$2p^6\, 3d^n + h\nu \rightarrow 2p^5\, 3d^{n+1}.$$

This intermediate state decays via autoionization: The core hole gets refilled by an electron from the valence shell and the excess energy is converted into the liberation of an additional

valence shell electron, leading to [87]:

$$2p^5\ 3d^{n+1} \rightarrow 2p^6\ 3d^{n-1} + e^-.$$

In terms of Auger notation, this relaxation step corresponds to a LMM transition. This process has the same initial and final state as the direct photoemission of a valence band electron:

$$2p^6\ 3d^n + h\nu \rightarrow 2p^6\ 3d^{n-1} + e^-.$$

As a result, there will be an interference between the two channels, leading to a strong augmentation of the emission probability around the energy of the threshold.

The quantum mechanical interference leads to a Fano-type resonance for the effective photoemission cross section as a function of photon energy $h\nu$ [88]. This description considers an initial state $|i\rangle$, a continuum state $|\psi_E\rangle$, and an intermediate state $|\phi\rangle$ which is coupled to the continuum. The transition probability follows the Fano-profile [72]:

$$S_q(E) = \frac{|\langle\widetilde{\psi}_E|T|i\rangle|^2}{|\langle\psi_E|T|i\rangle|^2} = \frac{(q+E)^2}{E^2+1}, \tag{3.15}$$

where E is the normalized energy relative to the resonance and q is a dimensionless symmetry parameter. It is given by the ratio of the matrix elements of the dipole transition operator T between the initial state $|i\rangle$ and the final states $|\psi_E\rangle$ and $|\widetilde{\psi}_E\rangle$. While the denomiator describes the dipole transition to an unperturbed state, the numerator describes the transition to a hybrid state:

$$|\widetilde{\psi}_E\rangle = a|\phi\rangle + \int dE' b_{E'}|\psi_{E'}\rangle, \tag{3.16}$$

with the coefficients a and b_E depending on the hybridization between the intermediate state $|\phi\rangle$ and the continuum state $|\psi_E\rangle$.

Accordingly, there are two ways in which a spectrum may be formed. Either a combination of direct photoemission and emission via autoionization or only direct emission in the absence of a resonant condition, classifying the taken spectra as on-resonant and off-resonant, respectively. By subtracting a spectrum taken under off-resonant conditions from a spectrum taken at the resonance, the density of states of the given chemical species can be estimated.

3.2 X-ray absorption spectroscopy

X-ray **a**bsorption **s**pectroscopy (XAS) is an element-specific method which employs local excitations for chemical and structural analysis. The attenuation of electromagnetic waves

while traversing through matter follows the Beer-Lambert-Bouguer law, which relates the decrease in intensity I of radiation travelling along z to a linear absorption coefficient μ [89–91]:

$$dI(h\nu, z) = -I(h\nu, z) \cdot \mu(h\nu)\, dz. \tag{3.17}$$

This material-specific quantity μ depends on the photon energy $h\nu$ and is generally a smooth function which has a proportionality of $\mu \propto (h\nu)^{-3}$ [92]. If the incident photons have an energy near the binding energy of an electron occupying a core level, μ exhibits a steep increase. This sharp rise in absorption is called an absorption edge.

XAS can be seen as an umbrella term covering several techniques which specialize themselves on different aspects of the absorption process and hence different energy regions [93–95]. This work investigates the **n**ear **e**dge **X**-ray **a**bsorption **f**ine **s**tructure (NEXAFS), which, as suggested by the name, deduces information from the immediate region around the absorption edge.

As in the closely related method PES, the transition probability and thus the cross section can be calculated via Fermi's golden rule [93]. In contrast to PES, which utilizes photon energies higher than the ionization potential and thus measures the free photoelectron, the final state $\langle \Psi_\mathrm{f}|$ in the NEXAFS process is an unoccupied bound state lying energetically below the vacuum level.

The absorption edge of interest in this study is the Mn $L_{3,2}$ edge, which, like in the previous example of a resonant excitation in PES, corresponds to the excitation of an electron occupying the $2p$ core level to a free $3d$ valence band state:

$$2p^6\, 3d^n + h\nu \rightarrow 2p^5\, 3d^{n+1}. \tag{3.18}$$

The transition probability for the L_1 edge, which describes an excitation from the $2s$ state is approximately two orders of magnitude lower [96].

A direct access to the absorption of a given sample can be achieved by measuring the intensity of the incident light before as well as after the radiation has passed through the sample. Such an experiment in transmission geometry has historically been the first realization of XAS and it is still a feasible detection mode if the sample is sufficiently thin [97]. For the bulk crystals investigated in this work, a different approach has to be taken. Here, secondary processes due to the relaxation of the excited state serve as a probe for the absorption coefficient. This relaxation occurs either non-radiatively or radiatively, i.e., by emission of an Auger electron or a fluorescent photon. These two relaxation channels form the basis for the detection modes **t**otal **e**lectron **y**ield (TEY) and **f**luorescence **y**ield (FY).

In the TEY detection mode, all electrons emerging from the sample are detected. These are mainly low-energy electrons occurring due to the formation of an electron avalanche

triggered by the primary Auger electrons. The fraction of this inelastic tail consisting of inelastically scattered Auger electrons comprises the desired NEXAFS signal [93]. The intensity of these inelastically scattered Auger electrons follows the the intensity of the elastic Auger electrons. Measuring the current flowing into the sample due to charge compensation of the emitted electrons is the most common way of measuring the TEY.

Alternatively, the fluorescent photons resulting from radiative relaxation also provide a measure for the absorption of radiation by the sample. Auger decay is the dominant relaxation channel in atoms with $Z < 90$ and is favored by two orders of magnitude over radiative decay, resulting in better signal-to-noise ratios for TEY compared to FY.

In principle, both TEY and FY signals provide a measure proportional to the total absorption, and they differ mainly in their signal-to-noise and signal-to-background ratios. Additionally, the interpretation of the FY signal may be complicated by self-absorption effects that occur when the fluorescent photon is reabsorbed by the material on its way to the surface. A major practical distinction between these two detection modes, however, lies in the depth information gained from the escaping secondary particles. Photons have a significantly longer inelastic mean free path at the energy scale of a XAS experiment. FY is consequently a more bulk sensitive approach, whereas TEY probes mainly near-surface layers.

3.2.1 X-ray magnetic circular dichroism

First implemented in 1987, **X**-ray **m**agnetic **c**ircular **d**ichroism (XMCD) expands upon the probe for elemental species and their chemical environment of XAS with an additional sensitivity on the magnetic structure of the system [98]. XMCD employs **r**ight and **l**eft **c**ircular **p**olarized light (RCP and LCP, respectively) to gain information on the magnetic properties of the valence band states.

Circularly polarized photons carry an angular momentum of $\pm\hbar$ which gets transferred to the excited electron during the absorption process. In the case of the $L_{3,2}$ edge, the excited photoelectron originates from the spin-orbit split core levels $2p_{3/2}$ and $2p_{1/2}$. Because of the SOC, the angular momentum L of the photon may be in part transferred to the photoelectron as a spin momentum S [99]. The resulting spin polarization will be opposite for the two edges L_3 and L_2 due to their opposite SOC of $L+S$ and $L-S$, respectively. The photoelectron thus carries the transferred angular momentum as a combination of angular and spin momentum, the latter of which is due to SOC.

The spin dependency of the absorption process is introduced by the unoccupied bound states. In the case of a magnetic transition metal, the d-shell has an effective spin moment due to an imbalance of spin-up and spin-down electrons. Since spin flips are forbidden in

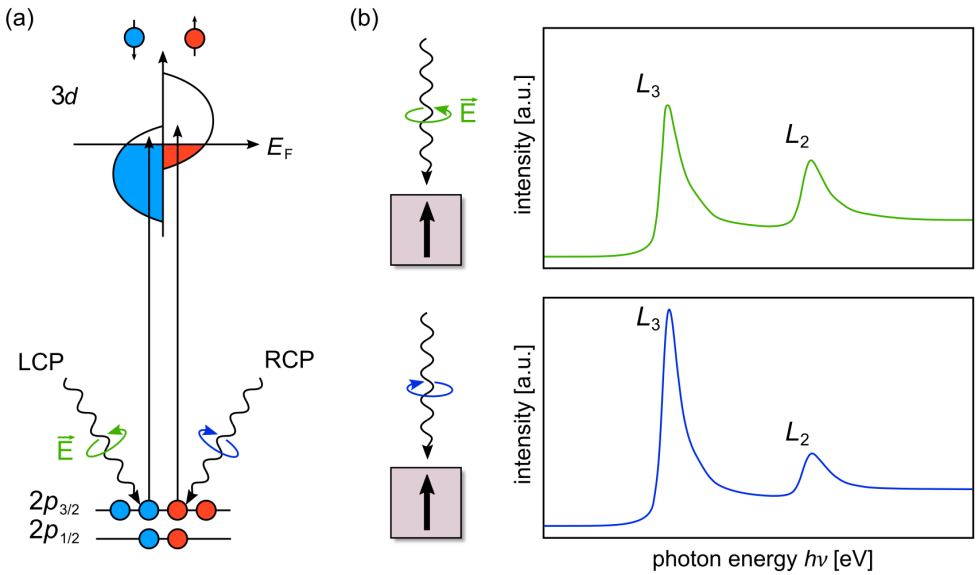

Figure 3.1: Schematic representation of the $L_{3,2}$ XMCD excitation process. (a) Circularly polarized light excites photoelectrons from the spin-orbit split $2p$ core levels to free valence band d-states. The spin orientation is dependent on the helicity of the polarized light as well as on the core level the electrons originate from. (b) Illustrative absorption spectra for excitations with equal magnetization orientation but opposite circularly polarized light.

dipole transitions, a spin-up electron can only be excited into a spin-up hole state, and vice versa. The measured intensity is proportional to the number of empty d-states. Furthermore, the transition probability is proportional to the relative orientation of the spin orientation and the magnetization axis. The maximal (minimal) cross section is obtained with (anti-)parallel alignment of the two [100]. In this way, the spin-split valence band states act as a detector for the spin of the excited photoelectron.

The basic excitation process is schematically depicted in Fig. 3.1 (a), along with two spectra expected for equal magnetization orientation but opposite helicity of the polarized light in panel (b).

3.2.2 X-ray magnetic linear dichroism

Linear dichroism in X-ray spectroscopy was initially used for analyzing the orientation of molecular orbitals [93]. Linearly polarized photons provide a probe sensitive for the charge anisotropy of the unoccupied valence band states, which is due to the electrostatic potential surrounding the excited atom. In the 1980s this concept was extended to magnetic systems where the anisotropy is caused by the alignment of local spins along a preferential magnetic axis [101, 102]. This alignment leads to a deformation of the charge via SOC and hence breaks the symmetry of the non-magnetic state.

Whereas XMCD yields directional information and enables statements on ferromagnetic systems, **X**-ray **m**agnetic **l**inear **d**ichroism (XMLD) probes axial anisotropies which are not detectable via XMCD and which allow for the investigation of antiferromagnetic ordering. The observed dichroism is maximal for a parallel orientation of the magnetic easy axis and one of the polarization vectors, whereas it is minimal for a perpendicular orientation of the three vector quantities. The XMLD signal, therefore, follows a $\cos^2(\Theta)$ behaviour, where Θ is the angle between the electric field vector and the magnetic axis [100]. Generally, the XMLD effect is rather weak in transitionmetals, due to the small size of the spin orbit coupling.

Since X(M)LD arises in non-magnetic systems whenever the local symmetry is lower than spherical, care has to be taken in order to distinguish magnetic from non-magnetic sources of anisotropy, i.e., measuring above and below the magnetic transition temperature.

3.3 Density functional theory

The experimental data in this work are often accompanied and supported by calculations in the framework of **d**ensity **f**unctional **t**heory (DFT) which were performed by collaborators. Even though this data is therefore technically not part of the work of the author of this thesis, it is nevertheless sensible to provide a brief outline of the central ideas of DFT and the specific approximations that were applied in the calculations presented later.

The solution of the many-body Schrödinger equations is a highly complex problem, the direct solution of which is not a feasible approach for problems of condensed matter physics. An alternative approach is provided through two theorems established by Hohenberg and Kohn [103]. First, the external potential of the system is determined by the electron density $\rho(\boldsymbol{r})$. From this theorem follows that the Hamiltonian of the system is uniquely defined by the electron density since the former is specified by the external potential and the total number of electrons and both of these quantities can be calculated from $\rho(\boldsymbol{r})$ [104]. The second theorem states that an arbitrary trial density ρ_t, which satisfies the total electron number, yields an energy $E[\rho_\mathrm{t}] \geq E_0$. Consequently, a minimization of the total energy by variation of $\rho(\boldsymbol{r})$ will yield the ground state electron density and thus the ground state energy E_0 of the system [104].

The search for a good approximation of the functional $E[\rho]$ is greatly facilitated by the Kohn-Sham equations, a set of non-linear equations that map the problem to a system of non-interacting electrons in an effective potential [105]. Here, only the exchange-correlation energy has to be approximated to account for effects not incorporated in the description via a set of single-particle equations.

There exist many practical approximations to the exchange-correlation energy, the applicability of which depends on the exact system under study. One system where the exchange-correlation energy can be derived exactly is the homogeneous electron gas with $\rho(\boldsymbol{r}) = \text{constant}$. A simple approximation to the exchange-correlation term is to set the exchange-correlation potential, which is obtained as the functional derivative of the energy functional, at any point to the known exchange potential of the homogeneous electron gas with the corresponding electron density of that point [106]. This approach utilizes only the local electron density to approximate the exchange-correlation energy and is thus called the **l**ocal **d**ensity **a**pproximation (LDA). While systems with delocalized electrons are often well described by this approximation, high discrepancies arise for systems with strongly correlated electrons. The impact of this effect can be partially offset with a corrective term to the DFT formalism, by using a Hubbard model to describe the localized d- or f-states. This description includes the addition of a Coulomb repulsion U and is therefore referred to as LDA+U.

The natural expansion of the purely local model is the inclusion of the rate-of-change of $\rho(\boldsymbol{r})$, that is, to add a gradient correction to the description. This inclusion is performed via the **g**eneralized **g**radient **a**pproximation (GGA) which also ensures the normalization criteria of the exchange hole [107].

In the discussion of the bulk electronic structure of HgTe, two additional functionals are employed, the **m**odified **B**ecke-**J**ohnson (mBJ) functional and the **H**eyd-**S**cuseria-**E**rnzerhof (HSE) hybrid functional [108–110]. The former is a semilocal extension of the Kohn-Sham framework which provides an enhanced accuracy in the calculation of band gaps while remaining computationally cheap [111]. The latter is a hybrid functional, i.e., a functional in which the exchange energy includes a certain amount of **H**artree-**F**ock (HF) exchange. For HSE, the HF exchange is limited to a short-range contribution which is implemented by an error-function-screened Coulomb potential which decomposes the potential to short- and long-range interactions [110]. The resulting screened Coulomb potential hybrid density functional can be expressed by [110]

$$E_{xc}^{\text{HSE}} = a\,E_x^{\text{HF,SR}}(\omega) + (1-a)\,E_x^{\text{GGA,SR}}(\omega) + E_x^{\text{GGA,LR}}(\omega) + E_c^{\text{GGA}}, \tag{3.19}$$

where a is the mixing parameter of the Hartree-Fock contribution and ω controls the cutoff for the short-range part of the interaction. The indices x and c denote the exchange and correlation, SR and LR the short- and long-range parts, respectively. The HSE06 functional, which is used for the calculation of the bulk band structure of HgTe, is a specific case of the above equation and is characterized by $a = 1/4$ and $\omega = 0.2\,\text{Å}^{-1}$.

3.4 Experimental setups and geometry

The measurements presented in this work were performed at various synchrotron and research facilities. Describing each setup in detail would create a lot of redundant information and hence would needlessly bloat this section. Instead, the setups will be separated by technique – Photoemission spectroscopy and X-ray absorption. For PES, an overview of a general experimental setup will be given, followed by a definition of a laboratory frame of reference, which applies to all measurements performed by that technique. Lastly, the experimental setups will be briefly described in detail, illuminating their more unique features and listing their key parameters. Where available, a reference describing the setup in more detail is provided.

3.4.1 Photoemission setups

Because of the high surface sensitivity of (AR)PES, contaminations of the material that would occur under ambient conditions are detrimental to the quality of the experiment. This is why these techniques are generally performed under **u**ltra **h**igh **v**acuum (UHV) conditions in order to prevent surface degradation. The most basic ARPES chamber consists of three segments – a load-lock, a preparation chamber, and an analyzer chamber or main chamber.

The load-lock serves the function of inserting the sample into the system and thus acts as a bridge between atmospheric pressure and UHV. The load-lock is vented, often using nitrogen gas, followed by pumping to restore the UHV pressure. Several samples may be inserted into the chamber in one cycle, depending on the particular design of the sample holding system. A pressure of $< 10^{-7}$ mbar can generally be achieved in just a few hours.

The preparation chamber is used for sample processing before the actual measurement. A feature often included is sputtering by Ar^+ ions to clean the sample surface of any contamination. Sample heating is done by resistive heating, which enables controllable and highly reproducible temperature setting up to 500° C, or by electron bombardment, reaching higher temperatures while sacrificing precise control. Additionally, the chamber may be equipped with evaporators, which can be used to introduce adatoms to the surface or to grow thin films of a material on a sample or substrate. A dedicated growth chamber is often used for the growth of more intricate materials and techniques like **m**olecular **b**eam **e**pitaxy (MBE). Furthermore, a preparation chamber often provides the possibility to apply **l**ow-**e**nergy **e**lectron **d**iffraction (LEED) to monitor the surface quality and gain additional information on its structure. Typical base pressures lie in the order of 10^{-10} mbar.

The main chamber hosts the three vital components of a PES experiment – a light source, a manipulator, and the electron spectrometer. The light source provides the photons required

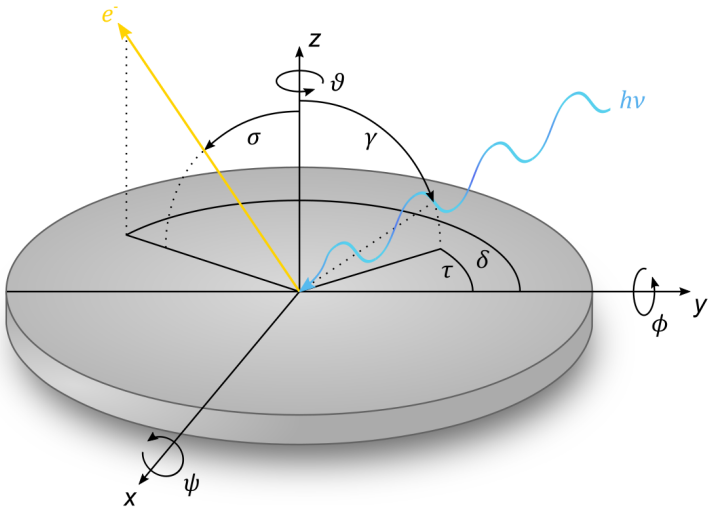

Figure 3.2: Schematic depiction of the experimental geometry. The x-, y- and z-axis are defined with respect to the analyzer and manipulator: the z-axis points from the sample surface to the analyzer entrance, the y-axis is defined as the manipulator axis and the x-axis corresponds to the direction perpendicular to the former two. The sample can be moved along x, y, and z and can be rotated by ϕ around the y-axis. Additionally, depending on the given manipulator, the sample may be tilted by ψ around x and rotated azimuthally by ϑ around the z-axis. The analyzer slit is either parallel to the x- or to the y-axis. Light incidence and the direction of electron emittance are defined by the angles τ, γ, and δ, σ, respectively. τ and δ are defined as azimuthal angles within $\mathcal{P}_{xy}$, whereas γ and σ are defined with respect to the z-axis.

for the excitation of electrons. The most widely used light sources include gas discharge lamps, X-ray tubes, synchrotron radiation, and laser devices. In gas discharge lamps, a plasma is created in the discharge chamber where relaxation processes lead to the emission of characteristic spectral lines, which can be isolated by the use of a monochromator. The discharge lamp used in the laboratory at the University of Würzburg operates with He gas. For He gas the most prominent lines are He I_α ($h\nu = 21.2\,\mathrm{eV}$) and He II_α ($h\nu = 40.8\,\mathrm{eV}$).

Synchrotron facilities utilize the collimated radiation emitted by relativistic charged particles subject to transverse acceleration. Synchrotrons underwent several generational jumps in the last decades, each improving the brilliance of the source. Nowadays, radiation is created and controlled by undulators which guide the electrons on a meandering path. The energy and polarization of the emitted photons can be adjusted within a certain range. The former is selected from the polychromatic radiation by a monochromator, the latter can be controlled via the movement of the electron relative to the undulator plane. Two additional features are the ability to strongly focus the beam, enabling spatially resolved measurements, and the pulsed nature of the radiation, which can be utilized in time-resolved experiments.

A more recent addition to the selection of photoemission light sources are laser-based devices, which combine the availability and size of laboratory sources with the ability to easily control polarization and the pulsed nature of synchrotron-based sources [112]. Laser sources exhibit an outstanding brilliance in the visible and UV regime. Commonly used instruments are based on Ti:sapphire lasers that can be operated at 6 eV or 6.3 eV [113]. These lasers enable comparatively small beam profiles while providing excellent energy resolution and photon flux. The reduced photon energy also entails an increase in momentum resolution because the electronic states are more widely dispersed in angle.

During the measurement, the sample is situated on the manipulator through which its position and alignment are controlled. The manipulator can have up to six degrees of freedom, three translational movements along x, y, and z as well as three rotational motions. The most basic rotation ϕ is around the manipulator axis. It is included in all setups presented in this section. Additional azimuthal and tilt rotations, ϑ and ψ, are defined as rotations around the z- and x-axis, respectively. A schematic illustration of the described geometry is depicted in Fig. 3.2. Two further entities relevant for the evaluation of more complex photoemission phenomena are the POI and the orientation of the analyzer entrance slit. The former is spanned by the axis of light incidence and the z-axis, pointing to the entrance lens of the analyzer. The latter is either aligned parallel or perpendicular to the manipulator axis, i.e., it lies in the $\mathcal{P}_{yz}$ or the $\mathcal{P}_{xz}$ plane, respectively. Furthermore, the manipulator is usually equipped with a continuous flow cryostat which allows for cooling of the sample. The realizable base temperature depends strongly on the particular setup, e.g. the availability of a cooling shield or the possibility to tighten up the contact between the sample holder and the manipulator head.

The last core component of the main chamber is the electron spectrometer. A hemispherical deflection analyzer was used in all setups. The electrons first enter an electrostatic lens system which selects the angle of detection, focuses the electrons on the entrance slit, and controls the energy under which the electrons enter the hemispherical detector. The detector consists of two concentric hemispheres, which are subject to an electrostatic potential difference. Only electrons with a kinetic energy equal to the chosen pass energy are mapped onto the electron counter. The electron detection is performed by a set of multichannel plates that amplify the incident photocurrent, a fluorescent screen which transforms the current into a fluorescent signal, and a CCD camera which captures the image. The analyzer can either be operated in angular or transmission mode. The former images the emission angle distribution whereas the latter maximizes the total transmission of electrons. The radially oriented axis of the two-dimensional detector image resolves the energy of the incoming electrons and captures an energy window of about 9 % of the pass energy. The perpendicular axis maps the emission angle or the spatial coordinate in the angular and transmission mode,

respectively. Because of the spherical symmetry of the analyzer, monoenergetic electrons entering the hemisphere through a straight entrance slit are mapped onto a curved line at the detector. This artifact can be compensated by either choosing a curved entrance slit, with a radius equal to half the mean radius of the hemisphere, or by taking a reference measurement from which the curvature can be extracted for the given experimental parameters.

Analyzers equipped with a VLEED spin detector have an additional operation mode in which the energy-selected electrons traverse an aperture, installed along the radial axis, after which their kinetic energy is regulated to 6 eV. The electrons are deflected onto the Fe(001)-p(1×1)O scattering target and the reflected electrons are counted by a channeltron. The spin polarization is measured in two sequential measurements by reversing the target magnetization. Modern detectors are equipped with two orthogonal scattering targets which allow for detection of the complete polarization vector. In order to circumvent the low figure of merit of the spin measurement, the number of simultaneously passing electrons has to be increased, and thus a significant loss in angular and energy resolution has to be accepted.

Laboratory at the University of Würzburg

The chamber in the laboratory of the Chair for Experimental Physics VII in Würzburg is equipped with a SES 200 analyzer (VG Scienta) with an acceptance angle of $\pm 7°$ [114]. The analyzer slit is oriented along the y-axis.

Furthermore, two light sources are employed at the chamber. A monochromatized He discharge lamp (Gammadata) and a non-monochromatized X-ray source XR50 (Specs) with two Anode materials Al and Mg, providing excitation energies of $h\nu = 1486.6\,\mathrm{eV}$ and $h\nu = 1253.6\,\mathrm{eV}$, respectively. The two sources are aligned along the y-axis with an incidence angle of $\gamma = 45°$.

For the angle-resolved measurements, a pass energy of $E_\mathrm{P} = 10\,\mathrm{eV}$ was chosen as a compromise between count rate and resolution, yielding an energy resolution of about $\Delta E = 8\,\mathrm{meV}$. The effective angle resolution is circa $\Delta\vartheta = 0.3°$. The manipulator has four movement parameters (x, y, z, ϕ) and enables a cooling down of the sample to $T \approx 40\,\mathrm{K}$. For a more detailed description of the main chamber and its capabilities, see Ref. [115]. The load-lock is designed in such a way that a UHV suitcase using the flag style sample holder system can be attached for a direct sample transfer.

Beamline I05 at the Diamond Light Source, UK

The beamline I05, part of the Diamond Light Source, is located at the Harwell Science and Innovation Campus in Oxfordshire and provides circularly and linearly polarized light

for a photon energy range of $h\nu = 18 - 240\,\mathrm{eV}$. With a small-sized beam spot of about $50 \times 50\,\mu\mathrm{m}^2$, it is suited for the investigation of spatial phenomena like the occurrence of different terminations.

All experiments were performed at the HR branch whose measurement chamber is equipped with a R4000 hemispherical analyzer (VG Scienta) with an angular range of $\pm 15°$. The field termination net is dismounted which removes the image of the net normally seen in the fixed operation mode. In all presented measurements the pass energy was $E_\mathrm{P} = 10\,\mathrm{eV}$, resulting in a total energy resolution $\Delta E \leq 10\,\mathrm{mev}$ for the utilized photon energies. The analyzer slit is oriented perpendicular to the POI. Using the notations of Fig. 3.2, the slit is parallel to the y-axis whereas the beam comes in at an angle $\tau = 90°$. The cryogenic sample manipulator has a minimum temperature of $T = 8\,\mathrm{K}$ while simultaneously allowing full 6-axis sample control. A technical description of the beamline and the HR branch can be found in Ref. [116].

Beamline 7.0.2.1 at the Advanced Light Source, USA

The **m**icroscopic **a**nd **e**lectronic **str**ucture **o**bservatory (MAESTRO), the alternative designation for the beamline 7.0.2.1, is part of the Advanced Light Source situated in the Lawrence Berkeley National Laboratory in Berkeley. The μARPES endstation has an energy range of $h\nu = 20 - 1000\,\mathrm{eV}$ with both circular and linear polarization. The effective spot profile has a size of about $10 \times 12\,\mu\mathrm{m}^2$ in normal emission.

The electron analyzer is a R4000 (VG Scienta) with a custom-made deflector lens system. The deflector enables the acquisition of a full ARPES band map without changing the experimental geometry. Routinely achievable energy resolutions are $\Delta E \leq 15\,\mathrm{eV}$. The incidence angles are $\tau = 90°$ and $\gamma = 54.75°$, making $\mathcal{P}_{xz}$ the plane of incidence. The analyzer slit lies in $\mathcal{P}_{xz}$, the band mapping is therefore done by tuning the tilt angle ψ, if the deflector is not used. The 6-axis cryogenic sample manipulator has a temperature range of $T = 15 - 2300\,\mathrm{K}$.

Beamline P04 of the PETRA III storage ring at DESY, Germany

P04 is a soft X-ray beamline situated at the **p**ositron-**e**lectron **t**andem **r**ing **a**ccelerator (PETRA-III) at the DESY (*deutsches Elektronen-Synchrotron*) in Hamburg. With available photon energies of $h\nu = 250 - 2200\,\mathrm{eV}$ and circularly polarized light, it is well suited for the investigation of bulk electronic structure as well as ResPES. A review of the beamline up to the endstation can be found in Ref. [117].

The endstation had several major upgrades and modifications in the timeframe of this

work. The machine will be presented as it was at the time at which the experiments were performed. The endstation ASPHERE III is equipped with an **a**ngular **s**pectrometer for **p**hotoelectrons with **h**igh **e**nergy **re**solution in the form of a DA30-L (VG Scienta) analyzer. Resonant photoemission was performed with a pass energy of $E_P = 100\,\text{eV}$ which yields a total energy resolution of about $\Delta E = 120\,\text{meV}$.

The light incidence is at $\tau = 0°$ and $\gamma = 73°$; the analyzer slit is parallel to the y-axis. Due to the high kinetic energies of the photoelectrons, a large section of momentum space can simultaneously be covered by a detection angle of 30° and the momentum mapping is therefore usually done via the deflection mode of the analyzer. Alternatively, the section of the measurement chamber hosting the electron analyzer can be turned around the manipulator axis by means of differentially pumped rotary feedthroughs. Furthermore, the drain current of the sample can be measured by an ampere meter (Keithley), allowing to perform XAS measurements in TEY detection mode, which are crucial for the determination of the absorption edges and thus for the execution of ResPES. Another feature, not utilized in this work, is a Mott detector, manufactured by VG Scienta, which allows for the detection of the spin asymmetry. The manipulator has full 6-axis motion control and cooling capabilities down to $T = 30\,\text{K}$.

μ-ARPES setup at the Hiroshima Synchrotron Radiation Center, Japan

Aside from a storage ring and beamline facilities, the **Hi**roshima **s**ynchr**o**tron **r**adiation center (HiSOR) also has a μ-ARPES laser setup. The light source is a Ti:sapphire based laser (Spectra Physics) whose fourth harmonic serves as excitation energy ($h\nu = 6.3\,\text{eV}$). The beam is focussed by an optical lense system before entering into the chamber and has a spot size of about $10 \times 10\,\mu\text{m}^2$. The total energy broadening is $\Delta E < 3\,\text{meV}$. The polarization can freely be tuned between linear and circular by the use of a $\lambda/4$-waveplate. Light incidence is at $\tau = 90°$ and $\gamma = 45°$, in normal emission.

The entrance slit of the R4000 electron analyzer (VG Scienta) is parallel to the x-axis. The 6-axis manipulator allows for computer-controlled sample translational movement as well as rotation around ϕ and ψ. The azimuthal angle ϑ can be manually tuned by an *in situ* wobble stick. A detailed description of the setup can be found in Ref. [118].

Laser-ARPES setup at the Forschungszentrum Jülich, Germany

The spin-ARPES setup at the Peter Grünberg Institute PGI-6 in Jülich combines a brilliant laser photon source ($h\nu = 6.02\,\text{eV}$) with an electron analyzer equipped with a VLEED-based FOCUS spin detector (FERRUM, Sherman function $S_{\text{eff}} = 0.29$). The continuous-

wave laser provides linearly polarized light with a beam spot size of $50 \times 50\,\mu m^2$ and incidence angles of $\tau = 90^\circ$ and $\gamma = 45^\circ$, in normal emission. The hemispherical analyzer (MB Scientific AB) enables, similar to the Scienta deflectors, mapping of electronic states perpendicular to the analyzer slit axis, which lies in the $\mathcal{P}_{yz}$ plane, by a combination of electrical and mechanical electron optics. The cryostat manipulator has four degrees of freedom and enables sample cooling down to $T = 20\,K$.

3.4.2 X-ray absorption setup

HECTOR endstation of the beamline BL29 at the ALBA synchrotron, Spain

The **B**eamline f**or** **re**sonant **a**bsorption and **s**cattering (BOREAS) is equipped with a high-field vector magnet for soft X-ray absoption and dichroism techniques. The magnet consists of three orthogonal superconducting coils, allowing for fields up to 6 T with a maximum ramp rate of $\pm 2\,T$ per minute. The beamline provides circularly and linearly polarized light from $h\nu = 80 - 4000\,eV$. The beamspot may be regulated down to $100 \times 100\,\mu m^2$, but in the presented data it was $200 \times 200\,\mu m^2$ in order to limit the scanning time to a reasonable length. For the utilized photon energies, the beamline has a resolving power of $E/\Delta E \geq 7000$.

The sample is mounted on a continuous flow cryostat, enabling sample cooling down to 2 K, while allowing for movement with four degrees of freedom. The sample holder is electrically isolated in order to measure the drain current necessary for TEY detection mode. Additionally, a Si diode for FY detection may be inserted perpendicular to the beam axis and the sample rotation axis. A characterization of the BOREAS beamline can be found in Ref. [119].

3.5 Sample synthesis and preparation

Mercury telluride HgTe

Bulk HgTe samples were grown by Lukas Lunczer, Raimund Schlereth, and Lena Fürst from the Chair of Experimental Physics III at the Julius Maximilians University of Würzburg. The growth was performed by MBE, which is ideally suited for highly controllable epitaxial crystal growth of thin films. The desired precursor materials are evaporated from effusion cells, forming a thermal molecular beam that reacts with the crystalline surface of the substrate, where the material condensates [120].

The substrate of choice is CdTe, since its 0.3 % larger lattice constant of $a_{\mathrm{CdTe}} = 6.48\,\text{Å}$ creates the necessary in-plane tensile strain in the HgTe film grown on top. Before inserting the substrate into vacuum conditions, the surface is wet etched by an aqueous HCl solution to remove surface oxidation as well as a pre-existing protective layer. Subsequently, the substrate is heated *in situ* at 200 °C for about 20 minutes to desorb any residual water molecules that may have been deposited during the short time between the etching and the introduction into the vacuum. Lastly, any remaining residuals are removed at 315 °C, while a constant Te flux is provided from 250 °C upwards in order to prevent the formation of thermal defects. In the same heating step, a 60 nm thick CdTe buffer layer is deposited from a CdTe-containing cell, to serve as a pristine *in situ* surface in the ensuing film growth.

Mercury is liquid under ambient conditions which poses a significant obstacle for the MBE growth of Hg-containing compounds. First, the beam equivalent pressure of Hg has to be two orders of magnitude higher than for Te and CdTe. In order to alleviate the resulting increased pressure during growth, liquid N_2 cryotraps are used to getter the Hg background [121]. Second, the high volatility of Hg dictates low substrate temperatures in order to reduce thermal desorption. Additionally, the Hg evaporator features a valve instead of a shutter, which allows for the complete separation of the evaporator from the growth chamber. The temperature of the effusion cells is kept constant during growth and the molecular flux is controlled by operating shutters and the valve for the CdTe and Te, and Hg evaporators, respectively.

After the deposition of the CdTe buffer layer, the substrate is cooled down to 180 °C, where an additional $Hg_{0.3}Cd_{0.7}Te$ buffer layer is then grown by co-evaporation of Hg and CdTe. The purpose of this layer is related to the transport properties of the film, which the buffer was shown to improve by reducing the roughness of the interface and by the screening of doping by the substrate [122]. As a final growth step, the actual HgTe film is grown by co-evaporation of Hg and Te. Here, a substrate temperature of just above 178 °C ensures a step flow growth mode and prevents the formation of islands [123]. Furthermore, a film thickness

of 100 nm was chosen to ensure three-dimensional transport properties, i.e., a sample in the 3D TI regime, while preserving the strain induced by the substrate before relaxation processes arise [124]. Lastly, the film is cooled down to room temperature, whereby a Hg flux down to 100 °C is provided to minimize desorption and re-evaporation of the volatile element.

Samples are grown under UHV conditions to ensure pristine sample quality. Since, in general, the photoemission setup and the growth chamber are locally separated, inhibiting a direct sample transfer without breaking the vacuum, it is imperative to find a way to transport the thin films to the measurement chamber while preserving a clean sample surface. The high volatility of mercury prevents the application of any heating-related preparation methods like Ar^+ ion bombardment with subsequent annealing or the thermal desorption of a protective layer, as has been applied in more temperature stable TI [125, 126]. As a result, in the few existing works, only ion bombardment was chosen as a compromise solution, which led to non-satisfactory results [127, 128]. Following a procedure that has already been successfully applied to vdW-layered systems, the approach of a protective layer, which is mechanically removed prior to the ARPES measurement, was chosen in the present work [129]. Here, a capping layer is grown at approximately room temperature on top of the final film. The sample is removed from the vacuum and a so-called top-post is attached *ex situ* on the sample, which serves as a lever for the mechanical removal of the capping layer under UHV conditions within the ARPES setup.

As in the case of epitaxially grown Bi_2Te_3, Te was chosen as the capping material due to a combination of availability in the growth chamber and the fact that the material is already present in the actual film. However, initial tests showed that only a fraction of the capping layer could be removed and only slight traces of Hg were observable with XPS. To gain a better understanding of the morphology of the protective layer, **s**canning **e**lectron **m**icroscopy (SEM), which enables the visualization of the surface condition, was employed. Fig. 3.3 (b) and (c) show SEM images taken with angles of 90° and 70° to the surface normal, respectively. In the former, the previously described layers can be seen, which are correspondingly labeled by the schematic depiction in Fig. 3.3 (a). While substrate, buffer layer, and thin film are relatively flat and homogeneous, the Te capping layer exhibits a polycrystalline structure consisting of elongated islands. Fig. 3.3 (c) enables a view of the surface of the protective layer, allowing us to see that the islands extend up to the surface, where they are separated from each other by small valleys, resulting in a rough surface topography. In order to connect the individual islands and to smoothen the surface, an additional 10 nm thick Ti layer was deposited on the Te cap. The desired effect was achieved and following characterization measurements showed that the majority of the capping layer could be removed by this modification [130].

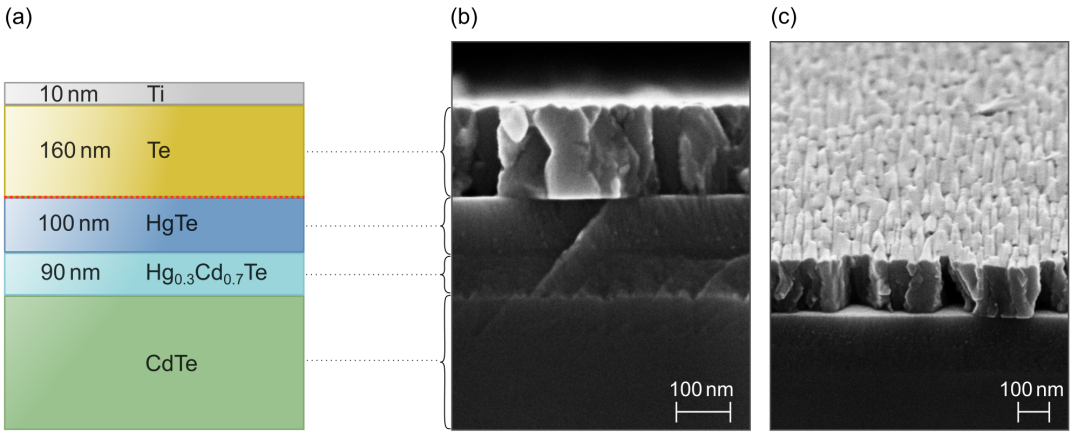

Figure 3.3: Representation of the stacking order of MBE grown HgTe. (a) Schematic depiction of the layer arrangement, protected from oxidation by a Ti-Te double layer. The stack is terminated by a thin Ti layer, linking the separate Te islands. The intended cleavage plane is indicated by a red dotted line. (b) SEM image showing the layer stack from the side view. This sample is a prototype whose protective layer consisted of only a 160 nm thick Te layer. (c) View on the same sample as shown in (b), tilted by 20°. The individual Te islands can be distinguished on the surface. SEM images by courtesy of Raimund Schlereth.

For ARPES, XPS, and STM measurements within the institute, the samples were also transferred via a UHV suitcase. This is a mobile transfer chamber that allows for sample transfer between compatible setups without breaking the vacuum, which is achieved by the usage of passively operating getter pumps. Due to small intermediate volumes, the samples can be transferred from the MBE chamber to the ARPES chamber within 12 hours. This method is not applicable for measurements performed at distant facilities, which is why preparation via mechanical exfoliation was exclusively used for synchrotron measurements.

Layered manganese bismuth tellurides $(MnBi_2Te_4)(Bi_2Te_3)_n$

The Mn-Bi-Te compounds were synthesized by Anna Isaeva and coworkers at the Leibniz Institute for Solid State and Materials Research in Dresden. The growth procedure comprises the formation of a melt of binary precursors and its slow cooling and annealing over several days. Bi_2Te_3 and α-MnTe (NiAs-type structure) serve as the precursors, providing the elemental components in the right stoichiometry. Additionally, when deducing the expected oxidation state $Mn^{2+}(Bi^{3+})_2(Te^{2-})_4$ from the isostructural compound $GeBi_2Te_4$, the precursors already provide the constituents in the right oxidation state [131, 132].
The small differences in the formation enthalpies of Bi_2Te_3 and the desired ternary compounds leave only a narrow energetic window for the growth process. The melting tem-

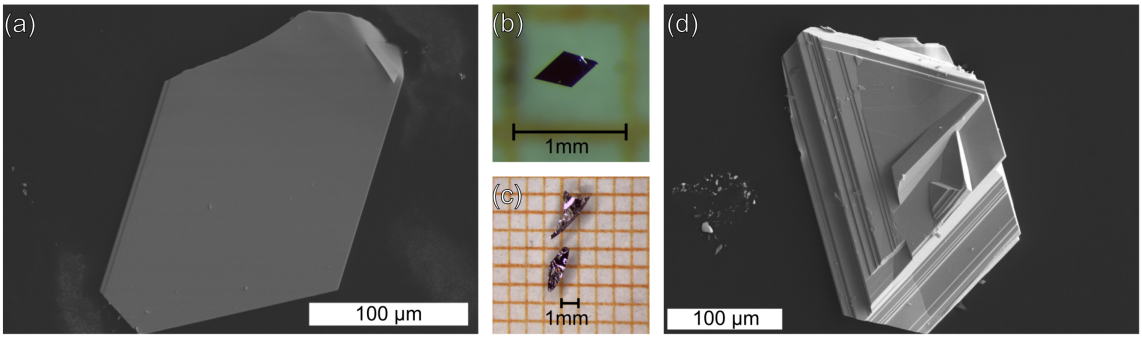

Figure 3.4: Optical and scanning electron microscopy images of $(MnBi_2Te_4)(Bi_2Te_3)_n$ for $n = 0$ and $n = 1$. (a), (b) SEM and optical image of $MnBi_2Te_4$. (c), (d) optical and SEM image of $MnBi_4Te_7$. The figures for $MnBi_2Te_4$ and $MnBi_4Te_7$ were taken from the joint publications Ref. [133] and Ref. [28], respectively.

peratures of Bi_2Te_3 and $MnBi_2Te_4$ differ only by 9 K; for the solidification temperatures, the difference is less than 6 K due to different undercooling [133]. The growth was performed via slow cooling over the Ostwald-Miers region between the onset temperatures of melting $T^{\text{ons}}_{\text{melt}} = 595\,^{\circ}\text{C}$ and solidification $T^{\text{ons}}_{\text{solid}} = 591\,^{\circ}\text{C}$ [132]. The cooling rate affects the average size of the resulting single crystals, with smaller rates resulting in larger crystals. Rates down to $-1\,\text{K}\,\text{h}^{-1}$ were used. The cooling is followed by annealing just below the Ostwald-Miers region at 590 °C for at least 5 days and subsequent water quenching [133].

In the case of the intercalated ternaries $(MnBi_2Te_4)(Bi_2Te_3)_n$ ($n = 1, 2$), slow cooling is not a feasible approach due to complex phase relations and even narrower energetics. Instead, the melt is annealed at 585 °C, in the existance range of the desired compounds, followed by water quenching to room temperature. The resulting compounds are isostructural to $GeBi_4Te_7$ and $GeBi_6Te_{10}$ despite a slight deviation from the ideal stoichiometry due to Mn/Bi intermixing and cation vacancies [27, 134, 135]. These two compounds are metastable and start to decompose above 250 °C [27].

Figs. 3.4 (a) and (b), and (c) and (d) show images of $(MnBi_2Te_4)(Bi_2Te_3)_n$ crystals for $n = 0$ and $n = 1$, respectively. Images in (a) and (d) display SEM images, whereas figures (b) and (c) are taken with an optical microscope. For a detailed description of the growth process of $MnBi_2Te_4$ as well as $MnBi_4Te_7$ and $MnBi_6Te_{10}$, the reader is reffered to Refs. [132, 133] and Refs. [27, 28], respectively.

For a lot of layered vdW materials like the topological insulator Bi_2Te_3, sizeable flakes are readily available and can easily be cleaved by an adhesive tape, which removes the topmost multilayers when pulled off. The sub-millimeter size of the $(MnBi_2Te_4)(Bi_2Te_3)_n$ crystals prevents a proper sticking of the adhesive tape to the surface. Instead, like for HgTe, the samples were cleaved by the usage of a top-post, which involves gluing a copper wire onto

the sample surface, parallel to its *c*-axis. Since the vdW bonding is comparatively weak, adhesiveness is less of a concern and an electrically conductive glue can be used, preventing charging issues during the experiment. The utilized epoxy glues are EJ2189 and H20E by Epoxy Technology, Inc. There were no noticeable differences between the two products. In experimental setups where no collection tray for used top posts was installed, an additional, thinner wire was used, linking the top post to the sample holder plate.

4 Bulk and surface electronic structure of HgTe(001)/CdTe

HgTe is a prototypical topologically non-trivial material with many-faceted properties, depending on its structural parameters. In a quantum well configuration, sandwiched between the trivial insulator CdTe and above a critical thickness, it exhibits the quantum spin Hall state and was the first-ever realized two-dimensional TI [12, 13]. As a bulk material, it may either appear as a topological semimetal, a three-dimensional TI, or as a Weyl semimetal, depending on the applied strain [17, 43]. Intermixing Hg with Cd atoms enables a temperature-dependent occurrence of pseudo-relativistic three-dimensional particles in the form of Kane fermions [136]. If magnetism is introduced into the system, for instance by doping with transition metal adatoms, it may also serve as a host for the quantum anomalous Hall effect [64]. Despite its persisting relevance and its apparent versatility, a comprehensive ARPES study combined with theoretical modeling was still lacking up to now. This chapter aims to provide a detailed experimental analysis of the electronic structure of bulk HgTe, i.e., in its 3D topological insulator phase.

The first section gives a brief overview of the material properties of HgTe relevant to the subsequent analysis. Furthermore, a summary of the sample characterization, which serves as preparatory work for the ensuing ARPES measurements, is given. The following sections will each investigate one aspect of the electronic structure in more detail. The three-dimensional bulk band dispersion is examined utilizing $h\nu$-dependent VUV photoemission. A further focus is placed on the character of the Hg 5*d* shallow core state and its impact on the low energy bands. This is followed by an investigation of the orbital character of the valence band states via polarization-dependent measurements. The findings are discussed in the context of the topological band inversion. Related to this is the examination of the topological surface state on *in situ* grown films. Lastly, the temperature dependence of the chemical potential will be examined.

Synchrotron-based measurements were performed at the beamline 7.0.2.1 of the Advanced Light Source in Berkeley, while high-resolution spectra using the $\mathrm{He\,I}_\alpha$-line were taken in the laboratory in Würzburg. The experimental results throughout this chapter are accompanied by theoretical data in the form of DFT calculations. These calculations were performed by Gianni Profeta and Giovanni Marini from the University of L'Aquila as well as Giorgio San Giovanni and Domenico Di Sante from the institute for theoretical physics and astrophysics from the University of Würzburg. The main results are intended to be published in Ref. [137].

4.1 Material properties and preceding characterization

Mercury telluride, HgTe, is a group II-VI direct gap semiconductor with zincblende type crystal structure, consisting of two **f**ace-**c**entered **c**ubic (fcc) lattices shifted with respect to each other by a quarter of the space diagonal. Each of the fcc sublattices is occupied by either the cations or the anions, i.e., Hg and Te, respectively. The system is classified by space group No. 216 with $F\bar{4}3m$ symmetry. The conventional unit cell as well as the first Brillouin zone, which forms a truncated octahedron, are depicted in Fig. 4.1 (a) and (b), respectively. The lattice constant of the cubic unit cell is $a_{\mathrm{HgTe}} = 6.46\,\text{Å}$ [138]. Emphasis is placed on the mirror symmetry along the systems $\langle 110 \rangle$ directions, corresponding to ΓK in reciprocal space, which become of particular relevance in the later course of the evaluation.

Section 2.2.1 introduced the physical mechanisms which induce the non-trivial band ordering and lead to HgTe being a topological semimetal. In the following evaluation of the experimental and theoretical data, we will encounter two additional symmetry-related effects, which further augment the band structure. The first is a strain-induced breaking of the cubic symmetry that opens a finite energy gap. Secondly, a $\boldsymbol{k}$-dependent splitting of the bulk bands occurs due to a lack of inversion symmetry in the zincblende structure. The latter will be discussed in more detail as part of the data evaluation in section 4.3.

The symmetry-induced zero energy gap at the Fermi energy renders unstrained bulk HgTe a semimetal. In order to observe the topological behavior via transport measurements, a finite energy gap has to be opened, which is usually done by breaking the cubic symmetry [140]. One approach is to reduce the dimensionality of the system to 2D by creating thin CdTe/HgTe/CdTe quantum wells [12]. The adopted approach in this work is the application of external strain, which is realized by growing HgTe on a lattice-mismatched substrate. While compressive strain would lead to an overlap of the two Γ_8 sub-bands, tensile strain separates the two, opening a band gap [17, 43]. The substrate of choice is the conventional insulator CdTe. With a lattice constant of $a_{\mathrm{CdTe}} = 6.48\,\text{Å}$, it exerts a biaxial tensile strain of 0.3 % to the HgTe grown on it [138]. The induced bulk band gap is in the order of a few meV, sufficient for transport measurements. From a photoemission point of view, this energy gap is not a prerequisite to observe the TSS. Nevertheless, the motivation is to investigate an as-grown material system and since the topological properties are generally envisioned in conjunction with technologies like novel concepts of computing, it is sensible to examine samples optimized for transport purposes.

Technically, the fcc labels for the reciprocal symmetry points are no longer accurate due to the decreased symmetry of the strained material. Instead, labels corresponding to the new tetragonal symmetry, added to the Fig. 4.1 (b) in green color, should be used. Practically speaking, for small perturbations the tetragonal **B**rillouin **z**one (BZ) can hardly be

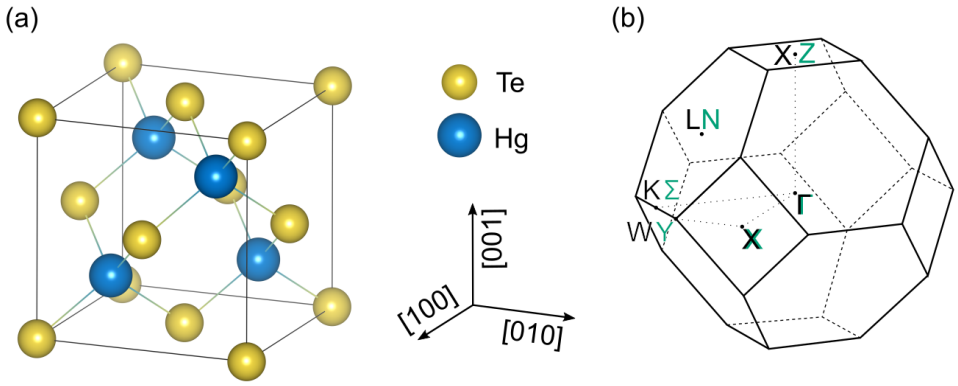

Figure 4.1: (a) Conventional cubic unit cell of the zincblende structure of HgTe. The Te and Hg atoms are depicted by yellow and blue spheres, respectively. The model was created by the program described in Ref. [139]. (b) First Brillouin zone of HgTe. The labels in black and green correspond to the face-centered cubic and body-centered tetragonal structure, respectively.

distinguished from the fcc BZ and, in order to facilitate any prospective comparisons with references for unstrained HgTe, the labels of higher symmetry will henceforth be used.

As described in the previous chapter, MBE-grown HgTe thin films were prepared in two different ways. For the measurements in the laboratory in Würzburg, samples were transferred via a portable UHV chamber without breaking the vacuum. Fig. 4.2 (a) depicts a LEED pattern of a pristine HgTe(001) surface. The topmost atomic layer has a fourfold symmetry with a lattice constant of $a_{\mathrm{HgTe}}/\sqrt{2} = 2.54\,\text{Å}$. The corresponding diffraction spots are colored green. An additional group of spots, marked in blue, pertains to a (2×1) surface reconstruction. This type of surface reconstruction can be attributed to a Te-termination and was found on CdTe and other II-VI compound semiconductors [141, 142]. Even for a macroscopic wafer size of $10 \times 10\,\mathrm{mm}^2$, only one of the two possible domains could be observed for a given sample. A c(2×2) reconstruction, previously found on HgTe and attributed to a Hg-termination, could not be observed [141, 143]. Lastly, a third set of spots can be identified, indicated by orange color, which has not been reported in any preceding study. These spots could be observed on samples transferred via suitcase as well as on cleaved samples. Similar spots could also be observed on samples where the cleaving process did not succeed and where only signatures of the Te capping layer could be seen in XPS. Moreover, on samples where the cleaving succeeded and which showed spectral signatures of Hg and Te in XPS, there were regions where this type of spots formed the only observable LEED pattern. These diffraction spots may hence be assigned to residual Te on the sample surface and indicate an excess of Te atoms at the surface, forming clusters.

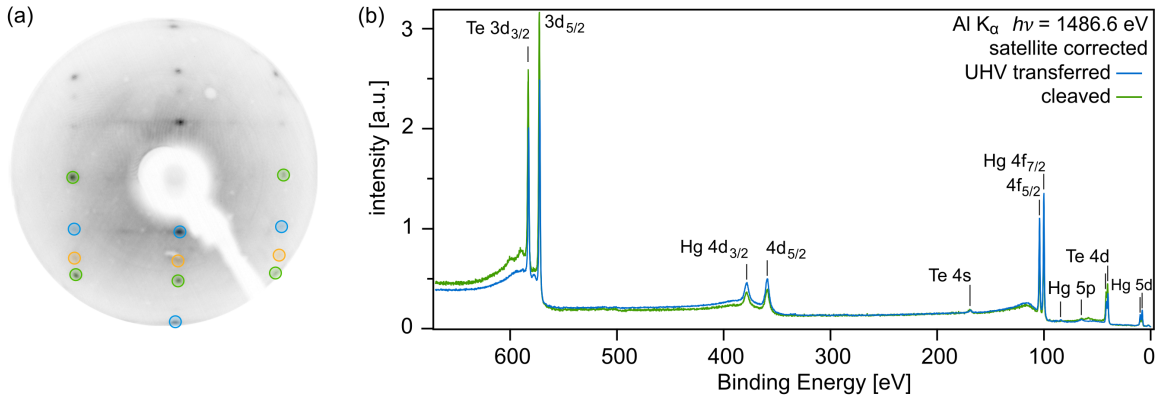

Figure 4.2: Surface characterization of cleaved and UHV transferred HgTe(001). (a) LEED pattern taken at $E = 34\,\mathrm{eV}$. The spot groups belonging together are marked in blue, green, and orange corresponding to the cubic surface unit cell, the (2×1) surface reconstruction, and the Te-related pattern, respectively. (b) XPS survey spectra taken with the Al K_α-line. The blue spectrum is taken on a sample transferred by the UHV suitcase whereas the green one is taken on a cleaved sample. The satellites caused by the unmonochromatized X-ray gun are removed in both spectra.

XPS can be employed to further investigate the elemental surface composition in order to gain information about the applied preparation method. For the measurements conducted at the ALS in Berkeley, a Te-Ti capping layer was deposited subsequent to the growth process and removed in the ARPES chamber. Fig. 4.2 (b) shows XPS survey scans for such a decapped as well as a directly transferred sample in green and blue color, respectively. Both spectra exclusively contain spectral lines that can be assigned to the species Hg and Te and no traces of additional contaminants can be detected. For the cleaved sample, the intensity of Te is enhanced whereas the weight of Hg is diminished. Quantitative evaluation of the data revealed a relative stochiometry of 1:1 for Hg:Te for the sample transferred via UHV suitcase [144, 145]. In the case of surface preparation by cleaving, the ratio is always shifted towards a higher Te concentration. Together with the LEED characterization, this draws the picture of a cleaving process that does produce a contaminant-free surface, albeit with traces of residual capping material. This sets the necessity for a small beam spot in order to optimize the performance of the photoemission experiment. Furthermore, the finding of exclusively Te-terminated surfaces is crucial concerning the theoretical approach to this system. Previous studies found that the resulting surface electronic structure is heavily dependent on the termination of the system. While for a Te-terminated surface, the Dirac point is located at the Γ-point, for a Hg-termination, three Dirac cones are expected at different time-reversal-invariant momenta [146–148]. The surface preparation was investigated in more detail in Refs. [130] and [149].

4.2 Bulk band structure

The dispersion of the electronic bulk states along the wave vector component k_z perpendicular to the surface dictates a careful photon-energy-dependent analysis. In the case of HgTe, the band inversion is expected to be located around $\boldsymbol{k} = 0$ in momentum space. The localization of the region of interest around the Γ-point, therefore, requires an educated choice for $h\nu$. Due to the potential step at the surface, the k_z momentum component is not conserved and a direct conversion of photon energy dependence to k_z-dispersion is thus impeded. However, the information can still be restored by the assumption of a free-electron-like final state in the form of equation 3.5, where the inner potential V_0 can be deduced from the experimentally observed periodicity $E(h\nu)$. From preceding theoretical and experimental studies on HgTe, it is evident that the electronic structure of the valence band ensemble exhibits a global maximum at the point of convergence of conduction and valence band [150–152]. This spectral signature can be used to determine the value of the inner potential V_0 by identifying the periodicity of the electronic structure.

Fig. 4.3 (a) shows a Fermi surface in form of a k_x-k_z-map for a photon energy range of $h\nu = 60 - 400\,\mathrm{eV}$. The white lines indicate the boundaries of the tetragonal Brillouin zone. The alignment of the Brillouin zone, the crystallographic directions of the conventional unit cell, and their relation to the orthogonal wave vector components is depicted in Fig. 4.3 (b). The k_z-axis coincides with the $[001]$ direction, which corresponds to the ΓX high-symmetry line. The wave vector component k_x is parallel to the $\left[1\bar{1}0\right]$ direction, and thus points along the ΓK high-symmetry direction. Together they span the (110) plane, which is colored in grey, whose intersection with the border of the BZ forms a hexagon. Returning to panel (a), at the center of each BZ a spectral feature can be seen, which can be attributed to the topmost valence band. The Γ-point just below $k_z = 6\,\mathrm{Å}^{-1}$ was chosen for further measurements, due to a conjunction of high photon flux and beneficial cross sections. The bright, curved double feature at about $k_z = 5\,\mathrm{Å}^{-1}$ is an artifact due to the excitation of the Hg $4f$ core levels by the second harmonic of the monochromator.

Fig 4.3 (c) displays the band structure along the high-symmetry cut that is marked in panel (a) by a green dotted line. For $k_x > 0$ and within the first BZ, the experimental data is overlaid by a calculation of the electronic bulk states, enabling an unambiguous identification of the observed spectral features. The topmost valence band, the $\Gamma_{8,\mathrm{hh}}$-band, is only visible for small but finite k_x values and vanishes for $|k_x| > 0.5\,\mathrm{Å}^{-1}$. Conversely, the dispersion of the Γ_6-band can be traced for the full momentum range and is accurately matched by the calculation. The state forms a local maximum at the X-point, outside the first BZ. Lastly, the highly dispersive feature can be assigned to the Γ_7 split-off state. The $\Gamma_{8,\mathrm{lh}}$-band forms the conduction band, which is not observable at the given temperature. Between the $\Gamma_{8,\mathrm{hh}}$-band

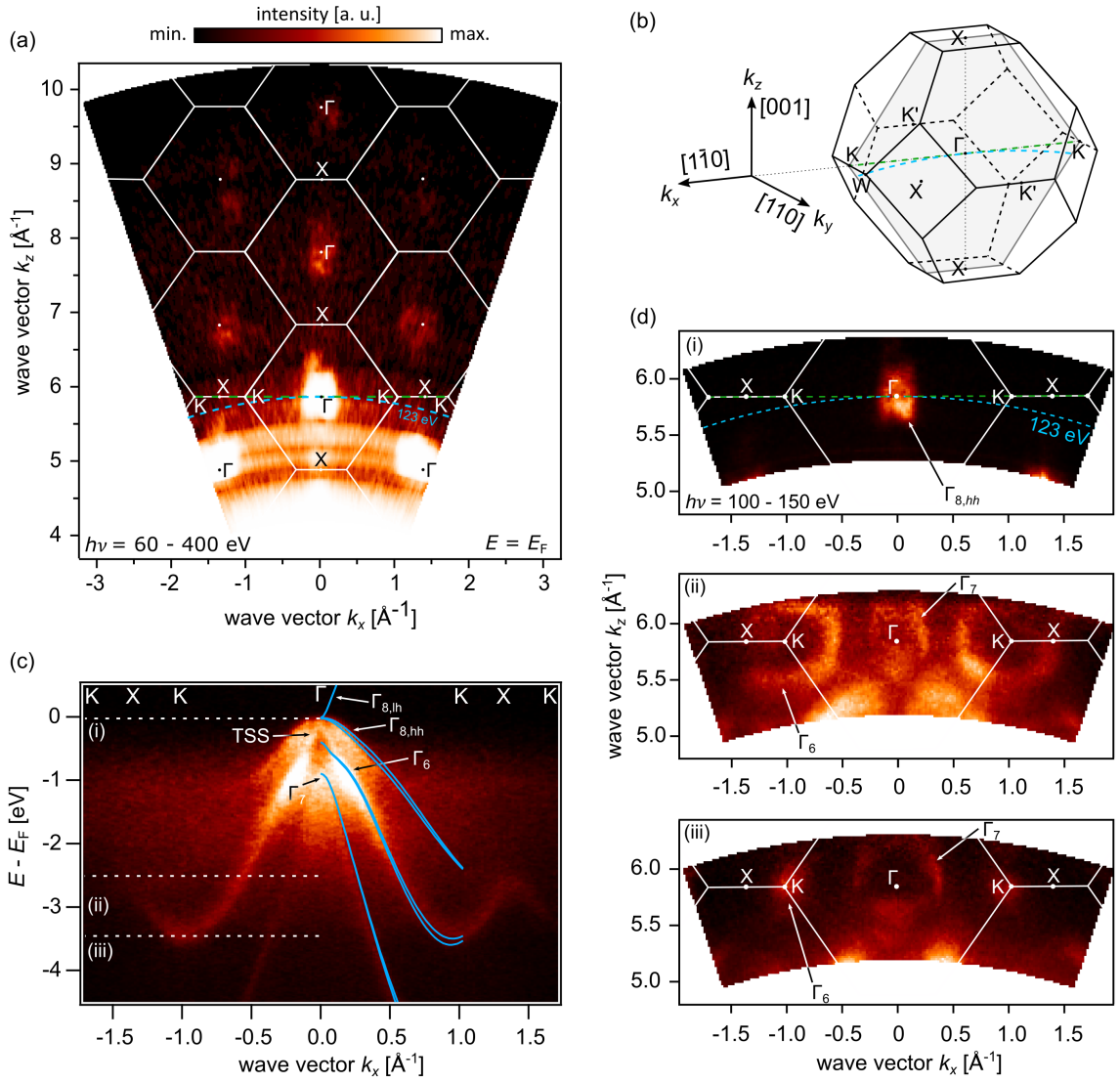

Figure 4.3: Photon-energy-dependent bulk band dispersion of HgTe(001). (a) Fermi surface map for photon energies of $h\nu = 60 - 400\,\mathrm{eV}$, converted to the wave vector component k_z. The white lines indicate the Brillouin zone boundaries for the (110) plane. The dashed green and blue lines correspond to a true high-symmetry cut and the cut received by measuring at a photon energy of $h\nu = 123\,\mathrm{eV}$, respectively. (b) fcc Brillouin zone with the (110) plane indicated by a grey hexagon. The direction of the three wave vector components is given along with their respective high-symmetry direction. (c) Band structure along a true high-symmetry line K-X-K-Γ-K-X-K. The dotted white lines mark the energy positions of the constant energy contours in panels (i)-(iii). (d) k_x-k_z constant energy contours for a photon range of $h\nu = 100 - 150\,\mathrm{eV}$. The panels (i), (ii) and (iii) are taken at $E - E_\mathrm{F}$ values of 0 eV, −2.5 eV, and −3.4 eV, respectively. All spectra were taken with p-polarized light.

and the Γ_6-band lies a state that is not reproduced by the bulk calculation. This state can be identified as the topological surface state. Its identification is discussed in more detail and experimentally substantiated in the following section. With a virtually linear dispersion, the TSS connects the top of the Γ_8-band with the second valence band at $k_x \approx \pm 0.12\,\text{Å}^{-1}$. The Dirac point is located at the merging point of the TSS and the Γ_8-band.

The dotted white lines, labeled (i)-(iii), indicate the energy positions of the k_x-k_z-maps in panel (d). The energies were chosen with the intent to further emphasize the symmetry of the k_z-dispersive electronic structure around the chosen Γ-point. Panel (i) shows the electronic structure at the Fermi level and, as before, highlights the global maximum of the valence band at the Γ-point. At the energy marked with (ii), the Γ_6-band exhibits its aforementioned local maximum at the X-point. The state forms circular intensities in the **c**onstant **e**nergy **c**ontour (CEC) that are arranged around the K-points. Lastly, the cut (iii) intersects the Γ_6-band at its minimum, highlighting the K-points.

In the following part, the band structure along $k_{||}$ will be further discussed. In order to examine the electronic states at the appropriate k_z-value, a photon energy of $h\nu = 123\,\text{eV}$ was chosen for these subsequent measurements. The probed slice along k_z is indicated by a dashed blue curve in Fig. 4.3 (a) and (b) and it is approximated as an even plane in Fig. 4.4 (a). At $k_{||} = 0$, this photon energy coincides with the Γ-point, whereas it deviates considerably from the high-symmetry line at the borders of the BZ. A fact that should be kept in mind when discussing the degree of agreement between theory and experiment at higher wave vectors.

Fig. 4.4 (b) shows the electronic structure along ΓK and ΓX for wave vectors $k_{||} < 0$ and $k_{||} > 0$, respectively. The experimental data is again superimposed by the corresponding bulk calculation and the different spectral features can be associated with their corresponding bulk state. We find the band ordering $\Gamma_8 > \Gamma_6 > \Gamma_7$, as expected for this II-VI semiconductor with an inverted bulk band structure. The notation as Γ-states is only valid at the Γ-point since the designation pertains to the symmetry properties at this particular high-symmetry point. The common convention of applying this notation even outside of $\boldsymbol{k} = 0$ is adapted.

It should be stressed that the experimental and theoretical results show a remarkable degree of agreement concerning energy onset as well as dispersion. A discernable deviation can only be noticed along the [100] direction at higher $k_{||}$ values, which can be attributed to the aforementioned divergence from the high-symmetry line when using a single photon energy. At the center of the BZ lies the TSS with its isotropic, linear dispersion up until $E - E_\text{F} \approx -0.5\,\text{eV}$, where it merges with the Γ_6-band. At the merging points, a strong influence on this bulk state can be seen even in the coarse overview scan. In the DFT calculation, the band displays a change of slope at the merging points with the TSS. Moreover, in the ARPES data, a sudden decrease in intensity can be seen in the region within these

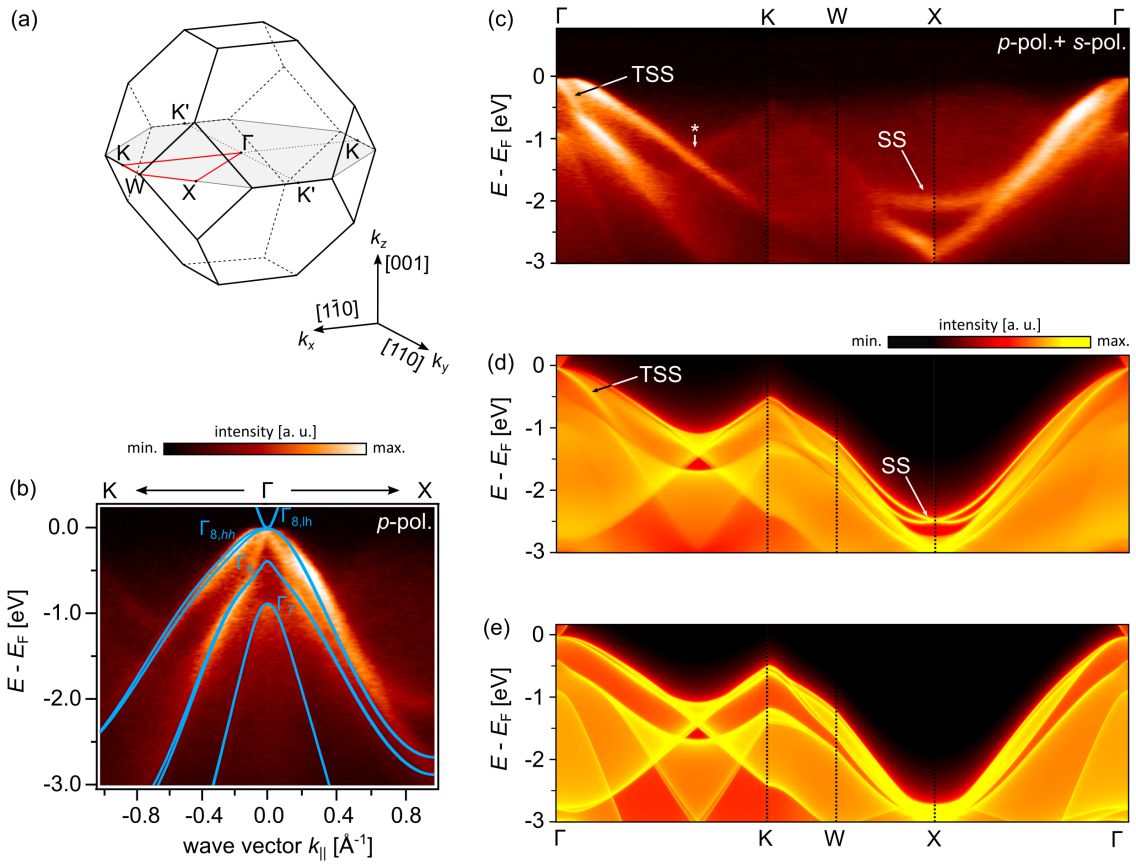

Figure 4.4: Bulk and surface electronic structure along $k_{||}$. (a) First BZ of the fcc crystal structure. The plane probed with $h\nu = 123\,\mathrm{eV}$ is emphasized in grey. The path along which the electronic structure is traced in panels (c)-(e) is marked in red. (b) Band structure along ΓX and ΓK for wave vectors $k_{||} > 0$ and $k_{||} < 0$, respectively. Measurements were taken with *p*-polarized light. The ARPES data is overlaid by the corresponding bulk calculation. (c) ARPES band structure along the high-symmetry path marked in (a). In addition to the TSS at Γ, another surface state can be identified at the X-point. Measurements taken with *p*- and *s*-polarized light were summed up in order to give a more complete visualization of the electronic structure. (d) Semi-infinite surface spectrum considering a Te-terminated surface. (e) Surface projected bulk bands. All ARPES spectra were taken with $h\nu = 123\,\mathrm{eV}$.

merging points. These aspects are addressed in more detail in section 4.4, where the orbital composition of the bulk states will be analyzed.

The evaluation of the electronic structure is complemented by a high-symmetry path shown in Figs. 4.4 (c)-(e). The chosen path Γ-K-W-X-Γ is marked in red in panel (a). The photoemission data shown in (c) comprises data taken with *p*- and *s*-polarized light in order to provide a more complete representation of the electronic structure. The calculated spectra in panels (d) and (e) present the band structure resulting from a semi-infinite approach and the bulk bands projected onto the (001) surface, respectively. In accordance with the results of the LEED analysis, a Te-terminated surface was adopted in both cases. Comparing the two spectra allows for an identification of the states that emerge due to the presence of a surface. In addition to the TSS at Γ, a second **s**urface **s**tate (SS) can be recognized at the X-point, which corresponds to $\overline{\mathrm{M}}$ in the surface BZ. Both features can be recognized in the experimental data. Furthermore, consistent with the ARPES data, all other spectral signatures can be attributed to the bulk.

A side effect of the (001)-projection is the appearance of backfolded bands. In particular, along ΓK, these backfolded bands cross the primary bands at a wave vector corresponding to the boundary of the surface BZ, i.e., at the $\overline{\mathrm{X}}$-point. This effect is also discernable in the ARPES data, albeit with a lower spectral weight of the backfolded bands. The crossing point is marked by an asterisk in Fig. 4.4 (c).

4.3 Influence of $p-d$ hybridization on the valence states

Throughout this chapter, a remarkable match between theory and the experiment could be seen with an excellent agreement regarding the energy onset of the bulk bands and their dispersion. With that in mind, it should be stressed that HgTe proved itself to be a material for which a description of the electronic structure is notoriously complicated [153–155]. This does not merely concern subtleties in the band structure but rather key properties like the size and even the sign of the band gap [154, 156]. This is, in part, due to a pronounced hybridization between the Hg $5d$ semicore levels and the Te p-derived valence states, which has been predicted theoretically but has not yet been demonstrated experimentally [157]. In this section, we will examine the ramifications of this hybridization on the low energy regime and show that a correct description of the Hg $5d$ states is crucial to a proper modeling of the whole valence band ensemble.

The tetrahedral space group T_d^2, inherent to the zinc blende structure, lacks, as stated before, inversion symmetry and, as a consequence, its symmetry representations allow for mixing of orbitals with even and odd momenta, i.e., *p*- and *d*-orbitals, respectively [157].

More explicitly, in the single group T_d the d-orbitals xy, xz, yz and z^2, x^2-y^2 have the symmetry representations Γ_{15} and Γ_{12}, respectively. In the double group, that is, when including the spin degree of freedom, these representations become $S^{-1}\times\Gamma_{15}\rightarrow\Gamma_8+\Gamma_7$ and $S^{-1}\times\Gamma_{12}\rightarrow\Gamma_8$. The cation d-orbitals can thus hybridize with the anion p-orbitals, which inherit the same symmetry representations, whereas they do not interact with the s-orbitals which have the Γ_6 representation. In II-VI semiconductors, this symmetry allowed interaction is combined with shallow cation d-states which lie energetically close to the valence band maximum. Of these transition metal chalcogenides AB (A = Zn, Cd, Hg; B = S, Se, Te), the compounds containing mercury exhibit the least bound cation d-orbitals [158–160]. The primary consequence of the $p-d$ coupling is a repulsion, shifting the valence band states to higher energies [157]. Secondly, the admixing of d-character into the valence states augments the effective SOC, diminishing its coupling strength and reducing the spin-orbit gap.

It thus becomes evident that an accurate description of HgTe has to include a careful treatment of the cation semicore states. Indeed, the correspondence between theory and experiment, established in the previous section, is substantially impaired by the choice of a different functional for the approximation of exchange and correlation.

Fig. 4.5 (a) contrasts the angle-integrated ARPES intensity of the Hg $5d$ levels with calculations based on different exchange-correlation functionals. The photoemission data, taken on an *in situ* transferred sample, and the calculated DOS, using the HSE06 functional, are represented by an orange- and blue-colored graph, respectively. Concerning the energy position, the HSE06 functional yields a decent match to the experimental data. By contrast, the calculated spectra based on LDA and the MBJ functional, depicted in grey and red, respectively, underestimate the binding energy of the Hg $5d$ states considerably. The predicted binding energies according to the LDA+U approach, however, exhibit a severe overestimation for reasonable values of U, that is, values that provide the best possible match in the low-energy valence band region.

Moreover, the experimental data demonstrates a fine structure splitting of the $5d_{5/2}$ and $5d_{3/2}$ lines into three and two components, respectively. This splitting can also be observed in the HSE06-, MBJ-, and LDA-based calculations. The individual components are marked by black lines in Fig. 4.5 (a). The fact that this effect is observable in the DFT calculation implies that it is an initial state effect of the $5d$ levels. The observed fine structure occurs due to a combination of a subband-splitting of the respective level and a finite dispersive character of these subbands. This is evidenced by Fig. 4.5 (b), which depicts the momentum-resolved calculation of the subbands constituting the Hg $5d_{5/2}$ level along ΓK. The assessment is validated by the ARPES data in Fig. 4.5 (c), which depicts the momentum-dispersive Hg $5d_{5/2}$ orbital along a true high-symmetry cut along ΓK, that is, a section extracted from

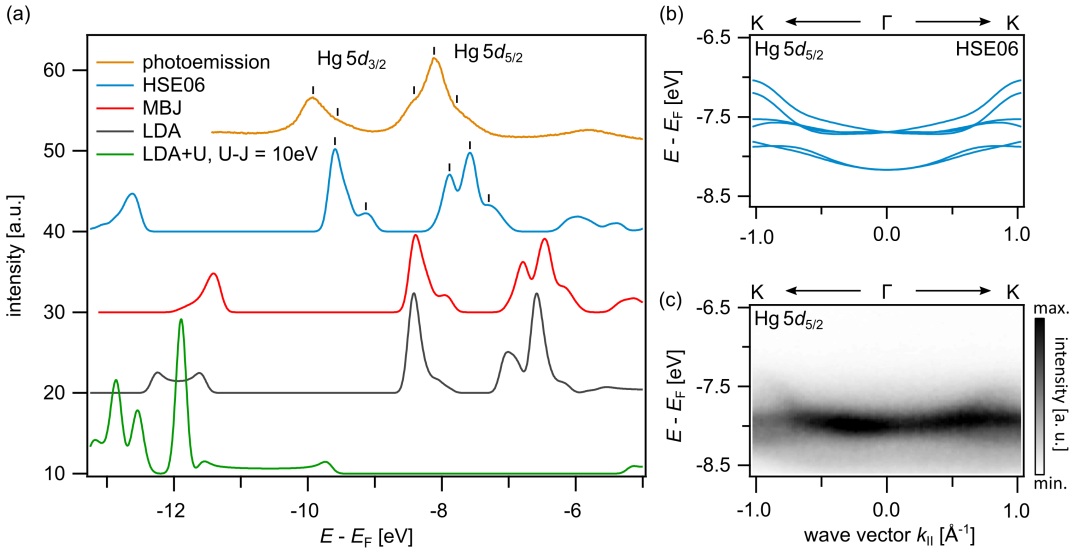

Figure 4.5: Energy position and dispersion of the Hg $5d$ shallow core level. (a) Photoemission EDC taken with $h\nu = 21.2\,\mathrm{eV}$ and density of states resulting from the application of various DFT functionals. The orange curve corresponds to photoemission data taken on an *in situ* transferred sample. Calculations based on the HSE, MBJ, LDA, and LDA+U functionals are depicted in blue, red, grey, and green color, respectively. (b) Calculated dispersion of the Hg $5d_{5/2}$ subshell using the HSE06 functional. (c) Momentum-resolved ARPRES intensity of the Hg $5d_{5/2}$ subshell taken from the k_x-k_z-map in Fig. 4.3 (a). Both panel (b) and (c) correspond to a true high-symmetry cut along ΓK.

a photon energy series converted to k_z. In particular, for $|k_x| > 0.6\,\mathrm{Å}^{-1}$ a spectral feature branches off from the main signal and reaches its maximum at the K-point. This behavior is further highlighted in Fig. A1 in the appendix. There, a set of high-symmetry sections along k_x at selected k_z values systematically show the occurrence of the band maximum of the $\Gamma_{5/2}$-state at the K-points. These maxima thus occur in momentum space at the positions of the global minima of the low-energy valence band states, a behavior that is qualitatively captured by the calculation. The $5d_{5/2}$ level has a total band width of approximately 1 eV, in line with the band width observed in the calculated band structure.

The interplay of the d-band position with the electronic structure of the low-energy valence state is explored in Fig. 4.6. Panel (a) shows the ARPES intensity along ΓK and ΓX for $k_{||} < 0$ and $k_{||} > 0$, respectively, again overlaid by the corresponding bulk bands as obtained from the HSE06 hybrid functional. Panel (b) compares the bulk valence band structure obtained from this calculation with results obtained from the MBJ functional, LDA, and LDA+U. All the band gaps are summarized in Tab. 4.1 for a more concise presentation. Furthermore, Fig. A2 in the appendix shows the superpositions of the individual functionals with the photoemission spectrum to provide an additional way to compare the data.

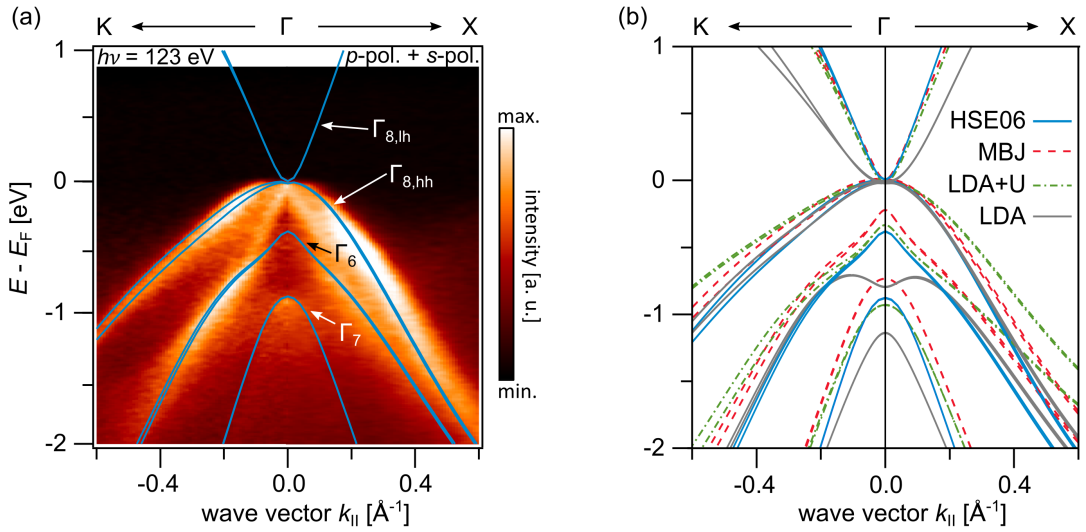

Figure 4.6: Valence band dispersion along the high-symmetry directions ΓK and ΓX. (a) Photoemission intensity band structure measured with $h\nu = 123\,\mathrm{eV}$ and p-polarized light. The data is overlaid by the bulk band calculation implementing the HSE06 functional. (b) Calculated bulk band structure applying various DFT functionals.

The MBJ functional underestimates the band offsets, thereby shifting the Γ_7- and Γ_6-states to lower binding energies. Away from Γ, the observed trend is continued and the bands appear less steep than their HSE06 counterparts, placing them energetically above the latter.

The bare LDA calculation, on the other hand, produces a sizeable overestimation of the energetic difference $\Delta E\,(\Gamma_8 - \Gamma_6)$. This shifts Γ_6 below the Γ_7-state, resulting in the diverging band ordering of $\Gamma_8 > \Gamma_7 > \Gamma_6$. The spin-orbit induced splitting $\Delta E\,(\Gamma_8 - \Gamma_7)$, however, is slightly underestimated. Both effects can be explained by an overestimation of the $p-d$ hybridization by the LDA calculation. This shifts the p-derived valence band states to higher energies, effectively placing the Γ_6-state below Γ_7. Additionally, the enhanced admixture of d-character into the Te p states decreases the effective SOC [157].

functional	$\Delta E\,(\Gamma_8 - \Gamma_7)$ [eV]	$\Delta E\,(\Gamma_8 - \Gamma_6)$ [eV]
HSE06	0.87	0.37
MBJ	0.74	0.23
LDA	0.77	1.12
LDA+U	0.91	0.3

Table 4.1: Compilation of the direct band gaps at Γ for the considered functionals. The values correspond to the calculated bulk bands shown in Fig. 4.6 (b).

This may be mitigated by introducing a Hubbard on-site energy U into the calculation that counteracts the overestimation by artificially pushing the d-levels to higher binding energies. The effect on the Hg $5d$ states is apparent in Fig. 4.5 (a). With this tunable parameter, the experimentally observed band ordering can be recovered, although the calculation loses its strict *ab initio* quality. A value of $U-J=10\,\mathrm{eV}$ has been used to reproduce the experimentally observed band positions. Away from Γ, however, the dispersion diverges from the ARPES data and was captured more accurately by the bare LDA.

This shows that a LDA+U approach is not sufficient to replicate the experimentally observed electronic structure. It improves on the weaknesses of the LDA, at the cost of a loss of performance in other areas. The external parameter also makes it unsuitable for drawing quantitative conclusions from it. The MBJ correction to the LDA formalism provides an alternative in the form of a semilocal approximation of the exact-exchange potential [109]. It is generally considered capable of capturing the band gaps of solids rather accurately while maintaining the computational inexpensiveness of the LDA calculation [111, 161].
Lastly, the HSE calculation is based on a hybrid functional in which a screened Coulomb potential is employed to calculate the HF exchange [110, 162]. This accelerates the spatial decay of the HF exchange and keeps the calculation efficient by limiting the description of the HF exchange to its short-range component [163]. Of the considered functionals, this is the only one to accurately describe both the Hg $5d$ levels as well as the low-energy valence band states.

Furthermore, all calculations show a spin splitting of the states away from Γ, which is not resolved by the measurement. This splitting is particularly pronounced in the $\Gamma_{8,\mathrm{hh}}$-band along ΓK and is the consequence of a previously mentioned but not discussed phenomenon, called the Dresselhaus effect. It occurs in systems, which combine SOC with **b**ulk **i**nversion **a**symmetry (BIA) and was first described for the zincblende crystal structure [164]. In the absence of spatial inversion symmetry, the constraint on the energy solutions ε, which linked a state with electron spin $\uparrow$ at $\boldsymbol{k}$ to a state with the same spin orientation at $-\boldsymbol{k}$, is lifted:

$$\varepsilon\left(\boldsymbol{k},\uparrow\right)\neq\varepsilon\left(-\boldsymbol{k},\uparrow\right). \tag{4.1}$$

In the presence of SOC, the spin degeneracy can thus be lifted which allows for the emergence of spin-polarized states.

Therefore, the Dresselhaus effect is a result of the combination of BIA and SOC. It is closely related to the Bychkov-Rashba effect, in which the asymmetry originates from **s**tructural **i**nversion **a**symmetry (SIA), i.e., either from the bulk asymmetry of uniaxial systems or from the breaking of translational symmetry due to the presence of a surface [165, 166].

The number of lifted degeneracies and the magnitude of the splitting depends on the considered lattice direction as well as on the particular band and its symmetry [164]. For the Γ_8-band and the [110] direction, the linear terms of the energy splittings ΔE_{D}, close to the Γ-point, can be described by:

$$\Delta E_{\mathrm{D,hh}} = \left(3\sqrt{3}/2\right) C_{[110]}\, k_x \quad \text{and} \quad \Delta E_{\mathrm{D,lh}} = \left(\sqrt{3}/2\right) C_{[110]}\, k_x, \tag{4.2}$$

where the two solutions correspond to the splittings of the heavy- and light-hole bands, respectively [167, 168]. It has been shown that these terms arise due to an admixture of d orbital character into the low energy valence states and that the coefficient $C_{[110]}$ can be approximated as [156, 167, 169]:

$$C_{[110]} = -A\,\frac{\Delta_{d,c}}{E(\Gamma_8) - E_{d,c}}. \tag{4.3}$$

Here, $E(\Gamma_8)$ is the energetic position of the Γ_8-band at $\boldsymbol{k} = 0$, and $E_{d,c}$ and $\Delta_{d,c}$ correspond to the energy position and the spin-orbit splitting of the cation d-states, respectively. The material parameter A has been estimated to 350 meVÅ for II-VI compounds [167]. This approximation allows the splitting of the Γ_8-state to be derived from quantities observable in the experiment.

Extracting the energy positions of the Hg $5d$ states from the data presented in Fig. 4.5, one can thus estimate the spin-orbit induced energy splitting of the p-derived low energy states. Using the values summarized in Tab. 4.2, we obtain $C^{\mathrm{exp}}_{[110]} = 80\,\mathrm{meV}$ and $C^{\mathrm{theo}}_{[110]} = 87.5\,\mathrm{meV}$, for the coefficients calculated based on ARPES measurements and the HSE calculation, respectively. It should be noted that the energetic position of the Γ_8-state cannot be precisely extracted from the photoemission data because, on the one hand, the band is overlaid by the strong signal from the TSS and, on the other hand, it may be truncated at the Fermi energy. Consequently, the experimental value should be treated as an upper limit.

The qualitative match reflects the previously observed agreement between the photoemission data and the HSE06 calculation. Furthermore, the formula shows the possibility to

method	$\Delta_{d,c}$ [eV]	$E_{d,c}$ [eV]	$E(\Gamma_8)$ [eV]
ARPES	1.85	8.1	0
HSE	1.9	7.6	0

Table 4.2: Compilation of the experimental and theoretical values for $\Delta_{c,d}$ and $E_{d,c}$, extracted from the data shown in Fig. 4.5 (a). The top of the Γ_8-band is located at E_{F} in the calculated spectrum and was assumed likewise in the ARPES data. For the latter, the value should therefore be regarded as a lower limit.

determine non-resolvable parameters from observable quantities of the experiment. Unfortunately, the value resulting from the HSE06 calculation $C^{\text{theo}}_{[110]}$ can not be directly compared to the linear splitting of the $\Gamma_{8,\text{hh}}$-band since the latter is additionally affected by the biaxial tensile strain the system is subject to.

4.4 Orbital composition of the bulk electronic structure of HgTe(001)

Analyzing the orbital symmetries enables a deeper understanding of the mechanisms of electronic correlation and their impact on the electronic states. The surface states of systems with strong SOC, for instance, exhibit intricate orbital textures, which can be evaluated as a fingerprint of the underlying physics [170–172]. Having a system with non-trivial band topology, we will focus on the orbital contributions to the bands subject to the band inversion. The symmetry of the initial state is experimentally accessible from ARPES in the form of dipole selection rules, the details of which were introduced in section 3.1.2 and will be briefly summarized in the following.

The transition probability and thus the measured emission current in the photoexcitation process is dependent on the product of the irreducible representations of the initial state $|\Psi_\text{i}\rangle$, the final state $|\Psi_\text{f}\rangle$, and the perturbation operator $\mathcal{H}_\text{int}$. This complex problem can be facilitated given a proper choice of simplifying assumptions (see Sec. 3.1.2). On the one hand, the transition matrix element can be expressed as $M_\text{f,i} \propto \langle\Psi_\text{f}|\boldsymbol{A}\cdot\boldsymbol{p}|\Psi_\text{i}\rangle \propto \langle\Psi_\text{f}|\boldsymbol{\varepsilon}\cdot\boldsymbol{r}|\Psi_\text{i}\rangle$, where $\boldsymbol{\varepsilon}$ is the directional unit vector along the polarization of the vector potential $\boldsymbol{A}$, $\boldsymbol{p}$ is the momentum operator and $\boldsymbol{r} = (x,y,z)^\text{T}$. On the other hand, symmetry constraints on the experimental geometry can be exploited, resulting in simplified selection rules. If both the POI and the detector slit of the analyzer are oriented parallel to a mirror plane of the crystal, there are only two possible irreducible representations: even and odd, with respect to the mirror plane. Overall, the integrand of the overlap integral $M_\text{f,i}$ has to be of even symmetry in order to yield a non-zero transition probability. Furthermore, the final state must exhibit even symmetry, since it would be undetectable by the analyzer if it had a node in the mirror plane [74]. This leaves the condition of the same parity for the initial state and the operator, i.e., $|\Psi_\text{i}\rangle$ and $\boldsymbol{A}\cdot\boldsymbol{p}$ are both either of even or odd symmetry.

For linearly polarized light, the incident photons can be either of *p*- or *s*-polarization, which exhibit even and odd parity with respect to the POI and thus to the mirror plane, respectively. Combined with the symmetry rule deduced above, this yields two scenarios

which can be summarized as:

$$\langle \Psi_\mathrm{f} | \boldsymbol{A} \cdot \boldsymbol{p} | \Psi_\mathrm{i} \rangle \begin{cases} p\text{-pol.}, \boldsymbol{A} \cdot \boldsymbol{p} \text{ even:} & \langle e|e|e\rangle \rightarrow |\Psi_\mathrm{i}\rangle \text{ even} \\ s\text{-pol.}, \boldsymbol{A} \cdot \boldsymbol{p} \text{ odd:} & \langle e|o|o\rangle \rightarrow |\Psi_\mathrm{i}\rangle \text{ odd,} \end{cases} \tag{4.4}$$

where e and o symbolize entities with even and odd symmetry, respectively.

In the zincblende crystal structure there exist six mirror planes, which are the $\{110\}$ planes of the lattice. With the (001) surface under consideration, this leaves the (110) and the $(1\bar{1}0)$ planes as applicable mirror planes for symmetry considerations of linear polarization-dependent ARPES. Fig. 4.7 (a) schematically displays the experimental geometry. The definition of the wave vector components is given along with the corresponding crystallographic directions. Light incidence is along the x-direction at an angle of $\gamma = 54.75°$. The POI and the analyzer slit both lie in $\mathcal{P}_{xz}$, which in turn coincides with the (110) plane of the crystal. The orientation of p- and s-polarization is indicated by a yellow and red arrow, respectively. Fig 4.7 (b) displays a CEC taken with p-polarized light at an energy $E - E_\mathrm{F} = -1\,\mathrm{eV}$. The white lines indicate the boundaries of the bulk BZ. In the center, two spectral signatures can be seen, the outer one exhibiting a diamond-like shape, whereas the inner feature shows a more circular structure. These two features can be attributed to the Γ_8- and Γ_6-band, respectively. The maximum of the Γ_7-state can be recognized as a faint rise in intensity at the center of the BZ. The corresponding band structure along ΓK is shown in panel (d). An intricate momentum-dependent intensity variation of the spectral weight of the bulk bands can be seen. The topmost Γ_8-state, for instance, is primarily visible in the vicinity of $k_x = 0$, exhibits a swift decay in intensity for larger wave vectors and is finally no longer discernable for $|k_x| > 0.5\,\mathrm{Å}^{-1}$. The Γ_6-band has a pronounced maximum in intensity for small but finite k_x, while it is nearly imperceptible within the branches of the TSS. Similar to the Γ_8-band, it exhibits diminished weight towards the boundary of the BZ. Lastly, the split-off state Γ_7 shows an overall rather low spectral weight, with a maximum in its intensity at $k_x = 0$.

In the same vein, a CEC at $E - E_\mathrm{F} = -1\,\mathrm{eV}$ as well as the electronic structure along ΓK is displayed for s-polarized light in Figs. 4.7 (c) and (e), respectively. In panel (c), the same electronic features can be seen as in the case of p-polarization, albeit with differently distributed spectral weight. Here, the Γ_8-band shows enhanced intensity along $k_y = 0$, whereas in the perpendicular direction, along $k_x = 0$, the intensity is significantly reduced. The Γ_6-band is overall only weakly defined with a slight increase in intensity along $k_y = 0$. The ARPES intensity along ΓK, shown in panel (e), mirrors these findings. The most prominent feature is the Γ_8-band up to the edge of the BZ, while the Γ_6-band is faintly visible at small but finite wave vectors. Similar to the case of p-polarized light, the Γ_6-state exhibits reduced

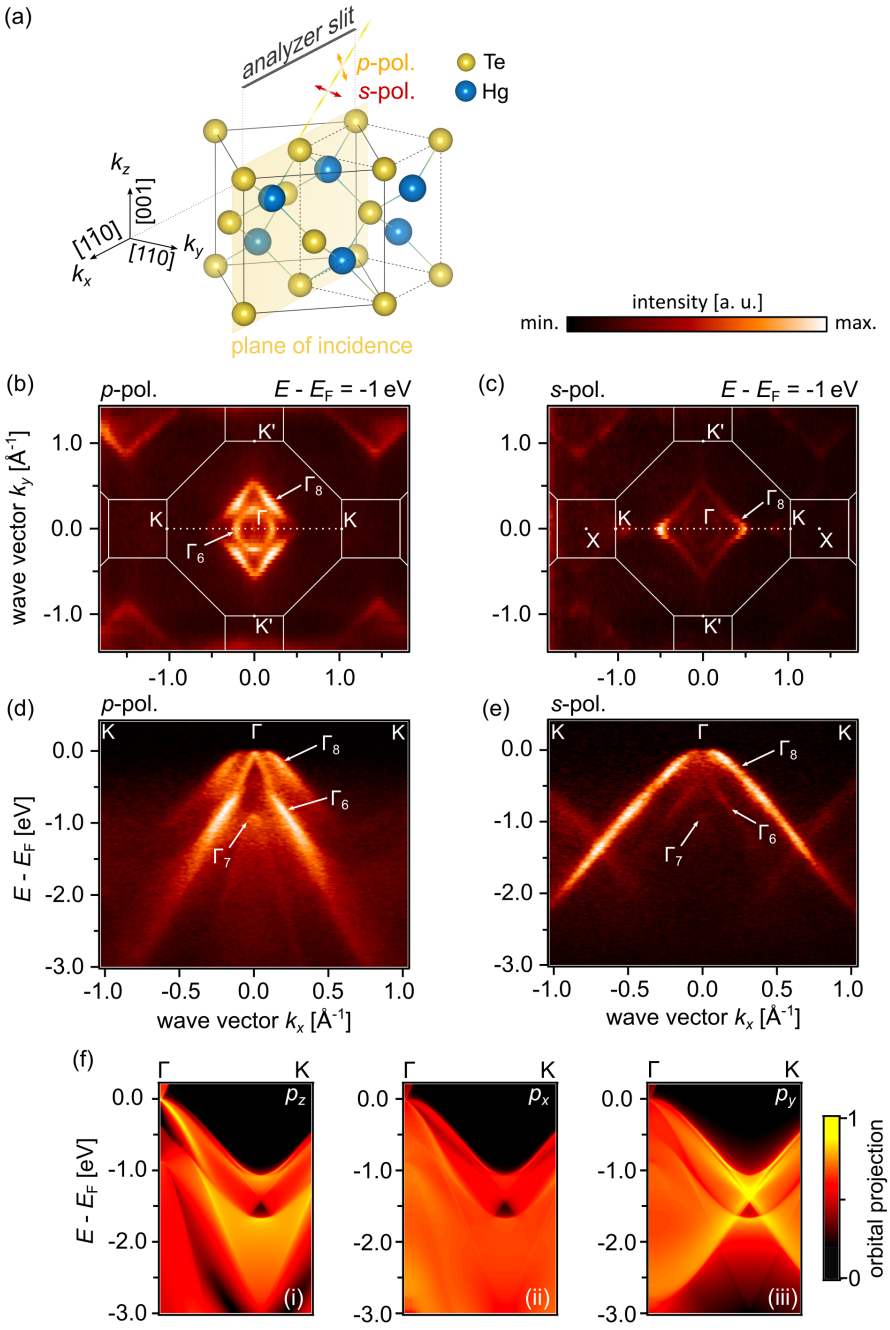

Figure 4.7: Orbital symmetry along the (110) direction of HgTe. (a) Schematic depiction of the geometrical arrangement of the experiment. The notation of the wave vector components is given along with the corresponding crystal directions. The analyzer slit is oriented parallel to the plane of incidence, which in turn coincides with the (110) mirror plane of the crystal. The crystal model was created by the program described in Ref. [139]. (b), (c) CEC at $E - E_F = -1\,\mathrm{eV}$, measured with p- and s-polarized light, respectively. The white lines mark the boundaries of the bulk BZ. (d), (e) electronic structure along the KΓK symmetry line marked by the dotted lines in (a) and (b). The spectra in panels (d) and (e) were taken with p-pol. and s-pol., respectively. (f) Surface spectra from the center of the BZ to the K-point, projected onto a Te-terminated surface. Going from left to right, the electronic structure was projected onto Tep_z-, p_x-, and p_y-orbitals.

intensity around $k_x = 0$, i.e., the region enclosed by the TSS, which is not observable with this polarization.

Due to the high intensity of the Γ_8-state, the previously mentioned backfolding is particularly apparent in this case. The crossing can be seen at about $|k_x| = 0.7\,\text{Å}^{-1}$ along ΓK. Likewise, in the corresponding CEC the spectral signature of the first BZ is mapped onto the X-points due to this backfolding effect.

As stated above, *p*-polarized light has even symmetry with respect to the mirror plane $\mathcal{P}_{xz}$, and thus can excite the even orbitals p_x and p_z within this mirror plane. Due to the incidence angle of $\gamma = 54.75°$, the polarization vector of the incoming photons has similar components along *x* and *z*. It is thus not straightforward to make statements, aside from the overall symmetry of the initial state, solely from experiment. In order to disentangle the orbital contributions to the observed spectrum, we examine the calculated surface electronic structure projected on the three orthogonal Te *p* orbitals, shown in Fig. 4.7 (f). The panels (i)-(iii) display the surface electronic structure projected onto p_z-, p_x-, and p_y-orbitals, respectively. Comparing the projections onto the even p_z- and p_x-orbitals with the measurement taken with *p*-polarized light, reveals a striking similarity concerning the key features formulated above. For the p_z-orbitals, the Γ_6-state has its maximal weight beyond the merging point with the TSS, with decreasing intensity towards the K-point. Close to the Fermi level, the most prominent feature is the TSS which has mostly p_z-character and is hardly distinguishable in the projection onto p_x-orbitals. Overall, the surface electronic structure shows comparatively weak contributions from the p_x-orbitals within the considered mirror plane. For the case of *s*-polarized light and the even p_y-orbital, a similar degree of correspondence can be observed, confirming the above assessment of the orbital symmetry. In panel (iii) the most prominent feature is the Γ_8-band with some additional contribution to the surface spectrum from the Γ_6-band away from the center of the BZ.

With the general orbital symmetry of the states established, we now take a closer look at the region of the bulk band inversion, which is located in the vicinity of the maximum of the Γ_6-state. There, a change in the orbital contribution, and thus a sudden attenuation of the spectral weight can be observed in both theory and experiment. Fig. 4.8 (a) shows the second derivative of a detailed spectrum taken with *p*-polarized light along ΓK. The heightened contrast for the curvature of the data enables the tracking of states which would remain elusive in the raw data. In addition to the key features already discussed, the Γ_6-band can be detected branching off at the contact points with the TSS at $k_x \approx \pm 0.12\,\text{Å}^{-1}$ and reaching its maximum at $E - E_\text{F} \approx -0.4\,\text{eV}$. Fig. 4.8 (b) displays the bare photoemission spectrum corresponding to the second derivative shown in (a). The experimental data is overlaid by the calculated bulk band structure. The dispersion near the top of the Γ_6-band nicely mirrors the band maximum unveiled in panel (a). In addition to the measurement taken with

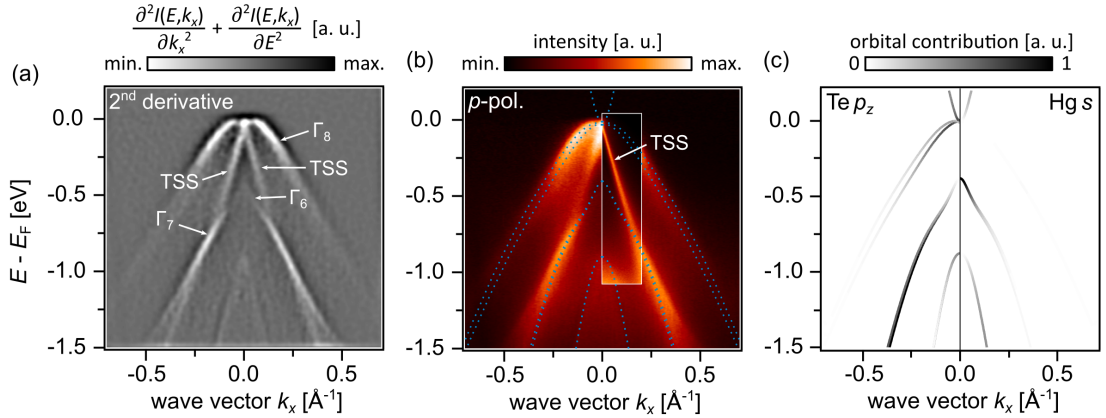

Figure 4.8: Experimental fingerprint and orbital character of the Γ_6 bulk state. (a) The second derivative of the spectrum shown in (b). The enhanced contrast for the curvature uncovers the faint top of the Γ_6-band. (b) ARPES spectrum measured with p-pol. light along the mirror plane (110). The inset depicts the surface spectrum measured with He I$_\alpha$-line (21.2 eV), showcasing the high sensitivity for the TSS at this photon energy. The experimental data is superimposed by the bulk calculation represented by dotted blue lines. (c) Bulk band structure projected onto Te p_z- and Hg s-orbital shown for $k_x < 0\,\text{Å}^{-1}$ and $k_x > 0\,\text{Å}^{-1}$, respectively.

p-polarization and $h\nu = 123\,\text{eV}$, the inset in Fig. 4.8 (b) also depicts the region around the right branch of the TSS for a measurement taken with the He I$_\alpha$-line of a monochromatized gas discharge lamp. This photon energy highlights the linear nature of the TSS and shows its dispersion up to $E - E_\text{F} = -1\,\text{eV}$. Whereas at $h\nu = 123\,\text{eV}$ the TSS slowly subsides before encountering the Γ_6-band and a pronounced kink can be seen at the merging point, the linear dispersion can be traced beyond this point in the He I$_\alpha$ data and appears to continuously merge with the bulk state.

One orbital which is involved in the formation of the valence band ensemble and crucial to the band inversion has been disregarded in the discussion thus far. The Hg 6s orbital exhibits even symmetry and hence should be primarily observable in the measurement taken with p-polarized light, shown in Fig. 4.7 (a) and (b). Instead, this measurement shows an unambiguous match to the surface band structure projected onto the p_z-orbital, with the pronounced signature of the Γ_6-band vanishing when approaching the center of the BZ. Fig. 4.8 (c) displays the bulk band structure projected onto the Te p_z and the Hg s orbital for $k_x < 0$ and $k_x > 0$, respectively. Here, the expected signature of the Hg 6s character can be seen in the Γ_6-state around the Γ-point. In a first approximation, the lack of spectral intensity within this region in the ARPES data is reflected by the difference in atomic cross sections for the Te 5p and Hg 6s states [173].

The projection onto p_z-orbitals on the left reproduces the spectral weight distribution found in (b). In particular, a decrease of the p_z-contribution in the Γ_8-state towards higher

wave vectors and in the Γ_6-state towards small vectors are reflected by the experimental data. This comparison strengthens the above assessment of the p_z-orbital being the main contributor to the ARPES spectrum taken with p-polarization along ΓK.

The sudden drop of the spectral weight of the Γ_6-band towards the Γ-point is accompanied by an increase of Hg 6*s* character, as can be seen in the right section of Fig. 4.8 (c), which links it directly to the bulk band inversion. This becomes apparent when tracing the dispersion of the TSS towards higher binding energies. The TSS merges with the Γ_6-band at the same wave vectors where the latter drops in intensity, that is, where the orbital character exhibits a change from Te p_z to Hg 6*s* character. This characteristic change in spectral weight can thus be considered as a direct experimental fingerprint and a visualization of the momentum-dependent topological band inversion in HgTe.

4.5 Temperature dependence of the chemical potential

Before proceeding to the magnetic compounds in the next chapter, a final remark regarding the temperature dependence of the electronic structure shall be made in this section.

Fig. 4.9 (a) shows the ARPES intensity of an *in situ* grown HgTe(001) sample taken with $h\nu = 21.2\,\mathrm{eV}$ and at $T = 40\,\mathrm{K}$. Panel (b) depicts the corresponding ARPES spectrum taken at $T = 300\,\mathrm{K}$. The Fermi energy, that is the zero position of the energy axis, has been determined for both spectra using a polycrystalline Au-sample. The spectra show a rigid energy shift with respect to each other. As a consequence, in the measurement at room temperature, the minimum of the conduction band can be seen, whereas it is absent at low temperatures. According to the calculations, this energy shift can be attributed to a pronounced asymmetry in the DOS $n(E)$ around E_F.

At non-zero temperatures, electrons are thermally excited from occupied to unoccupied states. The temperature-dependent occupation of electronic states follows the Fermi-Dirac statistics $f(E,\mu,T) = \left(1 + e^{E-\mu/k_\mathrm{B}T}\right)^{-1}$, where k_B is the Boltzmann constant and μ is the chemical potential. Due to the conservation of charge, the number of created holes has to equal the number of thermally excited electrons. This condition can be expressed by the occupation number of electrons and holes, given by the integrals [174]:

$$\int_{-\infty}^{\mu} n(E)(1 - f(E,\mu,T))dE = \int_{\mu}^{+\infty} n(E) f(E,\mu,T)\, dE. \tag{4.5}$$

.

If $n(E)$ is not constant, this relation can only be satisfied by an energy shift of the chemical

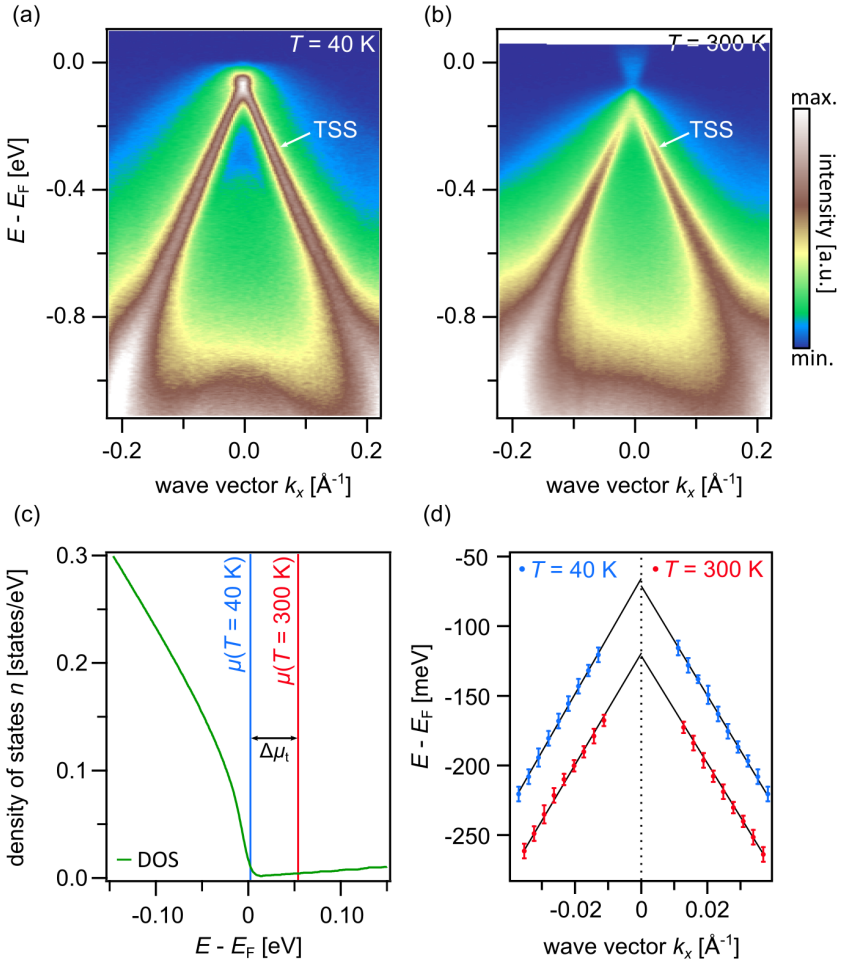

Figure 4.9: Temperature dependence of the chemical potential on HgTe(001). (a), (b) ARPES spectra taken with the He I$_\alpha$-line (21.2 eV) of a monochromatized gas discharge lamp at $T = 40$ K and $T = 300$ K, respectively. (c) The density of states near the Fermi energy. The energetic position of the chemical potential μ at $T = 40$ K and $T = 300$ K is indicated by a blue- and red-colored line, respectively. (d) Temperature-dependent dispersion of the TSS near the $\overline{\Gamma}$-point. Blue and red correspond to the data shown in panel (a) and (b), respectively. The values were extracted using momentum distribution curves and the error bars reflect the read-off error.

potential μ. This shift can be approximated to be proportional to the derivative of the DOS [174]:

$$\Delta\mu(T) \propto \left[\frac{1}{n(E)}\frac{\mathrm{d}n(E)}{\mathrm{d}E}\right]_{E=E_\mathrm{F}}. \tag{4.6}$$

Consequently, the chemical potential will shift towards higher energies for a declining DOS, that is, for $\mathrm{d}n(E)/\mathrm{d}E < 0|_{E_\mathrm{F}}$.

Indeed, the DOS presented in Fig. 4.9 (c) displays a highly asymmetric behavior with a steep decrease at the zero energy. Based on the calculations, an energy shift of $\Delta\mu_\mathrm{t} = 55$ meV

is expected. The energy positions of the chemical potential for $T = 40\,\mathrm{K}$ and $T = 300\,\mathrm{K}$ are indicated by a blue- and red-colored line, respectively. Similar shifts have been observed in Bi_2Te_2Se and FeSe [174, 175].

To compare this theoretically predicted shift with the experimentally observed one, the exact energetic position of the Dirac point is determined for both ARPES spectra. The Dirac point was chosen as the experimental fingerprint of the shift due to a lack of clearly observable signatures of the bulk states. Fig. 4.9 (d) displays the dispersion of each of the branches of the TSS near the Γ-point and up to the energy where the two branches cannot be differentiated from each other. The values were extracted using momentum distribution curves and the error bars reflect the read-off errors. A manual readout was chosen instead of curve fitting because, in addition to the TSS, a background signal of the bulk states is present, complicating the fitting of the individual line profiles. The projected energy position for each branch and temperature is determined by the respective regression line, shown in black in panel (d), whereas the errors are derived from the lines of minimal and maximal slope and are then treated by Gaussian error propagation. This results in an energy shift of $\Delta\mu_\mathrm{e} = (53 \pm 10)\,\mathrm{meV}$, which is in agreement with the theoretically predicted value.

This observation has strong implications on the transport properties of HgTe, which are highly susceptible to a relocation of the chemical potential. In addition to the requirement of low temperatures due to the small energy gap between the Γ_8-bands, attention must also be paid to the doping level of the system, otherwise, the chemical potential may no longer lie within the transport gap at the desired temperature.

Magnetic and electronic structure of $(MnBi_2Te_4)(Bi_2Te_3)_n$

5

The last chapter illuminated the key spectroscopic properties of a time-reversal invariant three-dimensional TI by examining tensile-strained HgTe. This spectroscopic investigation allowed to directly observe the change in orbital character associated with the band inversion as well as the presence of the TSS. Furthermore, it was shown that a theoretical description can prove challenging even for well-known systems and that a comprehensive understanding requires an accurate comparison of theory and experiment. States of higher binding energy like the Hg $5d$ states exert significant influence on the energetics of the valence band ensemble and should therefore be taken into account in a thorough description.

This chapter now examines the behavior of the electronic states of a topological insulator under the long-range ordering of magnetic moments. Since the states participating in the band inversion in the $(MnBi_2Te_4)(Bi_2Te_3)_n$ systems are both of p_z-character, there is no spectroscopic access to the change in orbital character and, therefore, the focus of the following sections will mainly lie on the TSS itself. The magnetic order is expected to break the TRS and, consequently, to break the protection of the Dirac point and to allow for the opening of a mass gap.

Hence, the d-states, in this case Mn $3d$, are again of vital importance for the states near the Fermi level. They provide the magnetic moments responsible for the (anti-)ferromagnetic ordering in the system and are energetically located much closer to the Fermi level than in the previous case. For this reason, after a brief introduction of the material family in chapter 5.1, the $3d$-states are explicitly studied by photoemission and absorption-based techniques in chapter 5.2, where both the electronic and magnetic properties are characterized. The last sections in chapter 5.3 present the spectroscopic investigation of the electronic states in momentum space. There, termination- and temperature-dependent aspects of the surface electronic structure are illuminated. The former are elaborated based on the TSS of $MnBi_4Te_7$, which is analyzed in detail, while the latter is discussed based on the surface electronic structure of $MnBi_2Te_4$.

5.1 Crystal structure and general properties of $(MnBi_2Te_4)(Bi_2Te_3)_n$

In past as well as in contemporary research, van der Waals materials have attracted scientific interest due to their striking electronic properties combined with a layered crystal structure, which facilitates the means of tuning the material properties like thickness control, doping, intercalation, or proximity effects [176–178].

The chalcogenide semiconductor $MnBi_2Te_4$, the progenitor of the heterostructural series investigated in the following sections, consists of **s**eptuple **l**ayers (SL), which are bonded to each other by van der Waals forces. These SL, in turn, comprise seven monoatomic layers with stacking sequence Te-Bi-Te-Mn-Te-Bi-Te, which are stacked along the crystallographic c-axis in a rhombohedral fashion, i.e., ABC-stacking order. $MnBi_2Te_4$ exhibits the $A^{IV}Bi_2Te_4$ structure type, where A^{IV} = Ge, Sn, Pb, which crystallizes with $R\bar{3}m$ symmetry (space group no. 166) [135, 179, 180]. Furthermore, this ternary compound is closely related to the binary layered 3D TI Bi_2Te_3, which is apparent in an alternative description of the system, where the central Te-layer in Bi_2Te_3 is substituted by an arrangement of edge-sharing, Mn-centered octahedra. The stacking sequences of selected members of the modular series are depicted in Fig. 5.1. As is the case for Bi_2Te_3, the unit cell of $MnBi_2Te_4$ consists of three SL due to the ABC-stacking order.

According to theoretical predictions, the system merges topological non-trivial behavior, known for heavy elements like Bi, with the ordering of magnetic moments provided by the transition metal Mn. Like in Bi_2Te_3 and related compounds, the band inversion occurs at the Γ-point between states with Bi p_z^+ and Te p_z^- orbital character [44]. Preceding theoretical studies predicted an antiferromagnetic long-range order of the magnetic moments below a Néel temperature of about $T_N = 24\,K$ [10, 181]. This ground state is expected to exhibit A-type AFM ordering, which implies out-of-plane ferromagnetic intralayer coupling paired with antiferromagnetic coupling between neighboring SL via superexchange [133, 182]. While TRS is broken in such a system, it is simultaneously invariant under the $S = \mathcal{T}\mathcal{L}$ symmetry, which comprises a combination of a time-reversal operation $\mathcal{T}$ and a primitive lattice translation $\mathcal{L}$. Thus, it can be classified by a $\mathbb{Z}_2$ topological invariant. Due to the out-of-plane orientation of the magnetic moments, the (0001) surface does not preserve the S symmetry and a gapped TSS is expected within the magnetically ordered regime.

Because of the strong intralayer exchange coupling, a single SL is predicted to act as a 2D ferromagnet irrespective of the details of its vicinity [182]. In addition, while the van der Waals gaps provide a facilitated approach of sample preparation via exfoliation, they also enable a means of modifying the magnetic and topological properties by intercalating other van der Waals materials and thus creating heterostructures [26, 27]. This idea is put into

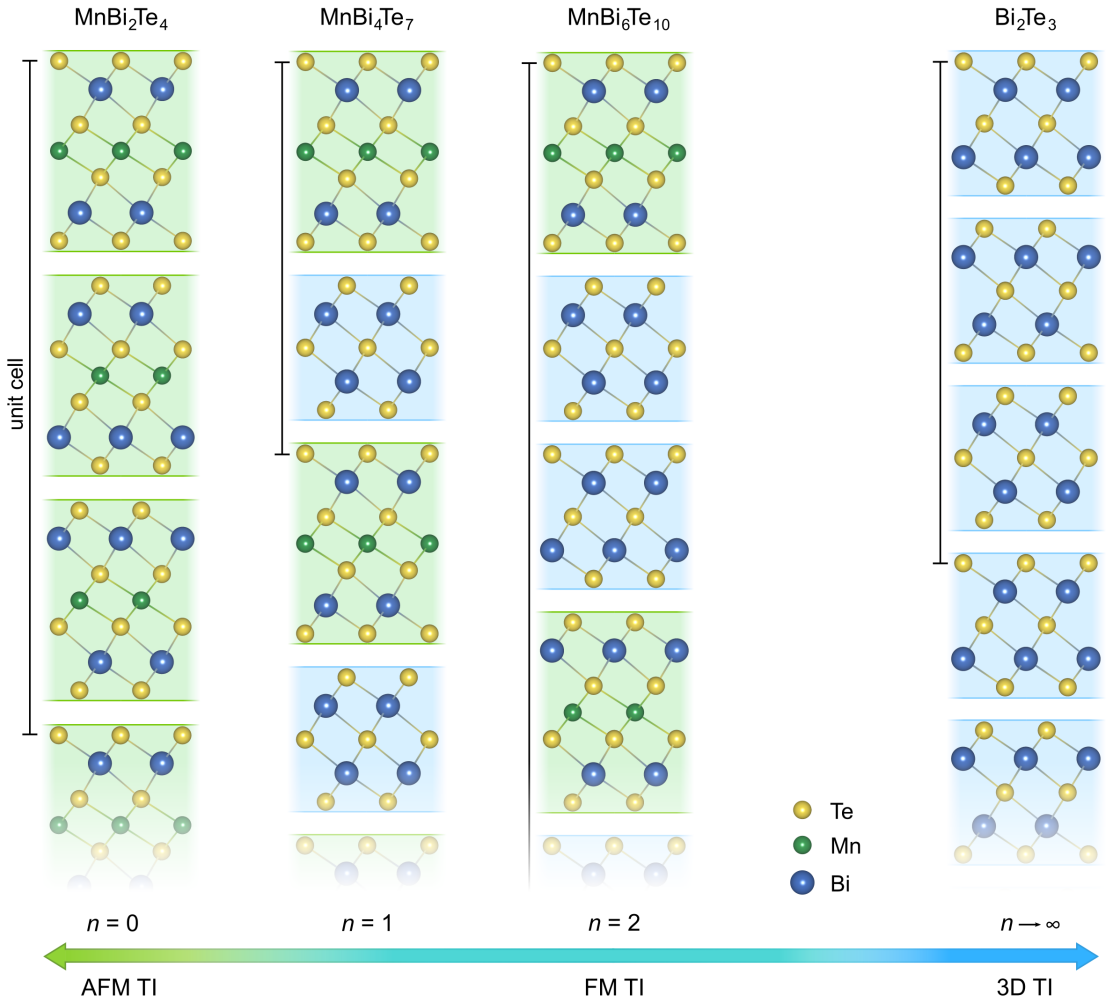

Figure 5.1: Depiction of the crystal structure of selected members of the modular series $(MnBi_2Te_4)(Bi_2Te_3)_n$. SL and QL are emphasized by green and blue color, respectively. The index n, which indicates the number of intercalated Bi_2Te_3 QL, is increasing from left to right. Starting with $MnBi_2Te_4$ and followed by $MnBi_4Te_7$ and $MnBi_6Te_{10}$, the series eventually concludes with the 3D TI Bi_2Te_3. At the bottom, the expected phase of the material is indicated. The intercalated QL augment the magnetic ground state of the system from an AFM ordering via a FM phase to a non-magnetic ground state.

practice in the modular series $(MnBi_2Te_4)(Bi_2Te_3)_n$, where an increasing number of non-magnetic (Bi_2Te_3)-layers is intercalated in the van der Waals gap of two neighboring SL. The first two members, $MnBi_4Te_7$ and $MnBi_6Te_{10}$, occur when one or two **q**uintuple **l**ayers (QL) are intercalated, respectively. Their respective stacking sequence is shown in Fig. 5.1. While the former compound crystallizes in a $P\bar{3}m1$ structure, the latter is of $R\bar{3}m$ symmetry. With the aforementioned ABC-stacking, the unit cells of $MnBi_4Te_7$ and $MnBi_6Te_{10}$ consist of 12 and 51 monoatomic layers, respectively. Regarding the magnetic order, the additional van der Waals layers alter the interlayer coupling of the Mn-containing SL and thus enrich the magnetic phase diagram. Overall, the coupling is weakened by the increased SL-SL distance and the phase transition temperatures of both compounds are consequently lowered. $MnBi_4Te_7$ is expected to exhibit a transition into an AFM state at about $T_N = 13\,K$ with an additional rearrangement of the Mn spins to a state with a net magnetic moment at lower temperatures. On the other hand, $MnBi_6Te_{10}$ shows a **f**erro**m**agnetic (FM) phase below $T_C = 12\,K$ [27]. It is noteworthy that Bi-Mn antisite defects and cation vacancies lead to a slight deviation from the ideal, integer stoichiometry [27, 133].

5.2 Magnetic and electronic properties of the Mn species in $(MnBi_2Te_4)(Bi_2Te_3)_n$

Before the surface electronic structure will be investigated by various ARPES-related techniques in the following section, the electronic and magnetic characteristics of the Mn species in $(MnBi_2Te_4)(Bi_2Te_3)_n$ for $n = 0$ and 1 will be discussed in more detail in this section. In the first part, the electronic properties will be investigated by means of XPS and ResPES, after which the magnetic properties will be explored by the absorption-based approaches XAS, XMCD, and XLD. These partially element-specific approaches enable a selective look at the Mn species, separated from the other elemental constituents. The main focus lies on the progenitor of the heterostructural series, $MnBi_2Te_4$. In addition, the evaluation will be accompanied by corresponding data sets on $MnBi_4Te_7$, highlighting the similarities and disparities within the two systems. The data sets discussed throughout this section were in part published in Refs. [9], [28], [133], and [183].

Fig. 5.2 displays a X-ray photoemission overview scan of the $MnBi_2Te_4$ compound. The photon energy of $h\nu = 1350\,eV$ was chosen as the optimal trade-off between the cross sections of the states of interest and the position of Auger lines within the energy region of the Mn $2p$ states. All the observed lines can be assigned to the elemental species composing the material and are labeled accordingly.

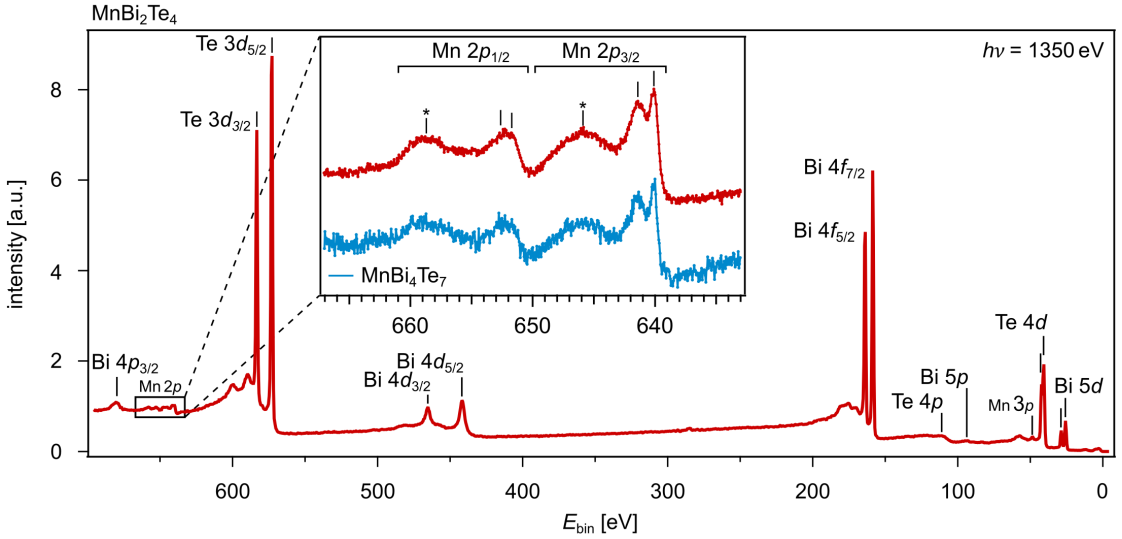

Figure 5.2: X-ray core level survey spectrum of $MnBi_2Te_4$. All the observed spectral lines can be assigned to the elemental species forming the compound. The zoom-in depicts a detailed spectrum of the Mn $2p$ region. Each of the two spin-orbit split $p_{3/2}$- and $p_{1/2}$-subshells displays a threefold splitting, with two relatively sharp features on the low binding energy side and a broader feature towards higher binding energies. Furthermore, a scan of the same energy region of the $MnBi_4Te_7$ compound is appended, exhibiting the same fine structure in its Mn $2p$ lines.

The inset shows a zoom-in on the energy region of the Mn $2p$ states in the form of a detailed spectrum. The spin-orbit split $p_{3/2}$- and $p_{1/2}$-subshells are well separated and each displays an intricate fine structure in the form of a threefold splitting. The fine structure comprises two rather sharp lines towards lower binding energies as well as a broader feature on the higher binding energy side. This spectral line shape is highly reminiscent of the Ni $2p$ lines in the transition metal chalcogenide NiO [184, 185]. There, the various features could be assigned to different photoemission final states. The broad feature, marked with an asterisk, can be attributed to an unscreened final state, whereas one of the low-energy doublets corresponds to a final state where the core hole gets screened by an electron provided by a ligand. Applying this explanation to the present material system, the former, unscreened final state equates to a $2p^5 3d^5$ configuration and the latter to a screened $2p^5 3d^6 \underline{L}$ configuration, where $\underline{L}$ denotes a hole at the ligand site. Although the origin of the partner in the doublet is not entirely undisputed, the conventional explanation attributes the additional feature to a non-local screening scenario in which the core hole gets screened by an electron originating from a neighboring octahedron, which results in $2p^5 3d^6$ for the site hosting the photohole and $3d^5 \underline{L}$ for the adjacent $MnTe_6$ unit. This assessment has been successfully applied to other stochiometric systems containing Mn [186, 187]. Indeed, in systems like $Ga_{1-x}Mn_xAs$ and $Ga_{1-x}Mn_xN$ in a highly diluted scenario, only the features associated

with unscreened and locally screened final states could be observed, whereas the peak related to non-local screening is absent due to a lack of neighboring units containing Mn [188, 189]. It should be noted that the broad feature might include additional minor contributions from final states like $2p^5 3d^7 \underline{L}^2$, whereby the exact weighting of the different contributions depends on the ionicity of the compound [190].

The inset of Fig. 5.2 also depicts the Mn $2p$ core levels of $MnBi_4Te_7$ in blue color. The spectra were taken with identical integration times and are scaled to equal peak areas. The lower signal-to-noise ratio is thus in line with the lower Mn concentration in the heterostructure. Furthermore, the spectrum exhibits the same fine structure as for $MnBi_2Te_4$, which is an indication for the similar chemical environment of the Mn species in both compounds.

From the Mn $2p$ core level we will now turn to the Mn $3d$ states, which lie in the valence band regime and which are investigated via resonant photoemission. The resonant excitation arises due to an additional excitation channel in which a core level electron, in this case from the Mn $2p$ state, is excited into an unoccupied $3d$ valence band state. This excited intermediate state relaxes by an $2p3d3d$ Auger decay. The change of spectral weight of the valence band in the vicinity of the resonant excitation depends on the interference of the discrete autoionization channel and the channel of direct photoemission, as both conclude in the same final state configuration $2p^6 3d^{n-1}$ starting from a $2p^6 3d^n$ ground state.

There are several factors why the $2p$ core level is preferable over the $3p$ state for a resonant excitation of the system. First, the resonance is enhanced in the former case and greatly exceeds the spectral weight contribution from the direct excitation of the valence states. The effect of the interference is thus diminished and the resonant spectrum is dominated by the autoionization channel [191, 192]. Second, the cross sections of the other valence band states in a $2p \rightarrow 3d$ transition are not expected to vary as strongly as in the utilized energy range for the $3p \rightarrow 3d$ resonance. Moreover, according to atomic cross section calculations, the cross section of the shallow Bi $5d$ and Te $4d$ core levels are only expected to vary by about 2% in the energy range between on- and off-resonance for the $2p \rightarrow 3d$ excitation [173]. Thus, these states can be used as a tool to normalize the respective spectra with an adequate accuracy. Last, in contrast to the $3p$ doublet, the $2p_{3/2}$ and $2p_{1/2}$ subshells can be clearly separated due to their higher spin-orbit splitting and the resonances from the L_3 and L_2 edges can be distinguished, facilitating the interpretation of the experimental data. In the following, resonant excitation is performed via the L_3 absorption edge due to its greater spectral enhancement compared to the L_2 edge [193].

Fig. 5.3 (a) shows angle-integrated spectra of the valence band region at various photon energies around the Mn L_3 absorption edge, the XAS spectrum of which is displayed in the inset panel. The energy of the utilized radiation with respect to the Mn L_3 edge is indicated by correspondingly colored arrows. A clear modulation and enhancement of the spectral

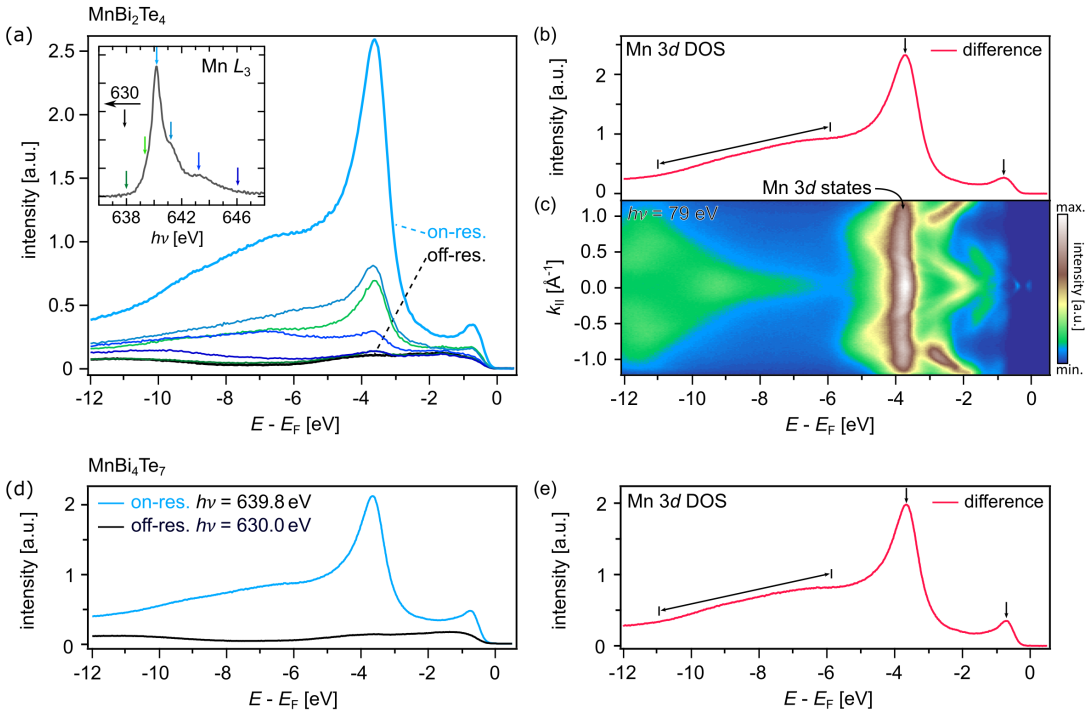

Figure 5.3: Resonant $2p \rightarrow 3d$ excitation of the Mn species in the $n = 0$ and 1 members of $(MnBi_2Te_4)(Bi_2Te_3)_n$. (a) $MnBi_2Te_4$ valence band EDC taken at various photon energies near the Mn $2p \rightarrow 3d$ absorption edge. The inset displays the Mn L_3 absorption edge with colored arrows indicating the excitation energy of the corresponding EDC. (b) Difference of the spectra taken under on-resonant ($h\nu = 640\,\text{eV}$) and off-resonant ($h\nu = 630\,\text{eV}$) conditions. The main contributions to the Mn $3d$ DOS are marked with black arrows. (c) Valence band spectrum of the (0001) surface of $MnBi_2Te_4$ taken with $h\nu = 79\,\text{eV}$. The weakly dispersive Mn $3d$ states are clearly discernable at $E - E_F = -3.7\,\text{eV}$ and are correspondingly labeled. (d) On- and off-resonant valence band regime of $MnBi_4Te_7$ near the Mn L_3 edge. (e) Difference spectrum of the EDC shown in (d). Again, the key features of the difference spectrum are marked by black arrows.

weight distribution can be seen when the incident photon energies match the maximum of the absorption edge, whereas the overall weight from the valence band states is relatively low prior to and beyond the absorption edge. The spectra used as measurements taken under on- and off-resonant conditions are labeled accordingly and equate to a photon energy of $h\nu = 640\,\text{V}$ and $h\nu = 630\,\text{eV}$, respectively. Due to the resonantly enhanced cross section, the contribution to the valence band by the Mn $3d$ states can be estimated by the difference spectrum of the on- and off-resonant spectra, which is shown in Fig. 5.3 (b). The three primary spectral features that comprise the difference spectrum are a relatively small line at $-1\,\text{eV}$, a main peak at $-3.7\,\text{eV}$ as well as a series of broader, not separately discernable features in the energy range of $-6\,\text{eV}$ to $-11\,\text{eV}$. Similar contributions to the Mn $3d$ excitation spectrum were observed in preceding studies investigating the $2p \rightarrow 3d$ and $3p \rightarrow 3d$ reso-

nances in NiAs-type MnTe [192, 194]. There, the different contributions could be attributed to different final state configurations. The first two features at $-1\,\mathrm{eV}$ and $-3.7\,\mathrm{eV}$ relate to a $3d^5\underline{L}$ final state, whereas the broader structure at higher binding energies correspond to a $3d^4$ final state configuration [194, 195]. As before, the $3d^5\underline{L}$ final state originates from a screening of the photo hole by an electron provided by a ligand via a ligand to metal charge transfer.

Overall, the resonantly excited valence band is strongly reminiscent of the Mn $3d$ DOS in diluted semiconductor systems like Mn-doped GaAs and Sb_2Te_3, indicating a localized nature of the transition metal states in the stoichiometric compound [196, 197]. Furthermore, the observed difference spectrum agrees qualitatively with the spin-polarized partial majority DOS of Mn in $MnBi_2Te_4$ derived from DFT calculations [198].

Fig. 5.3 (c) displays the same valence band region as an angle-resolved spectrum taken with $h\nu = 79\,\mathrm{eV}$. The main peak of the resonant data is recognizable as the most intense, weakly dispersive band at the same binding energy. The ARPES data serves to realize that the Mn states are energetically separated from the bulk band gap and thus from the topological surface state, which is faintly visible close to E_F. This will help to exclude scattering processes mediated by the Mn states as a mechanism for the gap opening of the TSS, like it was suggested for Mn-doped Bi_2Te_3 [199].

Panels (d) and (e) display the on- and off-resonance spectra as well as the corresponding difference spectrum for the $MnBi_4Te_7$ compound, respectively. The Mn $3d$ difference matches the spectrum in panel (b) qualitatively, and even quantitatively it differentiates itself mainly by a slightly more pronounced low-energy $3d^5\underline{L}$ peak, reflecting once again the similar chemical environment of the Mn species in $MnBi_4Te_7$ and $MnBi_2Te_4$.

After analyzing the electronic properties of the Mn species as well as the influence of its immediate chemical environment, the second half of this section will be spent examining its magnetic properties. The approaches of choice are the absorption-based spectroscopic techniques XMCD and XMLD, which enable insights on the magnetic ordering using circularly and linearly polarized light, respectively. Similar to the preceding ResPES measurements, these techniques utilize excitations of a core electron to unoccupied valence states and thereby provide chemical and orbital selectivity. As before, the optical excitation will be the $2p \rightarrow 3d$ transition, i.e., via the $L_{3,2}$ absorption edges, which are accessible with photons in the soft X-ray regime.

Fig. 5.4 (a) shows a XAS spectrum of the Mn $L_{3,2}$ absorption edge in $MnBi_2Te_4$, resulting from a summation of spectra taken with left and right circular polarization. For the case of Mn, the exact lineshape of its absorption spectrum is highly dependent on its oxidation state. With the aid of reference data for various manganese fluorides and oxides, the oxidation state of the Mn species in $MnBi_2Te_4$ can be unambiguously assigned to Mn^{2+} [200–202].

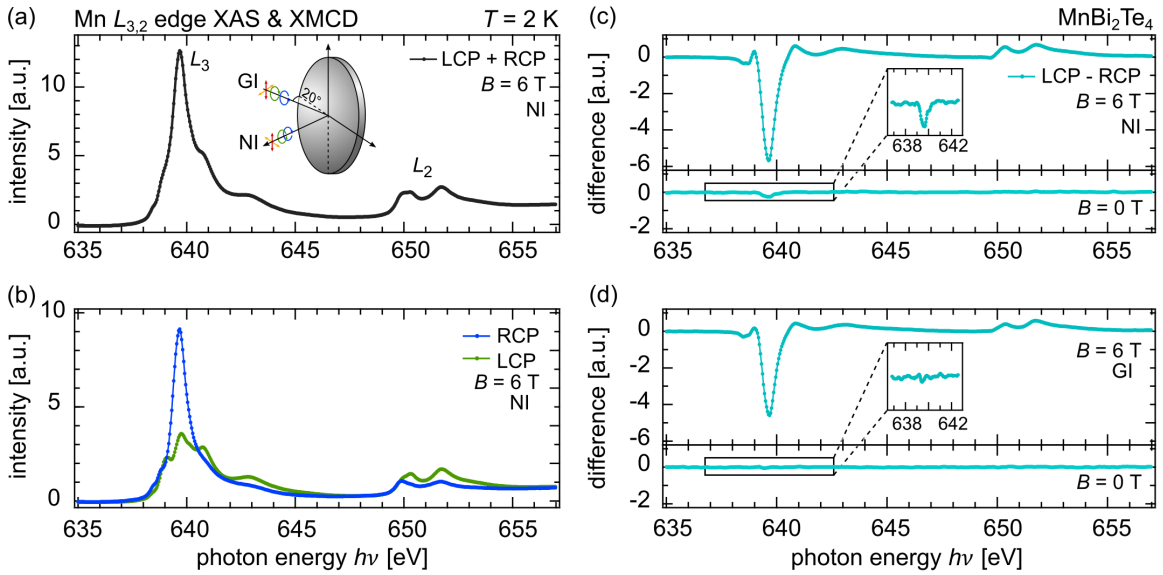

Figure 5.4: XAS and XMCD at the Mn $L_{3,2}$ absorption edge in $MnBi_2Te_4$. (a) XAS spectrum resulting from the summation of spectra taken with left and right circularly polarized light. Furthermore, the inset presents the notation of the light polarization as well as the geometry of the incoming light, which is used throughout this section. (b) Absorption spectra taken with left and right circular polarization depicted in green and blue, respectively. (c) Difference spectra taken in normal light incidence and magnetic fields of $B = 6\,\mathrm{T}$ and $B = 0\,\mathrm{T}$ for the upper and lower panel, respectively. (d) Same as panel (c) in the grazing light incidence geometry. All spectra were taken in the magnetically ordered regime at $T = 2\,\mathrm{K}$. The applied field as well as the geometry of the sample are denoted in their respective panel.

Following the same reasoning, no traceable amount of another Mn species with a differing valency can be observed. Therefore, it can be assumed that the Mn atoms occupying Bi sites via antisite defects retain their valence state.

The branching ratio of the L edges, which differs from the 2:1 ratio of the $2p$ initial state, as well as the complex multiplet structure of the absorption spectrum, arises due to the interaction of the excited valence shell with the created core hole. The multiplet structure matches the predicted multiplet structure of Mn $3d^5$ in an octahedral configuration [203]. The pre-peak just below the L_3 edge as well as the doublet structure of the first L_2 absorption peak can be associated with the strength of the crystal field splitting 10Dq. Their faint but recognizable appearance indicates a small but finite crystal field splitting.

The inset of panel Fig. 5.4 (a) shows a schematic of the experimental geometry that applies to all subsequent XMCD and XMLD spectra. The incident light impinges the sample at either normal incidence or at a grazing angle of 20°. The external magnetic field is always parallel to the axis of the light beam. All spectra presented in this figure were taken at $T = 2\,\mathrm{K}$.

For XMCD, the photon carries an angular momentum which is defined along the propagation direction of the light. During the excitation process, this angular momentum is transferred to the excited electron and can be partially carried as a spin momentum if the excited electron originates from a spin-orbit coupled core state. Since spin flips are forbidden in an optical excitation, the empty d-shell may act as a spin detector if it exhibits a spin polarization. XMCD thus considers a spin-dependent excitation process that probes the number of empty valence states of a given spin, where the quantization axis is given by the magnetization of the d-shell [204].

Fig. 5.4 (b) depicts an exemplary pair of spectra taken with right and left circular polarization in normal emission while applying an external field of $B = 6\,\mathrm{T}$. The differing line shapes and the opposite sign at the two absorption edges already indicate a sizeable dichroism signal and thus the presence of magnetic moments in the Mn species. The corresponding difference signal is shown in the upper part of Fig. 5.4 (c).

Figs. 5.4 (c) and (d) display the XMCD signal under varying external magnetic fields and incidence angles. Combining the information gained from these data sets allows for the deduction of some assertions on the magnetic ordering. Returning to the upper part of panel (c), a substantial dichroism signal of opposite sign is observed for the L_3 and L_2 edges. Looking at the lower part of the same panel, the signal collapses when reverting to remanence, as expected for a system with AFM ordering. It is noteworthy that even in remanence a weak residual dichroism signal can be observed. This shows the existence of a finite remanent magnetization in the probed volume of the sample and is in line with an A-type antiferromagnetic order. In the case of G-type antiferromagnetism, that is, antiferromagnetic intralayer coupling, no remanent signal would be expected because the magnetic moments are compensated on an atomic scale. A finite signal in remanence can be explained by a ferromagnetic intralayer coupling and by the finite and exponentially decaying probing depth of the TEY technique. Two assumptions were made with this statement. Both the size of the magnetic domains and the area of the terraces must not be too small compared to the spot size of the beam, that is, the probed area, since both correspond to an inversion of the magnetization of the topmost layer and would thus lead to a compensation of the measured signal.

Fig. 5.4 (d) displays the corresponding spectra in grazing light incidence geometry. Again, the lower and upper panel depict spectra taken at an external magnetic field of $B = 6\,\mathrm{T}$ and $B = 0\,\mathrm{T}$, respectively. In grazing light incidence, the measurements become mainly sensitive to the in-plane component of the magnetization. Compared to the measurement in normal incidence, there is a sizeable reduction of the dichroism, indicating a preferred orientation along the out-of-plane c-axis. Additionally, the lower panel shows the absence of a quantifiable remanent dichroism in grazing incidence, meaning there exists no

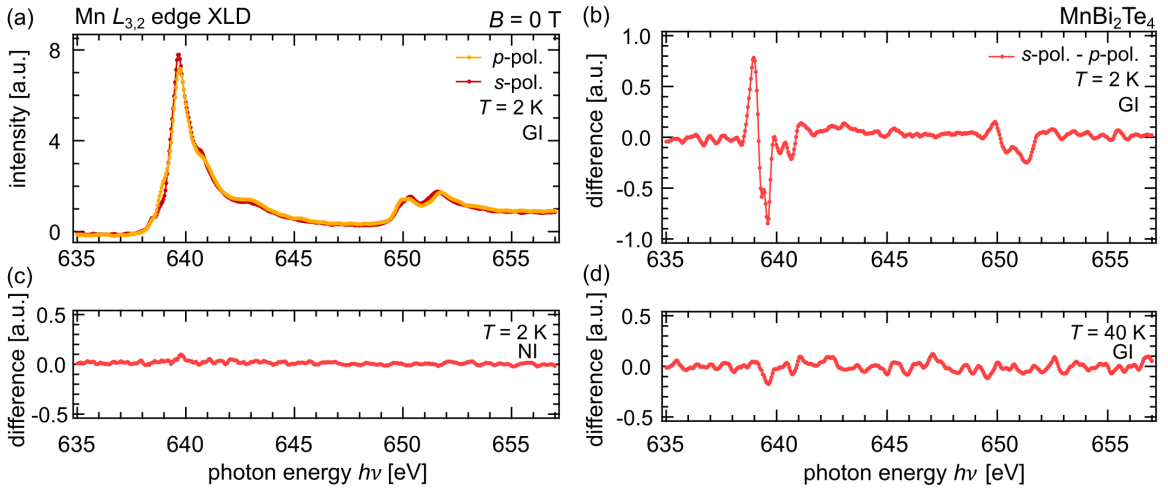

Figure 5.5: XLD at the Mn $L_{3,2}$ absorption edge in $MnBi_2Te_4$. (a) XAS data sets measured with s- and p-polarized light. (b) Difference spectrum obtained in grazing incidence and at $T = 2\,\mathrm{K}$. (c) Difference signal for normal light incidence and within the magnetic ordered phase. (d) Difference spectrum for an elevelated temperature of $T = 40\,\mathrm{K}$ and grazing incidence. All measurements were taken in remanence.

magnetic in-plane polarization in the probed volume. This, in turn, indirectly reinforces the above indication of a ferromagnetic intralayer coupling due to A-type antiferromagnetism, as it rules out that the remanent signal in normal incidence is caused by a measurement artifact. Furthermore, this result is consistent with other scientific studies in which a remanent XMCD signal was also observed [205].

XMCD alone is not a suitable method to study antiferromagnets as they are defined by a ground state with no global net magnetic moment. For this reason, additional XMLD measurements were performed which allow statements on the axial anisotropy of the system, in addition to the directional information provided by XMCD, by sensing anisotropies in the charge density of the valence states.

Fig. 5.5 (a) displays a pair of spectra taken with linear polarization in grazing incidence and at $T = 2\,\mathrm{K}$, well below the magnetic transition temperature. In this geometry, XMLD mainly probes the anisotropy between the out-of-plane direction and an in-plane axis perpendicular to it. Although not as prominent as for the XMCD measurements, a difference between the two curves can clearly be detected in the region of the absorption edges. These, as well as subsequent measurements, were performed without an applied external magnetic field.

The corresponding dichroism spectrum is shown in Fig. 5.5 (b), which confirms the already observed out-of-plane anisotropy of the Mn $3d$ charge distribution. Furthermore, panel (c) displays the dichroism spectrum in normal incidence, that is, the anisotropy be-

tween two perpendicular in-plane axes. Here, no dichroism can be observed, which confirms the c-axis as the sole direction of anisotropy of the charge density of the valence states.

This anisotropy may either arise due to the bonding configuration of the considered element, i.e., by the electrostatic potential, or by the presence of a magnetic ordering. In order to disentangle these two causes, the temperature dependence of the signal can be utilized, since the linear dichroism would persist the magnetic transition if it is caused by the electrostatic potential. Fig. 5.5 (d) shows the corresponding spectrum taken under grazing incidence and at $T = 40\,\mathrm{K}$, well above the magnetic ordering temperature. Indeed, despite the signal exhibiting a noticeably reduced signal-to-noise ratio, the signal collapses and no residual dichroism can be observed. This proves the magnetic nature of the out-of-plane anisotropy seen in panel (b).

The presence of an XLD signal which vanishes at elevated temperatures is a strong sign for AFM order in the system and has been used in the past to detect antiferromagnetism in other compounds [206, 207]. Combined with the geometry- and magnetic-field-dependent XMCD data, this confirms $MnBi_2Te_4$ as an antiferromagnet with an out-of-plane easy axis, as it was predicted in preceding theoretical studies [182]. In addition, strong indications pointing to an A-type spin alignment with ferromagnetic intralayer coupling could be found, which is in line with simultaneously conducted studies [10, 208].

With the AFM ground state established in $MnBi_2Te_4$, we will now turn to the first member of the modular series, $MnBi_4Te_7$. Fig. 5.6 shows XMCD and XMLD measurements at the Mn $L_{3,2}$ absorption edges with parameters equivalent to those in Figs. 5.4 and 5.5. Panel (a) displays spectra taken with right and left circular polarization in normal incidence and at $B = 6\,\mathrm{T}$ and $T = 2\,\mathrm{K}$. Similar to the former compound, a sizeable dichroism can be seen, which switches its primary sign when transitioning from the L_3 to the L_2 edge, demonstrating the presence of magnetic moments in the system. Panel (b) shows the corresponding difference signal in its upper section as well as the dichroism in remanence in its lower part. In contrast to $MnBi_2Te_4$, a significant remanent signal can be seen. The signal strength corresponds to about one-third of the signal in full magnetization, that is, $B = 6\,\mathrm{T}$, and hence shows that $MnBi_4Te_7$ exhibits a low-temperature state with soft ferromagnetic characteristics.

The second part of Fig. 5.6 presents XMLD data on $MnBi_4Te_7$. As before, the data was acquired without a magnetic field. Panel (c) shows spectra taken with p- and s-polarized light, which correspond to the data set with the strongest dichroism signal, i.e., grazing light incidence and $T = 2\,\mathrm{K}$. Fig. 5.6 (d) shows difference spectra in grazing incidence and varying temperatures, which are, from top to bottom, $T = 2\,\mathrm{K}$, $T = 9\,\mathrm{K}$, and $T = 40\,\mathrm{K}$. The series showcases the collapse of the linear dichroism at higher temperatures due to its magnetic origin. The bottom spectrum taken at $T = 40\,\mathrm{K}$ demonstrates, due to a high signal-to-noise ratio, that a finite residual XLD signal can be observed well above the magnetic

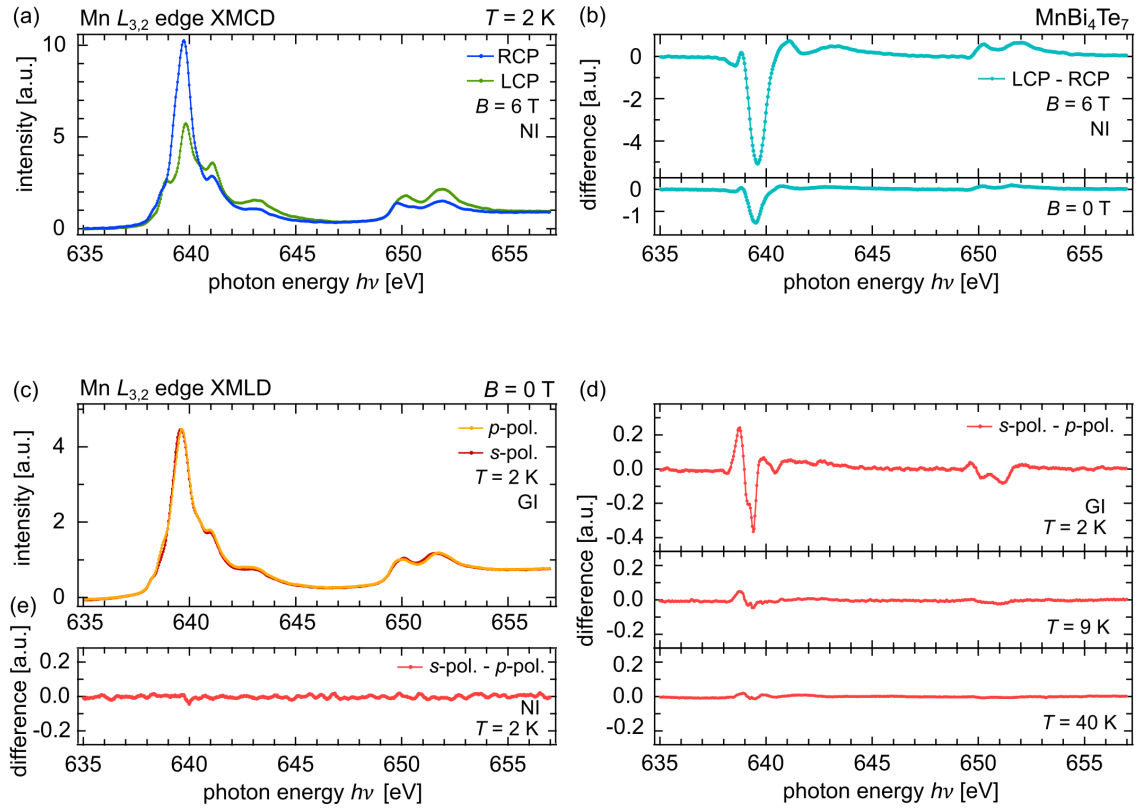

Figure 5.6: XMCD and XMLD at the Mn $L_{3,2}$ absorption edge in $MnBi_4Te_7$. (a) Exemplary absorption spectra taken with right and left circularly polarized light depicted in blue and green, respectively. (b) Dichroism signal taken at $T = 2\,\mathrm{K}$ and in normal incidence. The upper spectrum was taken at $B = 6\,\mathrm{T}$ while the lower one was taken in remanence. The upper curve corresponds to the curves shown in (a). (c) Absorption spectra taken with linear polarization in grazing light incidence geometry and at $T = 2\,\mathrm{K}$. (d) Difference spectra showing the linear dichroism in grazing incidence at various temperatures below and above the magnetic transition. From top to bottom, the panels display spectra taken at $T = 2\,\mathrm{K}$, $T = 9\,\mathrm{K}$, and $T = 40\,\mathrm{K}$, respectively. (e) Dichroism signal in normal light incidence and at $T = 2\,\mathrm{K}$. All XMLD spectra were taken without an external magnetic field.

transition temperature, which is probably due to finite contribution from the electrostatic potential.

At this point, it should be mentioned that the increased noise in some spectra like Fig. 5.5 (d) or 5.6 (e) are not due to a lack of integration time but are caused by an issue of the instrumentation which sometimes occurred. Consequently, these spectra and the statements made on the basis of them must be considered as lower limits, which are limited by the amount of noise. Fig. 5.6 (e) shows the dichroism signal under normal light incidence where once again no dichroism can be observed between the two perpendicular in-plane directions.

Discussion

The data presented throughout this section helped to create an understanding of the role of the Mn species in $MnBi_2Te_4$ and $MnBi_4Te_7$. The Mn $2p$ XPS lineshapes, akin to those found in other transition metal compounds, demonstrate the occurrence of charge transfer in both compounds by exhibiting several satellites which can be attributed to final states with various amounts of screening. In addition to lines corresponding to $2p^5 3d^5$ and $2p^5 3d^6\underline{L}$ final states, another spectral feature occurs, which can be assigned to a non-local scenario where an electron is provided by a neighboring octahedral unit. Similar effects due to charge transfer from the ligand can be encountered in the Mn $3d$ partial DOS, accessed via ResPES. In addition, Mn was shown to occur primarily at a valence of 2+, within the detection limit of XAS, by dispensing its two $4s$ electrons [208]. The remaining five $3d$ electrons fill up the majority spin d-shell according to Hund's rule. All components of the partial Mn $3d$ DOS are well below the Fermi level and thus energetically far away from the bulk band gap. Combined with a large spin splitting of over 7 eV, this ensures that no impurity states exist within the energy range of the topological surface state [10, 198, 209]. This, in turn, allows to exclude a non-magnetic gap opening mechanism due to scattering, which was proposed for compounds where impurity states lie close to the Dirac point [199, 210, 211].

A combination of XMCD and XMLD measurements leads to the conclusion that the magnetic ground state in $MnBi_2Te_4$ forms an antiferromagnetic ordering with an easy axis parallel to the [0001] direction, which is consistent with simultaneously conducted and collaborative studies [9, 133, 208]. Although the low residual remanence signal is not a piece of conclusive evidence for A-type ordering, it is a strong indication and difficult to explain by means of an antiferromagnetic intralayer coupling. The argumentation is further strengthened by the study in Ref. [212] where magnetic force microscopy was utilized to image the mesoscopic size of the magnetic domains as well as by Ref. [205] in which a similar remanent XMCD signal could be observed in $MnBi_2Te_4$.

The ferromagnetic intralayer coupling can be explained by Kramers-Anderson superexchange where two neighboring Mn atoms are connected by a bridging non-magnetic Te anion [213, 214]. The slightly distorted octahedral configuration results in a Mn-Te-Mn bonding angle close to 90° and thus induces ferromagnetic exchange coupling [10]. The interlayer coupling, on the other hand, can likewise be described by super-superexchange where the Mn-X-Mn bond with X = Te-Bi-Te:Te-Bi-Te has an effective bonding angle of 180° and is considerably weaker than the intralayer coupling due to the increased bonding length [25, 215].

$MnBi_4Te_7$, on the other hand, exhibits similar magnetic characteristics with an out-of-plane anisotropy and a ferromagnetic intralayer coupling due to a mostly unchanged single-

ion anisotropy. The main distinction between the two compounds, that is, an ordering with a net magnetic moment in $MnBi_4Te_7$, can be understood by the greatly reduced interlayer exchange coupling due to the intercalation of the non-magnetic (Bi_2Te_3)-layer. This seems to be in in contrast to other studies in which an antiferromagnetic ground state was observed for $MnBi_4Te_7$ and even $MnBi_6Te_{10}$ [216, 217]. One might argue that the surface sensitivity of the TEY detection mode combined with the increased distance of the magnetically active Mn layers leads to an increased effective magnetic moment within the probed volume. However, this argument is negated by studies in which a net magnetic moment could be observed by the use of a superconducting quantum interference device, which is a bulk sensitive method [27, 218]. These studies also showed that a ferromagnetic state is only realized well below the initial magnetic transition temperature of $T_N = 13\,K$ at about $5\,K$. In a synoptic view on the results in other publications, the observed magnetic state seems to depend not only on the temperature but also on the details of the samples, such as Bi-Mn antisite defects [216, 217, 219].

Ref. [220] proposes an explanation for these various observations in the literature. A model is presented that explains the occurrence of a finite remanent magnetization at lower temperatures. According to it, the ground state of an antiferromagnet depends on the relative strengths of the uniaxial anisotropy K and the exchange coupling J. A limiting case analysis reveals a scenario in which a metamagnetic state is formed within the antiferromagnetic phase that exhibits a finite magnetization if the uniaxial anisotropy outweighs the exchange coupling, that is, if $K/J \gg 1$. $MnBi_4Te_7$ corresponds to such a system in which the increased spacing between the SL causes a situation in which the uniaxial anisotropy is the dominating energy scale. With an increasing K/J ratio, the hysteresis loop of the system is expected to show a ferromagnet-like evolution. The fact that K increases with decreasing temperature explains that this phase is only observable at temperatures well below the Néel temperature. Indeed, several studies demonstrate this trend towards a more ferromagnetic behavior for temperatures well below T_N for all compounds with $n \geq 1$ [27, 219, 221–223]. The system thus possesses an intricate magnetic phase diagram with competing FM and AFM ordering, which exhibit varying thermal dependencies [29]. However, the extent of this effect still depends on the exact sample details.

With a further increased SL distance in $MnBi_6Te_{10}$, the ferromagnetic tendencies of $MnBi_4Te_7$ are expected to be additionally favored in this compound [224]. Indeed, it could be shown that, with an increasing number n of intercalated quintuple layers, the later members of the series approach a ferromagnetic order, which ultimately converges towards a stacking of two-dimensional ferromagnets [221].

5.3 Surface electronic structure of $(MnBi_2Te_4)(Bi_2Te_3)_n$

From the magnetic and electronic properties of the transition metal species Mn analyzed in the previous section, we now turn to the characteristics of the first three members of the $(MnBi_2Te_4)(Bi_2Te_3)_n$ series, in terms of their surface electronic structure. Compared to the preceding material system HgTe, in which sample preparation, k_z bulk dispersion, and a demanding theoretical description formed the main obstacles to a comprehensive analysis, these systems pose different challenges to their examination.

First, the heterostructural architecture of the compounds entails the occurrence of distinct surface terminations. Before exploring the rich physics of these systems, it is therefore decisive to find a route to identify these terminations by their spectral features. Second, compared to HgTe, whose spectra showed clearly distinct signatures of its bulk and surface electronic states, the surface spectra of these ternary van der Waals compounds exhibit a rather rich accumulation of electronic signatures which populate a comparatively small region in energy and momentum space. The main object of this section is therefore to disentangle these states, identify the topological surface states, and explore the underlying physics of their interaction. Lastly, the main appeal of these compounds lies in their intrinsic magnetic properties. Despite the high level of interest in current research, an unambiguous observation of the expected spectral behavior of a topological insulator under broken time-reversal invariance remains elusive.

These three aspects will be explored in the segments of this section. While the first part introduces an experimental route to identifying the surface terminations, the second one explores the surface electronic structure of the two terminations of the $MnBi_4Te_7$ compound. Temperature dependencies in the electronic structure are lastly discussed based on $MnBi_2Te_4$. The results presented throughout this section were in part published in Refs. [225], [28], and [183].

The measurements presented in this section were carried out at different experimental facilities. VUV-based synchrotron measurements were conducted at beamline I05 at the Diamond Light source in Oxfordshire. Spin-integrated and spin-resolved spectra were taken at a laser-based μ-ARPES chamber at the Hiroshima synchrotron radiation center and a Laser-ARPES setup at the Forschungszentrum Jülich, respectively. The specifications of each of these setups can be found in chapter 3.4.1.

5.3.1 Termination dependence of the electronic structure

The heterostructural nature of the $(MnBi_2Te_4)(Bi_2Te_3)_n$ series results in $n+1$ distinct ways to terminate the (0001) surface, as the weak van der Waals bonds are of similar strength

and no dominantly occurring termination is expected. This number takes the influence of subsurface layers on the topmost layer into account, which distinguishes the different QL for systems with $n \geq 2$. This situation is analogous to the topological insulator $PbBi_6Te_{10}$, where a set of three Dirac states could be observed, which was attributed to the three occurring terraces in this compound [226]. Therefore, the first step in the analysis of the complex surface electronic structure of these materials is the assignment of the surface spectra to their associated terminations.

The spectra of a theoretical approach such as DFT do not show sufficient quantitative agreement with the experimental data and even show qualitatively contradictory features, making them unsuitable to serve as a tool to assign the corresponding termination [30, 227]. Instead, a purely experimental approach is employed in order to ensure an unambiguous assignment by utilizing a spectral feature of the Mn species as a fingerprint of the topmost vdW layer. Depending on the stacking sequence near the surface, the topmost Mn layer is embedded at different depths within the crystal and spectral signatures originating from this species are damped accordingly. This is illustrated in Fig. 5.7 (a) for $MnBi_4Te_7$, where the outermost Mn atoms are located either $0.23c$ or $0.66c$ from the surface, that is 5.46 Å or 15.66 Å, depending on whether the surface is terminated by a SL or a QL, respectively.

In principle, any spectral feature of Mn could be used for this purpose. However, since the goal is a lateral mapping of the terminations, and since a change in photon energy is often accompanied by a shift in the beam position, it is a key requirement that the measurements of the experimental fingerprint and of the associated valence band structure are performed with a single photon energy. For this reason, strongly bound core levels are unsuitable, since, at the energies required to excite them, the valence band states have small photoexcitation cross sections [173].

As it was shown in the last section, the localized Mn $3d$ states, lying within the valence band region, are observable for different members of the series at equal binding energies. Furthermore, like the valence and surface states, they are observable by photon energies in the VUV range. Fig. 5.7 (b) shows a map of the Mn $3d$ intensity over the lateral coordinates of a $MnBi_4Te_7$ sample surface taken with $h\nu = 52\,\mathrm{eV}$. Apart from dark areas, which are off the sample, there are two main regions with increased and decreased intensity, displayed in green and blue colors, respectively. The corresponding energy distribution curves for two locations within these regions, marked with 1 and 2, are shown in Fig. 5.7 (c). The most prominent signal lies at $E - E_\mathrm{F} = 3.7\,\mathrm{eV}$ and corresponds to the main feature of the Mn $3d$ state. Due to the more attenuated signal of the blue curve, it can be attributed to a QL termination, whereas the green graph, with a more intense feature, corresponds to a termination by a SL.

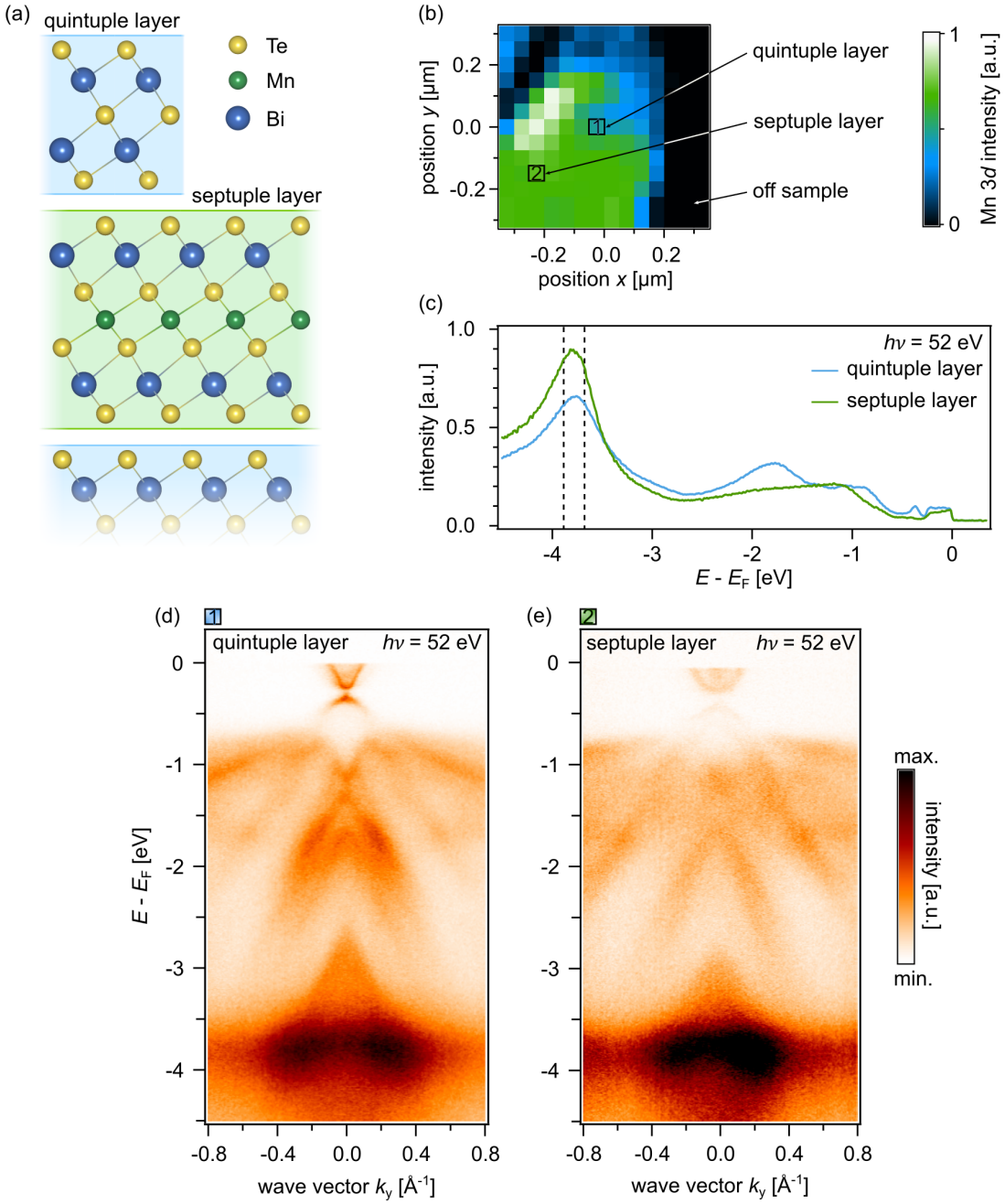

Figure 5.7: Identification of the surface terminations of $MnBi_4Te_7$. (a) Schematic representation of the two possible surface terminations in the form of a quintuple or septuple layer. For the former, the green manganese atoms are buried more than twice as deep within the bulk than for the latter. (b) Laterally resolved intensity of the Mn 3*d* valence state. In addition to areas that are off sample, two other types can be seen that can be identified as quintuple and septuple layers. Two locations on the sample from which the data in panels (c)-(e) were obtained are marked accordingly. (c) Angle-integrated valence band structure of the spots marked as 1 and 2 in (b), which can be identified as a quintuple and septuple layer, respectively. The energy window used for the Mn 3*d* intensity displayed in panel (b) is marked with dashed lines. (d), (e) Angle-resolved valence band spectra of the locations marked as 1 and 2 in panel (b), respectively. All spectra were taken with $h\nu = 52\,\mathrm{eV}$.

The corresponding angle-resolved spectra of this energy region are shown in Figs. 5.7 (d) and (e) for position 1 and 2, respectively. To sides of lower binding energy, beyond the dispersionless Mn $3d$ states, the main section of the valence bands can be seen, which in both cases show similar dispersion, albeit with differently distributed spectral weight. Near the Fermi edge, when approaching the energy gap of the bulk states, the overall intensity decreases and the most prominent features are a set of states centered around the Γ-point. Naturally, these features are mainly comprised of the topological states, and it is here that the main difference between the two spectra can be recognized. For the QL termination, two linearly dispersing branches can be discerned, which merge at $k_x = 0$ and which are separated from the bottom part by a gap. In the case of the SL termination, a more parabolic upper state and a rather faint lower part can be seen.

These data sets now serve as a reference for the subsequent laser-based measurements in which, due to the low excitation energy, no characteristic Mn features are accessible to provide a probe for the terminating layer. Fig. 5.8 displays the comparison for the two surfaces of a $MnBi_4Te_7$ sample. Panels (a) and (b) show a detailed view of the region of interest measured with $h\nu = 52\,\mathrm{eV}$ for the quintuple and septuple layer, respectively. The corresponding data sets taken with $h\nu = 6.3\,\mathrm{eV}$ are displayed in panels (c) and (d). The correspondence of the data sets recorded with different photon energies allows to assign the spectra acquired with laser-based ARPES to their respective termination. This assignment of terminations to the associated spectra is, in part, in contrast to other studies [29], in which the assignment was made based on a comparison with calculated spectra and, as a consequence, spectra showing characteristics of those in panels (a) and (c) were predominantly ascribed to a SL termination.

With the route to identifying the various terminations established, one is now in the position to examine the six distinct surface electronic structures of the first three members of the $(MnBi_2Te_4)(Bi_2Te_3)_n$ series. Fig. 5.9 presents a compilation of these spectra, with the upper section of each panel showing a schematic representation of the stacking sequence and the lower part displaying the corresponding ARPES spectrum, taken with a laser photon source. Panel (a) displays the surface spectrum of the $n = 0$ member of the series $MnBi_2Te_4$, which is composed exclusively of septuple layers. The comparatively faint topological surface state, labeled TSS, is dispersing linearly and the position of the Dirac point can be estimated to about $E - E_F = -0.25\,\mathrm{eV}$. In the energy region above the Dirac point – from now on referred to as the conduction band – are two more states labeled as CB1 and CB2, both of which lie within the upper branches of the TSS. The former state exhibits a parabolic dispersion, with a minimum at about $E - E_F = -0.19\,\mathrm{eV}$, whereas the latter appears as the bottom part of a feature that is cut off by the Fermi edge. Even though it is challenging to discern the topological surface state in this spectrum, the applied photon energy at the lower

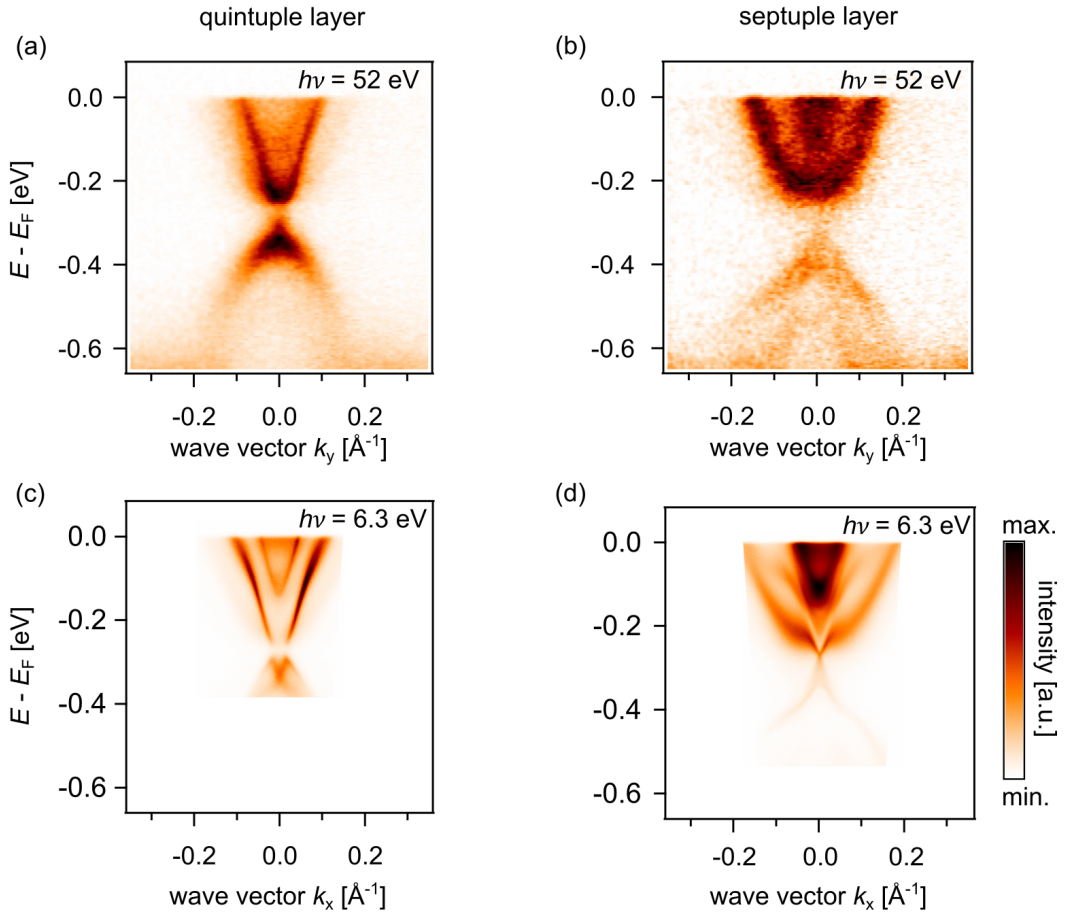

Figure 5.8: Comparison of the surface electronic structure of the two surface terminations of $MnBi_4Te_7$, obtained with synchrotron and laser excitation sources. (a), (b) Detailed surface electronic structure taken with $h\nu = 52\,\text{eV}$ on a quintuple and septuple termination, respectively. Both spectra are taken on the same positions as the spectra in panels (d) and (e) of Fig. 5.7. (c), (d) two distinct surface electronic structures, encountered with a photon energy of $h\nu = 6.3\,\text{eV}$. The laser spectra can be univocally assigned to the corresponding termination, due to the high agreement of panels (a) and (c) as well as (b) and (d).

end of the UV spectrum has nonetheless proven itself as the most suitable excitation energy, as can be seen by the photon energy series shown in Fig. A3 in the appendix.

Fig. 5.9 (b) and (c) display the previously presented spectra of the two distinct surfaces of the $MnBi_4Te_7$ compound, which are terminated by a $(MnBi_2Te_4)$- and a (Bi_2Te_3)-layer, respectively. For the SL termination, linearly dispersing Dirac states (TSS) can be seen, which converge at the Dirac point, which lies at about $E - E_F = -0.27\,\text{eV}$. The upper branches encounter a broad, parabolically dispersing conduction band state (CB1), with which they seem to merge. A second striking state, labeled CB2, with electron-like dispersion can be seen at lower binding energies. In between these two conduction band states, several up-

wards dispersing states can be observed, which will be discussed in the following section in more detail.

For the surface terminated by a QL, the approximately linear dispersing topological surface state can be traced up to the Fermi edge. Near $E - E_F = -0.27\,eV$, the state is discontinued and a spectral gap emerges. Below this gap, in the valence band regime, a set of hole-like dispersing states can be recognized, which appear to exhibit a Rashba-type splitting [166, 228]. As will be seen in the next section, the inner part of this state is the continuation of the topological surface state, with the Dirac point being located at $E - E_F = 0.33\,eV$. Within the upper branches of the topological state lies a parabolic conduction band state, labeled CB.

For the $MnBi_6Te_{10}$ compound, three different surface electronic structures are encountered, as shown in Figs. 5.9 (d)-(f). The electronic structure of a surface terminated by a $(MnBi_2Te_4)$-layer, as seen in panel (e), qualitatively resembles the ARPES spectrum of the same termination in $MnBi_4Te_7$. The Dirac point lies again at about $E - E_F = -0.27\,eV$ and the linearly dispersing surface state appears to merge with the conduction band state CB1. Compared to panel (b), the most prominent feature, labeled CB2, has shifted significantly towards lower binding energies. The overall blurriness of the spectrum impedes an exact detection of the intermediate states between CB1 and CB2.

For a surface terminated by a single QL, as shown in panel (f), the surface electronic structure exhibits a qualitative resemblance with the corresponding spectrum in panel (c). The topological surface state is again discontinued and has a spectral gap in its upper branches, although this time a flattened dispersion at small wave vectors, connecting the two branches, is recognizable. Overall, the spectrum is more electron doped, compared to its $MnBi_4Te_7$ counterpart, so that the Dirac point is shifted towards higher binding energies and lies at $E - E_F = -0.4\,eV$. The conduction band feature CB now consists of two parabolic bands with varying effective masses. The Fermi wave vector k_F of the TSS is considerably larger in this compound, which is due to the aforementioned energy shift of the spectrum, combined with the fact that the spectrum is taken along a different azimuthal direction, in which the surface state exhibits an outwards warping.

Lastly, this compound exhibits a third surface spectrum for surfaces that have an additional QL beneath the surface, i.e., QL-QL-SL stacking order. The corresponding ARPES spectrum is shown in Fig. 5.9 (d). Despite the unfavorable signal-to-noise ratio, it is still possible to trace the topological surface state, which again has a spectral gap around $E - E_F = -0.25\,eV$. Accordingly, the Dirac point is now located at approximately $E - E_F = -0.3\,eV$. Like for the single QL termination of $MnBi_4Te_7$, a single electron-like conduction band state is visible near the Fermi edge. With an increasing value of n, the electronic structure of the surface terminated by n quintuple layers is expected to approach that of pure Bi_2Te_3. This tendency is already more pronounced in the $n = 3$ compound $MnBi_8Te_{13}$ [222].

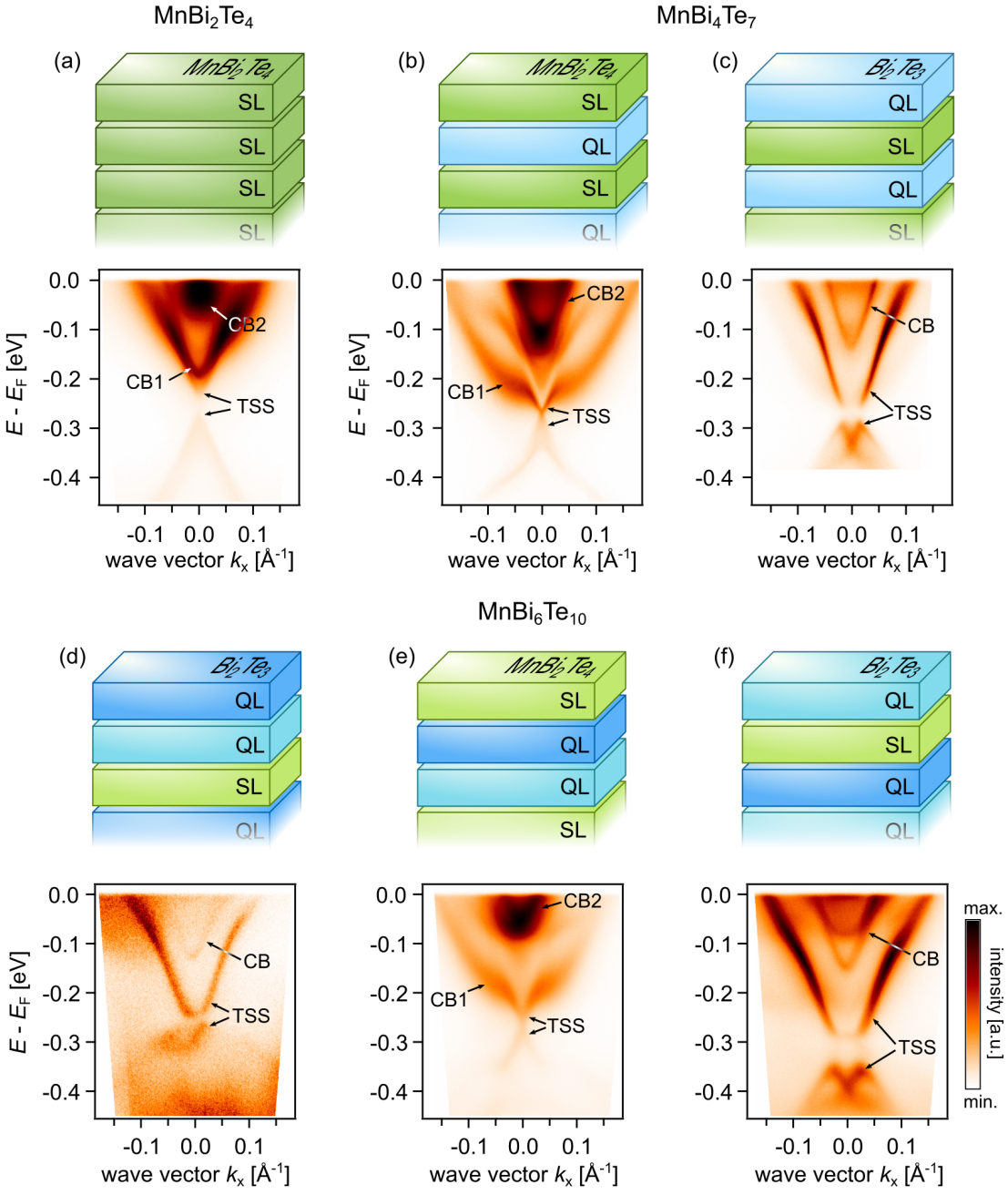

Figure 5.9: Surface electronic structure of the six distinct terminations of $(MnBi_2Te_4)(Bi_2Te_3)_n$ for n = 0, 1, and 2. Spectral features that can be identified as the topological surface state and conduction band states are labeled by TSS and CB, respectively. Above each spectrum, a graphical representation of the layer sequence is shown. SL and QL are represented by blocks in shades of green and blue, respectively. (a) ARPES spectra taken on the SL terminated $MnBi_2Te_4$. (b), (c) Surface electronic structure for SL and QL terminated $MnBi_4Te_7$, respectively. (d)-(f) Spectra taken on the three possible terminations QL-QL-SL, SL-QL-QL, and QL-SL-QL of $MnBi_6Te_{10}$. All spectra were taken with $h\nu = 6.3\,\mathrm{eV}$ and s-polarized light.

The fact that the *n*th member of the series exhibits different electronic structures on its *n* quintuple layer terminations distinguishes this material system from the van der Waals topological insulators Bi_2Te_3 and Bi_2Se_3 [229, 230]. For the latter two it was shown that the electronic structure is dominated by the topmost layer, whereas $(MnBi_2Te_4)(Bi_2Te_3)_n$ compounds show a sensitivity to the stacking sequence of the underlying layers.

The here presented measurements were each performed on a single sample prepared by exfoliation. On the one hand, this emphasizes the need for a micrometer-sized beam spot to individually address the different terminations, on the other hand, it shows the relevance of detailed knowledge of the characteristics of each termination, in order to prevent erroneous assessments.

In contrast to Bi_2Te_3 and Bi_2Se_3 based topological insulators, where the sample surface experiences a substantial doping effect by the adsorption of residual gases, the spectrum of $(MnBi_2Te_4)$-containing compounds showed no time-dependent aging effects [126, 231, 232].

5.3.2 Orbital complexity in the surface electronic structure of $MnBi_4Te_7$

Having a procedure for the assignment of the electronic structure to its corresponding surface termination established, this section will now focus on analyzing the intricacies of the surface electronic structure, particularly the topological surface state. The results will validate the assignment of the features of the surface electronic structure, which was already made in the last section. The surfaces considered here are again the septuple and quintuple layer termination of $MnBi_4Te_7$. The former will be explored by circular dichroic ARPES, whereas the latter will be examined via photon-energy-dependent measurements. In both cases, the findings are supplemented by spin-resolved ARPES. The experimental data of the quintuple layer termination is complemented by DFT calculations provided by Jorge Facio from the IFW Dresden. The calculations were performed using the GGA+U method. The details of the calculations can be found in Ref. [225] and in the corresponding supplementary material.

Septuple layer termination

First, the surface terminated by a septuple layer will be considered. Polarization-dependent ARPES is employed in the form of circular dichroism to investigate the character of the electronic states. The dichroism signal is defined as the difference of photoemission intensities taken with right and left circularly polarized photons $CD(k_x,k_y,E) = I_\mathrm{R}(k_x,k_y,E) - I_\mathrm{L}(k_x,k_y,E)$.

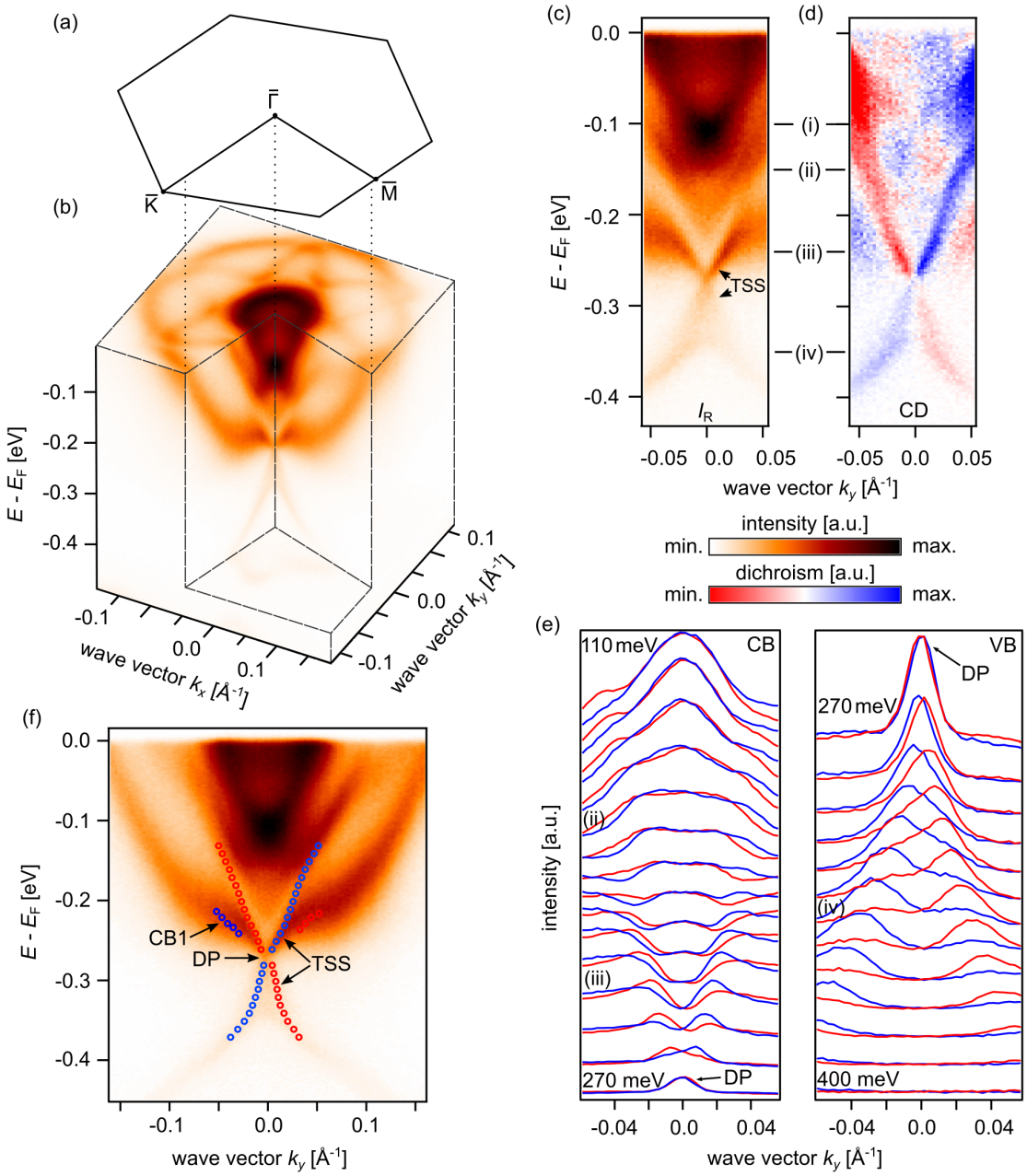

Figure 5.10: Circular dichroism in the surface electronic structure of the septuple layer termination of $MnBi_4Te_7(0001)$. (a) Surface Brillouin zone in which the positions of the high-symmetry points are denoted. It is aligned with the photoemission data in (b), which shows a three-dimensional representation of an ARPES dataset measured with *s*-pol. and which is truncated to present the electronic structure along the $\overline{\Gamma}\overline{\mathrm{K}}$ and $\overline{\Gamma}\overline{\mathrm{M}}$ directions. (c) Section of the band structure measured with right-handed circular polarization. The wave vector component k_y is perpendicular to the plane of light incidence. (d) Corresponding circular dichroism dataset defined by $I_\mathrm{R} - I_\mathrm{L}$. (e) Momentum distribution curves measured with right- and left-handed polarization, which are represented by blue and red color, respectively. The left panel depicts the energy region above the Dirac point, whereas the right panel presents the lower Dirac states. The momentum distribution curves at the Dirac point position $E - E_\mathrm{F} = -270\,\mathrm{meV}$ are shown in both panels and are correspondingly labeled. (f) ARPES intensity measured with *s*-pol. in which the dispersion of the TSS and the CB1 state are plotted. The position labels (i)-(iv) in (c)-(d) mark the energetic positions of the constant energy cuts in Fig. 5.11.

Fig. 5.10 (a) shows the hexagonal surface Brillouin zone of $MnBi_4Te_7(0001)$, in which the symmetry points $\overline{\Gamma}$, $\overline{M}$, and $\overline{K}$ are indicated. The Brillouin zone is aligned with the ARPES intensity cube presented in Fig. 5.10 (b), showing the relative orientation of the experimental setup and the crystal structure. The plane of incidence, as well as the analyzer slit, are parallel to the $(k_y = 0)$-plane.

The interpretation of the dichroism signal as a property of the electronic states, in contrast to an origin due to other experimental asymmetries, is facilitated, if the scattering plane of the incident photons is parallel to a mirror plane of the crystal [233]. By comparing panels (a) and (b) in Fig. 5.10, it can be seen that the setup geometry does not exactly match the crystal high-symmetry direction $\overline{\Gamma}\overline{M}$ in the present measurement, a fact that will be reencountered later in the evaluation. To a first approximation, however, the plane of incidence can be considered to be nearly parallel to this mirror plane.

The three-dimensional ARPES intensity $I(k_x, k_y, E)$ in Fig. 5.10 (b), acquired with s-polarized light, is sectioned along the two perpendicular symmetry directions $\overline{\Gamma}\overline{K}$ and $\overline{\Gamma}\overline{M}$, which demonstrates the intricate momentum- and energy-dependence of the surface electronic structure. Whereas the lower part of the Dirac cone is rather isolated from other electronic states and exhibits overall low spectral weight, the conduction band regime is occupied by superimposing states with various spectral intensities. Fig. 5.10 (c) shows a detailed view of the electronic structure in the vicinity of the Brillouin zone center taken with right-handed polarized light and along k_y, the direction perpendicular to the plane of incidence. The spectrum has the characteristics of the previous measurements, that is, a topological surface state whose upper branches encounter a conduction band state, about 40 meV above the Dirac point, after which the dispersion cannot be traced by the bare ARPES intensity. The panel to the right, Fig. 5.10 (d), shows the corresponding dichroism signal, which features several characteristics which are encountered in other topological materials.

As is the case for the non-magnetic parent compound Bi_2Te_3, the band inversion in the $(MnBi_2Te_4)(Bi_2Te_3)_n$ series occurs between Te p_z and Bi p_z orbitals with opposite parity, whose characters are intermixed with the in-plane p-orbitals due to SOC [10, 44, 170]. Omitting the prefactors for clarity, the wave functions of the upper and lower branches of the topological surface state, along k_y and in proximity to the Γ-point, can be written as

$$|\Phi_+\rangle = |p_z\uparrow\rangle - i|p_y\uparrow\rangle - |p_x\downarrow\rangle \quad \text{and} \quad |\Phi_-\rangle = |p_z\downarrow\rangle + i|p_y\downarrow\rangle + |p_x\uparrow\rangle,$$

respectively [234].

Apart from the characteristic inverted spin polarization, there is a change in the relative phases of the p-orbital components. In particular, the p_z- and p_y-orbitals exhibit a relative phase of $-\pi/2$ and $+\pi/2$ for $|\Phi_+\rangle$ and $|\Phi_-\rangle$, respectively. This total phase difference of

π yields a finite orbital angular momentum along the x-direction with an opposite sign for $|\Phi_+\rangle$ and $|\Phi_-\rangle$ [55, 235]. DFT calculations of this termination on $MnBi_4Te_7$ confirm this sign change between $|\Phi_+\rangle$ and $|\Phi_-\rangle$ [225]. This phase shift and the resulting sign change of the x-component of the orbital angular momentum are reflected in the sign change of the orbital-dependent photoemission matrix element.

The coupling of the circularly polarized photon to the excited Dirac electron can be illustrated in a simplified view of the matrix element by assuming excitation to a final state with s-symmetry, i.e., even symmetry. This is an assumption which was found to be valid for the related material Bi_2Se_3 at a nearly equal photon energy of $h\nu = 6\,\mathrm{eV}$ [236]. The electric field vector of cicurlarly polarized light at an incidence angle of 45° has the form $\boldsymbol{E} = (\varepsilon_x, \pm i\varepsilon_y, \varepsilon_z)^{\mathrm{T}}$. Under the given assumption, the components of the electric field vector $\varepsilon_{x,y,z}$ couple solely with the correspondingly aligned p-orbitals [170]. This results in intensities from the $|\Phi_\pm\rangle$ state in the form of

$$I_R \propto |T_z \mp T_y|^2 + |T_x|^2 \quad \text{and} \quad I_L \propto |T_z \pm T_y|^2 + |T_x|^2$$

for right- and left-handed circular polarization, respectively. Here, the matrix element T_i is given as $\langle \Phi_\mathrm{f} | \varepsilon_i \hat{i} | p_i \rangle$.

The relative phase of $\pm\pi/2$ between the p_z- and p_y-orbital is thus reflected in the relative phase between T_z and T_y. Consequently, the opposite sign of the circular dichroism signal when going from $+k_y$ to $-k_y$, as well as above and below the Dirac point, reflects the inversion of the orbital angular momentum and thus the helicity of the Dirac state. In fact, in Bi_2Te_3 and Bi_2Se_3, it has been shown that the change in sign of the circular dichroism intensity when crossing the Dirac point is a characteristic signature of a topological surface state [233, 237]. Coming back to Fig. 5.10 (d), the topological state is furthermore clearly distinguished from other conduction band states like CB1 due to the opposite signs of their dichroism signal. As a result, the dispersion of the upper branches can be traced over several hundreds of meV to much lower binding energies compared to the bare ARPES intensity. Viewed through the "lens of circular dichroism", the linear dispersion of the topological surface state is hence discernible.

To relate the now visible dispersion within this limited section of momentum space to the rest of the band structure, it was quantitatively traced using the momentum distribution curves in Fig. 5.10 (e) and plotted in the corresponding section of the band structure taken with s-polarization in Fig. 5.10 (f). In addition, the dichroic signal of the adjacent state CB1 is traced and plotted, to emphasize the different evolution of the two. This overlaid representation allows the surface state to be discerned outside the limited range of the dichroism measurement and to be identified as the strongly hexagonally warped state at the Fermi surface, which can be seen at the top surface of the data set in Fig. 5.10 (b).

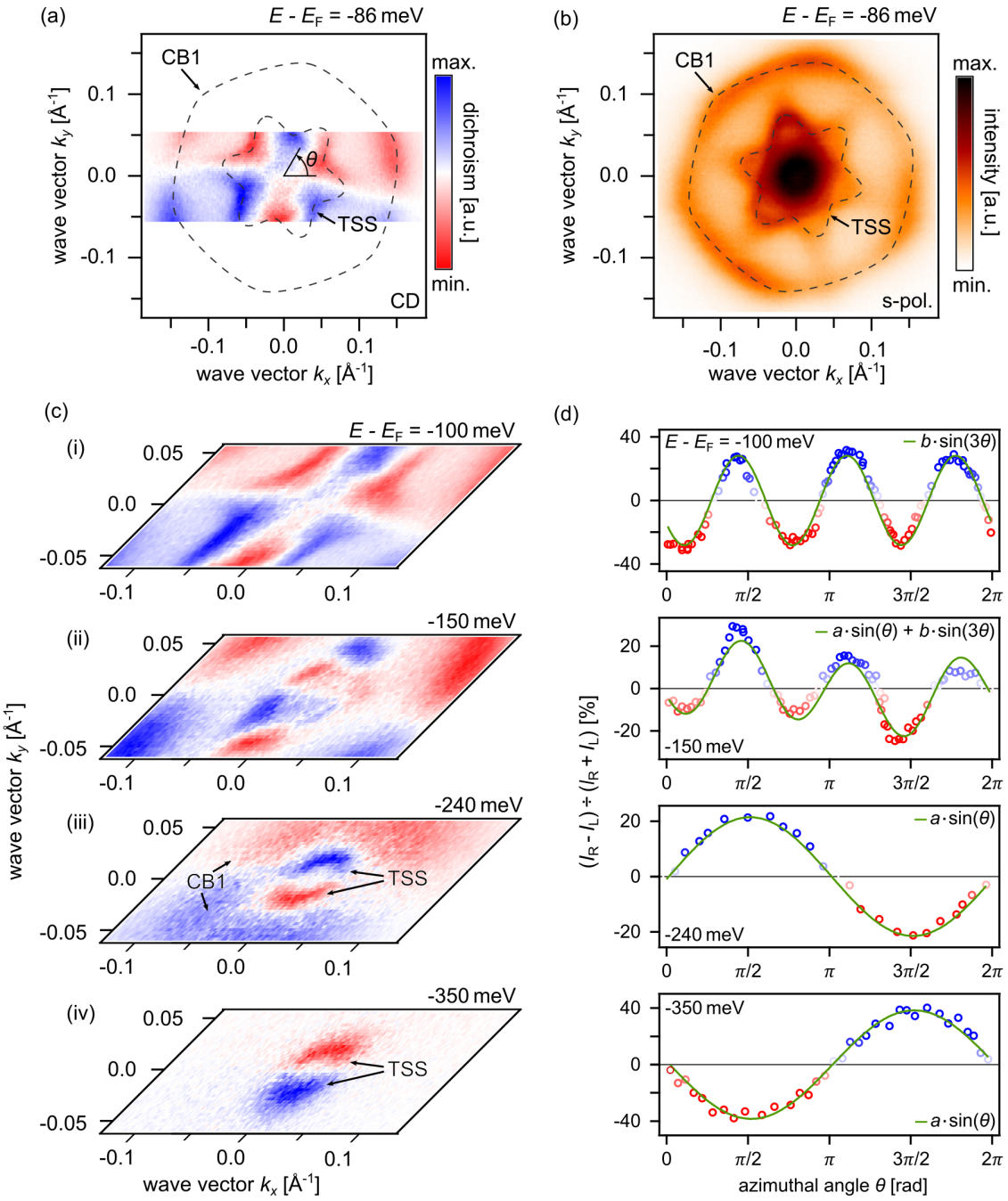

Figure 5.11: Circular dichroic signal of the hexagonally warped topological surface in $MnBi_4Te_7(0001)$. (a) Constant energy contour of the dichroic signal, defined as $I_R - I_L$, slightly below the Fermi level. The dashed lines serve as a guide to the eye for the topological surface state (TSS) and the outermost conduction band state (CB1). (b) Constant energy contour measured with *s*-pol. light at the same energetic position as (a). Again, the dispersion of TSS and CB1 are emphasized by a dashed line. (c) Contours of constant energy showing the energy-dependent evolution of the dichroic behavior of the topological surface state. The energy positions (i)-(iv) are marked in panels (c)-(e) in Fig. 5.10. Positions (i)-(iii) are energetically above the Dirac point, whereas (iv) lies below it. (d) Normalized dichroism $(I_R - I_L) \div (I_R + I_L)$ of the TSS at the energy positions of (c). In addition to the data points, which are shown in red, the best fit for the respective oscillatory function is plotted in blue.

This hexagonal distortion is highly reminiscent of the warping of the topological surface state in the paradigmatic TI Bi_2Te_3 [52]. In this material, as the energetic distance from the Dirac point increases, the upper branches of the TSS exhibit a deformation that gives it a hexagonal contour. This deformation ultimately concludes in a Fermi-surface whose contour is often commonly described as snowflake-like [238]. The same effect can be observed in Bi_2Se_3, albeit much less pronounced [239].

The energy- and momentum-dependent evolution of the CD pattern of the topological surface state is further illuminated in Fig. 5.11. Panels (a) and (b) display the CD signal and the bare ARPES intensity, measured by *s*-polarized light, in the form of a CEC near the Fermi level, respectively. The topological surface state (TSS) and the outermost conduction band state (CB1) are emphasized by dashed lines, which serve as guides to the eye. The topological state exhibits a six-fold symmetry in its dispersion and a three-fold symmetry in the periodicity of its CD pattern. The dichroism undergoes a change of sign along the $\overline{\Gamma}\overline{\mathrm{M}}$ direction, which is reminiscent of the symmetry of the out-of-plane spin angular momentum acquired by hexagonally warped surface states in Bi_2Te_3 [240].

Fig. 5.11 (c) shows the energy-dependent evolution of the CD signal at binding energies above and below the Dirac point. The energy positions (i)-(iv) are indicated in panels (c)-(e) of Fig. 5.10. At energies (iii) and (iv), which lie directly above and below the Dirac point, the dispersion exhibits the expected circular shape accompanied by a twofold CD pattern that inverts its sign when crossing the Dirac point. Following the TSS to higher energies in panels (ii) and (i), it can be seen that its hexagonal deformation is coupled with a rearrangement of the CD signal towards the pattern seen in (a).

As discussed above, the CD intensity reflects the orbital angular momentum of the wave function, for which it could be shown that it aligns antiparallel to the spin angular momentum in the surface state of Bi_2Te_3 [241, 242]. To quantitatively substantiate this interpretation, the dichroism asymmetry defined as $(I_\mathrm{R} - I_\mathrm{L})/(I_\mathrm{R} + I_\mathrm{L})$ has been extracted along the dispersion of each constant energy contour and plotted in Fig. 5.11 (d) as a function of the azimuthal angle Θ. The zero position and sense of rotation of Θ are indicated in 5.11 (a).

The projection of a chiral in-plane orbital angular momentum along the *x*-direction equates to a sinusoidal profile. Indeed, the shape of the asymmetry near the Dirac point matches this profile, as seen in positions (iii) and (iv). The corresponding panels contain the best fit according to a $f(\Theta) = a \cdot \sin(\Theta)$ function. Including the sign change above and below the Dirac point, both data sets are consistent with the expected waveform. A dichroism asymmetry of up to 40 % can be observed, which is consistent with values observed in Bi_2Te_3 and Bi_2Se_3 [241, 242]. As the binding energy decreases, another higher-order component arises which ultimately dominates the asymmetry lineshape and which can be seen in panels (ii) and (i). Due to the warping and the associated finite out-of-plane spin component, it is

expected that, in addition, an out-of-plane orbital angular momentum component aligned antiparallel to it will arise which follows a $\sin(3\Theta)$ function [241–243]. Accordingly, panels (i) and (ii) contain curve fittings in the form of a pure $b \cdot \sin(3\Theta)$ function as well as a superposition of both signals $a \cdot \sin(\Theta) + b \cdot \sin(3\Theta)$, respectively. These fit functions show a reasonable agreement with the experimental data and thus allows for a phenomenological description of the dichroism asymmetry in the unperturbed regime near the Dirac point and its evolution associated with the hexagonal warping. An equivalent trend could be observed in the much less warped surface state of Bi_2Se_3, whereas in Bi_2Te_3 with increasing energy another term of even higher-order proportional to $\sin(6\Theta)$ was found, which was attributed to an additional nonorthogonality of the in-plane component of the orbital angular momentum at higher wave vectors [242, 243].

In addition to the prefactors and the azimuthal angle, the functions were allowed an auxiliary phase to account for the rotation of the crystal with respect to the plane of incidence. In the region where the experimental data follow the $\sin(\Theta)$ lineshape, that is, in panels (iii) and (iv), this phase is not needed to obtain a satisfactory agreement with the data. In contrast, the $\sin(3\Theta)$ terms require this phase to describe the lineshape of the experiment. A zero line of the CD pattern along $k_y = 0$ reflects the rotational symmetry of a chiral configuration of the orbital angular momentum near the Dirac point. At higher wave vectors, this chirality is superimposed by a higher-order sinusoidal component, which lacks this rotational symmetry and whose zero line therefore aligns with the $\overline{\Gamma}\overline{\mathrm{M}}$ high-symmetry direction of the crystal.

Another key feature of a topological surface state is its chiral spin angular momentum [234]. To experimentally observe this characteristic signature, spin-resolved ARPES was employed. Fig. 5.12 (a) summarizes the geometrical layout of the experiment. The light incidence is along the x-direction with the analyzer slit and probed spin component S_y oriented perpendicular to it along the y-axis. The measurements are performed using s-polarized light due to the expected sensitivity to the tangentially aligned orbitals [170, 244].

Fig. 5.12 (b) shows the ARPES intensity along k_y. For the spin analysis, a contour of constant energy of the upper part of the Dirac cone, just above the Dirac point, is considered. This energy position of $E - E_\mathrm{F} = -240\,\mathrm{meV}$ corresponds to the dichroism pattern displayed in Fig. 5.11 (c) (iii). The momentum range and energy integration window are indicated by a dotted box and the corresponding spin-integrated energy contour is shown in panel (c). A dashed line serves as a guide to the eye and emphasizes the dispersion of the topological surface state. The attenuated intensity towards higher wave vectors originates from the conduction band state CB1. Fig. 5.12 (d) depicts the corresponding spin-resolved constant energy surface of the spin component along y. A two-dimensional color code, shown in Fig. 5.12 (f), was chosen to simultaneously represent the normalized photoemission inten-

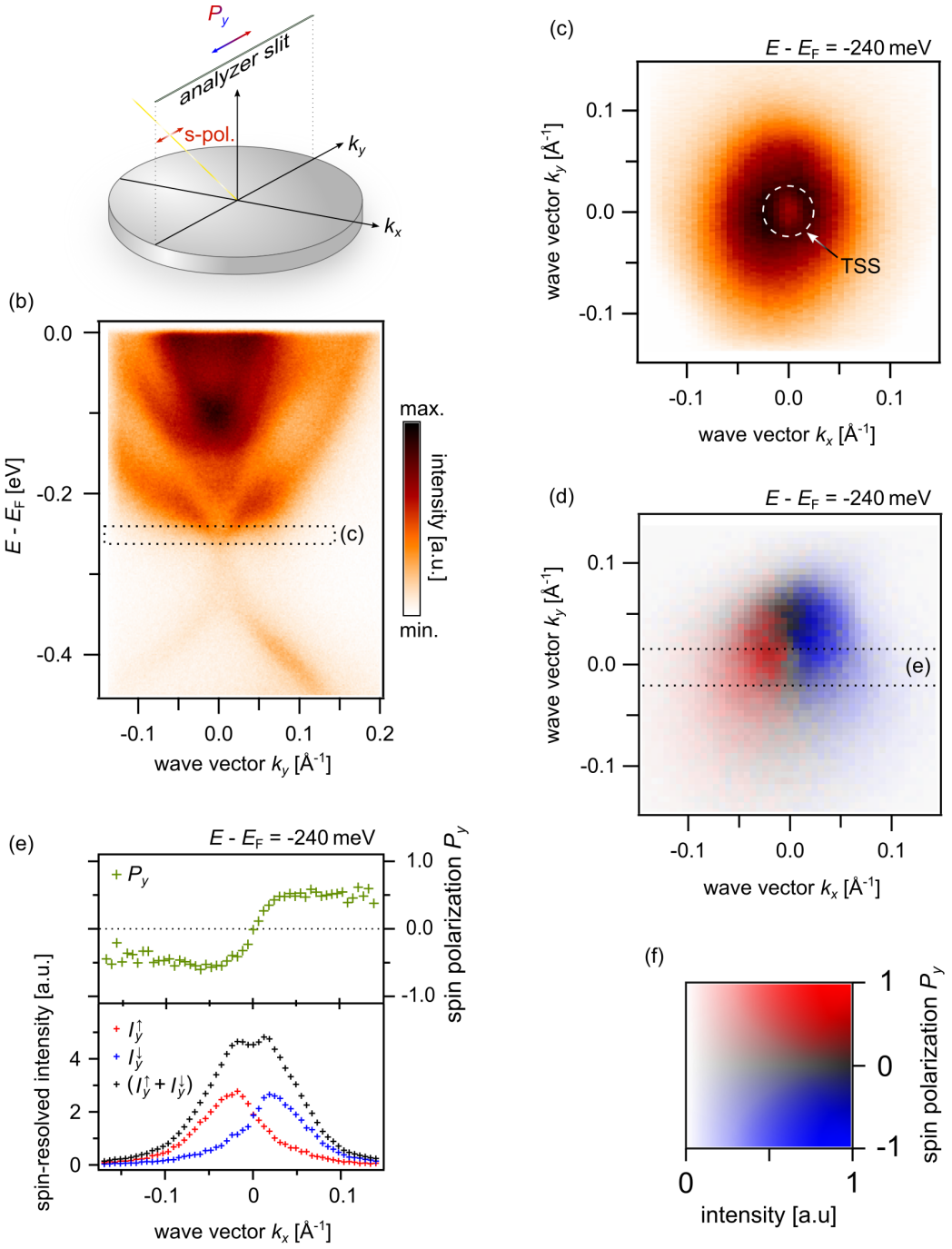

Figure 5.12: Spin-texture of the topological surface state on the septuple layer termination of $MnBi_4Te_7(0001)$. (a) Schematic depiction of the experimental geometry, including the light polarization and the detected component of the spin polarization P_y. (a) ARPES intensity along k_y, in which the energy and momentum integration window of the subsequent panels is indicated by a dotted rectangle. (c) Spin-integrated constant energy contour, showing the circular dispersion of the upper part of the topological surface state. (d) Corresponding spin-resolved constant energy contour, in which the integration window for panel (e) is indicated. (e) Spin polarization P_y and spin-resolved intensities $I_y^{\uparrow}$ and $I_y^{\downarrow}$ along $k_y = 0\,\text{Å}^{-1}$. (f) Two-dimensional color code for simultaneous visualization of the photoemission intensity and spin polarization, as used in panel (d).

sity and the spin polarization P_y calculated according to equations 3.11 and 3.12. Consistent with the expected chiral spin texture, the polarization becomes maximal along $k_y = 0$ and switches sign when going from $+k_x$ to $-k_x$. An excerpt in the form of momentum distribution curves, whose integration window is marked by dashed lines, demonstrates this behavior. The upper part of Fig. 5.12 (e) shows the inversion of polarization when crossing $k_x = 0$, while the lower section shows the separated spin up and down spectra $I^{\uparrow,\downarrow}$ calculated from the measured intensities $I^{+,-}$ according to equations 3.13 and 3.14, as well as their sum.

The spin-resolved Fermi surface in Fig. 5.12 (d) is slightly skewed towards positive k_y. This distortion is most likely due to the fact that the lens tables of the deflector are not optimized for a projection onto the aperture of the spin detector, which is located adjacent to the microchannel plate for spin-integrated measurements. This is combined with the low kinetic energy of the photoelectrons due to their excitation by a laser source, which causes the effect to increase with increasing energetic distance from the Fermi level. Since the aberration increases with decreasing kinetic energy and the overall intensity of the lower Dirac state is rather faint, no data set could be acquired below the Dirac point, presenting the switch in the polarization of the in-plane spin angular momentum.

Quintuple layer termination

The most striking spectroscopic feature of the QL termination is the occurrence of a spectral-weight gap in the energy range of the upper Dirac states. This gap was interpreted in disparate ways, leading to conflicting assertions concerning its origin. These interpretations ranged from a mass gap of the Dirac state [28–30, 245] to an intact Dirac point at either the flat portion of the upper part [227, 246] or at the lower Rashba-like split part of the dispersion [221]. In this section, photon-energy-dependent and spin-resolved ARPES data are presented, confirming the latter hypothesis, in which the spectral gap arises due to hybridization with the bulk valence band maximum.

Fig. 5.13 (a) and (b) show the ARPES intensity measured with $h\nu = 6.3\,\mathrm{eV}$ and $h\nu = 61\,\mathrm{eV}$, respectively. The notation of the in-plane momentum components refers to their relative orientation to the incidence of light, that is, k_x and k_y are parallel and perpendicular to the plane of incidence, respectively. Again, the laser-based measurements were performed using *s*-polarized light, whereas *p*-polarization was used for the spectra acquired with VUV light. Both spectra exhibit a quite similar spectral-weight distribution, in particular a high intensity for the linear section of the upper state (TSS) with a highly supressed intensity in the flat region towards the $\overline{\Gamma}$-point as well as an increase in intensity in the center of the Rashba-like section of the lower band. In contrast, the data in Fig. 5.13 (c), measured with $h\nu = 79\,\mathrm{eV}$, represent the "counterpart" regarding the distribution of spectral weight,

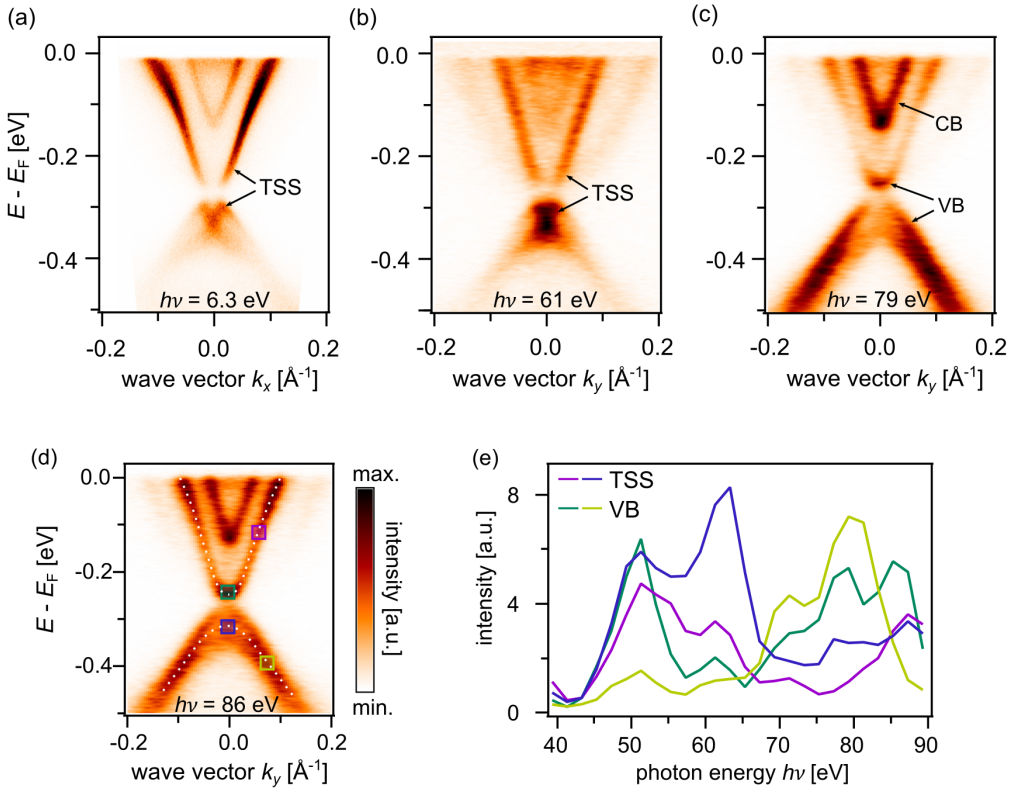

Figure 5.13: Photon energy dependence of the surface electronic structure of the quintuple layer termination of $MnBi_4Te_7$. (a) ARPES intensity obtained with *s*-polarized light and a photon energy of $h\nu = 6.3\,\text{eV}$. (b), (c) ARPES intensity along $\overline{\Gamma}\overline{\text{K}}$ taken with *p*-polarization and $h\nu = 61\,\text{eV}$ and $h\nu = 79\,\text{eV}$, respectively. (d) ARPES intensity taken with *p*-polarized light and a photon energy of $h\nu = 86\,\text{eV}$. The dotted line serves as a guide to the eye by emphasizing the dispersion of the states above and below the gap. The colored squares mark the regions of interest of the photon energy series. (d) Photon-energy-dependent evolution of selected points of the ARPES intensity. The graphs are colored according to their respective region of interest in panel (d).

in that the previously suppressed parts of the valence band states (VB) and the electron-like conduction band state (CB) show enhanced intensity.

The abrupt change in intensity occurs both above and below the gap and at similar wave vectors for all three photon energies. The fact that this change occurs for characteristic points in momentum space and for different photon energies is a strong indication for a momentum-dependent variation of the initial state wave function in the form of a change in its orbital composition [247]. This point is further elucidated by a more systematic examination of the photon energy dependence. Fig. 5.13 (d) displays the surface spectrum taken with $h\nu = 86\,\text{eV}$, where it exhibits a more uniform spectral-weight distribution. Along the band dispersion, four areas of interest are marked with colored squares. The violet and blue square correspond to regions that show an increased intensity in (a) and (b), i.e., the topo-

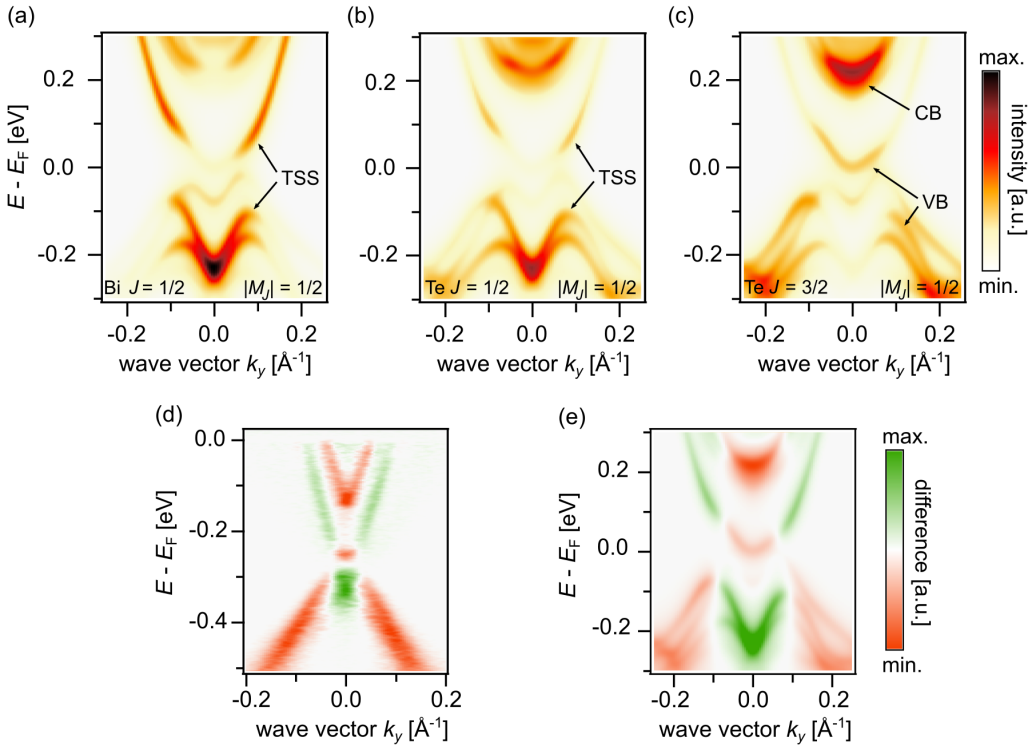

Figure 5.14: Surface and orbital projected DFT simulation. (a)-(c) Orbital projected surface spectral density. The respective orbital contribution is denoted at the bottom of each panel. (d) Difference spectrum of the ARPES intensities measured at $h\nu = 61\,\mathrm{eV}$ and $h\nu = 79\,\mathrm{eV}$, which are shown in Fig. 5.13 (b) and Fig. 5.13 (c), respectively. (d) Difference between the surface spectral densities projected on Bi $J = 1/2$ and Te $J = 3/2$ orbitals with $|M_J| = 1/2$. The respective spectra can be found in (a) and (c).

logical surface state, whereas sections of the valence band states (VB), which are prominent in (c), are marked with green and yellow squares. Two dotted lines serve as guides to the eye for the dispersion of the two considered bands. Fig. 5.13 (e) displays the photon-energy-dependent evolution of the intensity in these regions for a range of $h\nu = 40\,\mathrm{eV}$ to $h\nu = 90\,\mathrm{eV}$. The data was normalized by the beamline flux published in Ref. [116]. It can be seen that the two sections labeled as TSS and VB each exhibit a characteristic $h\nu$-dependence, with the violet and blue as well as the green and yellow following a similar trend in their respective evolutions. This further substantiates the assertion of a momentum-dependent change in the orbital composition of these states. The complete data of the $h\nu$-series can be seen in the appendix in Fig. A4. There, the overview over all angle-resolved spectra, corresponding to the data points presented in Fig. 5.13 (e), reemphasizes the photon-energy- and momentum-dependent change in the cross section in the states sorrounding the spectral-weight gap.

These experimental findings are supported by DFT calculations in the form of atom- and orbital-projected surface spectral densities. The finite probing depth of the ARPES ex-

periment was qualitatively simulated by assuming an exponential decay from the surface with a decay constant $\lambda = 10\,\text{Å}$. Fig. 5.14 (a), (b), and (c) show the calculated spectral densities projected onto the Bi $J = 1/2$, Te $J = 1/2$, and Te $J = 3/2$ orbital, respectively. The simulations nicely reproduce the gap in the ARPES spectrum, independently of the orbital under consideration. This is in line with the experimental data, for which the gap is always observable, regardless of the photon energy. Furthermore, striking similarities can be found between certain orbital projections and the observed spectral-weight distribution in the ARPES experiment. More precisely, the projections onto Bi $J = 1/2$ and Te $J = 1/2$ states resemble the ARPES spectra taken with $h\nu = 6.3\,\text{eV}$ and $h\nu = 61\,\text{eV}$, whereas the projection onto the Te $J = 3/2$ state bears a strong resemblance to the measurement taken with $h\nu = 79\,\text{eV}$. This close correlation enables the former orbitals to be identified as the main constituents to the topological surface state, and the latter to be identified as the primary contributor to the valence and conduction band states. The different orbital contributions to the band structure induce the distinct cross sections observed in the $h\nu$-dependent data and allow to discern them via experiment.

The qualitative agreement between experiment and theory is emphasized in Figs. 5.14 (d) and (e). The spectra depict the difference of measurements taken with $h\nu = 61\,\text{eV}$ and $h\nu = 79\,\text{eV}$ as well as the difference of the orbital projections onto Bi $J = 1/2$ and Te $J = 3/2$ states, respectively. Sections of the topological surface state are therefore visible in green and valence and conduction band states appear in orange. This visualization illustrates the simultaneous change in orbital character in the states above and below the gap at a characteristic wave vector. Following this analysis and its interpretation, the Dirac point can be located in the lower section of the spectrum where it forms the crossing point of the states at $\overline{\Gamma}$.

This conclusion is substantiated by spin-resolved ARPES data and DFT calculations of the in-plane spin component. Fig. 5.15 (a) shows ARPES data along $\overline{\Gamma}\overline{\text{K}}$ taken with s-polarization and $h\nu = 6.3\,\text{eV}$. The experimental geometry is the same as shown in Fig. 5.12 (a). The dotted lines mark the energy position of the spin-resolved momentum distribution curves in (b). A spin-resolved constant energy contour close to the Fermi level at energy position (i) is presented in Fig. 5.15 (d). The momentum map images the y-component of the polarization S_y and reveals the chiral spin texture of the topological surface state. Moreover, panel (b) shows the spin intensities $I_y^{\uparrow}$ and $I_y^{\downarrow}$ along k_x for all four energy positions (i)-(iv). It is found that the spin polarizations above and below the gap, i.e., at energies (ii) and (iii), coincide with one another, as would be expected for the proposed hybridization scenario. The polarization reverses its sign only at energy (iv), when the Dirac point is traversed.

The spin-resolved momentum distribution curves in panel (b) were extracted from their respective constant energy contour using integration windows as exemplified by dotted lines

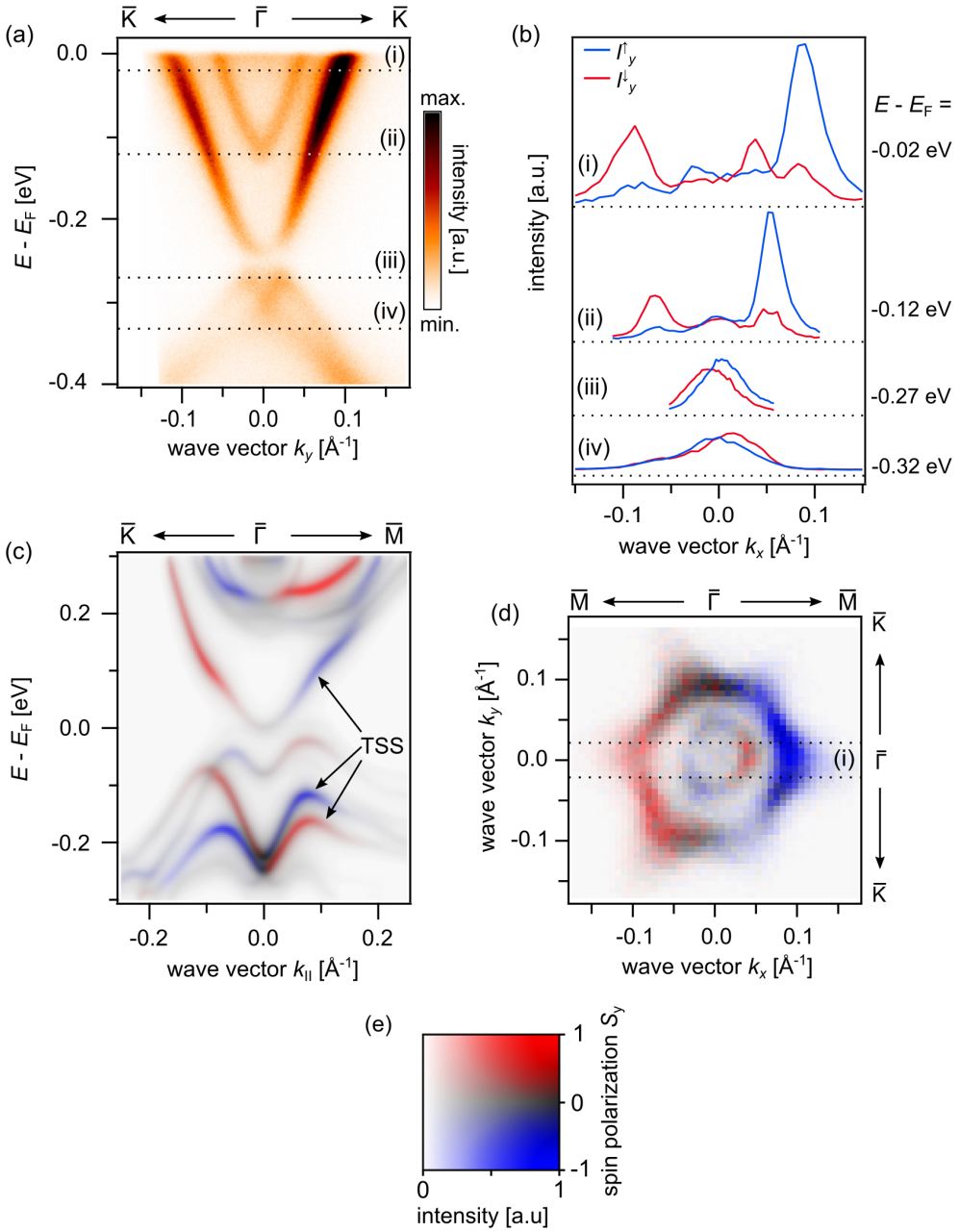

Figure 5.15: Spin-resolved surface electronic structure as measured by ARPES and calculated by DFT. (a) ARPES intensity along $\overline{\Gamma}\overline{K}$. (b) Momentum distribution curves of the two antiparallel spin channels $I_y^{\uparrow,\downarrow}$ at the binding energies (i)-(iv) as indicated in (a). The zero line of each pair is indicated by a dotted line. (c) Spin-resolved calculated surface spectral density along $\overline{K}\overline{\Gamma}\overline{M}$ taking into account the contributions by Te and Bi $J = 1/2$ orbitals. The red and blue colors denote the polarization of the tangential spin component perpendicular to $k_{\|}$. (d) Spin-resolved Fermi surface at the energy position (i). The dotted lines mark the momentum integration window for the curves in (b). (e) Two-dimensional color code adopted for the simultaneous depiction of photoemission intensity and spin polarization.

in (d). The spin-resolved momentum maps are subject to the same distortion already discussed in the context of Fig. 5.12 (d). This aberration shifts the detected intensity with decreasing kinetic energy of the photoelectrons to increasingly higher wave vectors. Curves (iii) and especially (iv) should, therefore, not be evaluated quantitatively. Nonetheless, the graphs provide a qualitative representation of the binding energy-dependent evolution of the in-plane spin polarization S_y.

This evolution is also reflected in the spin-resolved DFT calculation in Fig. 5.15 (c), which depicts the surface spectral density projected onto Bi and Te $J = 1/2$ along $\overline{\mathrm{K}}\overline{\Gamma}\overline{\mathrm{M}}$. Red and blue colors denote the tangential spin polarization perpendicular to $k_{\|}$. As in the ARPES experiment, the sign of the spin polarization persists beyond the hybridization gap and inverts only upon crossing the Dirac point.

In addition, in both experiment and theory, a spin polarization can be attributed to the conduction band states, the sign of which is inverted compared to the topological surface state. A similar observation could also be made for the non-magnetic topological insulator Bi_2Se_3, where it was attributed to the emergence of a surface resonance [248].

Discussion

The two surface terminations investigated throughout this section exhibit intricate surface electronic spectra. By using circular dichroic, spin-resolved, and photon-energy-dependent ARPES experiments, the surface band structure could be studied in terms of its spin and orbital angular momentum, enabling an unambiguous classification of the topological bands. Circular dichroism reveals that the topological surface state of a surface terminated by a $(MnBi_2Te_4)$-layer disperses linearly over several hundred meV. Additionally, the chiral texture of the orbital and spin angular momentum in the vicinity of the Dirac point is demonstrated. At lower binding energies, the rotational symmetry of the topological state is lifted and a hexagonal warping to the contour of its Fermi surface is introduced. This reduction of symmetry allows for an out-of-plane component of the spin and orbital angular momenta to be formed away from the mirror planes along $\overline{\Gamma}\overline{\mathrm{M}}$. Consequently, the maximal out-of-plane angular momentum is expected along $\overline{\Gamma}\overline{\mathrm{K}}$ which corresponds to the concave sections of the snowflake-like shaped Fermi surface. The emergence of an out-of-plane orbital angular momentum at higher energies as well as its threefold symmetry could be established by analyzing the circular dichroism as a function of the azimuthal angle Θ.

For the (Bi_2Te_3)-layer termination, a combination of photon-energy-dependent and spin-resolved ARPES enables an unambiguous classification of the gap in the surface spectral weight. The former reveals an abrupt change in the cross section of the adjacent states at a characteristic wave vector that can be attributed to a change in their orbital composition.

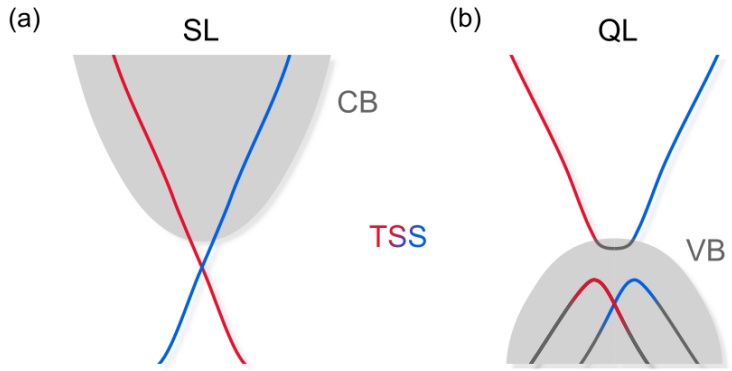

Figure 5.16: Schematic representation of the surface electronic structures of $MnBi_4Te_7$. (a) Freestanding Dirac point below the conduction band states in the case of a septuple layer termination. (b) The Dirac point is embedded within the valence band continuum. The topological surface state (TSS) is depicted in blue and red colors and the conduction (CB) and valence band (VB) states in grey tones.

The latter proves that the sign of the in-plane spin polarization persists across the gap and reverses only after crossing the Dirac point. These conclusions based on experimental data are validated by orbital-projected and spin-resolved DFT calculations. The quintuple layer terminated surface thus exhibits a more complex band structure due to hybridization with valence band states.

Apart from the hybridization gap, the most striking dissimilarity between the two terminations lies in the position of the Dirac point in relation to the trivial states. Fig. 5.16 shows schematic representations of the surface electronic structures of both terminations, which emphasize the characteristics of each. For a septuple layer termination, depicted in (a), a freestanding, linearly dispersing Dirac cone is encountered, with its Dirac point located within the bulk gap. In contrast, in the case of a quintuple layer termination, the Dirac point lies within the region of the projected bulk valence states, as shown in panel (b). This carries direct implications for the observation of transport phenomena in this compound, more precisely, the realization of a half-integer Hall conductance $\sigma_{xy} = \pm e^2/2h$. Based on the observed energetic position, a half-quantized Hall conductance can only be realized through the isolated Dirac point of a surface terminated by a septuple layer, in accordance with experiments previously performed on $MnBi_2Te_4$ [6, 7]. On the other hand, for a surface terminated by a quintuple layer, the edge modes will invariably be buried within the projected bulk valence band states, prohibiting the emergence of a quantized Hall conductance regardless of the chemical potential of the system. These findings can be extended to the corresponding terminations of $MnBi_6Te_{10}$, due to their qualitative similarities in their surface electronic structure.

5.3.3 Temperature dependence and magnetic gap opening in $MnBi_2Te_4$

The predicted hallmark characteristic of a Dirac surface state under the influence of broken time-reversal symmetry is the emergence of a mass gap at the Dirac point. In the case of an antiferromagnetic order, the $\mathbb{Z}_2$ invariant is preserved within the bulk due to the symmetry $\mathcal{S} = \mathcal{T}\mathcal{L}$, which is the combination of a time-reversal operation $\mathcal{T}$ and a translation $\mathcal{L}$ along a vector of the primitive lattice [65]. The response of the topological surface state to the antiferromagnetic order, therefore, depends on the considered surface and its relative orientation with respect to the geometry of the magnetic ordering.

The long-range antiferromagnetic order in $MnBi_2Te_4$ is of A-type, i.e., ferromagnetic intralayer coupling with antiparallel alignment to adjacent layers, as could be shown in chapter 5.2. As a result, on the (0001) surface, a magnetic gap opening of the TSS is expected at the transition to the magnetic ground state. In the paramagnetic phase above T_N, this mass gap should vanish due to the restored invariance to the $\mathcal{T}$ operation. Predicted magnitudes for the energy scale of this mass gap range from several tens of meV up to 88 meV [9, 10, 249]. Despite an enormous experimental effort, it has yet not been possible to unambiguously demonstrate a temperature-dependent evolution from a pristine Dirac state to a gapped TSS in the AFM regime [9, 205, 249–257]. On the contrary, studies often present conflicting results and no consensus has been established as to whether the TSS exhibits a gap feature, regardless of the magnetic state. In particular, it appears that two general types of TSS in $MnBi_2Te_4$ are being reported. One, which is seen as a sharply dispersing feature in the ARPES spectra and which appears as gapless or with a strongly diminished gap (Refs. [205, 249, 250, 252–254, 256]), and one that shows a reduced spectral weight of the TSS and seems to exhibit a mass gap (Refs. [9, 205, 251, 255, 257]). The electronic structure of the $MnBi_2Te_4$ crystals investigated in this work falls in the second category. A temperature-dependent emerging or closing of a mass gap at the Dirac point of the respective TSS could not be demonstrated in either case.

The objective of this section is to analyze temperature dependencies in the surface spectrum, to explore why it is so challenging to identify the formation of a mass gap in the TSS, and to discuss these aspects in the context of the result of the numerous concurrently conducted studies.

Fig. 5.17 (a) shows the ARPES intensity of the (0001) surface of $MnBi_2Te_4$ taken at $T = 11\,\mathrm{K}$, well below the magnetic transition temperature $T_N = 24\,\mathrm{K}$. Despite the rather faint intensity, the photon energy of $h\nu = 6.3\,\mathrm{eV}$ employed here has proven to be the most suitable excitation energy, among those available throughout this study, for observing the TSS. For an overview over a wider photon energy range see Fig. A3 in the appendix. In addition to the TSS, two additional conduction band states can be seen, labeled CB1 and

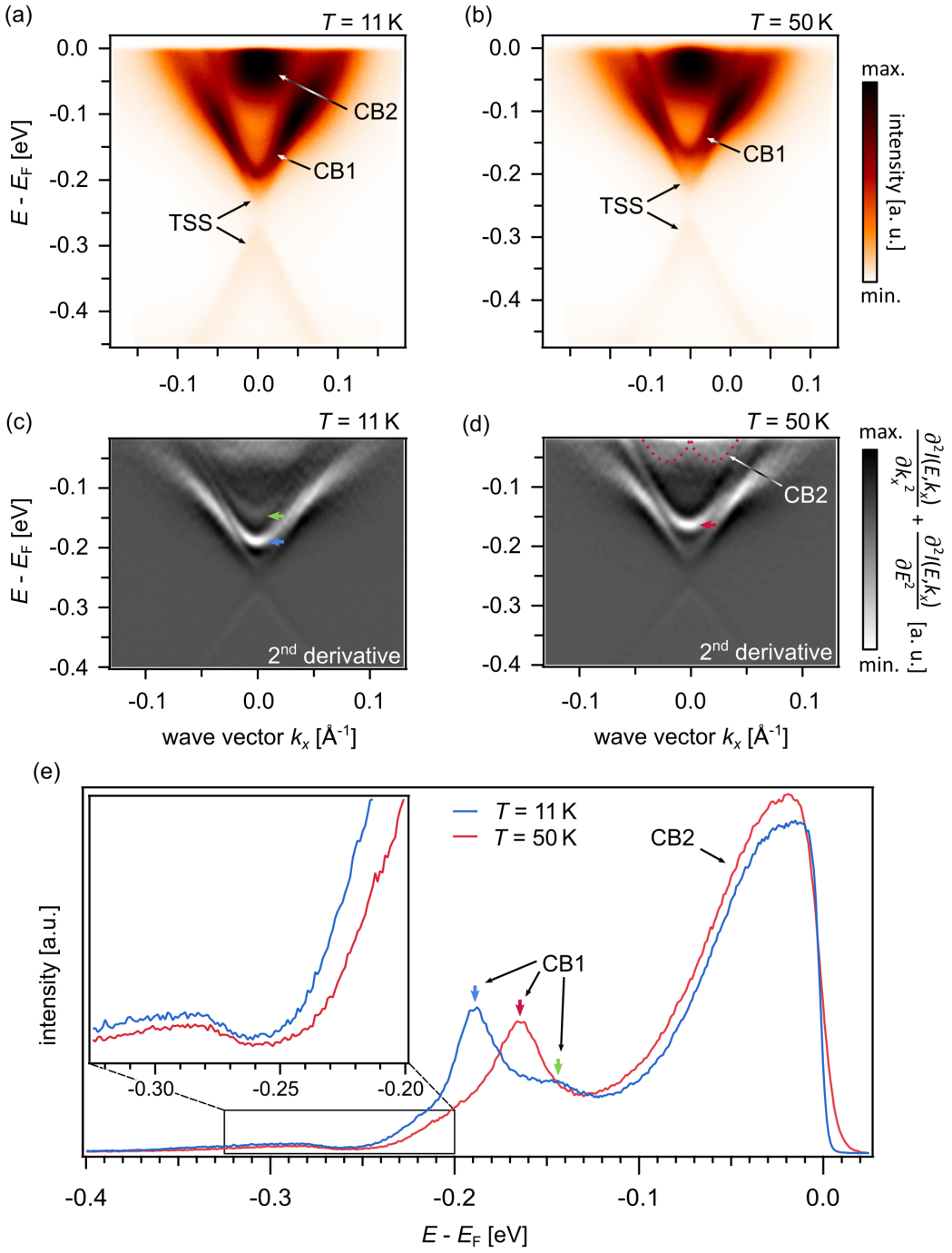

Figure 5.17: Temperature dependence of the surface electronic structure of $MnBi_2Te_4$. (a), (b) ARPES intensity taken at $T = 11\,\mathrm{K}$ and $T = 50\,\mathrm{K}$, respectively. (c), (d) Excerpt of the second derivative along the energy axis of the spectra shown in (a) and (b), respectively. The band bottom of the exchange split conduction band state CB1 is marked with colored arrows. (e) Energy distribution curve at the $\overline{\Gamma}$-point depicting the data taken at $T = 11$ in blue and the measurement at $T = 50\,\mathrm{K}$ in red color. Again, the intensities corresponding to the minima of the CB1 state are indicated by colored arrows. The inset shows a zoomed-in view of the energy range around the Dirac point.

CB2. The former shows an electron-like parabolic dispersion, whereas the latter appears as a patch of intensity, cut off at the Fermi energy.

The spectrum under an increased temperature of $T = 50\,\mathrm{K}$ is shown in panel (b). Both spectra were acquired by taking k_x-k_y-maps in order to ensure a cut at $\overline{\Gamma}$ along k_y. The most recognizable difference to the spectrum below T_N is a shift of the main spectral weight of the CB1 state towards higher energies, whereas no apparent change in the dispersion of the TSS can be detected. To facilitate the identification of any potential differences, the second derivative of each spectrum is shown in Figs. 5.17 (c) and (d). In this way, it can be recognized that CB1 splits into two states below T_N, the minima of which are marked with a green and a blue arrow. At $T = 50\,\mathrm{K}$, the state is restored into one parabolically dispersing band, marked by a red arrow in panel (d). This splitting of CB1 is also observed in EDC taken with $h\nu = 21\,\mathrm{eV}$, displayed in Fig. 5.18 (c), where the increase in its total full width half maximum is indicated by a black line. Above T_N, the width of the total peak remains constant and no changes are observed in the spectra taken at $T = 40\,\mathrm{K}$ and $80\,\mathrm{K}$.

The nature of this state has been debated in numerous publications. On the one hand, it was interpreted as the minimum of the bulk conduction band [249, 250]. On the other hand, photon-energy-dependent studies could not find any significant dispersion along k_z, implying a two-dimensional character of the state [183, 257]. In the latter case, a potential physical origin could be the occurrence of band bending near the surface, which led to similar two-dimensional parabolic bands in Bi_2Se_3 [258]. Fig. 5.18 (a) shows EDC at $\overline{\Gamma}$ for a photon energy range of $h\nu = 20\,\mathrm{eV}$ to $h\nu = 29\,\mathrm{eV}$. In addition to CB1 and CB2, the bulk valence band (BVB) maximum is also indicated. For the latter, a dispersion with varying photon energy can be unambiguously identified, showing two maxima in the displayed range. This periodicity is in line with Refs. [250, 257], in which a similar k_z-dispersion has been observed in the BVB. For CB1, an equivalent evaluation is not as straightforward, since there exist several states within the relevant energy range which exhibit distinct cross-section variations. The two most prominent features are marked by black dashes. Within the limited accuracy, no dispersive behavior can be attributed to these two states. The energetic position and relative distance of these two spectral features fit those of the upper part of the TSS and the lower part of CB1, which is marked by a blue arrow in Fig. 5.17 [257].

A similar effect of shifting spectral weight due to multiple states can also be observed in the energy range of CB2, where towards lower photon energies CB2 is gradually replaced by a second state, presumably the minimum of the bulk conduction band.

The splitting of CB1 below the transition temperature indicates a correlation between the magnetic order and the electronic states in form of exchange interactions. Indeed, it was demonstrated in Ref. [251] that the splitting sets in at T_N and exhibits a power-law behavior.

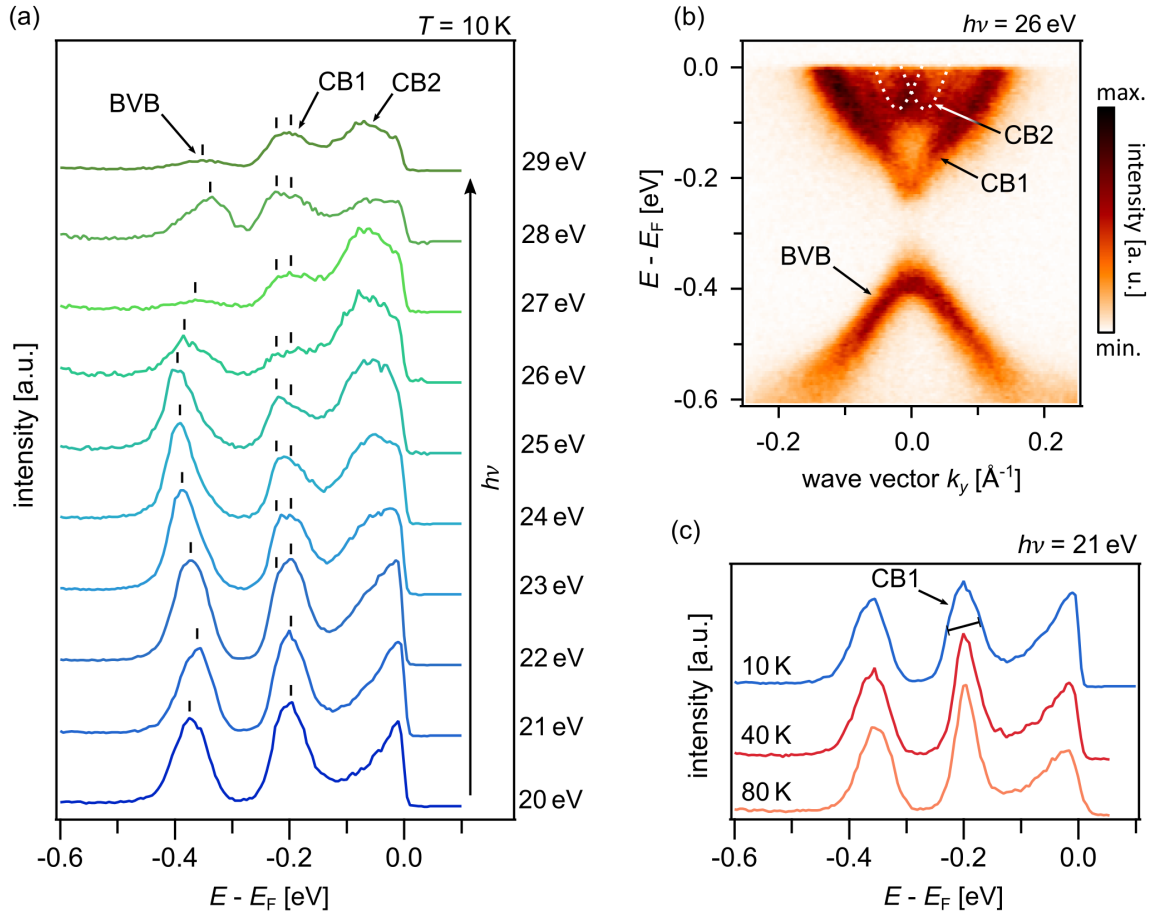

Figure 5.18: Photon energy and temperature dependence in the VUV regime. (a) Photon energy series of the EDC taken at $\overline{\Gamma}$ ranging from $h\nu = 20\,\text{eV}$ to $29\,\text{eV}$. The dispersing band maximum of the bulk valence band (BVB), as well as the main contributors to the spectral weight at the energy position of the lower conduction band state (CB1), are marked by black lines. All spectra were taken at $T = 10\,\text{K}$. (b) ARPES intensity taken at $h\nu = 26\,\text{eV}$. The dispersion of the Rashba-type split upper conduction band state (CB2) is indicated by dotted white lines. (c) Temperature dependence of the EDC at $\overline{\Gamma}$ measured with $h\nu = 21\,\text{eV}$. Spectra taken at $T = 10\,\text{K}$, $40\,\text{K}$, and $80\,\text{K}$ are depicted in blue, red, and orange color, respectively. The increase in the full width at half maximum of CB1 below T_N is indicated by a black arrow.

Fig. 5.17 (e) shows the EDC of both APRES spectra in Fig. 5.17 (a) and (b) for $k_x = 0$. The graphs corresponding to temperatures of $T = 11\,\mathrm{K}$ and $T = 50\,\mathrm{K}$ are depicted in blue and red, respectively. The band minima of the CB1 state are again marked by the correspondingly colored arrows. In addition to the splitting of CB1, a reduction in the intensity of CB2 can be recognized, accompanied by a slight flattening of the peak maximum. In momentum space, the state shows a dispersion with Rashba-like splitting, as indicated by dotted lines in Figs. 5.17 (d) and 5.18 (b) [251, 252, 255]. The outlined parabolas are based on the experimental data in Refs. [249, 253, 256], in which the Rashba-like dispersion is clearly identifiable. The temperature-dependent redistribution of the spectral weight of this state has been reported in Refs. [251, 255] and was attributed to a lifting of the degeneracy at the Kramers point due to the onset of magnetic ordering.

Focussing now on the TSS, the inset in Fig. 5.17 (e) shows a zoomed-in view on the energy region around the Dirac point location. The topological state has a comparatively low spectral weight, which impedes a clear assertion on possible temperature dependencies. In addition, the splitting of CB1 results in a shift of its spectral weight towards the region of interest, partially superimposing the signal of the TSS. Moreover, the top of the valence band exhibits a similar temperature-dependent splitting, as can be seen in Refs. [205, 252, 253], further complicating an unambiguous analysis of the TSS.

One possible approach involves the fitting of each spectral component of the EDC by Voigt profiles and deducing any changes the TSS undergoes from a change in the fitting parameters [251]. The faint spectral intensity combined with the number of necessary profiles in order to account for all spectral components, which entails a proportional number of free parameters, impedes curve fitting as a sensible means of an examination of possible temperature dependencies. In conclusion, no temperature-dependent behavior of the TSS can be identified in the surface spectra of $MnBi_2Te_4$, despite sample temperatures well below and above the magnetic ordering temperature T_N.

Regarding this lack of an experimental fingerprint, the explanatory approaches given in the numerous publications diverge quite strongly as they try to account for the diverse observed phenomena. In the following, selected interpretations will be discussed and their assertions will be contrasted with the experimental findings presented in this thesis. We return to the previously mentioned Dirac state, which shows a sharp and linearly dispersing TSS at similar or equal photon energies to those used here [249, 250, 253]. In the corresponding publications, several proposals have been made, suggesting a deviation of the surface magnetic ordering from that of the bulk [249, 250, 253]. These presumed surface magnetic structures include a paramagnetic phase at the surface due to disordered spin moments, A-type antiferromagnetism along certain in-plane directions, which gives rise to a mirror symmetry protected TSS, as well as G-type ordering, in which case the $\mathcal{S} = \mathcal{T}\mathcal{L}$

symmetry holds along all three lattice vectors and thus induces a $\mathcal{S}$ protected Dirac state on all surfaces [249, 250, 253].

For an in-plane orientation of the surface magnetic moments, a weakening of the interlayer coupling is assumed for the surface spins to overcome the magnetic anisotropy. The resulting interaction extension to the Hamiltonian takes the form $m\sigma_x$ and consequently shifts the Dirac point perpendicular to the magnetic moments. This scenario can be excluded by the XMCD and XMLD measurements presented in chapter 5.2. Neither could a linear dichroism signal between two perpendicular oriented in-plane directions be observed nor could a residual XMCD signal be observed under grazing incidence. The latter observation can only be explained if the moments are arranged in such a way that they compensate each other or if they are, by accident, aligned perpendicular to the plane of light incidence. Moreover, the applied TEY detection mode is rather surface sensitive, a property that is further enhanced in grazing incidence geometry, thus reinforcing the conclusion by constraining the probed volume closer to the surface.

Additionally, the energy splitting at the Kramers point of the CB2 state also indicates an out-of-plane surface magnetic order [251, 255]. The occurrence of a Rashba-split state in a system with preserved bulk inversion symmetry implies a surface character of said state. An in-plane magnetic ordering on the surface would, therefore, induce a relative displacement of the two parabolas. Instead, an energy splitting at the crossing point occurs, as reported in Refs. [251, 255], which strongly hints towards the presence of an out-of-plane magnetic moment at the surface.

A G-type antiferromagnetic order and thus a $\mathcal{S}$ symmetry protection at the (0001) surface is highly improbable due to the strong ferromagnetic intralayer coupling of the magnetic moments [9, 249]. Moreover, a G-type spin arrangement fails to account for the residual XMCD signal observed in normal incidence, as seen in Fig 5.4 (c).

In Ref. [205], a model was proposed which could explain the discrepancies in the magnitude of the observed mass gap. According to it, structural deformations within the topmost SL, mainly variations of the interblock vdW spacing, should have a significant influence on the gap size in the magnetic ground state. Like in other vdW-layered topological systems, an increase in the vdW spacing induces a relocalization of the TSS towards deeper-lying septuple layers, which in turn attenuates the effective magnetic moment on the TSS due to the antiparallel moment of the second layer [259]. According to this study, the effect should be strong enough to cause a full closing of the mass gap at an increased vdW spacing of about 15 %, explaining the inconsistent observations in the literature [205].

6 Concluding discussion & outlook

The discovery of topological insulators constitutes a landmark in modern condensed matter research. Continuous breakthroughs in this field enrich the playground for researchers with new exotic quantum phenomena. Although the principles of topological non-trivial phases spread out to other fields like optics, acoustics, electronic circuits, or classical mechanics, the primary focus of contemporary research remains in its field of origin, that is, condensed matter physics [260–263].

While most approaches to a practical application of topological materials envisage a utilization of their unique transport properties, photoemission spectroscopy remains one of the major experimental techniques for the identification of new topological materials, or even new topological phases, and the study of their detailed electronic properties. The appeal of photoemission naturally lies in the direct visualization of the electronic states near the surface in momentum space. Yet, it offers a more sophisticated access to the electronic structure by exploring additional parameters of the experiment like photon energy dependencies, matrix element effects in conjunction with symmetry considerations, lineshapes of core levels, resonant excitation, temperature dependencies, and spin-resolved measurements. Throughout this work, these extensions to the conventional ARPES experiment were applied to two prominent materials and it was demonstrated that they are essential to acquire a comprehensive understanding of the complex electronic structure and to unambiguously confirm the relevant topological features. In this last chapter, the core features of both systems are first compared, after which the main results of this work are summarized and an outlook on future scientific avenues is given.

This thesis addresses the electronic structure of the two material systems HgTe and $(MnBi_2Te_4)(Bi_2Te_3)_n$ by a detailed investigation employing comprehensive ARPES experiments. These experiments allow to put the theoretically expected topological properties of the electronic band structures of both systems to scrutiny. Placing these findings in a common context, one can highlight not only the obvious similarities but also the diverse disparities between the two. In principle, both materials were investigated with regards to similar aspects like their inverted bulk band structure, the topological surface state, the orbital composition of these states, the influence of the cation d-states on the valence band regime, and temperature dependencies. However, the performed experiments as well as their evaluation tend to differ for the two systems due to their different properties.

The two systems are primarily in the limelight of current research as they both exhibit an inverted bulk band structure with a TSS close to or at the Fermi level. HgTe represents an example for a prototypical 3D $\mathbb{Z}_2$ TI, whereas the inclusion of magnetic adatoms in $(MnBi_2Te_4)(Bi_2Te_3)_n$ induces a breaking of the TRS, making the emerging topological phase dependent on the interplay of the magnetic ordering and the dimensionality of the system [10, 182]. Here, the latter was fixed to a 3D regime as the investigated samples were bulk crystals. For HgTe, the different orbital characters of the states participating in the bulk band inversion offer a spectroscopic access through symmetry considerations of the matrix element. In the second compound, $(MnBi_2Te_4)(Bi_2Te_3)_n$, this inversion occurs between states with equal orbital symmetry, which impedes an equivalent consideration of the corresponding bulk states.

Although in both materials the topological non-triviality is based on the specific energetic ordering of *p*- and *s*-derived states near the Fermi level, it was found that more localized *d*-states also play an integral role. In HgTe, a pronounced $p-d$ hybridization between the *p*-derived valence band states and the Hg $5d$ states results in a level repulsion as well as in an admixture of *d*-orbital character into said valence states, reducing the effective SOC. Consequently, an accurate description of this $p-d$ hybridization is decisive for a quantitative understanding of the global valence band structure. For $(MnBi_2Te_4)(Bi_2Te_3)_n$, the primary influence of the Mn $3d$ states on the surface electronic structure can be observed when entering the magnetically ordered state. While no unambiguous statements could be made regarding the TSS, a clear exchange splitting can be observed in the energetically adjacent surface states.

This last aspect is directly related to the investigated temperature dependencies. At the start of this thesis, the temperature-dependent TRS-breaking and gap opening in $(MnBi_2Te_4)(Bi_2Te_3)_n$ formed a major objective in the investigation of these magnetic TI. In practice, however, an intricate surface electronic structure as well as a reduced transition temperature in the compounds with $n \geq 1$ form obstructions to an unambiguous observation of this expected behavior. For this reason, the effects of magnetic order on the electronic structure can only be observed in terms of the non-topological states. In HgTe, on the other hand, a different temperature dependency could be identified that manifests itself in a significant shift of the chemical potential due to an asymmetric DOS at the Fermi level.

In addition to those already mentioned, there are other aspects such as the layered and heterostructural architecture of $(MnBi_2Te_4)(Bi_2Te_3)_n$ compared to the more three-dimensional and cubic structure of HgTe. Rather than comparing the two systems further, the following outlines the key findings of this work for each system and presents them along with possible prospects for their future exploration.

Chapter 4 introduced a renewed approach to the surface preparation of MBE-grown HgTe thin films, previously applied only to vdW-layered compounds [129]. The deposition and subsequent mechanical exfoliation of a protective capping layer allow for *ex situ* transport and storage of the samples without degradation of the actual sample interface. This, in turn, allows for a photon-energy-dependent investigation of the k_z-dispersive bulk band structure of HgTe through the use of synchrotron radiation. In addition, a point that has long proved challenging, an accurate description of the band structure through DFT, could be addressed using the experimental data as a reference. In this context, the influence of $p-d$ interaction on the low lying Hg $5d$ semicore levels and the Te $5p$-derived valence states and its consequent relevance in the description of the bulk band structure could be demonstrated. The effect appears in all II-VI semiconductors due to the presence of BIA in the zincblende structure but is particularly pronounced in HgTe due to the shallow energy position of the Hg $5d$ states [157]. The effect of hybridization on the low-energy states is twofold. On the one hand, it raises the energy of the valence band maximum due to a level repulsion. On the other hand, the admixture of d-orbital character into the p-derived valence states reduces the effective SOC. Experimentally, the hybridization manifests itself in a fine structure splitting of the spin-orbit subshells as well as a finite band dispersion of the cation d-shells. Additionally, an empirical law was used to estimate the magnitude of the $\Gamma_{8,\mathrm{hh}}$-subband splitting along ΓK and a substantial degree of agreement was found between the values from the experimental data and the calculation based on the HSE06 functional.

The orbital composition of the bulk electronic structure was probed utilizing the dipole selection rules which allow for selective excitations of electrons from orbitals of a certain symmetry, that is, even or odd with regard to the considered mirror plane. In conjunction with orbital-projected DFT calculations, it could be shown that along ΓK p-polarization probes mainly the even p_z-orbitals, whereas s-polarized light excites the odd p_y-states. Near the top of the Γ_6-state, a sudden change in orbital composition could be detected, which manifests itself in a reduction of the cross section. This change occurs at the merging points of the TSS with the bulk state and can be attributed to a switch to s-character at the maximum of the Γ_6-band. It is thus a consequence of the non-trivial topology of this system and hence constitutes, apart from the presence of the topological surface state, a direct experimental fingerprint of the bulk band inversion in HgTe. The comprehensive spectroscopic findings of this work may serve as an important benchmark for future experimental or theoretical studies of topological effects in this or in a variety of related systems [264].

The process of discovering a novel topological phase often involves a theoretical prediction, which is followed by a subsequent search for a suitable material system that may host these novel physics. HgTe stands out in this cycle by providing a platform in which several distinct topological classes can be realized in a single material class by tuning external

parameters like film thickness, lattice strain, and doping, all of which can be manipulated via the growth by MBE [17, 18, 20, 21]. The results presented in this work lay the foundation for a spectroscopic exploration of these phenomena. One such venue is the formation of massless Kane fermions, which can be encountered in the semiconductor-to-semimetal transition of $Hg_{1-x}Cd_xTe$ [18]. The concentration- and temperature-dependent transition involves energy scales that can be resolved by the experiment, making ARPES the ideal technique to investigate the changes in band order and orbital composition that accompany the transition [136]. Another pathway is the exploration of the thickness-dependent transition from 3D TI behavior to the 2D quantum well state. Below a sample thickness of 18 nm, a significant subband splitting of the $\Gamma_{8,\mathrm{hh}}$-state sets in, which constitutes another approach of breaking the semimetallic ground state of HgTe and of opening an energy gap necessary for the observation of the topological transport properties [265].

Many tools introduced in the examination of the electronic structure of HgTe are utilized in the investigation of the second material system in this thesis, $(MnBi_2Te_4)(Bi_2Te_3)_n$. This heterostructural series provides the combination of the topological properties of its parent compound Bi_2Te_3 and a long-range magnetic ordering through the incorporation of Mn atoms into the lattice. The intrinsic magnetic ground state of these systems facilitates a spectroscopic examination when compared to doped systems like $V:(Bi_{1-x}Sb_x)_2Te_3$, in which the doping-induced disorder impedes the acquisition of high-quality photoemission data. In addition, the vdW-layered structure of these systems allows for a manipulation of the magnetic ground state by intercalation of non-magnetic (Bi_2Te_3)-layers in the vdW gaps.

Chapter 5.2 examines the electronic and magnetic properties of the Mn species in $MnBi_2Te_4$ and $MnBi_4Te_7$. The transition metal is addressed through the elemental selectivity of resonant excitation and X-ray absorption techniques. Regarding the electronic properties, XPS and ResPES show strong indications for a local screening effect through the Te ligand as well as non-local screening by neighboring octahedral units. Moreover, the representation of the partial DOS of Mn, acquired through ResPES, helps to exclude a direct hybridization of the states involved in the non-trivial ordering with the localized Mn states. This is evidenced by the energetic separation of the occupied Mn majority states from the Fermi level, where the inverted bands and the TSS are located. Qualitatively, the Mn species in $MnBi_2Te_4$ and $MnBi_4Te_7$ exhibit identical behavior, owing to an equal immediate chemical environment within the septuple layer.

Regarding the magnetic ordering, XMCD and XMLD unveil diverging ground states in the two compounds due to the additional spacing between the monoatomic Mn layers in $MnBi_4Te_7$, which alters the interlayer coupling. In $MnBi_2Te_4$, a combination of out-of-plane linear dichroism and a nearly vanishing remanent XMCD signal in normal incidence

represents strong indications for an A-type AFM order as the magnetic ground state. In contrast, $MnBi_4Te_7$ exhibits, apart from a likewise out-of-plane anisotropy, a substantial finite out-of-plane XMCD signal in remanence. At first glance, the latter finding appears to be in contrast to other publications which found antiferromagnetic behavior in $MnBi_4Te_7$ and even in $MnBi_6Te_{10}$ [216, 217]. A model proposed by Ref. [220] accounts for the diverging observations by describing $MnBi_4Te_7$, and to an extent also $MnBi_6Te_{10}$, as systems whose magnetic properties depend on the relative strength of the exchange coupling J and the uniaxial anisotropy K. The temperature-dependent evolution of K explains the transition to a more ferromagnet-like behavior at temperatures well below the initial transition temperature T_N. In addition, the previously mentioned cation antisite defects and Mn vacancies may provide a rationale for these divergent magnetic behaviors by causing different ground state properties by altering the magnetic interlayer exchange coupling, making the magnetic properties of a particular crystal additionally dependent on the details of the lattice disorder.

In summary, the data presented here, along with other studies in the literature, offer a picture of $MnBi_4Te_7$ that exhibits AFM-like behavior just below the ordering temperature that undergoes a spin-flip transition at even lower temperatures to a state with FM-like ordering [28, 220, 221].

The final section of this work is dedicated to the intricate surface electronic structure by combining spatially resolved, photon energy- and polarization-dependent measurements as well as spin-resolved ARPES. Chapter 5.3.1 introduces a procedure to assign the surface spectra to their respective surface termination. An electronic state of the Mn species was chosen as an experimental fingerprint for the stacking order near the surface, since a particular stacking sequence of the topmost vdW layers uniquely corresponds to a certain depth of the first Mn layer, attenuating its signal accordingly. The Mn $3d$ state constitutes an electronic state which is accessible by photon energies that also have favorable cross sections for the valence states and, therefore, allows for a simultaneous detection of the two, without the necessity of changing the photon energy. Only for laser-based ARPES, conventional VUV photoemission has to serve as a reference, due to the limited excitation energy of the former. Thus, a self-contained route for the identification of the distinct surface spectra could be established and the nine surface spectra of the first three members of the $(MnBi_2Te_4)(Bi_2Te_3)_n$ series could be assigned to their respective terminations.

Subsequently, the diverging properties of the topological surface state on the two terminations of $MnBi_4Te_7$ were investigated. On a surface terminated by a $(MnBi_2Te_4)$ septuple layer, circular dichroic ARPES unveils a virtually linear dispersion of the TSS whose Dirac point is located in the projected bulk band gap. In contrast, the topological state on a (Bi_2Te_3)-terminated surface exhibits a spectral weight gap in the energy range of its upper branches due to hybridization with the valence bulk states, as could be demonstrated using

photon-energy-dependent ARPES supplemented by orbital-projected DFT surface calculations. Additionally, the Dirac point of this termination is located within the bulk continuum, rendering it unfit for the observation of transport phenomena involving a magnetic gap opening. This, of course, entails implications for the realization of transport phenomena in all heterostructural members of the series. Although their electronic structure is not determined by the topmost layer alone and the layers underneath the surface also have an influence on it, equivalent terminations in different systems, such as $MnBi_4Te_7$ and $MnBi_6Te_{10}$, nevertheless bear qualitative similarities.

Lastly, the controversial predicament of the magnetic gap opening in $MnBi_2Te_4$ was addressed. The surface spectra showed clear indications of an influence of the magnetic ordering on the trivial states in the form of an exchange splitting of CB1 as well as a shift in the spectral weight of CB2, that can be attributed to a lifting of the degeneracy at the Kramers point of this Rashba-like state. Despite these clear fingerprints of the influence of the magnetic ordering on the surface electronic structure, the spectra do not allow for unambiguous statements regarding the temperature-dependent behavior of the TSS. This is due to a low cross section of the state in combination with a temperature-dependent overlap with the CB1 state, in particular, the lower part of the exchange split state intrudes the energy region of the Dirac cone. To address this problem unambiguously, it is, therefore, advisable to choose a system that has a free-standing Dirac point that can be examined separately from any other perturbing states. As demonstrated in this work, $MnBi_4Te_7$ meets this requirement, however, the reduced interlayer coupling and the consequently lowered Néel temperature demands an equally lower measurement temperature, which could not be met by the experimental setups employed in this thesis.

Concerning this issue, it should be mentioned that some very recent publications succeeded in demonstrating a temperature-dependent gap opening in the ferromagnetic members of this modular series [219, 266]. In Ref. [219], it was found that the magnetic ordering in $MnBi_6Te_{10}$ depends on the details of the applied growth routine and thus crystals can be synthesized in a controlled manner that exhibit AFM or FM ordering. This, in turn, is consistent with the above observation that the ferromagnetic tendencies of members with higher n depend on the details of the crystal structure and its disorder. For $MnBi_6Te_{10}$ with a FM ordering, a mass gap at the Dirac point can be observed, the magnitude of which follows a power-law behavior, whereas in AFM $MnBi_6Te_{10}$ no temperature-dependent evolution can be detected and the Dirac point remains preserved below T_N [219]. In the same vein, Ref. [266] also demonstrates a similar behavior of the TSS on the ($MnBi_2Te_4$)-termination of $MnBi_8Te_{16}$, which exhibits a FM ground state. The gap likewise vanishes in the paramagnetic phase. Lastly, there are recent, unpublished experiments at the Chair for Experimental Physics VII, conducted by P. Kagerer, on a monolayer $MnBi_2Te_4$ on bulk Bi_2Te_3. This sys-

tem is effectively an extreme case of $(MnBi_2Te_4)(Bi_2Te_3)_n$ for $n \to \infty$, retaining a single SL as the terminating layer [267]. As in the two previously mentioned studies, a temperature-dependent opening of a gap at the Dirac point can also be observed in such a system. All three of these examples evidence that a magnetism-induced mass gap can indeed be observed in ferromagnetic ($MnBi_2Te_4$)-derived systems. Why this type of gap remains elusive in the AFM phase remains an open question.

$MnBi_2Te_4$ and its derivates are novel material platforms that attracted a great deal of attention due to the combination of intrinsic magnetism and topological non-trivial band ordering. The results of this thesis, together with experiments by collaborators [9, 28, 225] and consistent with other publications [10, 25, 32, 208, 217, 221, 222, 245, 249–252, 254], establish the $(MnBi_2Te_4)(Bi_2Te_3)_n$ series as the first instance of intrinsic magnetic topological materials. In particular, it has been experimentally demonstrated that the progenitor $MnBi_2Te_4$ represents a novel topological phase, the antiferromagnetic TI [65]. Despite numerous publications, there are still several experimental avenues to be explored. In the future, this material platform could open new ways to explore magnetic topological effects such as the quantum anomalous Hall effect, axion electrodynamics, or the topological magnetoelectric effect in a well-controlled and versatile system [21, 23, 268]. Higher number members like $MnBi_8Te_{13}$ have already been synthesized and shown to exhibit ferromagnetic order below $T_C = 10.5\,K$ [222]. Further separation of the magnetically active vdW layers would ultimately culminate in a vanishing interlayer coupling, making the system a stacking of independent 2D ferromagnets.

In the opposite direction, in the thin film limit, transport studies on exfoliated single crystals show indications for the QAH and the axion insulator state in odd- and even-layered films, respectively [6, 7]. Additionally, in a forced ferromagnetic configuration, $MnBi_2Te_4$ is expected to exhibit a type-II Weyl semimetal phase [10]. Highly controlled synthesis methods like MBE, which are already being reported on, will facilitate the exploration of the thin film properties by providing sample growth with adjustable film thickness, stacking sequence, and the possibility of surface or bulk doping [269, 270].

Furthermore, like in Bi_2Te_3, the cations and anions can be substituted by Sb and Se, respectively, creating the isostructural compounds $MnBi_2Se_4$ and $MnSb_2Te_4$, as well as its $n = 1$ member $MnSb_4Te_7$. All three compounds have been synthesized and exhibit magnetic and topological properties similar to their $MnBi_2Te_4$ counterparts [271–273]. Recent studies showed that the cation intermixing of Mn and Sb in $MnSb_2Te_4$ alters the ground state of the system, favoring a ferromagnetic interlayer coupling with increasing antisite defects [274, 275]. Stabilizing the ferromagnetic order could enable the realization of a TRS-breaking type-II Weyl semimetal phase in $MnSb_2Te_4$ [276]. The alloying of $MnBi_2Te_4$ and $MnSb_2Te_4$ can, therefore, in addition to a tunability of the position of the chemical potential

like in $(Bi_{1-x}Sb_x)_2Te_3$, be used to alter the magnetic properties of the system [277, 278].

Given all these opportunities to achieve new quantum phases by fine-tuning the material parameters, the next logical step in the exploration of ($MnBi_2Te_4$)-based topological insulators is controlled sample synthesis using MBE. Furthermore, a developed growth method also opens up the possibilities for characterization by means of transport experiments. Here, the energetic position of the Dirac point with respect to the Fermi level and the bulk bands, in particular, are essential for the implementation of $MnBi_2Te_4$-derived materials in transport devices. The results of this work have illustrated the effectiveness of PES in addressing the electronic structure of single crystals as well as MBE-grown samples, thus pointing to the feasibility of PES as an auxiliary method for device optimization. Like over the course of the last decade, photoemission spectroscopy with all its extensions will continue to provide deep insights into the electronic structure of topological materials to sustain seminal research.

Appendix

In this appendix, data sets are presented that could not be shown in their entirety in the main body of this thesis. For HgTe, these are a more comprehensive compilation of the k_z-dependence of the ARPES intensity of the bulk valence and Hg $5d$ semicore states as well as direct comparisons between the experimental spectra along KΓX and DFT bulk calculations utilizing different functionals. For $(MnBi_2Te_4)(Bi_2Te_3)_n$, this includes a complete angle-resolved photon energy series of $MnBi_2Te_4(0001)$ and of the quintuple layer termination of $MnBi_4Te_7(0001)$. Parts of these four figures were presented in chapters 4.3, 5.3.3, and 5.3.2.

Fig. A1 shows soft X-ray ARPES spectra of HgTe extracted from the k_z-converted photon energy series displayed in Fig. 4.3 (a). Panel (a) displays a representation of the bulk Brillouin zones stacked along k_z in order to visualize the position of the chosen high-symmetry paths in momentum space. Figs.A1 (c)-(f) show alternately the electronic structure along ΓKXKΓ and XKΓKX. A clear dispersion in the semicore Hg $5d_{5/2}$ state at $E - E_F = -8\,\text{eV}$ is discernable. Along k_x, maxima can be identified at the K-points, which simultaneously represent the wave vectors where the valence bands exhibit their global minimum. This correlation between the dispersions of the valence and semicore states represents one manifestation of the occurring $p-d$ hybridization.

Fig. A2 displays the comparison between the experimental spectra along ΓK and ΓX and all four functionals discussed throughout the main body of this work. This presentation thus complements Fig. 4.6 in section 4.3 in which only the HSE functional was directly compared to the experimental data and the calculations were contrasted to each other.

Fig. A3 presents the photon energy series on $MnBi_2Te_4$ ranging from $h\nu = 20\,\text{eV}$ to $h\nu = 31\,\text{eV}$. In principle, the spectra show the same spectral features as the previously discussed laser-based data, although the most prominent feature of each spectrum depends strongly on the particular photon energy. Concerning the conduction band states, for example, at $h\nu = 20$ the most pronounced feature is the CB1 state, whereas CB2 is mostly visible at $h\nu = 27\,\text{eV}$. The energy distribution curves in Fig. 5.18 (a) correspond to cuts extracted at $k_y = 0$ of the first ten panels, that is, at photon energies $h\nu = 20\,\text{eV}$ to $h\nu = 29\,\text{eV}$.

Fig. A4 shows the complete angle-resolved data sets corresponding to the extracted intensities of selected regions of interest, presented in Fig. 5.13 (e). The overview of all considered photon energies highlights the photon energy- and momentum-dependent shift in the spectral weight of these spectra, which can be linked to a change in orbital character at these characteristic wave vectors, as has been discussed in chapter 5.3.2.

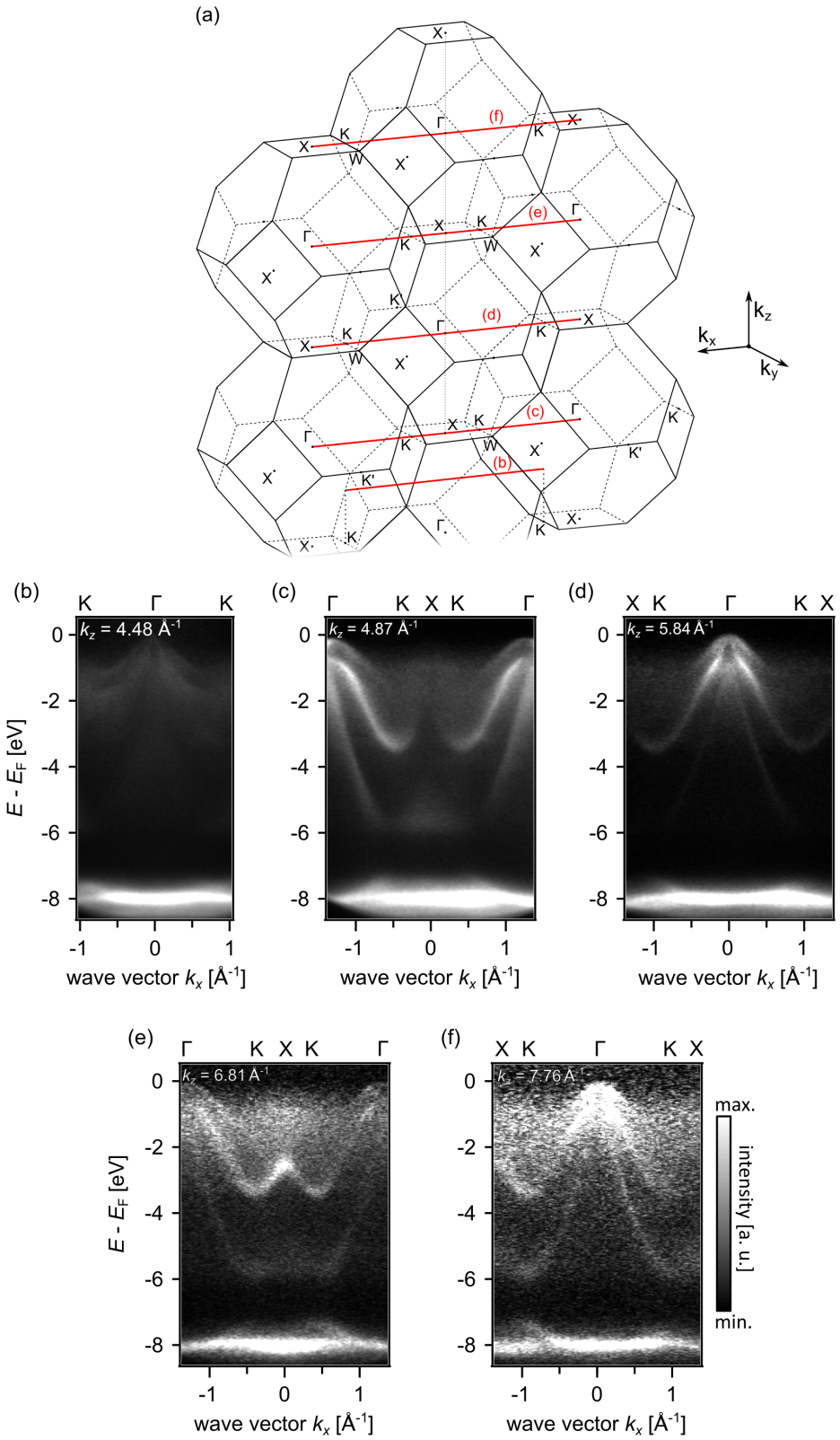

Figure A1: k_z-dependent electronic structure of HgTe(001). (a) Bulk Brillouin zones stacked along k_z in order to demonstrate the position of the subsequent spectra in momentum space. The probed high-symmetry cuts are indicated by red lines and correspondingly labeled. (b)-(f) Photon energy-dependent ARPES spectra converted to show the data as a function of the perpendicular wave vector component k_z. Consequently, the spectra correspond to true high-symmetry cuts in momentum space whose position is indicated in (a).

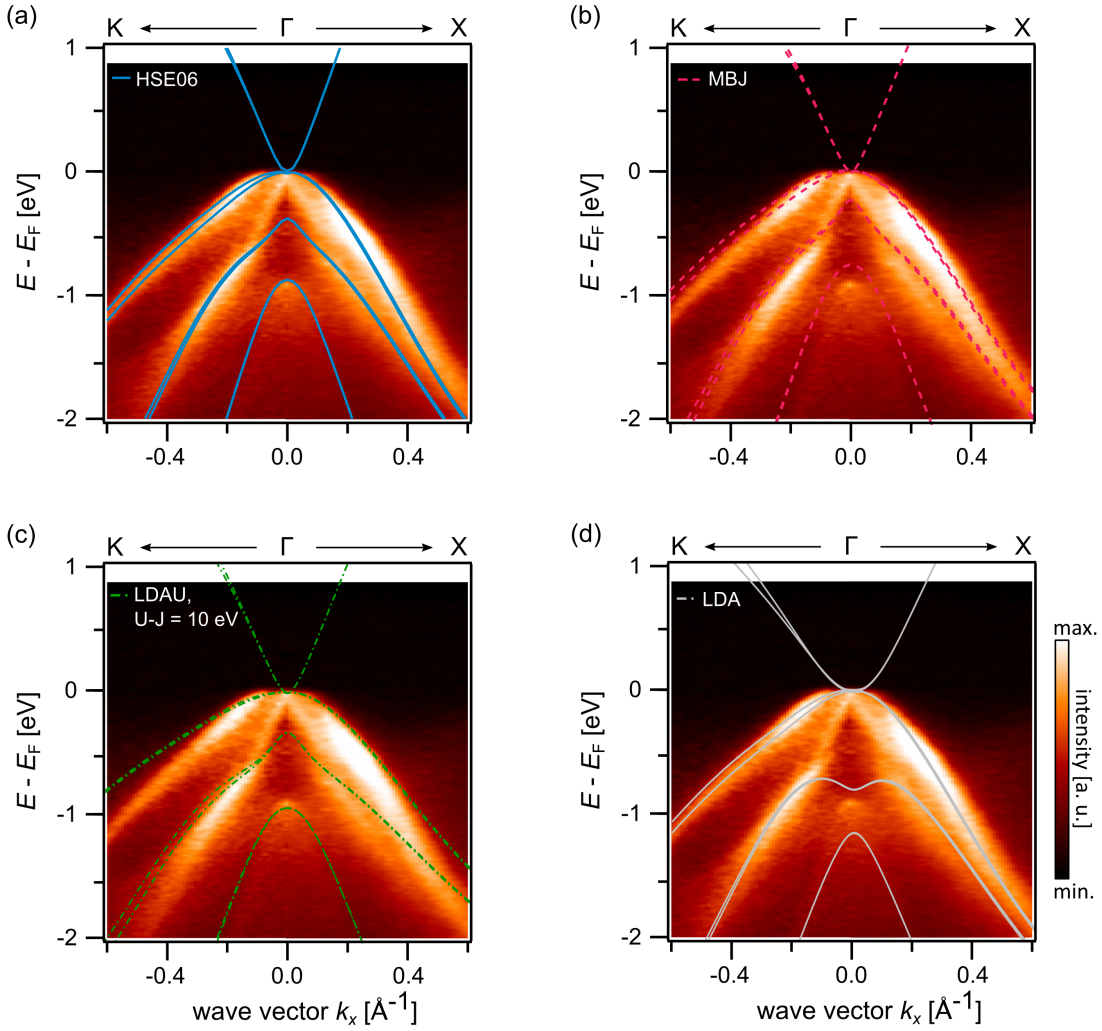

Figure A2: Comparison of experimental data and DFT calculations utilizing various functionals. Each spectrum shows the electronic structure along ΓK and ΓX for $k_{\parallel} < 0$ and $k_{\parallel} > 0$. In each panel, the experimental data is overlaid by the corresponding bulk calculation. The applied functionals are (a) HSE06, (b) MBJ, (c) LDA+U, and (d) LDA.

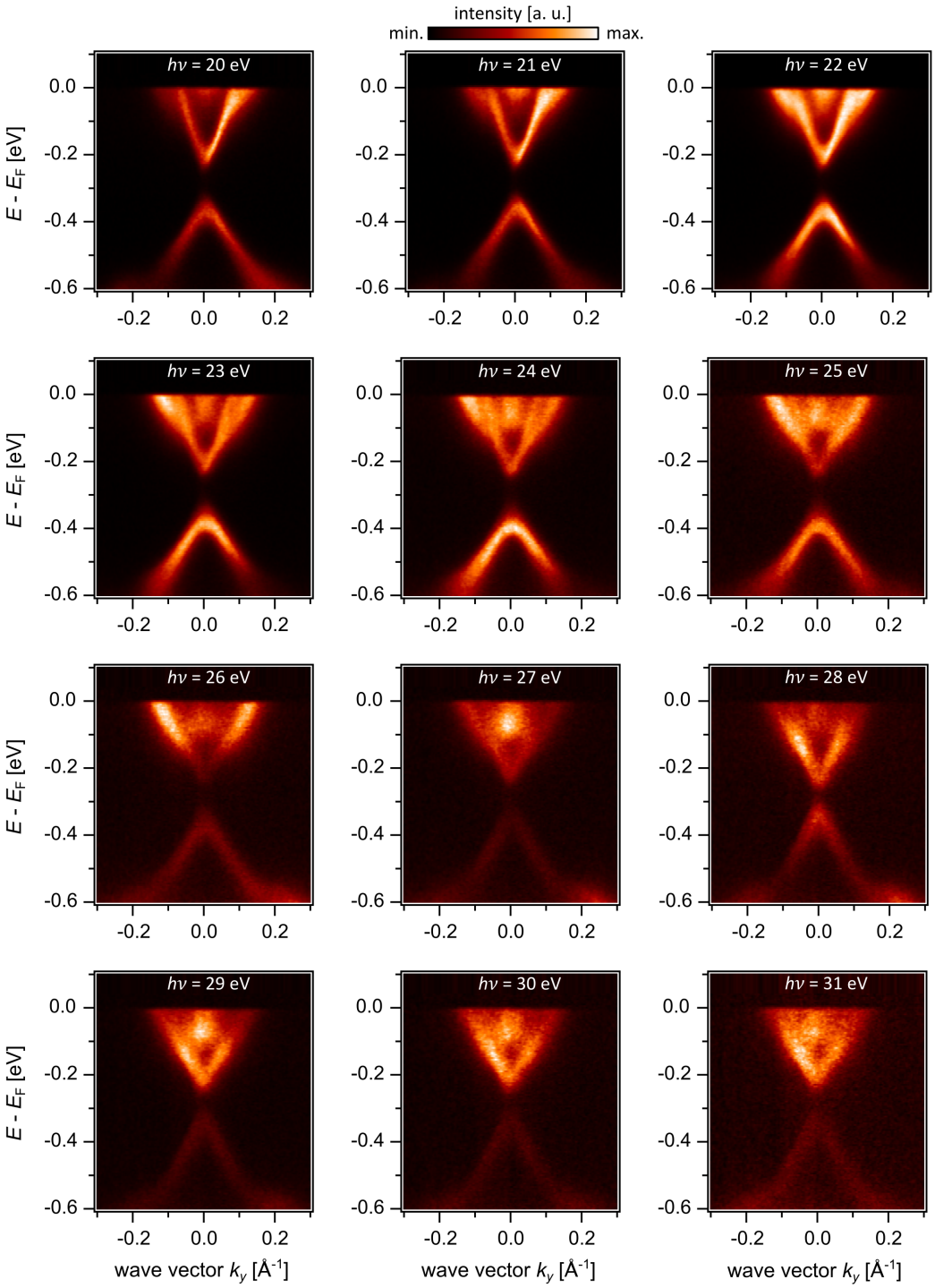

Figure A3: Photon energy series on $MnBi_2Te_4(0001)$. The series ranges from $h\nu = 20\,\mathrm{eV}$ to $h\nu = 31\,\mathrm{eV}$. The applied photon energy is denoted in the corresponding spectrum.

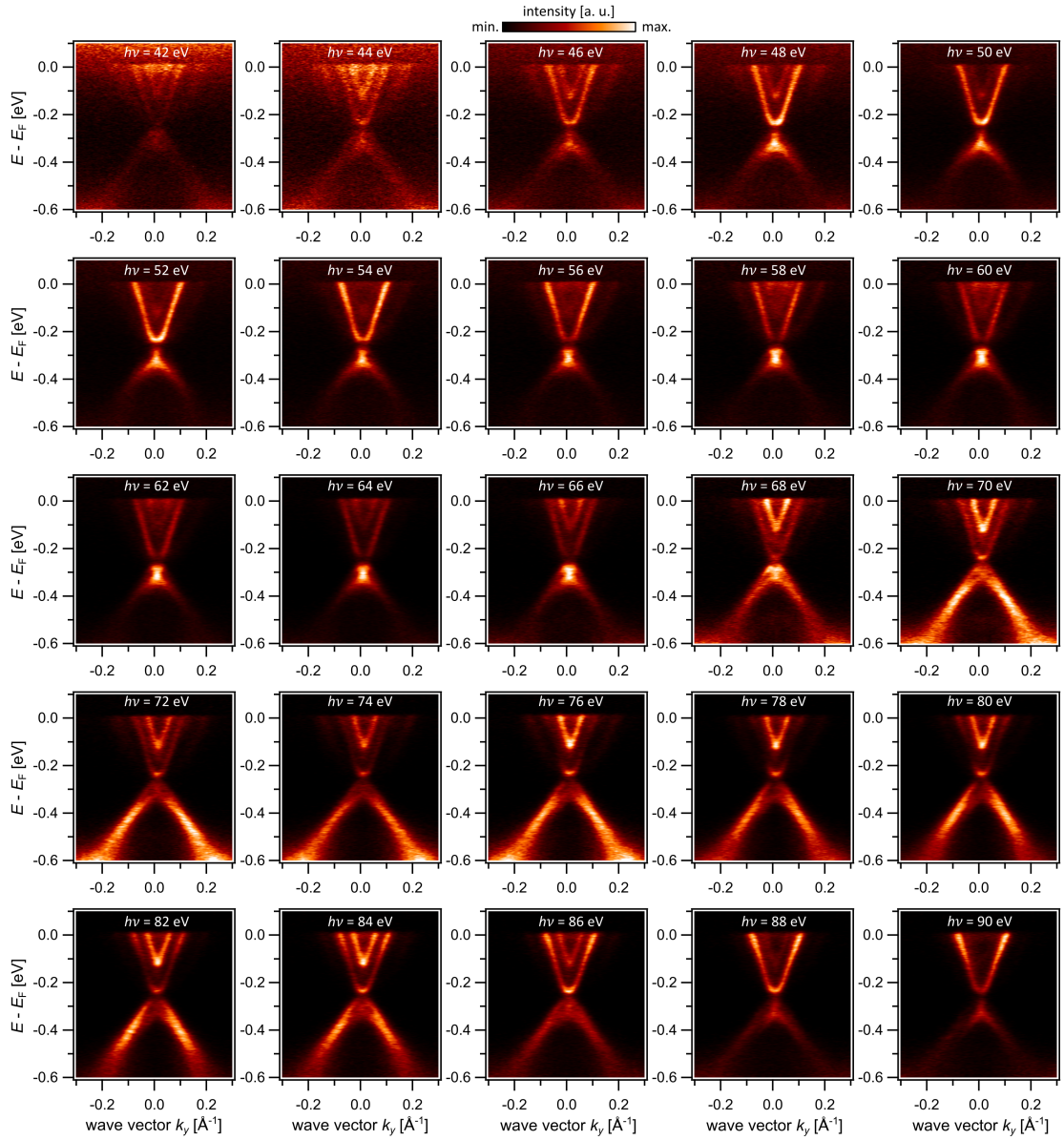

Figure A4: Photon energy series of the quintuple layer termination of $MnBi_4Te_7(0001)$. The series ranges from $h\nu = 42\,\text{eV}$ to $h\nu = 90\,\text{eV}$. The applied photon energy is denoted in the corresponding spectrum.

Bibliography

[1] M. Fruchart and D. Carpentier, "An introduction to topological insulators", Comptes Rendus Physique **14**, 779–815 (2013).

[2] B. Jeckelmann and B. Jeanneret, "The quantum Hall effect as an electrical resistance standard", Reports on Progress in Physics **64**, 1603 (2001).

[3] D. Aasen, M. Hell, R. V. Mishmash, A. Higginbotham, J. Danon, M. Leijnse, T. S. Jespersen, J. A. Folk, C. M. Marcus, K. Flensberg, and J. Alicea, "Milestones toward Majorana-based quantum computing", Physical Review X **6**, 031016 (2016).

[4] H. Ren, F. Pientka, S. Hart, A. T. Pierce, M. Kosowsky, L. Lunczer, R. Schlereth, B. Scharf, E. M. Hankiewicz, L. W. Molenkamp, B. I. Halperin, and A. Yacoby, "Topological superconductivity in a phase-controlled Josephson junction", Nature **569**, 93–98 (2019).

[5] C.-Z. Chang, W. Zhao, D. Y. Kim, H. Zhang, B. A. Assaf, D. Heiman, S.-C. Zhang, C. Liu, M. H. Chan, and J. S. Moodera, "High-precision realization of robust quantum anomalous Hall state in a hard ferromagnetic topological insulator", Nature materials **14**, 473–477 (2015).

[6] C. Liu, Y. Wang, H. Li, Y. Wu, Y. Li, J. Li, K. He, Y. Xu, J. Zhang, and Y. Wang, "Robust axion insulator and Chern insulator phases in a two-dimensional antiferromagnetic topological insulator", Nature materials **19**, 522–527 (2020).

[7] Y. Deng, Y. Yu, M. Z. Shi, Z. Guo, Z. Xu, J. Wang, X. H. Chen, and Y. Zhang, "Quantum anomalous Hall effect in intrinsic magnetic topological insulator $MnBi_2Te_4$", Science **367**, 895–900 (2020).

[8] E. Bocquillon, R. S. Deacon, J. Wiedenmann, P. Leubner, T. M. Klapwijk, C. Brüne, K. Ishibashi, H. Buhmann, and L. W. Molenkamp, "Gapless Andreev bound states in the quantum spin Hall insulator HgTe", Nature Nanotechnology **12**, 137–143 (2017).

[9] M. M. Otrokov, I. I. Klimovskikh, H. Bentmann, D. Estyunin, A. Zeugner, Z. S. Aliev, S. Gaß, A. U. B. Wolter, A. V. Koroleva, A. M. Shikin, M. Blanco-Rey, M. Hoffmann, I. P. Rusinov, A. Y. Vyazovskaya, S. V. Eremeev, Y. M. Koroteev, V. M. Kuznetsov, F. Freyse, J. Sánchez-Barriga, I. R. Amiraslanov, M. B. Babanly, N. T. Mamedov, N. A. Abdullayev, V. N. Zverev, A. Alfonsov, V. Kataev, B. Büchner, E. F. Schwier, S. Kumar, A. Kimura, L. Petaccia, G. D. Santo, R. C. Vidal, S. Schatz, K. Kißner, M. Ünzelmann, C. H. Min, S. Moser, T. R. F. Peixoto, F. Reinert, A. Ernst,

P. M. Echenique, A. Isaeva, and E. V. Chulkov, "Prediction and observation of an antiferromagnetic topological insulator", Nature **576**, 416–422 (2019).

[10] J. Li, Y. Li, S. Du, Z. Wang, B.-L. Gu, S.-C. Zhang, K. He, W. Duan, and Y. Xu, "Intrinsic magnetic topological insulators in van der Waals layered $MnBi_2Te_4$-family materials", Science Advances **5**, eaaw5685 (2019).

[11] R. Mong and V Shivamoggi, "Edge states and the bulk-boundary correspondence in Dirac Hamiltonians", Physical Review B **83**, 125109 (2011).

[12] B. A. Bernevig, T. L. Hughes, and S.-C. Zhang, "Quantum spin Hall effect and topological phase transition in HgTe quantum wells", Science **314**, 1757–1761 (2006).

[13] M. König, S. Wiedmann, C. Brüne, A. Roth, H. Buhmann, L. W. Molenkamp, X.-L. Qi, and S.-C. Zhang, "Quantum spin Hall insulator state in HgTe quantum wells", Science **318**, 766–770 (2007).

[14] L. Fu, C. L. Kane, and E. J. Mele, "Topological insulators in three dimensions", Physical Review Letters **98**, 106803 (2007).

[15] J. E. Moore and L. Balents, "Topological invariants of time-reversal-invariant band structures", Physical Review B **75**, 121306 (2007).

[16] R. Roy, "Topological phases and the quantum spin Hall effect in three dimensions", Physical Review B **79**, 195322 (2009).

[17] D. M. Mahler, J.-B. Mayer, P. Leubner, L. Lunczer, D. D. Sante, G. Sangiovanni, R. Thomale, E. M. Hankiewicz, H. Buhmann, C. Gould, and L. W. Molenkamp, "Interplay of Dirac nodes and Volkov-Pankratov surface states in compressively strained HgTe", Physical Review X **9**, 031034 (2019).

[18] M. Orlita, D. M. Basko, M. S. Zholudev, F. Teppe, W. Knap, V. I. Gavrilenko, N. N. Mikhailov, S. A. Dvoretskii, P. Neugebauer, C. Faugeras, A.-L. Barra, G. Martinez, and M. Potemski, "Observation of three-dimensional massless Kane fermions in a zinc-blende crystal", Nature Physics **10**, 233–238 (2014).

[19] M. Vergniory, L Elcoro, C. Felser, N. Regnault, B. A. Bernevig, and Z. Wang, "A complete catalogue of high-quality topological materials", Nature **566**, 480–485 (2019).

[20] R. Yu, W. Zhang, H.-J. Zhang, S.-C. Zhang, X. Dai, and Z. Fang, "Quantized anomalous Hall effect in magnetic topological insulators", Science **329**, 61–64 (2010).

[21] S. Grauer, K. Fijalkowski, S. Schreyeck, M. Winnerlein, K. Brunner, R. Thomale, C. Gould, and L. W. Molenkamp, "Scaling of the quantum anomalous Hall effect as an indicator of axion electrodynamics", Physical Review Letters **118**, 246801 (2017).

[22] Q. L. He, L. Pan, A. L. Stern, E. C. Burks, X. Che, G. Yin, J. Wang, B. Lian, Q. Zhou, E. S. Choi, K. Murata, X. Kou, Z. Chen, T. Nie, Q. Shao, Y. Fan, S.-C. Zhang, K. Liu, J. Xia, and K. L. Wang, "Chiral Majorana fermion modes in a quantum anomalous Hall insulator–superconductor structure", Science **357**, 294–299 (2017).

[23] C.-Z. Chang, J. Zhang, X. Feng, J. Shen, Z. Zhang, M. Guo, K. Li, Y. Ou, P. Wei, L.-L. Wang, Z.-Q. Ji, Y. Feng, S. Ji, X. Chen, J. Jia, X. Dai, Z. Fang, S.-C. Zhang, K. He, Y. Wang, L. Lu, X.-C. Ma, and Q.-K. Xue, "Experimental Observation of the Quantum Anomalous Hall Effect in a Magnetic Topological Insulator", Science **340**, 167–170 (2013).

[24] M. Li, C.-Z. Chang, B. J. Kirby, M. E. Jamer, W. Cui, L. Wu, P. Wei, Y. Zhu, D. Heiman, J. Li, and J. S. Moodera, "Proximity-driven enhanced magnetic order at ferromagnetic-insulator–magnetic-topological-insulator interface", Physical Review Letters **115**, 087201 (2015).

[25] Y. Gong, J. Guo, J. Li, K. Zhu, M. Liao, X. Liu, Q. Zhang, L. Gu, L. Tang, X. Feng, D. Zhang, W. Li, C. Song, L. Wang, P. Yu, X. Chen, Y. Wang, H. Yao, W. Duan, Y. Xu, S.-C. Zhang, X. Ma, Q.-K. Xue, and K. He, "Experimental realization of an intrinsic magnetic topological insulator", Chinese Physics Letters **36**, 076801 (2019).

[26] Z. S. Aliev, I. R. Amiraslanov, D. I. Nasonova, A. V. Shevelkov, N. A. Abdullayev, Z. A. Jahangirli, E. N. Orujlu, M. M. Otrokov, N. T. Mamedov, M. B. Babanly, and E. V. Chulkov, "Novel ternary layered manganese bismuth tellurides of the MnTe-Bi_2Te_3 system: Synthesis and crystal structure", Journal of Alloys and Compounds **789**, 443–450 (2019).

[27] D. Souchay, M. Nentwig, D. Günther, S. Keilholz, J. de Boor, A. Zeugner, A. Isaeva, M. Ruck, A. U. B. Wolter, B. Büchner, and O. Oeckler, "Layered manganese bismuth tellurides with $GeBi_4Te_7$-and $GeBi_6Te_10$-type structures: towards multifunctional materials", Journal of Materials Chemistry C **7**, 9939–9953 (2019).

[28] R. C. Vidal, A. Zeugner, J. I. Facio, R. Ray, M. H. Haghighi, A. U. Wolter, L. T. C. Bohorquez, F. Caglieris, S. Moser, T. Figgemeier, T. R. Peixoto, H. B. Vasili, M. Valvidares, S. Jung, C. Cacho, A. Alfonsov, K. Mehlawat, V. Kataev, C. Hess, M. Richter, B. Büchner, J. van den Brink, M. Ruck, F. Reinert, H. Bentmann, and A. Isaeva, "Topological electronic structure and intrinsic magnetization in $MnBi_4Te_7$: A Bi_2Te_3 derivative with a periodic Mn sublattice", Physical Review X **9**, 041065 (2019).

[29] J. Wu, F. Liu, M. Sasase, K. Ienaga, Y. Obata, R. Yukawa, K. Horiba, H. Kumigashira, S. Okuma, T. Inoshita, and H. Hosono, "Natural van der Waals heterostructural single crystals with both magnetic and topological properties", Science Advances **5**, eaax9989 (2019).

[30] C. Hu, K. N. Gordon, P. Liu, J. Liu, X. Zhou, P. Hao, D. Narayan, E. Emmanouilidou, H. Sun, Y. Liu, H. Brawer, A. P. Ramirez, L. Ding, H. Cao, Q. Liu, D. Dessau, and N. Ni, "A van der Waals antiferromagnetic topological insulator with weak interlayer magnetic coupling", Nature communications **11**, 1–8 (2020).

[31] N. H. Jo, L.-L. Wang, R.-J. Slager, J. Yan, Y. Wu, K. Lee, B. Schrunk, A. Vishwanath, and A. Kaminski, "Intrinsic axion insulating behavior in antiferromagnetic $MnBi_6Te_10$", Physical Review B **102**, 045130 (2020).

[32] X. Wu, J. Li, X.-M. Ma, Y. Zhang, Y. Liu, C.-S. Zhou, J. Shao, Q. Wang, Y.-J. Hao, Y. Feng, E. F. Schwier, S. Kumar, H. Sun, P. Liu, K. Shimada, K. Miyamoto, T. Okuda, K. Wang, M. Xie, C. Chen, Q. Liu, C. Liu, and Y. Zhao, "Distinct topological surface states on the two terminations of $MnBi_4Te_7$", Physical Review X **10**, 031013 (2020).

[33] N. W. Ashcroft and N. D. Mermin, *Solid state physics*, Vol. 2005 (Holt, Rinehart and Winston, New York, 1976).

[34] F. Bloch, "Über die quantenmechanik der elektronen in kristallgittern", Zeitschrift für Physik **52**, 555–600 (1929).

[35] C. Kittel, *Einführung in die Festkörperphysik* (Oldenbourg Wissenschaftsverlag, 2013).

[36] O. Madelung, *Introduction to solid-state theory*, Vol. 2 (Springer Science & Business Media, 2012).

[37] F. Reinert, "Spin-orbit interaction in the photoemission spectra of noble metal surface states", Journal of Physics: Condensed Matter **15**, S693 (2003).

[38] S. G. Davison and M. Stęślicka, *Basic theory of surface states*, Vol. 46 (Oxford University Press, 1996).

[39] M. Z. Hasan and C. L. Kane, "Colloquium: topological insulators", Reviews of modern physics **82**, 3045 (2010).

[40] X.-L. Qi and S.-C. Zhang, "Topological insulators and superconductors", Reviews of modern physics **83**, 1057 (2011).

[41] C. L. Kane and E. J. Mele, "Z2 topological order and the quantum spin Hall effect", Physical Review Letters **95**, 146802 (2005).

[42] L. Fu and C. L. Kane, "Topological insulators with inversion symmetry", Physical Review B **76**, 045302 (2007).

[43] C. Brüne, C.-X. Liu, E. G. Novik, E. M. Hankiewicz, H. Buhmann, Y. L. Chen, X. L. Qi, Z. X. Shen, S.-C. Zhang, and L. W. Molenkamp, "Quantum Hall effect from the topological surface states of strained bulk HgTe", Physical Review Letters **106**, 126803 (2011).

[44] H. Zhang, C.-X. Liu, X.-L. Qi, X. Dai, Z. Fang, and S.-C. Zhang, "Topological insulators in Bi_2Se_3, Bi_2Te_3 and Sb_2Te_3 with a single Dirac cone on the surface", Nature physics **5**, 438–442 (2009).

[45] Y. L. Chen, J. G. Analytis, J.-H. Chu, Z. K. Liu, S.-K. Mo, X. L. Qi, H. J. Zhang, D. H. Lu, X. Dai, Z. Fang, S. C. Zhang, I. R. Fisher, Z. Hussain, and Z.-X. Shen, "Experimental realization of a three-dimensional topological insulator, Bi_2Te_3", Science **325**, 178–181 (2009).

[46] Y. Xia, D. Qian, D. Hsieh, L. Wray, A. Pal, H. Lin, A. Bansil, D. Grauer, Y. S. Hor, R. J. Cava, and M. Z. Hasan, "Observation of a large-gap topological-insulator class with a single Dirac cone on the surface", Nature physics **5**, 398–402 (2009).

[47] D. Hsieh, Y. Xia, D. Qian, L. Wray, F. Meier, J. H. Dil, J. Osterwalder, L. Patthey, A. V. Fedorov, H. Lin, A. Bansil, D. Grauer, Y. S. Hor, R. J. Cava, and M. Z. Hasan, "Observation of time-reversal-protected single-Dirac-cone topological-insulator states in Bi_2Te_3 and Sb_2Te_3", Physical Review Letters **103**, 146401 (2009).

[48] L. Fu and C. L. Kane, "Time reversal polarization and a Z2 adiabatic spin pump", Physical Review B **74**, 195312 (2006).

[49] Y. Tokura, K. Yasuda, and A. Tsukazaki, "Magnetic topological insulators", Nature Reviews Physics **1**, 126–143 (2019).

[50] C. Wu, B. A. Bernevig, and S.-C. Zhang, "Helical liquid and the edge of quantum spin Hall systems", Physical Review Letters **96**, 106401 (2006).

[51] X.-L. Qi and S.-C. Zhang, "The quantum spin Hall effect and topological insulators", arXiv preprint arXiv:1001.1602 (2010).

[52] L. Fu, "Hexagonal warping effects in the surface states of the topological insulator Bi_2Te_3", Physical Review Letters **103**, 266801 (2009).

[53] C.-X. Liu, X.-L. Qi, H. Zhang, X. Dai, Z. Fang, and S.-C. Zhang, "Model Hamiltonian for topological insulators", Physical Review B **82**, 045122 (2010).

[54] J. Chu and A. Sher, *Physics and properties of narrow gap semiconductors* (Springer, 2008).

[55] S. R. Park and C. Kim, "Microscopic mechanism for the Rashba spin-band splitting: Perspective from formation of local orbital angular momentum", Journal of Electron Spectroscopy and Related Phenomena **201**, 6–17 (2015).

[56] Z. Zhu, Y. Cheng, and U. Schwingenschlögl, "Band inversion mechanism in topological insulators: A guideline for materials design", Physical Review B **85**, 235401 (2012).

[57] V. Zelevinsky, *Quantum physics. Vol. 1. From basics to symmetries and perturbations* (WILEY-VCH, 2011).

[58] W. Zhi-Yong and X. Cai-Dong, "Zitterbewegung in quantum field theory", Chinese Physics B **17**, 4170 (2008).

[59] F. Schwabl, "Quantenmechanik", Springer **4**, 183 (2007).

[60] K. v. Klitzing, G. Dorda, and M. Pepper, "New method for high-accuracy determination of the fine-structure constant based on quantized Hall resistance", Physical Review Letters **45**, 494 (1980).

[61] D. J. Thouless, M. Kohmoto, M. P. Nightingale, and M. den Nijs, "Quantized Hall conductance in a two-dimensional periodic potential", Physical Review Letters **49**, 405 (1982).

[62] M. Kohmoto, "Topological invariant and the quantization of the Hall conductance", Annals of Physics **160**, 343–354 (1985).

[63] F. D. M. Haldane, "Model for a quantum Hall effect without Landau levels: Condensed-matter realization of the "parity anomaly"", Physical Review Letters **61**, 2015 (1988).

[64] C.-X. Liu, X.-L. Qi, X. Dai, Z. Fang, and S.-C. Zhang, "Quantum anomalous Hall effect in $Hg_{1-y}Mn_yTe$ quantum wells", Physical Review Letters **101**, 146802 (2008).

[65] R. S. Mong, A. M. Essin, and J. E. Moore, "Antiferromagnetic topological insulators", Physical Review B **81**, 245209 (2010).

[66] H. Hertz, "Ueber einen Einfluss des ultravioletten Lichtes auf die electrische Entladung", Annalen der Physik **267**, 983–1000 (1887).

[67] W. Hallwachs, "Ueber den Einfluss des Lichtes auf electrostatisch geladene Körper", Annalen der Physik **269**, 301–312 (1888).

[68] A. Einstein, "Über einem die Erzeugung und Verwandlung des Lichtes betreffenden heuristischen Gesichtspunkt", Annalen der Physik **4** (1905).

[69] S. Hüfner, *Photoelectron spectroscopy: principles and applications* (Springer Science & Business Media, 2013).

[70] F. Reinert and S. Hüfner, "Photoemission spectroscopy - from early days to recent applications", New Journal of Physics **7**, 97 (2005).

[71] M. P. Seah and W. Dench, "Quantitative electron spectroscopy of surfaces: A standard data base for electron inelastic mean free paths in solids", Surface and interface analysis **1**, 2–11 (1979).

[72] A. Tejeda and D. Malterre, *A Primer in Photoemission: Concepts and Applications* (EDP sciences, 2019).

[73] A. Damascelli, Z. Hussain, and Z.-X. Shen, "Angle-resolved photoemission studies of the cuprate superconductors", Reviews of modern physics **75**, 473 (2003).

[74] A. Damascelli, "Probing the electronic structure of complex systems by ARPES", Physica Scripta **2004**, 61 (2004).

[75] B. Feuerbacher and R. F. Willis, "Photoemission and electron states at clean surfaces", Journal of Physics C: Solid State Physics **9**, 169 (1976).

[76] T. Miller, W. E. McMahon, and T.-C. Chiang, "Interference between bulk and surface photoemission transitions in Ag (111)", Physical Review Letters **77**, 1167 (1996).

[77] E. D. Hansen, T. Miller, and T.-C. Chiang, "Surface photoemission in Ag (100)", Physical Review B **55**, 1871 (1997).

[78] E. Kisker, R. Clauberg, and W. Gudat, "Electron spectrometer for spin-polarized angle-and energy-resolved photoemission from ferromagnets", Review of Scientific Instruments **53**, 1137–1144 (1982).

[79] G.-C. Wang, R. Celotta, and D. T. Pierce, "Polarized low-energy-electron diffraction from W (100)", Physical Review B **23**, 1761 (1981).

[80] F. U. Hillebrecht, R. M. Jungblut, L. Wiebusch, C. Roth, H. B. Rose, D. Knabben, C. Bethke, N. B. Weber, S. Manderla, U. Rosowski, and E. Kisker, "High-efficiency spin polarimetry by very-low-energy electron scattering from Fe(100) for spin-resolved photoemission", Review of Scientific Instruments **73**, 1229–1234 (2002).

[81] J. Osterwalder, "Spin-polarized photoemission", in *Magnetism: a synchrotron radiation approach* (Springer, 2006), pp. 95–120.

[82] P. D. Johnson, "Spin-polarized photoemission", Reports on Progress in Physics **60**, 1217 (1997).

[83] D. Tillmann, R. Thiel, and E. Kisker, "Very-low-energy spin-polarized electron diffraction from Fe (001)", Zeitschrift für Physik B Condensed Matter **77**, 1–2 (1989).

[84] R. Bertacco, M. Merano, and F. Ciccacci, "Spin dependent electron absorption in Fe (001)-p (1× 1) O: A new candidate for a stable and efficient electron polarization analyzer", Applied Physics Letters **72**, 2050–2052 (1998).

[85] O. Rader, C. Pampuch, A. M. Shikin, W. Gudat, J. Okabayashi, T. Mizokawa, A. Fujimori, T. Hayashi, M. Tanaka, A. Tanaka, and A. Kimura, "Resonant photoemission of $Ga_{1-x}Mn_xAs$ at the Mn *L* edge", Physical Review B **69**, 075202 (2004).

[86] J. Okabayashi, A. Kimura, T. Mizokawa, A. Fujimori, T. Hayashi, and M. Tanaka, "Mn 3*d* partial density of states in $Ga_{1-x}Mn_xAs$ studied by resonant photoemission spectroscopy", Physical Review B **59**, R2486 (1999).

[87] L. Ley, M. Taniguchi, J. Ghijsen, R. L. Johnson, and A. Fujimori, "Manganese-derived partial density of states in $Cd_{1-x}Mn_xTe$", Physical Review B **35**, 2839 (1987).

[88] U. Fano, "Effects of configuration interaction on intensities and phase shifts", Physical Review **124**, 1866 (1961).

[89] A. Beer, "Bestimmung der Absorption des rothen Lichts in farbigen Flussigkeiten", Ann. Physik **162**, 78–88 (1852).

[90] J.-H. Lambert, *Photometria, sive de mensura et gradibus luminis, colorum et umbrae* (sumptibus viduae E. Klett, 1760).

[91] P. Bouguer, *Essai d'optique, sur la gradation de la lumiere* (Claude Jombert, 1729).

[92] M. Newville, "Fundamentals of XAFS", Reviews in Mineralogy and Geochemistry **78**, 33–74 (2014).

[93] J. Stöhr, *NEXAFS spectroscopy*, Vol. 25 (Springer Science & Business Media, 2013).

[94] J. Haase, "SEXAFS und NEXAFS. Röntgen-Absorptionsspektroskopie an Adsorbat-bedeckten Oberflächen", Chemie in unserer Zeit **26**, 219–231 (1992).

[95] B. K. Teo, *EXAFS: basic principles and data analysis*, Vol. 9 (Springer Science & Business Media, 2012).

[96] M. L. Baker, M. W. Mara, J. J. Yan, K. O. Hodgson, B. Hedman, and E. I. Solomon, "*K*-and *L*-edge X-ray absorption spectroscopy (XAS) and resonant inelastic X-ray scattering (RIXS) determination of differential orbital covalency (DOC) of transition metal sites", Coordination Chemistry Reviews **345**, 182–208 (2017).

[97] B. M. Kincaid and P. Eisenberger, "Synchrotron Radiation Studies of the *K*-Edge Photoabsorption Spectra of Kr, Br_2, and $GeCl_4$: a Comparison of Theory and Experiment", Physical Review Letters **34**, 1361 (1975).

[98] G. Schütz, W. Wagner, W. Wilhelm, P. Kienle, R. Zeller, R. Frahm, and G. Materlik, "Absorption of circularly polarized X-rays in iron", Physical Review Letters **58**, 737 (1987).

[99] J. Stöhr, "X-ray magnetic circular dichroism spectroscopy of transition metal thin films", Journal of Electron Spectroscopy and Related Phenomena **75**, 253–272 (1995).

[100] J. Stöhr, H. A. Padmore, S. Anders, T. Stammler, and M. R. Scheinfein, "Principles of X-ray magnetic dichroism spectromicroscopy", Surface review and letters **5**, 1297–1308 (1998).

[101] B. T. Thole, G. Van der Laan, and G. A. Sawatzky, "Strong magnetic dichroism predicted in the $M_{4,5}$ X-ray absorption spectra of magnetic rare-earth materials", Physical Review Letters **55**, 2086 (1985).

[102] G. van der Laan, B. T. Thole, G. A. Sawatzky, J. B. Goedkoop, J. C. Fuggle, J.-M. Esteva, R. Karnatak, J. Remeika, and H. A. Dabkowska, "Experimental proof of magnetic X-ray dichroism", Physical Review B **34**, 6529 (1986).

[103] P. Hohenberg and W. Kohn, "Inhomogeneous electron gas phys. rev. 136", B864 (1964).

[104] N. Harrison, "An introduction to density functional theory", Nato Science Series Sub Series III Computer and Systems Sciences **187**, 45–70 (2003).

[105] W. Kohn and L. J. Sham, "Self-consistent equations including exchange and correlation effects", Physical Review **140**, A1133 (1965).

[106] D. Sholl and J. A. Steckel, *Density functional theory: a practical introduction* (John Wiley & Sons, 2011).

[107] J. P. Perdew, K. Burke, and M. Ernzerhof, "Generalized gradient approximation made simple", Physical Review Letters **77**, 3865 (1996).

[108] A. D. Becke and E. R. Johnson, "A simple effective potential for exchange", The Journal of chemical physics **124**, 221101 (2006).

[109] F. Tran and P. Blaha, "Accurate band gaps of semiconductors and insulators with a semilocal exchange-correlation potential", Physical Review Letters **102**, 226401 (2009).

[110] J. Heyd, G. E. Scuseria, and M. Ernzerhof, "Hybrid functionals based on a screened Coulomb potential", The Journal of chemical physics **118**, 8207–8215 (2003).

[111] D. Koller, F. Tran, and P. Blaha, "Merits and limits of the modified Becke-Johnson exchange potential", Physical Review B **83**, 195134 (2011).

[112] J. Koralek, J. Douglas, N. Plumb, J. Griffith, S. Cundiff, H. Kapteyn, M. Murnane, and D. Dessau, "Experimental setup for low-energy laser-based angle resolved photoemission spectroscopy", Review of Scientific Instruments **78**, 053905 (2007).

[113] J. Faure, J. Mauchain, E. Papalazarou, W. Yan, J. Pinon, M. Marsi, and L. Perfetti, "Full characterization and optimization of a femtosecond ultraviolet laser source for time and angle-resolved photoemission on solid surfaces", Review of Scientific Instruments **83**, 043109 (2012).

[114] N. Mårtensson, P. Baltzer, P. A. Brühwiler, J.-O. Forsell, A. Nilsson, A. Stenborg, and B. Wannberg, "A very high resolution electron spectrometer", Journal of Electron Spectroscopy and Related Phenomena **70**, 117–128 (1994).

[115] G. Nicolay, "Vielteilchenanregungen nahe der Fermienergie am Beispielsystem der Shockley-Oberflächenzustände", PhD thesis (Universität des Saarlandes, 2002).

[116] M. Hoesch, T. K. Kim, P. Dudin, H. Wang, S. Scott, P. Harris, S. Patel, M. Matthews, D. Hawkins, S. G. Alcock, T. Richter, J. J. Mudd, M. Basham, L. Pratt, P. Leicester, E. C. Longhi, A. Tamai, and F. Baumberger, "A facility for the analysis of the electronic structures of solids and their surfaces by synchrotron radiation photoelectron spectroscopy", Review of Scientific Instruments **88**, 013106 (2017).

[117] J. Viefhaus, F. Scholz, S. Deinert, L. Glaser, M. Ilchen, J. Seltmann, P. Walter, and F. Siewert, "The variable polarization XUV beamline P04 at PETRA III: Optics, mechanics and their performance", Nuclear Instruments and Methods in Physics Research Section A: Accelerators, Spectrometers, Detectors and Associated Equipment **710**, 151–154 (2013).

[118] H. Iwasawa, E. F. Schwier, M. Arita, A. Ino, H. Namatame, M. Taniguchi, Y. Aiura, and K. Shimada, "Development of laser-based scanning μ-ARPES system with ultimate energy and momentum resolutions", Ultramicroscopy **182**, 85–91 (2017).

[119] A. Barla, J. Nicolás, D. Cocco, S. M. Valvidares, J. Herrero-Martín, P. Gargiani, J. Moldes, C. Ruget, E. Pellegrin, and S. Ferrer, "Design and performance of BOREAS, the beamline for resonant X-ray absorption and scattering experiments at the ALBA synchrotron light source", Journal of synchrotron radiation **23**, 1507–1517 (2016).

[120] A. Y. Cho and J. Arthur, "Molecular beam epitaxy", Progress in solid state chemistry **10**, 157–191 (1975).

[121] P. Leubner, "Strain-engineering of the topological insulator HgTe", PhD thesis (Julius-Maximilians-Universität Würzburg, 2016).

[122] C. Becker, C Brüne, M Schäfer, A Roth, H Buhmann, and L. Molenkamp, "The influence of interfaces and the modulation doping technique on the magneto-transport properties of HgTe based quantum wells", physica status solidi c **4**, 3382–3389 (2007).

[123] S. Oehling, M. Ehinger, W. Spahn, A. Waag, C. R. Becker, and G. Landwehr, "Mechanisms of molecular beam epitaxial growth of (001) HgTe", Journal of applied physics **79**, 748–751 (1996).

[124] C. Ames, "Molecular beam epitaxy of 2D and 3D HgTe, a topological insulator", PhD thesis (Julius-Maximilians-Universität Würzburg, 2015).

[125] K. Virwani, S. E. Harrison, A. Pushp, T. Topuria, E. Delenia, P. Rice, A. Kellock, L. Collins-McIntyre, J. Harris, T. Hesjedal, and S. Parkin, "Controlled removal of amorphous Se capping layer from a topological insulator", Applied Physics Letters **105**, 241605 (2014).

[126] H. Maaß, S. Schreyeck, S. Schatz, S. Fiedler, C. Seibel, P. Lutz, G. Karczewski, H. Bentmann, C. Gould, K. Brunner, L. W. Molenkamp, and F. Reinert, "Electronic structure and morphology of epitaxial Bi_2Te_2Se topological insulator films", Journal of Applied Physics **116**, 193708 (2014).

[127] O. Crauste, Y. Ohtsubo, P. Ballet, P. A. L. Delplace, D. Carpentier, C. Bouvier, T. Meunier, A. Taleb-Ibrahimi, and L. Lévy, "Topological surface states of strained mercury-telluride probed by ARPES", arXiv preprint arXiv:1307.2008 (2013).

[128] S. H. Yao, B. Zhou, M. H. Lu, Z. K. Liu, Y. B. Chen, J. G. Analytis, C. Brüne, W. H. Dang, S.-K. Mo, Z.-X. Shen, I. R. Fisher, L. W. Molenkamp, H. L. Peng, Z. Hussain, and Y. L. Chen, "Observing electronic structures on ex-situ grown topological insulator thin films", physica status solidi (RRL)–Rapid Research Letters **7**, 130–132 (2013).

[129] C. I. Fornari, P. H. O. Rappl, S. L. Morelhão, T. R. F. Peixoto, H. Bentmann, F. Reinert, and E. Abramof, "Preservation of pristine Bi_2Te_3 thin film topological insulator surface after ex situ mechanical removal of Te capping layer", APL Materials **4**, 106107 (2016).

[130] S. Buchberger, "Elektronische und strukturelle Eigenschaften von epitaktisch gewachsenem HgTe(001) als dreidimensionaler topologischer Isolator", BA thesis (Julius-Maximilians-Universität Würzburg, 2019).

[131] O. Karpinskii, L. Shelimova, and M. Kretova, "Crystal structure and point defects of $Ge_{1\pm\delta}Bi_2Te_4$", Inorganic materials **33**, 793–797 (1997).

[132] A. Zeugner, "Troubleshooting the compounds' side of bismuth telluride based topological insulators", PhD thesis (Technische Universität Dresden, 2019).

[133] A. Zeugner, F. Nietschke, A. U. B. Wolter, S. Gaß, R. C. Vidal, T. R. F. Peixoto, D. Pohl, C. Damm, A. Lubk, R. Hentrich, S. K. Moser, C. Fornari, C. H. Min, S. Schatz, K. Kißner, M. Ünzelmann, M. Kaiser, F. Scaravaggi, B. Rellinghaus, K. Nielsch, C. Hess, B. Büchner, F. Reinert, H. Bentmann, O. Oeckler, T. Doert, M. Ruck, and A. Isaeva, "Chemical aspects of the candidate antiferromagnetic topological insulator $MnBi_2Te_4$", Chemistry of Materials **31**, 2795–2806 (2019).

[134] L. Shelimova, O. Karpinskii, M. Kretova, and G. Lubman, "A physicochemical investigation of the layered semiconducting compounds $Ge_3Bi_2Te_6$, $GeBi_2Te_4$, and $GeBi_4Te_7$", INORGANIC MATERIALS **29**, 56–60 (1993).

[135] L. Shelimova, O. Karpinskii, P. Konstantinov, E. Avilov, M. Kretova, and V. Zemskov, "Crystal structures and thermoelectric properties of layered compounds in the ATe-Bi_2Te_3 (A= Ge, Sn, Pb) systems", Inorganic Materials **40**, 451–460 (2004).

[136] F. Teppe, M. Marcinkiewicz, S. S. Krishtopenko, S. Ruffenach, C. Consejo, A. M. Kadykov, W. Desrat, D. But, W. Knap, J. Ludwig, S. Moon, D. Smirnov, M. Orlita, Z. Jiang, S. V. Morozov, V. Gavrilenko, N. N. Mikhailov, and S. A. Dvoretskii, "Temperature-driven massless Kane fermions in HgCdTe crystals", Nature communications **7**, 1–6 (2016).

[137] R. C. Vidal, G. Marini, L. Lunczer, S. Moser, L. Fürst, C. Jozwiak, A. Bostwick, E. Rotenberg, C. Gould, H. Buhmann, G. Sangiovanni, D. Di Sante, G. Profeta, L. W. Molenkamp, H. Bentmann, and F. Reinert, "Spectroscopic signatures of the topological band inversion in HgTe(001)", In preparation, 2021.

[138] T. Skauli and T. Colin, "Accurate determination of the lattice constant of molecular beam epitaxial CdHgTe", Journal of crystal growth **222**, 719–725 (2001).

[139] K. Momma and F. Izumi, "VESTA 3 for three-dimensional visualization of crystal, volumetric and morphology data", Journal of applied crystallography **44**, 1272–1276 (2011).

[140] X. Dai, T. L. Hughes, X.-L. Qi, Z. Fang, and S.-C. Zhang, "Helical edge and surface states in HgTe quantum wells and bulk insulators", Physical Review B **77**, 125319 (2008).

[141] C. Heske, U. Winkler, H. Neureiter, M. Sokolowski, R. Fink, E. Umbach, C. Jung, and P. R. Bressler, "Preparation and termination of well-defined CdTe (100) and Cd (Zn) Te (100) surfaces", Applied Physics Letters **70**, 1022–1024 (1997).

[142] C. Kumpf, W. Weigand, A. Müller, J. Wagner, V. Wagner, P. Bach, G. Schmidt, L. W. Molenkamp, J. Geurts, and E. Umbach, "Surface reconstructions of II-VI compound semiconductor surfaces", physica status solidi c **4**, 3183–3190 (2007).

[143] S. Oehling, M. Ehinger, T. Gerhard, C. R. Becker, G. Landwehr, M. Schneider, D. Eich, H. Neureiter, R. Fink, M. Sokolowski, and E. Umbach, "Termination, surface structure and morphology of the molecular beam epitaxially grown HgTe(001) surface", Applied Physics Letters **73**, 3205–3207 (1998).

[144] J. C. Vickerman and I. S. Gilmore, *Surface analysis: the principal techniques* (John Wiley & Sons, 2011).

[145] R. F. Reilman, A. Msezane, and S. T. Manson, "Relative intensities in photoelectron spectroscopy of atoms and molecules", Journal of Electron Spectroscopy and Related Phenomena **8**, 389–394 (1976).

[146] B. Yan and S.-C. Zhang, "Topological materials", Reports on Progress in Physics **75**, 096501 (2012).

[147] S.-C. Wu, B. Yan, and C. Felser, "Ab initio study of topological surface states of strained HgTe", EPL (Europhysics Letters) **107**, 57006 (2014).

[148] F. Virot, R. Hayn, M. Richter, and J. van den Brink, "Engineering topological surface states: HgS, HgSe, and HgTe", Physical Review Letters **111**, 146803 (2013).

[149] J. Issing, "Elektronische Struktur des epitaktisch gewachsenen dreidimensionalen topologischen Isolators HgTe(001)", MA thesis (Julius-Maximilians-Universität Würzburg, 2020).

[150] C. Janowitz, N. Orlowski, R. Manzke, and Z. Golacki, "On the band structure of HgTe and HgSe - view from photoemission", Journal of alloys and compounds **328**, 84–89 (2001).

[151] S. Bloom and T. K. Bergstresser, "Band structure of HgSe and HgTe", physica status solidi (b) **42**, 191–196 (1970).

[152] M. N. Secuk, M. Aycibin, B. Erdinc, S. E. Gulebaglan, E. K. Dogan, and H. Akkus, "Ab-initio calculations of structural, electronic, optical, dynamic and thermodynamic properties of HgTe and HgSe", American Journal of Condensed Matter Physics **4**, 13–19 (2014).

[153] J. Vidal, X. Zhang, L. Yu, J.-W. Luo, and A. Zunger, "False-positive and false-negative assignments of topological insulators in density functional theory and hybrids", Physical Review B **84**, 041109 (2011).

[154] A. Svane, N. E. Christensen, M. Cardona, A. N. Chantis, M. Van Schilfgaarde, and T. Kotani, "Quasiparticle band structures of β-HgS, HgSe, and HgTe", Physical Review B **84**, 205205 (2011).

[155] J. W. Nicklas and J. W. Wilkins, "Accurate electronic properties for (Hg,Cd)Te systems using hybrid density functional theory", Physical Review B **84**, 121308 (2011).

[156] M. Cardona, R. K. Kremer, R. Lauck, G. Siegle, A. Muñoz, and A. H. Romero, "Electronic, vibrational, and thermodynamic properties of metacinnabar β-HgS, HgSe, and HgTe", Physical Review B **80**, 195204 (2009).

[157] S.-H. Wei and A. Zunger, "Electronic structure and stability of II-VI semiconductors and their alloys: The role of metal *d* bands", Journal of Vacuum Science & Technology A: Vacuum, Surfaces, and Films **6**, 2597–2611 (1988).

[158] L. Ley, R. A. Pollak, F. R. McFeely, S. P. Kowalczyk, and D. A. Shirley, "Total valence-band densities of states of III-V and II-VI compounds from X-ray photoemission spectroscopy", Physical Review B **9**, 600 (1974).

[159] N. J. Shevchik, J. Tejeda, D. W. Langer, and M. Cardona, "Photoemission and density of valence states of the H-YI compounds II. ZnSe, CdS, and HgS", physica status solidi (b) **60**, 345–355 (1973).

[160] C. Vesely, R. Hengehold, and D. Langer, "UV photoemission measurements of the upper *d* levels in the IIB-VIA compounds", Physical Review B **5**, 2296 (1972).

[161] H. Jiang, "Band gaps from the Tran-Blaha modified Becke-Johnson approach: A systematic investigation", The Journal of chemical physics **138**, 134115 (2013).

[162] J. Heyd, J. E. Peralta, G. E. Scuseria, and R. L. Martin, "Energy band gaps and lattice parameters evaluated with the Heyd-Scuseria-Ernzerhof screened hybrid functional", The Journal of chemical physics **123**, 174101 (2005).

[163] A. V. Krukau, O. A. Vydrov, A. F. Izmaylov, and G. E. Scuseria, "Influence of the exchange screening parameter on the performance of screened hybrid functionals", The Journal of chemical physics **125**, 224106 (2006).

[164] G. Dresselhaus, "Spin-orbit coupling effects in zinc blende structures", Physical Review **100**, 580 (1955).

[165] E. Rashba and V. Sheka, "Symmetry of energy bands in crystals of wurtzite type II. Symmetry of bands with spin-orbit interaction included", New Journal of Physics, English translation (2015).

[166] Y. A. Bychkov, "Properties of 2D electron gas with lifted spectral degeneracy", JETP lett. **39**, 78–81 (1984).

[167] M. Cardona, N. E. Christensen, and G. Fasol, "Terms linear in k in the band structure of zinc-blende-type semiconductors", Physical Review Letters **56**, 2831 (1986).

[168] M. P. Surh, M.-F. Li, and S. G. Louie, "Spin-orbit splitting of GaAs and InSb bands near Γ", Physical Review B **43**, 4286 (1991).

[169] M. Cardona, N. E. Christensen, and G. Fasol, "Relativistic band structure and spin-orbit splitting of zinc-blende-type semiconductors", Physical Review B **38**, 1806 (1988).

[170] Y. Cao, J. A. Waugh, X.-W. Zhang, J.-W. Luo, Q. Wang, T. J. Reber, S. K. Mo, Z. Xu, A. Yang, J. Schneeloch, G. D. Gu, M. Brahlek, N. Bansal, S. Oh, A. Zunger, and D. S. Dessau, "Mapping the orbital wavefunction of the surface states in three-dimensional topological insulators", Nature Physics **9**, 499–504 (2013).

[171] L. Bawden, J. M. Riley, C. H. Kim, R. Sankar, E. J. Monkman, D. E. Shai, H. I. Wei, E. B. Lochocki, J. W. Wells, W. Meevasana, T. K. Kim, M. Hoesch, Y. Ohtsubo, P. L. Fèvre, C. J. Fennie, K. M. Shen, F. Chou, and P. D. C. King, "Hierarchical spin-orbital polarization of a giant Rashba system", Science Advances **1**, e1500495 (2015).

[172] M. Ünzelmann, H. Bentmann, P. Eck, T. Kißlinger, B. Geldiyev, J. Rieger, S. Moser, R. C. Vidal, K. Kißner, L. Hammer, M. A. Schneider, T. Fauster, G. Sangiovanni, D. D. Sante, and F. Reinert, "Orbital-driven Rashba effect in a binary honeycomb monolayer AgTe", Physical Review Letters **124**, 176401 (2020).

[173] J. J. Yeh and I. Lindau, "Atomic subshell photoionization cross sections and asymmetry parameters: $1 \leq Z \leq 103$", Atomic data and nuclear data tables **32**, 1–155 (1985).

[174] J. Nayak, G. H. Fecher, S. Ouardi, C. Shekhar, C. Tusche, S. Ueda, E. Ikenaga, and C. Felser, "Temperature-induced modification of the Dirac cone in the tetradymite topological insulator Bi_2Te_2Se", Physical Review B **98**, 075206 (2018).

[175] L. Rhodes, M. Watson, A. Haghighirad, M. Eschrig, and T. Kim, "Strongly enhanced temperature dependence of the chemical potential in FeSe", Physical Review B **95**, 195111 (2017).

[176] A. K. Geim, "Graphene: status and prospects", Science **324**, 1530–1534 (2009).

[177] A. K. Geim and I. V. Grigorieva, "Van der Waals heterostructures", Nature **499**, 419–425 (2013).

[178] P. Ajayan, P. Kim, and K. Banerjee, "Van der Waals materials", Physics Today **69**, 38 (2016).

[179] K. Kuroda, H. Miyahara, M. Ye, S. V. Eremeev, Y. M. Koroteev, E. E. Krasovskii, E. V. Chulkov, S. Hiramoto, C. Moriyoshi, Y. Kuroiwa, K. Miyamoto, T. Okuda, M. Arita, K. Shimada, H. Namatame, M. Taniguchi, Y. Ueda, and A. Kimura, "Experimental verification of $PbBi_2Te_4$ as a 3D topological insulator", Physical Review Letters **108**, 206803 (2012).

[180] K. Okamoto, K. Kuroda, H. Miyahara, K. Miyamoto, T. Okuda, Z. S. Aliev, M. B. Babanly, I. R. Amiraslanov, K. Shimada, H. Namatame, M. Taniguchi, D. A. Samorokov, T. V. Menshchikova, E. V. Chulkov, and A. Kimura, "Observation of a highly spin-polarized topological surface state in $GeBi_2Te_4$", Physical Review B **86**, 195304 (2012).

[181] S. Eremeev, M. Otrokov, and E. V. Chulkov, "Competing rhombohedral and monoclinic crystal structures in $MnPn_2Ch_4$ compounds: An ab-initio study", Journal of Alloys and Compounds **709**, 172–178 (2017).

[182] M. M. Otrokov, I. P. Rusinov, M. Blanco-Rey, M Hoffmann, A. Y. Vyazovskaya, S. V. Eremeev, A Ernst, P. M. Echenique, A. Arnau, and E. V. Chulkov, "Unique thickness-dependent properties of the van der Waals interlayer antiferromagnet $MnBi_2Te_4$ films", Physical Review Letters **122**, 107202 (2019).

[183] R. C. Vidal, H. Bentmann, T. R. F. Peixoto, A. Zeugner, S. Moser, C.-H. Min, S. Schatz, K. Kißner, M. Ünzelmann, C. I. Fornari, H. B. Vasili, M. Valvidares, K. Sakamoto, D. Mondal, J. Fujii, I. Vobornik, S. Jung, C. Cacho, T. K. Kim, R. J. Koch, C. Jozwiak, A. Bostwick, J. D. Denlinger, E. Rotenberg, J. Buck, M. Hoesch, F. Diekmann, S. Rohlf, M. Kalläne, K. Rossnagel, M. M. Otrokov, E. V. Chulkov, M. Ruck, A. Isaeva, and F. Reinert, "Surface states and Rashba-type spin polarization in antiferromagnetic $MnBi_2Te_4$ (0001)", Physical Review B **100**, 121104 (2019).

[184] M. Van Veenendaal and G. Sawatzky, "Nonlocal screening effects in $2p$ X-ray photoemission spectroscopy core-level line shapes of transition metal compounds", Physical Review Letters **70**, 2459 (1993).

[185] D. Alders, F. C. Voogt, T. Hibma, and G. A. Sawatzky, "Nonlocal screening effects in $2p$ X-ray photoemission spectroscopy of NiO (100)", Physical Review B **54**, 7716 (1996).

[186] M. van Veenendaal, "Competition between screening channels in core-level X-ray photoemission as a probe of changes in the ground-state properties of transition-metal compounds", Physical Review B **74**, 085118 (2006).

[187] T. Pincelli, V. Lollobrigida, F. Borgatti, A. Regoutz, B. Gobaut, C. Schlueter, T. L. Lee, D. J. Payne, M. Oura, K. Tamasaku, A. Y. Petrov, P. Graziosi, F. M. Granozio, M. Cavallini, G. Vinai, R. Ciprian, C. H. Back, G. Rossi, M. Taguchi, H. Daimon, G. van der Laan, and G. Panaccione, "Quantifying the critical thickness of electron hybridization in spintronics materials", Nature communications **8**, 1–8 (2017).

[188] S. Thorpe, F. Arciprete, E. Placidi, F. Patella, M. Fanfoni, A. Balzarotti, S. Colonna, F. Ronci, A. Cricenti, A. Verdini, L. Floreano, and A. Morgante, "XPS and STM study of Mn incorporation on the GaAs(001) surface", Superlattices and Microstructures **46**, 258–265 (2009).

[189] J. I. Hwang, Y. Ishida, M. Kobayashi, H. Hirata, K. Takubo, T. Mizokawa, A. Fujimori, J. Okamoto, K. Mamiya, Y. Saito, Y. Muramatsu, H. Ott, A. Tanaka, T. Kondo, and H. Munekata, "High-energy spectroscopic study of the III-V nitride-based diluted magnetic semiconductor $Ga_{1-x}Mn_xN$", Physical Review B **72**, 085216 (2005).

[190] A. E. Bocquet, T. Mizokawa, T. Saitoh, H. Namatame, and A. Fujimori, "Electronic structure of 3*d*-transition-metal compounds by analysis of the 2*p* core-level photoemission spectra", Physical Review B **46**, 3771 (1992).

[191] A. Tanaka and T. Jo, "Resonant 3d, 3p and 3s photoemission in transition metal oxides predicted at 2p threshold", Journal of the Physical Society of Japan **63**, 2788–2807 (1994).

[192] H. Sato, A. Tanaka, A. Furuta, S. Senba, H. Okuda, K. Mimura, M. Nakatake, Y. Ueda, M. Taniguchi, and T. Jo, "Resonant photoemission spectroscopy in the mn $2p-3d$ excitation region of NiAs-type MnTe", Journal of the Physical Society of Japan **68**, 2132–2138 (1999).

[193] H. Sato, S. Senba, H. Okuda, M. Nakateke, A. Furuta, Y. Ueda, M. Taniguchi, A. Tanaka, and T. Jo, "Mn $2p-3d$ resonant photoemission spectroscopy of MnY (Y= S, Se, Te)", Journal of electron spectroscopy and related phenomena **88**, 425–428 (1998).

[194] H. Sato, T. Mihara, A. Furuta, M. Tamura, K. Mimura, N. Happo, M. Taniguchi, and Y. Ueda, "Chemical trend of occupied and unoccupied Mn 3*d* states in MnY (Y= S, Se, Te)", Physical Review B **56**, 7222 (1997).

[195] Y. Ueda, H. Sato, M. Taniguchi, N. Happo, T. Mihara, H. Namatame, T. Mizokawa, and A. Fujimori, "Mn 3*d* states in NiAs-type MnTe studied by means of synchrotron radiation photoemission", Journal of Physics: Condensed Matter **6**, 8607 (1994).

[196] I. Di Marco, P. Thunström, M. Katsnelson, J. Sadowski, K. Karlsson, S. Lebègue, J. Kanski, and O. Eriksson, "Electron correlations in Mn_xGa_{1-x} as as seen by resonant electron spectroscopy and dynamical mean field theory", Nature communications **4**, 1–6 (2013).

[197] M. F. Islam, C. M. Canali, A. Pertsova, A. Balatsky, S. K. Mahatha, C. Carbone, A. Barla, K. A. Kokh, O. E. Tereshchenko, E. Jiménez, N. B. Brookes, P. Gargiani, M. Valvidares, S. Schatz, T. R. F. Peixoto, H. Bentmann, F. Reinert, J. Jung, T. Bathon, K. Fauth, M. Bode, and P. Sessi, "Systematics of electronic and magnetic properties in the transition metal doped Sb_2Te_3 quantum anomalous Hall platform", Physical Review B **97**, 155429 (2018).

[198] D. S. Lee, T.-H. Kim, C.-H. Park, C.-Y. Chung, Y. S. Lim, W.-S. Seo, and H.-H. Park, "Crystal structure, properties and nanostructuring of a new layered chalcogenide semiconductor, Bi_2MnTe_4", CrystEngComm **15**, 5532–5538 (2013).

[199] J. Sánchez-Barriga, A. Varykhalov, G. Springholz, H. Steiner, R. Kirchschlager, G. Bauer, O. Caha, E. Schierle, E. Weschke, A. A. Ünal, S. Valencia, M. Dunst, J. Braun, H. Ebert, J. Minár, E. Golias, L. V. Yashina, A. Ney, V. Holý, and O. Rader, "Nonmagnetic band gap at the Dirac point of the magnetic topological insulator $(Bi_{1-x}Mn_x)_2Se_3$", Nature communications **7**, 1–10 (2016).

[200] R. Qiao, T. Chin, S. J. Harris, S. Yan, and W. Yang, "Spectroscopic fingerprints of valence and spin states in manganese oxides and fluorides", Current Applied Physics **13**, 544–548 (2013).

[201] H. Kurata and C. Colliex, "Electron-energy-loss core-edge structures in manganese oxides", Physical Review B **48**, 2102 (1993).

[202] B. Gilbert, B. H. Frazer, A. Belz, P. G. Conrad, K. H. Nealson, D. Haskel, J. C. Lang, G. Srajer, and G. De Stasio, "Multiple scattering calculations of bonding and X-ray absorption spectroscopy of manganese oxides", The Journal of Physical Chemistry A **107**, 2839–2847 (2003).

[203] G. Van der Laan and I. W. Kirkman, "The $2p$ absorption spectra of $3d$ transition metal compounds in tetrahedral and octahedral symmetry", Journal of Physics: Condensed Matter **4**, 4189 (1992).

[204] J. Stöhr, "Exploring the microscopic origin of magnetic anisotropies with X-ray magnetic circular dichroism (XMCD) spectroscopy", Journal of Magnetism and Magnetic Materials **200**, 470–497 (1999).

[205] A. M. Shikin, D. A. Estyunin, I. I. Klimovskikh, S. O. Filnov, E. F. Schwier, S. Kumar, K. Miyamoto, T. Okuda, A. Kimura, K. Kuroda, K. Yaji, S. Shin, Y. Takeda, Y. Saitoh, Z. S. Aliev, N. T. Mamedov, I. R. Amiraslanov, M. B. Babanly, M. M. Otrokov, S. V. Eremeev, and E. V. Chulkov, "Nature of the Dirac gap modulation and surface magnetic interaction in axion antiferromagnetic topological insulator $MnBi_2Te_4$", Scientific Reports **10**, 1–13 (2020).

[206] P. Kuiper, B. G. Searle, P. Rudolf, L. Tjeng, and C. Chen, "X-ray magnetic dichroism of antiferromagnet Fe_2O_3: the orientation of magnetic moments observed by Fe $2p$ X-ray absorption spectroscopy", Physical Review Letters **70**, 1549 (1993).

[207] D. Alders, L. H. Tjeng, F. C. Voogt, T. Hibma, G. A. Sawatzky, C. T. Chen, J. Vogel, M. Sacchi, and S. Iacobucci, "Temperature and thickness dependence of magnetic moments in NiO epitaxial films", Physical Review B **57**, 11623 (1998).

[208] J.-Q. Yan, Q. Zhang, T. Heitmann, Z. Huang, K. Chen, J.-G. Cheng, W. Wu, D. Vaknin, B. C. Sales, and R. J. McQueeney, "Crystal growth and magnetic structure of $MnBi_2Te_4$", Physical Review Materials **3**, 064202 (2019).

[209] Z. A. Jahangirli, E. H. Alizade, Z. S. Aliev, M. M. Otrokov, N. A. Ismayilova, S. N. Mammadov, I. R. Amiraslanov, N. T. Mamedov, G. S. Orudjev, M. B. Babanly, A. M. Shikin, and E. V. Chulkov, "Electronic structure and dielectric function of Mn-Bi-Te layered compounds", Journal of Vacuum Science & Technology B, Nanotechnology and Microelectronics: Materials, Processing, Measurement, and Phenomena **37**, 062910 (2019).

[210] A. M. Black-Schaffer, A. Balatsky, and J. Fransson, "Filling of magnetic-impurity-induced gap in topological insulators by potential scattering", Physical Review B **91**, 201411 (2015).

[211] Y. Xu, J. Chiu, L. Miao, H. He, Z. Alpichshev, A. Kapitulnik, R. R. Biswas, and L. A. Wray, "Disorder enabled band structure engineering of a topological insulator surface", Nature communications **8**, 1–7 (2017).

[212] P. M. Sass, W. Ge, J. Yan, D Obeysekera, J. Yang, and W. Wu, "Magnetic imaging of domain walls in the antiferromagnetic topological insulator $MnBi_2Te_4$", Nano letters **20**, 2609–2614 (2020).

[213] H. Kramers, "L'interaction entre les atomes magnétogènes dans un cristal paramagnétique", Physica **1**, 182–192 (1934).

[214] P. Anderson, "Antiferromagnetism. theory of superexchange interaction", Physical Review **79**, 350 (1950).

[215] D. Zhang, M. Shi, T. Zhu, D. Xing, H. Zhang, and J. Wang, "Topological axion states in the magnetic insulator $MnBi_2Te_4$ with the quantized magnetoelectric effect", Physical Review Letters **122**, 206401 (2019).

[216] J.-Q. Yan, Y. Liu, D. S. Parker, Y. Wu, A. Aczel, M. Matsuda, M. A. McGuire, and B. C. Sales, "A-type antiferromagnetic order in $MnBi_4Te_7$ and $MnBi_6Te_{10}$ single crystals", Physical Review Materials **4**, 054202 (2020).

[217] L. Ding, C. Hu, F. Ye, E. Feng, N. Ni, and H. Cao, "Crystal and magnetic structures of magnetic topological insulators $MnBi_2Te_4$ and $MnBi_4Te_7$", Physical Review B **101**, 020412 (2020).

[218] H. Xie, D. Wang, Z. Cai, B. Chen, J. Guo, M. Naveed, S. Zhang, M. Zhang, X. Wang, F. Fei, H. Zhang, and F. Song, "The mechanism exploration for zero-field ferromagnetism in intrinsic topological insulator $MnBi_2Te_4$ by Bi_2Te_3 intercalations", Applied Physics Letters **116**, 221902 (2020).

[219] C. Yan, Y. Zhu, S. Fernandez-Mulligan, E. Green, R. Mei, B. Yan, C. Liu, Z. Mao, and S. Yang, "Delicate ferromagnetism in $MnBi_6Te_{10}$", arXiv preprint: 2107.08137 (2021).

[220] A. Tan, V. Labracherie, N. Kunchur, A. U. Wolter, J. Cornejo, J. Dufouleur, B. Büchner, A. Isaeva, and R. Giraud, "Metamagnetism of weakly coupled antiferromagnetic topological insulators", Physical Review Letters **124**, 197201 (2020).

[221] I. I. Klimovskikh, M. M. Otrokov, D. Estyunin, S. V. Eremeev, S. O. Filnov, A. Koroleva, E. Shevchenko, V. Voroshnin, A. G. Rybkin, I. P. Rusinov, M. Blanco-Rey, M. Hoffmann, Z. S. Aliev, M. B. Babanly, I. R. Amiraslanov, N. A. Abdullayev, V. N. Zverev, A. Kimura, O. E. Tereshchenko, K. A. Kokh, L. Petaccia, G. D. Santo, A. Ernst, P. M. Echenique, N. T. Mamedov, A. M. Shikin, and E. V. Chulkov, "Tunable 3D/2D magnetism in the $(MnBi_2Te_4)(Bi_2Te_3)_m$ topological insulators family", npj Quantum Materials **5**, 1–9 (2020).

[222] C. Hu, L. Ding, K. N. Gordon, B. Ghosh, H.-J. Tien, H. Li, A. G. Linn, S.-W. Lien, C.-Y. Huang, S. Mackey, J. Liu, P. V. S. Reddy, B. Singh, A. Agarwal, A. Bansil, M. Song, D. Li, S.-Y. Xu, H. Lin, H. Cao, T.-R. Chang, D. Dessau, and N. Ni, "Realization of an intrinsic ferromagnetic topological state in $MnBi_8Te_{13}$", Science Advances **6**, eaba4275 (2020).

[223] B. Chen, D. Wang, Z. Jiang, B. Zhang, S. Cui, J. Guo, H. Xie, Y. Zhang, M. Naveed, Y. Du, X. Wang, H. Zhang, F. Fei, D. Shen, Z. Sun, and F. Song, "Coexistence of ferromagnetism and topology by charge carrier engineering in the intrinsic magnetic topological insulator $MnBi_4Te_7$", Physical Review B **104**, 075134 (2021).

[224] J. Wu, F. Liu, C. Liu, Y. Wang, C. Li, Y. Lu, S. Matsuishi, and H. Hosono, "Toward 2D magnets in the $(MnBi_2Te_4)(Bi_2Te_3)_n$ bulk crystal", Advanced Materials **32**, 2001815 (2020).

[225] R. C. Vidal, H. Bentmann, J. I. Facio, T. Heider, P. Kagerer, C. I. Fornari, T. R. F. Peixoto, T. Figgemeier, S. Jung, C. Cacho, B. Büchner, J. van den Brink, C. M. Schneider, L. Plucinski, E. F. Schwier, K. Shimada, M. Richter, A. Isaeva, and F. Reinert, "Orbital complexity in intrinsic magnetic topological insulators $MnBi_4Te_7$ and $MnBi_6Te_{10}$", Physical Review Letters **126**, 176403 (2021).

[226] M. Papagno, S. V. Eremeev, J. Fujii, Z. S. Aliev, M. B. Babanly, S. K. Mahatha, I. Vobornik, N. T. Mamedov, D. Pacile, and E. V. Chulkov, "Multiple coexisting Dirac surface states in three-dimensional topological insulator $PbBi_6Te_{10}$", ACS nano **10**, 3518–3524 (2016).

[227] L. Xu, Y. Mao, H. Wang, J. Li, Y. Chen, Y. Xia, Y. Li, D. Pei, J. Zhang, H. Zheng, K. Huang, C. Zhang, S. Cui, A. Liang, W. Xia, H. Su, S. Jung, C. Cacho, M. Wang, G. Li, Y. Xu, Y. Guo, L. Yang, Z. Liu, Y. Chen, and M. Jiang, "Persistent surface states with diminishing gap in $MnBi_2Te_4/Bi_2Te_3$ superlattice antiferromagnetic topological insulator", Science Bulletin **65**, 2086–2093 (2020).

[228] H. Bentmann, S. Abdelouahed, M. Mulazzi, J. Henk, and F. Reinert, "Direct observation of interband spin-orbit coupling in a two-dimensional electron system", Physical Review Letters **108**, 196801 (2012).

[229] C.-Z. Chang, P. Tang, X. Feng, K. Li, X.-C. Ma, W. Duan, K. He, and Q.-K. Xue, "Band engineering of Dirac surface states in topological-insulator-based van der Waals heterostructures", Physical Review Letters **115**, 136801 (2015).

[230] Y. Zhao, C.-Z. Chang, Y. Jiang, A. DaSilva, Y. Sun, H. Wang, Y. Xing, Y. Wang, K. He, X. Ma, Q.-K. Xue, and J. Wang, "Demonstration of surface transport in a hybrid Bi_2Se_3/Bi_2Te_3 heterostructure", Scientific Reports **3**, 1–7 (2013).

[231] P. D. C. King, R. C. Hatch, M. Bianchi, R. Ovsyannikov, C. Lupulescu, G. Landolt, B. Slomski, J. H. Dil, D. Guan, J. L. Mi, E. D. L. Rienks, J. Fink, A. Lindblad, S. Svensson, S. Bao, G. Balakrishnan, B. B. Iversen, J. Osterwalder, W. Eberhardt, F. Baumberger, and P. Hofmann, "Large tunable Rashba spin splitting of a two-dimensional electron gas in Bi_2Se_3", Physical Review Letters **107**, 096802 (2011).

[232] C. Chen, S. He, H. Weng, W. Zhang, L. Zhao, H. Liu, X. Jia, D. Mou, S. Liu, J. He, Y. Peng, Y. Feng, Z. Xie, G. Liu, X. Dong, J. Zhang, X. Wang, Q. Peng, Z. Wang, S. Zhang, F. Yang, C. Chen, Z. Xu, X. Dai, Z. Fang, and X. J. Zhou, "Robustness of topological order and formation of quantum well states in topological insulators

exposed to ambient environment", Proceedings of the National Academy of Sciences **109**, 3694–3698 (2012).

[233] Y. H. Wang, D. Hsieh, D. Pilon, L. Fu, D. R. Gardner, Y. S. Lee, and N. Gedik, "Observation of a warped helical spin texture in Bi_2Se_3 from circular dichroism angle-resolved photoemission spectroscopy", Physical Review Letters **107**, 207602 (2011).

[234] H. Zhang, C.-X. Liu, and S.-C. Zhang, "Spin-orbital texture in topological insulators", Physical Review Letters **111**, 066801 (2013).

[235] J.-H. Park, C. H. Kim, J.-W. Rhim, and J. H. Han, "Orbital Rashba effect and its detection by circular dichroism angle-resolved photoemission spectroscopy", Physical Review B **85**, 195401 (2012).

[236] J. Sánchez-Barriga, A. Varykhalov, J. Braun, S.-Y. Xu, N. Alidoust, O. Kornilov, J. Minár, K. Hummer, G. Springholz, G. Bauer, R. Schumann, L. Yashina, H. Ebert, M. Hasan, and O. Rader, "Photoemission of Bi_2Se_3 with circularly polarized light: probe of spin polarization or means for spin manipulation?", Physical Review X **4**, 011046 (2014).

[237] M. R. Scholz, J. Sánchez-Barriga, J. Braun, D. Marchenko, A. Varykhalov, M. Lindroos, Y. J. Wang, H. Lin, A. Bansil, J. Minár, H. Ebert, A. Volykhov, L. V. Yashina, and O. Rader, "Reversal of the circular dichroism in angle-resolved photoemission from Bi_2Te_3", Physical Review Letters **110**, 216801 (2013).

[238] J. Sánchez-Barriga, M. R. Scholz, E. Golias, E. Rienks, D. Marchenko, A. Varykhalov, L. V. Yashina, and O. Rader, "Anisotropic effect of warping on the lifetime broadening of topological surface states in angle-resolved photoemission from Bi_2Te_3", Physical Review B **90**, 195413 (2014).

[239] K. Kuroda, M. Arita, K. Miyamoto, M. Ye, J. Jiang, A. Kimura, E. E. Krasovskii, E. V. Chulkov, H. Iwasawa, T. Okuda, K. Shimada, Y. Ueda, H. Namatame, and M. Taniguchi, "Hexagonally deformed *fermi* surface of the 3D topological insulator Bi_2Se_3", Physical Review Letters **105**, 076802 (2010).

[240] S. Souma, K. Kosaka, T. Sato, M. Komatsu, A. Takayama, T. Takahashi, M. Kriener, K. Segawa, and Y. Ando, "Direct measurement of the out-of-plane spin texture in the Dirac-cone surface state of a topological insulator", Physical Review Letters **106**, 216803 (2011).

[241] S. R. Park, J. Han, C. Kim, Y. Y. Koh, C. Kim, H. Lee, H. J. Choi, J. H. Han, K. D. Lee, N. J. Hur, M. Arita, K. Shimada, H. Namatame, and M. Taniguchi, "Chiral orbital-angular momentum in the surface states of Bi_2Se_3", Physical Review Letters **108**, 046805 (2012).

[242] W. Jung, Y. Kim, B. Kim, Y. Koh, C. Kim, M. Matsunami, S. ichi Kimura, M. Arita, K. Shimada, J. H. Han, J. Kim, B. Cho, and C. Kim, "Warping effects in the band and angular-momentum structures of the topological insulator Bi_2Te_3", Physical Review B **84**, 245435 (2011).

[243] Y. Wang and N. Gedik, "Circular dichroism in angle-resolved photoemission spectroscopy of topological insulators", physica status solidi (RRL)–Rapid Research Letters **7**, 64–71 (2013).

[244] H. Bentmann, H. Maaß, J. Braun, C. Seibel, K. A. Kokh, O. E. Tereshchenko, S. Schreyeck, K. Brunner, L. W. Molenkamp, K. Miyamoto, M. Arita, K. Shimada, T. Okuda, J. Kirschner, C. Tusche, H. Ebert, J. Minár, and F. Reinert, "Profiling spin and orbital texture of a topological insulator in full momentum space", Physical Review B **103**, L161107 (2021).

[245] K. N. Gordon, H. Sun, C. Hu, A. G. Linn, H. Li, Y. Liu, P. Liu, S. Mackey, Q. Liu, N. Ni, and D. Dessau, "Strongly gapped topological surface states on protected surfaces of antiferromagnetic $MnBi_4Te_7$ and $MnBi_6Te_{10}$", arXiv preprint arXiv:1910.13943 (2019).

[246] S. Tian, S. Gao, S. Nie, Y. Qian, C. Gong, Y. Fu, H. Li, W. Fan, P. Zhang, T. Kondo, S. Shin, J. Adell, H. Fedderwitz, H. Ding, Z. Wang, T. Qian, and H. Lei, "Magnetic topological insulator $MnBi_6Te_{10}$ with a zero-field ferromagnetic state and gapped Dirac surface states", Physical Review B **102**, 035144 (2020).

[247] C.-H. Min, H. Bentmann, J. N. Neu, P. Eck, S. Moser, T. Figgemeier, M. Ünzelmann, K. Kissner, P. Lutz, R. J. Koch, C. Jozwiak, A. Bostwick, E. Rotenberg, R. Thomale, G. Sangiovanni, T. Siegrist, D. D. Sante, and F. Reinert, "Orbital fingerprint of topological Fermi arcs in the Weyl semimetal TaP", Physical Review Letters **122**, 116402 (2019).

[248] C. Jozwiak, J. A. Sobota, K. Gotlieb, A. F. Kemper, C. R. Rotundu, R. J. Birgeneau, Z. Hussain, D.-H. Lee, Z.-X. Shen, and A. Lanzara, "Spin-polarized surface resonances accompanying topological surface state formation", Nature communications **7**, 13143 (2016).

[249] Y.-J. Hao, P. Liu, Y. Feng, X.-M. Ma, E. F. Schwier, M. Arita, S. Kumar, C. Hu, R. Lu, M. Zeng, Y. Wang, Z. Hao, H.-Y. Sun, K. Zhang, J. Mei, N. Ni, L. Wu, K. Shimada, C. Chen, Q. Liu, and C. Liu, "Gapless surface Dirac cone in antiferromagnetic topological insulator $MnBi_2Te_4$", Physical Review X **9**, 041038 (2019).

[250] Y. Chen, L. Xu, J. Li, Y. Li, H. Wang, C. Zhang, H. Li, Y. Wu, A. Liang, C. Chen, S. Jung, C. Cacho, Y. Mao, S. Liu, M. Wang, Y. Guo, Y. Xu, Z. Liu, L. Yang, and Y. Chen, "Topological electronic structure and its temperature evolution in antiferromagnetic topological insulator $MnBi_2Te_4$", Physical Review X **9**, 041040 (2019).

[251] D. A. Estyunin, I. I. Klimovskikh, A. M. Shikin, E. F. Schwier, M. M. Otrokov, A. Kimura, S. Kumar, S. O. Filnov, Z. S. Aliev, M. B. Babanly, and E. V. Chulkov, "Signatures of temperature driven antiferromagnetic transition in the electronic structure of topological insulator $MnBi_2Te_4$", APL Materials **8**, 021105 (2020).

[252] H. Li, S.-Y. Gao, S.-F. Duan, Y.-F. Xu, K.-J. Zhu, S.-J. Tian, J.-C. Gao, W.-H. Fan, Z.-C. Rao, J.-R. Huang, J.-J. Li, D.-Y. Yan, Z.-T. Liu, W.-L. Liu, Y.-B. Huang, Y.-L. Li, Y. Liu, G.-B. Zhang, P. Zhang, T. Kondo, S. Shin, H.-C. Lei, Y.-G. Shi, W.-T. Zhang, H.-M. Weng, T. Qian, and H. Ding, "Dirac surface states in intrinsic magnetic topological insulators $EuSn_2As_2$ and $MnBi_2nTe_{3n+1}$", Physical Review X **9**, 041039 (2019).

[253] P. Swatek, Y. Wu, L.-L. Wang, K. Lee, B. Schrunk, J. Yan, and A. Kaminski, "Gapless Dirac surface states in the antiferromagnetic topological insulator $MnBi_2Te_4$", Physical Review B **101**, 161109 (2020).

[254] Y. Hu, L. Xu, M. Shi, A. Luo, S. Peng, Z. Y. Wang, J. J. Ying, T. Wu, Z. K. Liu, C. F. Zhang, Y. L. Chen, G. Xu, X.-H. Chen, and J.-F. He, "Universal gapless Dirac cone and tunable topological states in $(MnBi_2Te_4)_m$ $(Bi_2Te_3)_n$ heterostructures", Physical Review B **101**, 161113 (2020).

[255] D. Nevola, H. X. Li, J.-Q. Yan, R. Moore, H.-N. Lee, H. Miao, and P. D. Johnson, "Coexistence of surface ferromagnetism and a gapless topological state in $MnBi_2Te_4$", Physical Review Letters **125**, 117205 (2020).

[256] C. Yan, S. Fernandez-Mulligan, R. Mei, S. H. Lee, N. Protic, R. Fukumori, B. Yan, C. Liu, Z. Mao, and S. Yang, "Origins of electronic bands in antiferromagnetic topological insulator $MnBi_2Te_4$", arXiv preprint arXiv:2105.07093 (2021).

[257] X.-M. Ma, Y. Zhao, K. Zhang, S. Kumar, R. Lu, J. Li, Q. Yao, J. Shao, F. Hou, X. Wu, M. Zeng, Y.-J. Hao, Z. Hao, Y. Wang, X.-R. Liu, H. Shen, H. Sun, J. Mei, K. Miyamoto, T. Okuda, M. Arita, E. F. Schwier, K. Shimada, K. Deng, C. Liu, J. Lin,

Y. Zhao, C. Chen, Q. Liu, and C. Liu, "Realization of a tunable surface Dirac gap in Sb-doped $MnBi_2Te_4$", Physical Review B **103**, L121112 (2021).

[258] M. Bahramy, P. King, A. de la Torre, J. Chang, M. Shi, L. Patthey, G. Balakrishnan, P. Hofmann, R. Arita, N. Nagaosa, and F. Baumberger, "Emergent quantum confinement at topological insulator surfaces", Nature communications **3**, 1–7 (2012).

[259] S. Eremeev, M. Vergniory, T. V. Menshchikova, A. Shaposhnikov, and E. V. Chulkov, "The effect of van der Waal's gap expansions on the surface electronic structure of layered topological insulators", New Journal of Physics **14**, 113030 (2012).

[260] G. Liang and Y. Chong, "Optical resonator analog of a two-dimensional topological insulator", Physical Review Letters **110**, 203904 (2013).

[261] C. He, X. Ni, H. Ge, X.-C. Sun, Y.-B. Chen, M.-H. Lu, X.-P. Liu, and Y.-F. Chen, "Acoustic topological insulator and robust one-way sound transport", Nature physics **12**, 1124–1129 (2016).

[262] S. Imhof, C. Berger, F. Bayer, J. Brehm, L. W. Molenkamp, T. Kiessling, F. Schindler, C. H. Lee, M. Greiter, T. Neupert, and R. Thomale, "Topolectrical-circuit realization of topological corner modes", Nature Physics **14**, 925–929 (2018).

[263] R. Süsstrunk and S. D. Huber, "Observation of phononic helical edge states in a mechanical topological insulator", Science **349**, 47–50 (2015).

[264] S. Chadov, X. Qi, J. Kübler, G. H. Fecher, C. Felser, and S. C. Zhang, "Tunable multifunctional topological insulators in ternary heusler compounds", Nature materials **9**, 541–545 (2010).

[265] E. Olshanetsky, Z. Kvon, G. Gusev, A. Levin, O. Raichev, N. Mikhailov, and S. Dvoretsky, "Persistence of a two-dimensional topological insulator state in wide HgTe quantum wells", Physical Review Letters **114**, 126802 (2015).

[266] R. Lu, H. Sun, S. Kumar, Y. Wang, M. Gu, M. Zeng, Y.-J. Hao, J. Li, J. Shao, X.-M. Ma, Z. Hao, K. Zhang, W. Mansuer, J. Mei, Y. Zhao, C. Liu, K. Deng, W. Huang, B. Shen, K. Shimada, E. Schwier, C. Liu, Q. Liu, and C. Chen, "Half-magnetic topological insulator with magnetization-induced Dirac gap at a selected surface", Physical Review X **11**, 011039 (2021).

[267] P. Kagerer, "Private Communication", 2021.

[268] D. Xiao, J. Jiang, J.-H. Shin, W. Wang, F. Wang, Y.-F. Zhao, C. Liu, W. Wu, M. H. Chan, N. Samarth, and C.-Z. Chang, "Realization of the axion insulator state in quantum anomalous hall sandwich heterostructures", Physical Review Letters **120**, 056801 (2018).

[269] P. Kagerer, C. I. Fornari, S. Buchberger, S. L. Morelhão, R. C. Vidal, A. Tcakaev, V. Zabolotnyy, E. Weschke, V. Hinkov, M. Kamp, B. Büchner, A. Isaeva, H. Bentmann, and F. Reinert, "Molecular beam epitaxy of antiferromagnetic ($MnBi_2Te_4$)(Bi_2Te_3) thin films on BaF_2 (111)", Journal of Applied Physics **128**, 135303 (2020).

[270] K. Zhu, Y. Bai, X. Hong, Z. Geng, Y. Jiang, R. Liu, Y. Li, M. Shi, L. Wang, W. Li, Q.-K. Xue, X. Feng, and K. He, "Investigating and manipulating the molecular beam epitaxy growth kinetics of intrinsic magnetic topological insulator $MnBi_2Te_4$ with *in situ* angle-resolved photoemission spectroscopy", Journal of Physics: Condensed Matter **32**, 475002 (2020).

[271] T. Zhu, A. J. Bishop, T. Zhou, M. Zhu, D. J. O'Hara, A. A. Baker, S. Cheng, R. C. Walko, J. J. Repicky, T. Liu, J. A. Gupta, C. M. Jozwiak, E. Rotenberg, J. Hwang, I. Žutić, and R. K. Kawakami, "Synthesis, magnetic properties, and electronic structure of magnetic topological insulator $MnBi_2Se_4$", Nano Letters (2021).

[272] S. Wimmer, J. Sánchez-Barriga, P. Küppers, A. Ney, E. Schierle, F. Freyse, O. Caha, J. Michalička, M. Liebmann, D. Primetzhofer, M. Hoffman, A. Ernst, M. M. Otrokov, G. Bihlmayer, E. Weschke, B. Lake, E. V. Chulkov, M. Morgenstern, G. Bauer, G. Springholz, and O. Rader, "Ferromagnetic $MnSb_2Te_4$: A topological insulator with magnetic gap closing at high Curie temperatures of 45-50 K", arXiv preprint arXiv:2011.07052 (2020).

[273] S. Huan, S. Zhang, Z. Jiang, H. Su, H. Wang, X. Zhang, Y. Yang, Z. Liu, X. Wang, N. Yu, Z. Zou, D. Shen, J. Liu, and Y. Guo, "Multiple magnetic topological phases in bulk van der Waals crystal $MnSb_4Te_7$", Physical Review Letters **126**, 246601 (2021).

[274] T. Murakami, Y. Nambu, T. Koretsune, G. Xiangyu, T. Yamamoto, C. M. Brown, and H. Kageyama, "Realization of interlayer ferromagnetic interaction in $MnSb_2Te_4$ toward the magnetic Weyl semimetal state", Physical Review B **100**, 195103 (2019).

[275] Y. Liu, L.-L. Wang, Q. Zheng, Z. Huang, X. Wang, M. Chi, Y. Wu, B. C. Chakoumakos, M. A. McGuire, B. C. Sales, W. Wu, and J. Yan, "Site mixing for engineering magnetic topological insulators", Physical Review X **11**, 021033 (2021).

[276] S. V. Eremeev, I. P. Rusinov, Y. M. Koroteev, A. Y. Vyazovskaya, M. Hoffmann, P. M. Echenique, A. Ernst, M. M. Otrokov, and E. V. Chulkov, "Topological magnetic materials of the ($MnBi_2Sb_4$)·(Sb_2Te_3)$_n$ van der Waals compounds family", The Journal of Physical Chemistry Letters **12**, 4268–4277 (2021).

[277] B. Chen, F. Fei, D. Zhang, B. Zhang, W. Liu, S. Zhang, P. Wang, B. Wei, Y. Zhang, Z. Zuo, J. Guo, Q. Liu, Z. Wang, X. Wu, J. Zong, X. Xie, W. Chen, Z. Sun, S. Wang, Y. Zhang, M. Zhang, X. Wang, F. Song, H. Zhang, D. Shen, and B. Wang, "Intrinsic magnetic topological insulator phases in the Sb doped $MnBi_2Te_4$ bulks and thin flakes", Nature communications **10**, 1–8 (2019).

[278] S. H. Lee, D. Graf, L. Min, Y. Zhu, H. Yi, S. Ciocys, Y. Wang, E. Choi, R. Basnet, A. Fereidouni, A. Wegner, Y.-F. Zhao, K. Verlinde, J. He, R. Redwing, V. Gopalan, H. O. Churchill, A. Lanzara, N. Samarth, C.-Z. Chang, J. Hu, and Z. Mao, "Evidence for a magnetic-field-induced ideal type-II Weyl state in antiferromagnetic topological insulator $Mn(Bi_{1-x}Sb_x)_2Te_4$", Physical Review X **11**, 031032 (2021).

List of own publications

- **R. C. Vidal**, G. Marini, L. Lunczer, S. Moser, L. Fürst, J. Issing, C. Jozwiak, A. Bostwick, E. Rotenberg, C. Gould, H. Buhmann, W. Beugling, G. Sangiovanni, D. Di Sante, G. Profeta, L. W. Molenkamp, H. Bentmann, and F. Reinert, "Topological band inversion in HgTe(001): Surface and bulk signatures from photoemission", Physical Review B **107**, L121102 (2023).

- **R. C. Vidal**, H. Bentmann, J. I. Facio, T. Heider, P. Kagerer, C. I. Fornari, T. R. F. Peixoto, T. Figgemeier, S. Jung, C. Cacho, B. Büchner, J. van den Brink, C. M. Schneider, L. Plucinski, E. F. Schwier, K. Shimada, M. Richter, A. Isaeva, and F. Reinert, "Orbital complexity in intrinsic magnetic topological insulators $MnBi_4Te_7$ and $MnBi_6Te_{10}$", Physical Review Letters **126**, 176403 (2021).

- T. R. F. Peixoto, H. Bentmann, P. Rüßmann, A.-V. Tcakaev, M. Winnerlein, S. Schreyeck, S. Schatz, **R. C. Vidal**, F. Stier, V. Zabolotnyy, R. J. Green, C. H. Min, C. I. Fornari, H. Maaß, H. B. Vasili, P. Gargiani, M. Valvidares, A. Barla, J. Buck, M. Hoesch, F. Diekmann, S. Rohlf, M. Kalläne, K. Rossnagel, C. Gould, K. Brunner, S. Blügel, V. Hinkov, L. W. Molenkamp, and F. Reinert, "Non-local effect of impurity states on the exchange coupling mechanism in magnetic topological insulators", npj Quantum Materials **5**, 1-6 (2020).

- P. Kagerer, C. Fornari, S. Buchberger, S. Morelhão, **R. Vidal**, A. Tcakaev, V. Zabolotnyy, E. Weschke, V. Hinkov, M. Kamp, B. Büchner, A. Isaeva, H. Bentmann, and F. Reinert, "Molecular beam epitaxy of antiferromagnetic $(MnBi_2Te_4)(Bi_2Te_3)$ thin films on BaF_2 (111)", Journal of Applied Physics **128**, 135303 (2020).

- C. I. Fornari, H. Bentmann, S. L. Morelhão, T. R. Peixoto, P. H. Rappl, A.-V. Tcakaev, V. Zabolotnyy, M. Kamp, T.-L. Lee, C.-H. Min, P. Kagerer, **R. C. Vidal**, A. Isaeva, M. Ruck, V. Hinkov, F. Reinert, and E. Abramof, "Incorporation of europium in Bi_2Te_3 topological insulator epitaxial films", The Journal of Physical Chemistry C **124**, 16048-16057 (2020).

- M. Ünzelmann, H. Bentmann, P. Eck, T. Kißlinger, B. Geldiyev, J. Rieger, S. Moser, **R. C. Vidal**, K. Kißner, L. Hammer, M. A. Schneider, T. Fauster, G. Sangiovanni, D. D. Sante, and F. Reinert, "Orbital-driven Rashba effect in a binary honeycomb monolayer AgTe", Physical Review Letters **124**, 176401 (2020).

- A. Tcakaev, V. Zabolotnyy, R. Green, T. Peixoto, F. Stier, M. Dettbarn, S. Schreyeck, M. Winnerlein, **R. C. Vidal**, S. Schatz, H. B. Vasili, M. Valvidares, K. Brunner, C. Gould, H. Bentmann, F. Reinert, L. W. Molenkamp, and V. Hinkov, "Comparing magnetic ground-state properties of the V- and Cr-doped topological insulator $(Bi,Sb)_2Te_3$", Physical Review B **101**, 045127 (2020).

- **R. C. Vidal**, A. Zeugner, J. I. Facio, R. Ray, M. H. Haghighi, A. U. Wolter, L. T. C. Bohorquez, F. Caglieris, S. Moser, T. Figgemeier, T. R. Peixoto, H. B. Vasili, M. Valvidares, S. Jung, C. Cacho, A. Alfonsov, K. Mehlawat, V. Kataev, C. Hess, M. Richter, B. Büchner, J. van den Brink, M. Ruck, F. Reinert, H. Bentmann, and A. Isaeva, "Topological electronic structure and intrinsic magnetization in $MnBi_4$ Te_7: A Bi_2Te_3 derivative with a periodic Mn sublattice", Editors' Suggestion, Physical Review X **9**, 041065 (2019).

- M. M. Otrokov, I. I. Klimovskikh, H. Bentmann, D. Estyunin, A. Zeugner, Z. S. Aliev, S. Gaß, A. Wolter, A. Koroleva, A. M. Shikin, M. Blanco-Rey, M. Hoffmann, I. P. Rusinov, A. Yu Vyazovskaya, S. V. Eremeev, Y. M. Koroteev, V. M. Kuznetsov, F. Freyse, J. Sánchez-Barriga, I. R. Amiraslanov, M. B. Babanly, N. T. Mamedov, N. A. Abdullayev, V. N. Zverev, A. Alfonsov, V. Kataev, B. Büchner, E. F. Schwier, S. Kumar, A. Kimura, L. Petaccia, G. Di Santo, **R. C. Vidal**, S. Schatz, K. Kißner, M. Ünzelmann, C. H. Min, S. Moser, T. R. F. Peixoto, F. Reinert, A. Ernst, P. M. Echenique, A. Isaeva, and E. V. Chulkov, "Prediction and observation of an antiferromagnetic topological insulator", Nature **576**, 416-422 (2019).

- **R. C. Vidal**, H. Bentmann, T. R. F. Peixoto, A. Zeugner, S. Moser, C.-H. Min, S. Schatz, K. Kißner, M. Ünzelmann, C. I. Fornari, H. B. Vasili, M. Valvidares, K. Sakamoto, D. Mondal, J. Fujii, I. Vobornik, S. Jung, C. Cacho, T. K. Kim, R. J. Koch, C. Jozwiak, A. Bostwick, J. D. Denlinger, E. Rotenberg, J. Buck, M. Hoesch, F. Diekmann, S. Rohlf, M. Kalläne, K. Rossnagel, M. M. Otrokov, E. V. Chulkov, M. Ruck, A. Isaeva, and F. Reinert, "Surface states and Rashba-type spin polarization in antiferromagnetic $MnBi_2Te_4(0001)$", Editors' Suggestion, Rapid Communication, Physical Review B **100**, 121104 (2019).

- A. Zeugner, F. Nietschke, A. U. Wolter, S. Gaß, **R. C. Vidal**, T. R. Peixoto, D. Pohl, C. Damm, A. Lubk, R. Hentrich, S. K. Moser, C. Fornari, C. H. Min, S. Schatz, K. Kißner, M. Ünzelmann, M. Kaiser, F. Scaravaggi, B. Rellinghaus, K. Nielsch, C. Hess, B. Büchner, F. Reinert, H. Bentmann, O. Oeckler, T. Doert, M. Ruck, and A. Isaeva, "Chemical aspects of the candidate antiferromagnetic topological insulator $MnBi_2Te_4$", Chemistry of Materials **31**, 2795-2806 (2019).

Danksagung

Eine Arbeit wie die hier vorliegende ist schlussendlich nicht das Werk von nur einer Person. In diesem letzten Abschnitt möchte ich mir die Zeit nehmen, all denjenigen zu danken, die auf ihre Art zum Gelingen beigetragen haben. Diese Beiträge - fachlicher oder persönlicher Natur - waren entscheidende Unterstützungen in der Entstehungsphase dieser Arbeit.
Allen voran gilt mein Dank natürlich meinem Doktorvater Prof. Friedrich Reinert, der mir durch sein Vertrauen in meine wissenschaftliche Arbeit ein freies Herangehen an meine Thematik ermöglicht hat. Des Weiteren bot er mir die Möglichkeit an verschiedenen Konferenzen, Workshops und Retreats teilzunehmen, welche durch interessante Vorträge und anregende Diskussionen stets eine Bereicherung waren. Außerdem bot sein Lehrstuhl mir die Gelegenheiten zu den zahlreichen Strahlzeiten, ohne die diese Arbeit nicht hätte entstehen können.
Mein Dank gilt auch Dr. Hendrik Bentmann, der mit einer herausragenden und intensiven Betreuung sowie unzähligen konstruktiven Diskussionen maßgeblich zum Gelingen dieser Arbeit beigetragen hat. Durch viele Denkanstöße und Anregungen bezüglich der Datenanalyse und -interpretation hat er mein Verständnis gefördert und damit die gemeinsamen Publikationen ermöglicht. Für all das und seine unerschöpfliche Geduld gilt ihm mein besonderer Dank.
Prof. Dr. Ralph Claessen möchte ich für die Erstellung des Zweitgutachtens danken.
Mehrere Korrekturleser haben mir dabei geholfen die ein oder andere Falte in meiner Arbeit auszubügeln. Mein Dank gilt hier Dr. Hendrik Bentmann, Max Ünzelmann und Lisa Mündlein.
Die Daten, welche im Laufe der Arbeit vorgestellt werden sind größtenteils im Rahmen mehrerer externer Messzeiten entstanden. Diese wurden nicht alleine durchgeführt sondern stets mit einigen meiner Kollegen aus dem Lehrstuhl in Teamarbeit durchgeführt. Ich danke deshalb Philipp Kagerer, Dr. Thiago Peixoto, Sonja Schatz, Tim Figgemeier, Katharina Kißner, Max Ünzelmann, Celso Fornari und Dr. Chul-Hee Min, die sich mit mir die eine oder andere Nacht um die Ohren geschlagen haben und diese mit physikalischen und nichtphysikalischen Gesprächen gefüllt haben.
Vor Ort haben wir zudem stets fachliche Unterstützung von den Wissenschaftlern des jeweiligen Instituts erhalten, die uns in die Bedienung der vorhandenen Instrumente eingeführt haben sowie teilweise beratend für die Durchführung der Messung zur Hilfe standen.
Eli Rotenberg und seinem Team rund um die MAESTRO Endstation danke ich für eine lehrreiche und ertragreiche Messzeit inklusive unerwarteter Erdbeben-Sicherheitsübung.

Besonders ist an dieser Stelle Dr. Simon Moser zu erwähnen, der nicht nur als Bindeglied zwischen den Kontinenten fungiert hat, sondern auch die Messzeit und die Zeit danach mit seiner wissenschaftlicher Expertise und seinem Charme bereichert hat.
Für die Messzeit am ALBA Synchrotron standen vor Ort Manual Valvidares und Hari Babu Vasili tatkräftig zur Hilfe. Zudem danke ich Pierluigi Gargiani, der geduldig meine Fragen zur Auswertung von den dort aufgenommenen Daten beantwortet hat.
Cephise Cacho und Sungwong Jung haben an der i05 Beamline des Diamond Synchrotrons ein produktives Arbeitsumfeld geschaffen, das es ermöglicht, vielseitige und hochqualitative Messungen innerhalb der begrenzten Zeit durchzuführen.
Kenya Shimada und Eike Schwier danke ich für die Messzeit an ihrem μ-ARPES Aufbau in Hiroshima.
Für die Strahlzeiten an PetraIII danke ich Moritz Hoesch, der sich, zusammen mit seinem Team, um die Strahllinie und alles darum herum gekümmert hat. Für eine reibungslose Benutzung der UHV-Kammer ASPHERE III waren die Kollegen von der Universität Kiel ein wichtiger Bestandteil. Hier sind allen voran Dr. Matthias Kalläne und Dr. Jens Buck aus der Arbeitsgruppe um Prof. Kai Roßnagel zu nennen.
Des Weiteren danke ich Prof. Claus Michael Schneider und Dr. Lukasz Plucinski für die Möglichkeit, Experimente an ihrem Laser-ARPES Aufbau durchzuführen. Für die Unterstützung bei der Ausführung der Experimente und der darauffolgenden Auswertung danke ich zudem Tristan Heider.
Theoretische Berechnungen stellen ebenfalls einen wichtigen Bestandteil dieser Arbeit dar. Für das Materialsystem HgTe sind hier Prof. Giorgio Sangovanni und Dr. Domenico Di Sante zu nennen, die eine fruchtbare Kooperation mit Prof. Gianni Profeta und Dr. Giovanni Marini eingeleitet haben und sich an den zahlreichen, regen Diskussionen beteiligt haben. Im Falle der $MnBi_2Te_4$-basierten Systeme danke ich Dr. Jorge Facio und Dr. Manuel Richter für die theoretischen Daten sowie anregende Diskussionen bezüglich der Interpretation. Ohne diesen wichtigen Beitrag seitens der Theorie ist eine eindeutige Interpretation der Photoemissionsdaten oftmals nicht möglich.
Einen wichtigen Beitrag stellt selbstverständlich auch das Her- und Bereitstellen der Proben dar. Hier bedanke ich mich bei Dr. Raimund Schlereth, Lukas Lunczer und Lena Fürst aus dem Lehrstuhl um Prof. Hartmut Buhmann und Prof. Laurens Molenkamp für die HgTe-Dünnschichten. Im Falle der magnetischen Systeme gilt mein Dank Dr. Alexander Zeugner und Dr. Anna Isaeva, die oft auch kurzfristig noch Proben zur Verfügung stellen konnten.
Im Laufe meiner Promotion hatte ich zudem das Vergnügen zwei Bachelorarbeiten sowie eine
Masterarbeit zu betreuen. Die interessierten Fragen der Studenten haben das ein ums andere mal dafür gesorgt, dass ich mich sich selbst noch tiefer mit gewissen Thematiken auseinan-

der gesetzt habe. Auch wenn ihre Ergebnisse nicht direkt Teil dieser Arbeit geworden sind beziehungsweise diese nur tangiert haben, habe ich die Zeit dennoch genossen. Danke euch Dreien.
Neben all diesen wissenschaftlichen Beiträgen habe ich auch noch meinen Kollegen aus dem Lehrstuhl dafür zu danken, dass mir dort eine unvergleichliche Zeit bereitet haben. Allen voran sind das natürlich meine Bürokollegen Katharina Kißner, Max Ünzelmann und Tim Figgemeier die neben wissenschaftlichen Diskussionen auch anderweitig dafür gesorgt haben, dass es nie zu Langeweile kam. Die frühmorgentlichen Joggingtouren mit Max und die zeitweise schon wöchentlichen Besuche im Pham Wok sind nur zwei der Dinge an die ich noch lange mit einem Lächeln auf dem Gesicht zurück denken werde. Dank Philipp Kagerer wurde keine noch so lange Nachtschicht langwierig, solange noch genug Snacks zur Hand waren, und sei es zur Not Garnelen-Suppe aus dem Automaten. Mit Kiana Baumgärtner und Dr. Christian Metzger habe ich viele schöne Spiele- und Kochabende verbracht, auch wenn ich manchmal den Enthusiasmus der beiden bremsen und dafür sorgen musste, dass man sich nicht zu weit vom eigentlichen Rezept entfernt. Danke euch allen für die tolle Zeit.
Mein ganz persönlicher Dank gilt vor allem auch meinem persönlichen Umfeld. Das sind zum einen meine engen Freunde, die mir scheinbar immer zu den richtigen Momenten zur Zerstreuung abseits der Physik verholfen haben. Andererseits aber natürlich meine Familie, mein Vater Feridun Yücedinc, meine Mutter Begoña Crespo Vidal und meine Schwester Meral Crespo Vidal, die mir immer emotional zur Seite standen und denen ich mich trotz der räumlichen Entfernung immer nah gefühlt habe.
Danken möchte ich auch meiner Partnerin Isabel Roos, die mir während der Vorbereitung für das Promotionskolloquium viel Rückhalt gegeben hat. Danke, dass du so bist, wie du bist.